COLLISIONAL EFFECTS IN THE ABSORPTION
SPECTRA OF THE OXYGEN A BAND AND
NITRIC OXIDE FUNDAMENTAL BAND

DISSERTATION

Robert S. Pope, Captain, USAF

AFIT/DS/ENP/98-03

19990402 004

DEPARTMENT OF THE AIR FORCE
AIR UNIVERSITY

AIR FORCE INSTITUTE OF TECHNOLOGY

DTIC QUALITY INSPECTED 2

Wright-Patterson Air Force Base, Ohio

AFIT/DS/ENP/98-03

AFIT/DS/ENP/98-03

COLLISIONAL EFFECTS IN THE ABSORPTION SPECTRA

OF THE OXYGEN A BAND AND NITRIC OXIDE FUNDAMENTAL BAND

DISSERTATION

Presented to the Faculty of the School of Engineering

of the Air Force Institute of Technology

Air Education and Training Command

In Partial Fulfillment of the

Requirements for the Degree of

Doctor of Philosophy
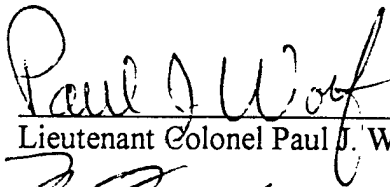
Robert S. Pope, B.S., M.S.

Captain, USAF

December 1998

COLLISIONAL EFFECTS IN THE ABSORPTION SPECTRA

OF THE OXYGEN A BAND AND NITRIC OXIDE FUNDAMENTAL BAND

Robert S. Pope, B.S., M.S.
Captain, USAF

Approved:

_____
Lieutenant Colonel Paul J. Wolf (Chairman)
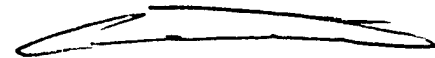
_____
Dr. Milton E. Franke (Dean's Representative)

_____
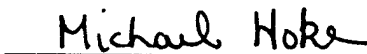Lieutenant Colonel Glen P. Perram

_____
Dr. Dennis W. Quinn

_____
Dr. Michael Hoke

Accepted:

_____
Dr. Robert A. Calico
Dean, Graduate School of Engineering

Acknowledgements

Table of Contents

List of Figures

x

List of Tables

AFIT/DS/ENP/98-03

Abstract

Fourier transform spectroscopy (FTS) was used to measure pressure broadening rate coefficients in the absorption spectra of both the oxygen A band at 13122 cm^{-1} and the nitric oxide fundamental band at 1876 cm^{-1}. FTS facilitated the simultaneous acquisition of high-precision lineshape data for many rotational lines, which allowed the data to be used to explore the observed trends with initial rotational level. Oxygen spectra were recorded at 0.032 cm^{-1} resolution with He, Ne, Ar, Kr, Xe, O_2, N_2, CO, CO_2, and SF_6 collision partners at bath gas pressures from 100 – 800 torr. Nitric oxide spectra were recorded at 0.004 or 0.005 cm^{-1} resolution using noble gas collision partners with bath gas pressures from 10 – 200 torr.

Pressure broadening coefficients and cross sections were determined in the P and R branches for every resolved line for each of the fifteen collision pairs studied. Oxygen broadening coefficients for $J'' = 5$ ranged from 3.98 ± 0.11 cm^{-1}/torr for collisions with Ne to 8.8 ± 0.3 cm^{-1}/torr for collisions with SF_6. Nitric oxide broadening coefficients for $J'' = 4.5$ ranged from 5.4 ± 0.2 cm^{-1}/torr for collisions with Ne to 7.74 ± 0.10 cm^{-1}/torr for collisions with Xe. The broadening coefficients showed a decreasing trend with increasing initial rotational quantum number, J''. For example, broadening coefficients for O_2+Ar ranged from 7.1 ± 0.6 cm^{-1}/torr for $J'' = 1$ to 4.1 ± 0.4 cm^{-1}/torr for $J'' = 20$. Instrumental broadening was found to be on the same order as the measurement uncertainty and no Dicke narrowing was observed so a Voigt profile was used to fit each

line. In addition, broadening coefficients and qualitative evidence of line coupling were found for the Q branch of NO+Ar and pressure-induced line shifting coefficients were measured for O_2+Xe.

Elastic and inelastic theories of pressure broadening were used to interpret the observed broadening cross sections. The elastic model showed a strong correlation between the magnitude of the cross sections and the polarizability and mass of the perturber. The model also correlated well with the expected quadrupole-induced dipole potential for O_2. The elastic model, however, did not predict the observed decrease in broadening coefficient with increasing J''.

The inelastic contribution to pressure broadening was modeled using both angular-momentum-based and energy-based fitting laws. The power-law version of the energy-corrected-sudden law (ECS-P) and the hybrid exponential/power-gap law with m-conserving degeneracy (EPGL-0) provided the best fits to the O_2 data. While both inelastic models correctly reproduced the observed trends with J'', the fitting parameters of the ECS-P law correlated with physical properties of the interaction (reduced mass and the order of the intermolecular potential), while the EPGL-0 parameters showed no correlation. These results indicate that the inelastic component is an important contribution to collisional broadening in diatomic molecules and that the angular-momentum picture sheds more light on the important parameters of the interaction than does the energy-based picture.

COLLISIONAL EFFECTS IN THE ABSORPTION SPECTRA

OF THE OXYGEN A BAND AND NITRIC OXIDE FUNDAMENTAL BAND

I. Introduction

The central focus of this research project was to study collisional effects on the

absorption spectra of the diatomic molecules O_2 and NO. Collisional effects on spectral

lines have been studied for over a century. However, recent advances in instrumentation

have dramatically improved the ability to measure these effects in the laboratory, while

advances in theory have made steps toward an improved understanding of the underlying

collision process.

In the most general sense, the interaction of an atom or molecule with a

monochromatic wave of infinite duration would produce an infinitely-narrow spectral

line. However, the radiation absorbed by atoms and molecules is of finite duration,

governed by the lifetime of the states connected by the absorption transition. The

resulting natural line shape is described by a Lorentzian profile with a width called the

natural width.

For a moving absorber, the frequency perceived by the absorbing molecule is

Doppler-shifted from the value for the same transition in a stationary molecule. A gas in

thermal equilibrium has molecules with a Maxwell-Boltzmann distribution of velocities.

This thermal distribution of velocities produces a spectral line with a with a Gaussian

lineshape. For molecules in thermal equilibrium at room temperature, the Doppler width is several orders of magnitude larger than the natural width, so the natural width can be neglected.

Collisions between the absorbing atom or molecule and bath gas atoms or molecules further perturb the lineshape. For molecular absorbers, these collisions may be either elastic or inelastic in the resulting internal energy distributions. Elastic collisions change the phase of the rotating molecule with respect to the radiation, which broadens the resulting spectral line. Inelastic collisions transfer energy between translation and an internal mode of the molecule, like rotation or vibration. In this case, the collision changes the states involved in the absorption transition, causing the radiation oscillation at the original frequency to be terminated and replaced with an oscillation at a new frequency. This interruption of the wavetrain at the original frequency broadens the resulting spectral line. In the impact approximation, which assumes collisions to be both binary and instantaneous, both the elastic and inelastic mechanisms produce spectral lines which are described with a Lorentzian lineshape.

Pressure broadening and Doppler broadening occur simultaneously but independently, so the observed lineshape is a convolution of the two shapes and is called the Voigt lineshape. Collisions can also cause additional, more subtle changes to the observed spectral line, such as shifting, narrowing, and coupling. One can picture collision-induced line shifting as occurring because the collision partner perturbs the potential energy surfaces of the absorber, changing the distance between the energy levels and thus the frequency of the transition. Collisional narrowing occurs because of limitations placed on the mean free path of the absorbing molecules in a bath gas of

2

perturbing molecules. Finally, at high pressures, closely-spaced transitions may collisionally transfer populations between the spectral lines, coupling the lines. Each of these mechanisms alters the shape and width of the spectral lines.

The shapes and widths of spectral lines are important for several reasons. The Air Force relies on absorption or emission spectra collected from satellites and other sensor platforms to measure such atmospheric parameters as temperature, pressure, humidity, and abundance of various molecular species. These measurements are then used in such diverse applications as meteorology, remote monitoring of pollutants or effluent signatures, and determination of transmission windows for laser propagation in the atmosphere. However, proper interpretation of the remote-sensing data requires precise knowledge of spectroscopic line positions, intensities, widths, and shapes. Collisions can modify the spectra to the point where collision-free parameters will produce incorrect answers in these important applications. Therefore, any improvement in the measurement precision and accuracy of collisional effects on these spectroscopic parameters is important.

A second, more narrowly focused practical application of collisional effects in the O_2 absorption spectra is associated with the operating characteristics of the chemical oxygen-iodine laser (COIL), currently in development for use in the Air Force's airborne laser. The COIL chemically produces the excited $^1\Delta$ state of O_2 and then collisionally transfers energy to the iodine atom, pumping the upper laser level. Collisions rapidly establish an equilibrium between these oxygen and iodine species within the laser device. The populations of the upper and lower levels of the iodine atom can be expressed in terms of the ground and $^1\Delta$ concentrations of O_2 and a temperature-dependent equilibrium

3

constant, $K(T)$. The laser gain in the COIL device depends on $K(T)$; thus a direct measure of the temperature in the supersonic expansion would be a way to determine the operating conditions of the laser. Measurement of the linewidths of the O_2 A band could be a possible way to measure the temperature.

In general, the Air Force has a strong interest in chemical kinetics, since an understanding of reaction rates and energy transfer processes is necessary to model everything from lasers to chemical explosives to plasmas. The collisional transfer of energy among rotational-vibrational states is described by state-to-state rate coefficients. While precise values of these state-to-state rate coefficients are vital to modeling processes such as rocket fuel combustion and chemical laser operation, the necessary coefficients are very difficult and time-consuming to measure. On the other hand, it is relatively easy to simultaneously measure pressure broadening rate coefficients for an entire rotational-vibrational band. If a set of pressure broadening coefficients could be used to generate state-to-state rate coefficients, this would be a great help to the modeling of many important kinetic processes. This research project shows some ways that pressure broadening coefficients may be related to the state-to-state rate coefficients.

In addition to the practical benefits provided by a knowledge of kinetic rate coefficients, the collisional effects observed in absorption spectra offer a window into the physics of the collision process. The theories that describe collisional broadening, shifting, narrowing, and coupling, do so in terms of physical parameters of the interaction, such as intermolecular potential, and the energy or momentum transferred during the collision process. Relating the observed broadening coefficients to some of these parameters, then, should help describe the physics of the collision.

4

In this research project, the line widths of absorption transitions were measured to determine pressure broadening coefficients in the oxygen A band centered at 13122 cm^{-1} in the near infrared. Because the oxygen A band is a weak absorber and lies in a relatively empty portion of the spectrum, it is well suited for atmospheric remote sensing applications [107], including lidar measurements of temperature, pressure, and density, as well as satellite measurements of cloud top heights. This project also studied collisional effects in nitric oxide. Line widths of absorption transitions were measured in the NO fundamental band centered at 1876 cm^{-1} in the mid-infrared. Nitric oxide is a major pollutant in automobile as well as power plant exhausts. Also, measurements of NO concentrations in the stratosphere are important because of the crucial role that NO plays in the chemical cycle which determines the ozone concentration in the stratosphere [127]. The nitric oxide fundamental transition is also significant because of its interesting spectroscopy, since it is the only stable, gas-phase diatomic molecule currently known which exhibits Λ doubling.

Absorption spectra in this study were recorded using a BOMEM DA8.002 Fourier Transform Spectrometer (FTS). FTS has both advantages and disadvantages over other spectroscopic methods for studies of collisional effects. The primary advantage of grating spectrometers is the ability to quickly measure across a wide spectral range, in almost any part of the spectrum from far infrared to vacuum ultraviolet at modest resolution. Laser spectroscopy, on the other hand, offers extremely high resolution, but tunable lasers can typically scan only about 1 cm^{-1} at a time and finding a tunable laser with the necessary output power in the wavelength range of interest can be quite a challenge. The FTS couples the broadband acquisition capability and wide choice of

wavelengths of a grating spectrometer with higher resolution than is typically available on a grating instrument, though still below the resolutions available in a laser-based technique. The ability to acquire data over a wide spectral range allows simultaneous measurement of a molecule's entire ro-vibrational band, while the wide choice of wavelength ranges allows the same FTS instrument to be used for measurement on both the oxygen A band at 13122 cm^{-1} and the nitric oxide fundamental band at 1876 cm^{-1}. Fourier transform spectroscopy facilitated the simultaneous acquisition of high-precision lineshape data for many rotational lines, which allowed the data to be used to explore the observed trends with initial rotational level. The resolution of the FTS instrument is high enough to accurately extract pressure broadening and line coupling information; however the higher resolution of a laser is required to see some of the more subtle effects like Dicke narrowing and pressure-induced line shifting.

For molecular oxygen, spectra were recorded with He, Ne, Ar, Kr, Xe, O_2, N_2, CO, CO_2, and SF_6 collision partners, each at several pressures so trends with pressure could be analyzed. For nitric oxide, spectra were recorded with the noble gases He, Ne, Ar, Kr, and Xe, each again at several pressures. The noble gases were selected because they are structureless, non-reactive, spherical perturbers, greatly reducing the number of possible physical parameters that could influence the collision process. With the noble gases, the only significant physical parameters are the mass, radius, and polarizability of the atom. The five molecular perturbers were selected to explore some other possible physical parameters which might influence the collisional broadening, such as molecular geometry and dipole moment. Finally, a spectrum of NO+Ar was recorded at high pressure (> 1 atm) to look for evidence of line coupling in the Q branch of nitric oxide.

The characteristic deviations from a sum-of-isolated-lines profile were observed, qualitatively indicating the presence of line coupling.

This research provides a large amount of new spectroscopic data. Previously in the oxygen A band, only self- and air-broadening had been systematically studied. Ritter [106] performed a cursory, unpublished, examination of pressure broadening with the noble gases, measuring a small number of lines at only one pressure to determine the broadening coefficients. More recently, research groups using diode lasers have measured a few lines for the oxygen A band in collisions with oxygen, helium, and nitrogen [14, 31, 63, 103, 104]. The current research project provides a much more accurate, precise, and comprehensive look. This is the first study of pressure broadening in the oxygen A band using FTS. It is also the first examination of O_2 broadened with the molecules CO, CO_2, and SF_6 and the first systematic study of broadening with N_2.

This project is also the first complete study of the NO fundamental band broadened with the noble gases. Previous researchers have reported very few results of broadening with the noble gases. Only NO+Ar has been studied systematically. A few lines have been reported for broadening with helium and krypton but no previous results have been reported for broadening with neon or xenon. This study also reports the first pressure broadening coefficients of NO+Ar in the Q branch, and the first indication of line coupling in the Q branch measured with infrared spectroscopy. Since the O_2 and NO broadening coefficients from this study are new and of high precision, they are directly useful; they will be submitted to AFRL for possible inclusion in the HITRAN [56] atmospheric transmission database.

The broadening coefficients were also converted to broadening cross sections and broadening rate coefficients for analysis of the underlying physical mechanisms. The cross sections were analyzed using two major theories of pressure broadening: one based on elastic collisions and the other based on inelastic collisions. The results of these analyses were examined for clues to the underlying physical mechanisms. Trends were observed which related to the multipole moments of the absorbing molecules, the polarizability of the perturbers, the order of the resulting inverse-power potential between the absorber and perturber, and the reduced mass of the collision pair.

The results of this study were also used to examine a recently-proposed model for atom-diatom collisions which is based on the transfer of angular momentum during the collision. This was the first examination of the AM fitting law of Osborne and McCaffery [86] for trends with initial rotational state and was also the first look at the applicability of this theory to pressure broadening.

The next chapter, Chapter II, presents a brief overview of the relevant theory related to this research. Chapter III briefly discusses the results of previous researchers in the oxygen A band and the NO fundamental band. Chapter IV describes the experiment and analysis process in detail. This chapter also presents the quantitative broadening coefficients for each collision pair studied, the pressure-induced line shifting coefficients for O_2+Xe, and the qualitative evidence of line coupling in the Q branch of NO in collisions with argon. Chapter V describes the analysis of the pressure broadening coefficients using both elastic and inelastic theories of pressure broadening. This chapter also examines the AM fitting law of Osborne and McCaffery [86]. Finally, Chapter VI summarizes this research project and proposes a few ideas for possible further work.

II. Theory

This chapter presents the basic elements of lineshape theory necessary to understand the current research project. The lineshape of a collision-free spectrum is first discussed, followed by an explanation of the various collisional effects on the lineshape. These collisions may be either elastic or inelastic. A simple elastic model of pressure broadening is developed, followed by more complicated models which consider inelastic collisions. The inelastic mechanism is a collisional transfer of energy between translation and rotation. Direct calculations of this RT transfer prove difficult and highly complex, so several semi-empirical fitting laws have been proposed to model the observed broadening behavior. Recently, Osborne and McCaffery [86] proposed an RT fitting law based on the transfer of momentum during the collision. This theory is described in detail, since its derivation provides a clear picture of the collisional interaction.

In the simplest possible picture, a spectral line can be described by three observables: the position, width, and area under the line. The position is determined by the separation between the energy levels connected by the photon transition. The area is controlled by the intensity of the radiation, which is due to the transition probability and the statistical distribution of states. The width is determined by both collisional and collision-free factors.

Even for the interaction of radiation with an isolated, stationary molecule, the spectral line will not be infinitely-narrow. Because Heisenberg's uncertainty principle precludes an absolutely precise determination of the energy of molecular levels, a

9

transition between two such levels will produce a spectral line which also displays some uncertainty. This uncertainty manifests itself in the width of the spectral line, which is a Lorentzian profile with a width, called the natural width, determined by the lifetimes of the states. The normalized Lorentzian lineshape is given by [62]

$$L(v) = \frac{1}{\pi}\left(\frac{\Delta v}{(v_0 - v)^2 + (\Delta v)^2}\right) \qquad (1)$$

where v_0 is the line center position and Δv is the half width at half maximum (HWHM). The natural linewidth is equal to the sum of the inverse lifetimes of connected states: $\Delta v = (1/4\pi)(1/t_1 + 1/t_2)$. Thus, states with shorter lifetimes produce lines with larger natural widths.

Now consider the case of a moving molecule. The transition frequency between any two energy levels will be Doppler shifted from the value for the same transition in a stationary molecule. A spread in frequencies results from the large number of molecules in the gas moving in different direction at different velocities. A gas in thermal equilibrium has molecules with a Maxwell-Boltzmann distribution of velocities. This thermal distribution of velocities produces a spectral line with a with a Gaussian lineshape [62]

$$G(v) = \frac{1}{\Delta v_D}\sqrt{\frac{\ln 2}{\pi}}\exp\left(-\frac{\ln 2 (v - v_0)^2}{\Delta v_D^2}\right) \qquad (2)$$

10

where $\Delta\nu_D$ is the Doppler HWHM, given by [62]

$$\Delta\nu_D = \nu_0 \sqrt{\frac{2kT\ln 2}{mc^2}} \qquad (3)$$

where k is Boltzmann's constant, T is temperature, m is the mass of the molecule, and c is the speed of light. For molecules in thermal equilibrium at room temperature, the Doppler width is several orders of magnitude larger than the natural width, so the natural width can be neglected. The next step, then, is to consider various effects of collisions among the molecules in the gas which can alter the shape of the spectral line.

2.1. Collisional Effects on Spectral Lines

As the number of molecules in a given volume increase (equivalent to increasing the pressure) the molecules will begin to interact, or collide, with one another. Some of these collisions will occur while the molecule is interacting with the electromagnetic radiation, so the collisions can be expected to further alter the shape of the spectral line. The most general collisional modification of the spectral line is called collisional broadening or pressure broadening. Other collisional effects include pressure-induced line shifting, pressure narrowing or Dicke narrowing, and line coupling or line mixing. Each of these processes produces a characteristic change to the line profile, so a careful study of the shapes of spectral lines as a function of pressure can be a powerful way to probe the collision behavior of atoms and molecules. Each of these collisional effects will be discussed in the following sections.

11

2.1.1. Pressure Broadening and Line Shifting. Pressure broadening has been studied now for over a century and several mechanisms have been proposed to explain the observed behavior. However, a simple comprehensive picture of the process of collisional broadening has yet to be identified. This section describes some of the major pressure broadening theories. Several good review articles and references on pressure broadening are available [15, 32, 53, 100] so this section will summarize only those parts of the theory needed to understand this research project.

Early theories of pressure broadening treated the collisions as elastic. In 1895, Michelson made the first important contribution to the subject when he identified the mechanism of pressure broadening as the sudden and complete interruption of the vibrations of atomic radiation by collisions with neighboring atoms [53]. Lorentz, in 1906, showed that the effect of random sudden collisions was equivalent to an additional damping force, proportional to velocity, exerted on the atomic oscillators [53]. This mechanism produces the Lorentzian line shape of pressure broadening. Weisskopf, in 1932, perceived the interruption of oscillation visualized by Michelson and Lorentz as an interruption of phase [53]. If the phase change induced by the collision is greater than some critical value, then the wave train is effectively terminated and it is thus the average time between collisions which determines the width of the resulting Lorentzian profile.

In the elastic-collision model, the radiating atom is treated as an oscillator which experiences phase-changing collisions. The oscillator is described by its time-dependent amplitude [32]

$$x(t) = x_0 \exp\left[i v_0 t + i \eta(t)\right] \tag{4}$$

12

where v_0 is the line center position and $\eta(t)$ represents the sum of all phase shifts due to elastic collisions in the time from 0 to t. Using the impact approximation, which assumes that all collisions are binary and that the collision duration is small compared to the time between collisions, the average phase shift per collision can be related to the correlation between the oscillator before and after the interaction. This can be described by the correlation function [32]

$$\phi(\tau) = \exp\left[-N\langle v\rangle\tau(\sigma_b - i\sigma_s)\right] \tag{5}$$

where N is the number of particles per unit volume, τ is the correlation time, and $\langle v\rangle$ is the mean relative velocity. The correlation function describes the mathematical relation between the oscillator at times t and $t + \tau$. During this interval, the change of $\phi(\tau)$ depends on the number of collisions and on the average phase change per collision. The terms σ_b and σ_s are given by [32]

$$\sigma_b = 2\pi\int_0^\infty [1 - \cos\eta(b)]b\,db \tag{6}$$

$$\sigma_s = 2\pi\int_0^\infty [\sin\eta(b)]b\,db \tag{7}$$

13

where b is the impact parameter, or distance of closest approach between two collision partners. The intensity profile of the resulting spectral line is then given by the complex Fourier transform of the correlation function. This intensity profile is [32]

$$I(v) = \frac{1}{\pi} \left(\frac{N\langle v \rangle \sigma_b}{\left(v_0 - v + N\langle v \rangle \sigma_s\right)^2 + \left(N\langle v \rangle \sigma_b\right)^2} \right)$$ (8)

Comparing Equation (8) with Equation (1), one can see that the resulting line profile is a Lorentzian with HWHM $\Delta v = N\langle v \rangle \sigma_b$. Additionally, there is a shift of line center given by $\delta v = N\langle v \rangle \sigma_s$. Thus both line broadening and shifting are proportional to number density N and mean velocity $\langle v \rangle$. The quantity $\sigma_b - i\sigma_s$ is a complex collision cross section. The broadening of the line is associated with the real part σ_b, while the shift is associated with the imaginary part, $-\sigma_s$.

The phase change η is related to the interatomic potential by [53]

$$\eta(b) = \frac{1}{\hbar} \int_{-\infty}^{\infty} V(r(t)) dt$$ (9)

where r is the distance between the two atoms and t is the time, measured from the time of closest approach of the colliding atoms. Assuming straight-line trajectories of atoms with a relative average collision velocity $\langle v \rangle$ then the interatomic distance as a function of time is [54]

14

$$r(t)^2 = b^2 + \langle v \rangle^2 t^2 \tag{10}$$

The straight-line trajectory is a reasonable approximation for heavy collision partners, but begins to break down for light partners, such as helium, when the interaction potential can be expected to bend the trajectory. Substituting (10) into (9) gives

$$\eta(b) = \frac{2}{\hbar \langle v \rangle} \int_0^\infty \frac{V(r) r \, dr}{\left(r^2 - b^2\right)^{1/2}} \tag{11}$$

Substituting Equation (11) into Equation (6) provides a relation between the broadening cross section and the interatomic potential.

The interaction potential between the collision partners depends on the electrostatic forces produced by each collision partner and the distance between them. For example, the interaction between two bodies possessing permanent dipole moments depends on the strength of the two dipole moments and varies with the separation distance as r^{-3}. Similarly, a dipole-quadrupole interaction depends on the dipole and quadrupole moments and varies as r^{-4}, while a quadrupole-quadrupole interaction depends on the quadrupole moments and varies as r^{-5}. If a collision partner does not have a permanent dipole or quadrupole moment, such as a noble gas atom, the other partner may induce one through its own electric field. The ability to induce a dipole on a nonpolar collision partner depends on the polarizability of the nonpolar partner. For example, a dipole induced-dipole interaction depends on the dipole moment of partner A,

15

the polarizability of partner B, and varies with distance as r^{-6}. Similarly, a quadrupole induced-dipole depends on the quadrupole moment of partner A, the polarizability of partner B, and varies with distance as r^{-7}. In general, a spherically-symmetric potential may be expressed in the form

$$V(r) = C_n \frac{\xi_A \xi_B}{r^n} \tag{12}$$

where ξ_A is the magnitude of the highest-order multipole moment of partner A, ξ_B is the appropriate multipole moment or polarizability of partner B, n is the order of the potential, and C_n is a collection of constants. For example, the potential between a dipole and a non-polar perturber is [122]

$$V(r,\theta) = -\frac{\mu_A^2 \alpha_B (3\cos^2\theta + 1)}{2r^6} \tag{13}$$

where μ_A is the dipole moment of molecule A and α_B is the polarizability of the nonpolar atom B. If the anisotropy is not too great, Equation (13) can be approximated as

$$V(r) \approx C_6 \frac{\mu_A^2 \alpha_B}{r^6} \tag{14}$$

Weisskopf derived this theory for atom-atom collisions, in which case the spherical symmetry of the potential is a justifiable approximation. The anisotropy of the molecular

16

potential may introduce a *J*-dependence in the elastic theory, though this has not been explored. The effect of the anisotropy of the potential in the case of atom-molecule collision will be discussed later in this chapter.

Combining Equations (12), (11) and (6) and collecting all the terms which do not vary with perturber species together in a constant C_A produces

$$\sigma_b = C_A \left(\frac{\xi_B}{\langle v \rangle} \right)^{\frac{2}{n-1}}$$

(15)

The only perturber-dependent parameter in the relative velocity is the reduced mass term, $\mu^{-1/2}$. Collecting the remaining terms of the relative velocity together with the other non-perturber-dependent parameters in a coefficient C, one obtains

$$\sigma_b = C \xi_B^{\left(\frac{2}{n-1} \right)} \mu^{\left(\frac{1}{n-1} \right)}$$

(16)

Equation (16) indicates that the mechanism of pressure broadening depends not only on the order of the intermolecular potential, but on the reduced mass of the absorber-perturber pair and on the appropriate multipole moment or polarizability of the perturber. Equation (16) is a new way to look at the classical elastic theory and has not been previously published. Note that by using Equations (7), (11), and (12), one could derive a similar relation for the pressure shifting cross section σ_s.

17

The elastic-collision theory of Weisskopf was developed for atom-atom collisions, which it describes well. Molecules, however, have internal rotational and vibrational structure which is not present in atoms and which is not considered in this theory. While the classical elastic collision theory predicts a Lorentzian line with broadening and shifting proportional to pressure, and while it predicts dependencies on intermolecular potential and the physical parameters of the perturber, it does not predict any dependence on the rotational quantum number of the absorbing molecule. The pressure broadening cross sections for both the oxygen A band and the nitric oxide fundamental band show a clear dependence on rotational quantum number, as do most other published pressure broadening results in molecules [106, 118, 123]. Thus, while the classical theory may be able to indicate some of the mechanisms of pressure broadening in molecules, it cannot provide the whole picture.

Clearly, a theory is required which considers the quantum structure of the molecular absorber and which can reproduce the observed dependence of the broadening cross section on rotational quantum number. Anderson [5, 128] developed a theory which uses classical trajectories for the collision partners, but uses quantum mechanics and second-order perturbation theory to describe the collisional broadening of the molecules. This model accounts for inelastic collisions, as well as elastic collisions. This is significant, since many researchers contend that rotationally-inelastic collisions are the dominant mechanism in molecular pressure broadening [123].

The semi-classical theory of Anderson predicts a Lorentzian lineshape, like the classical theory, but the pressure broadening cross section is now given by [114]

$$\sigma_b = \int_0^\infty 2\pi b S(b) db \qquad (17)$$

where $S(b)$ describes the joint probability of a simultaneous collision and photon transition (absorption or emission). To produce a large broadening cross section, two conditions must occur at the same time: the photon transition must be quantum-mechanically allowed and there must be a large probability of collisionally coupling a particular initial and final state (through either elastic or inelastic collisions). The probability of photon interaction is governed by the well-known dipole (or higher-order) selection rules. The collision probability, however, depends on the classical trajectory of the collision pair and the potential energy surface upon which the collision occurs. This calculation is quite complicated and requires an accurate analytical form of the intermolecular potential. This theory has been refined by other researchers to allow curved trajectories [114] and to include the case of overlapping, non-isolated lines [41, 108], which has improved its ability to model the pressure broadening cross sections for many collision pairs. However, the complexity of Equation (17) is such that a simple physical picture of the mechanism of pressure broadening is obscured, so Anderson's model was not used in this research project.

In addition to the classical approach of Weisskopf and the semiclassical approach of Anderson, there is a fully quantum mechanical method for the calculation of pressure broadening cross sections [28, 29]. This method, called the close-coupled procedure, is even more complicated than the semiclassical method, since the trajectories are now also treated quantum-mechanically. Since the fully-quantal method also fails to paint a simple physical picture of pressure broadening, it was not used in this research project.

2.1.2. Combined Doppler and Collisional Effects. This chapter has so far

discussed the effect of thermal motions of molecules, which leads to a Gaussian

lineshape, and the effect of collisions between molecules, which leads to a Lorentzian

lineshape. In truth, both of these effects occur simultaneously. The combined profile is a

convolution of the two broadening mechanisms and is called the Voigt lineshape [62]:

$$V(v) = A \frac{\ln 2}{\pi^{3/2}} \frac{\Delta v_P}{(\Delta v_D)^2} \int_{-\infty}^{\infty} \frac{\exp(-t^2)dt}{\left(\frac{\Delta v_P}{\Delta v_D}\right)^2 \ln 2 + \left(\frac{v - v_0}{\Delta v_D} \ln 2 - t\right)^2} \qquad (18)$$

The Gaussian and Lorentzian lineshapes are each characterized by three parameters: line

center position, intensity, and width. The Voigt lineshape is characterized by four

parameters: line center position v_0, intensity A, Doppler HWHM Δv_D, and pressure-

broadened HWHM Δv_P. At low pressures, $\Delta v_D \gg \Delta v_P$ and the Voigt reduces to a

Gaussian shape, while at high pressures, $\Delta v_D \ll \Delta v_P$ and the Voigt reduces to a

Lorentzian shape.

There is an additional effect of collisions on the Doppler part of the lineshape

which is called Dicke narrowing [129]. In this mechanism, collisions change the velocity

of the radiating molecules, which causes a decrease in the Doppler width. This process

may be understood in terms of the uncertainty principle. The Doppler shift of a photon

absorbed by a molecule provides information on the velocity, or rate of change of

displacement, of that molecule. From the uncertainty principle, one cannot know the

instantaneous velocity of a molecule at a precise location in space, but can only know its

average velocity over a displacement Δx which satisfies the condition $\Delta x \Delta p \geq h/2\pi$. If we assume that the momentum carried by the absorbed photon, $p = h/\lambda$, generates an approximately equal uncertainty in the momentum of the molecule, then the uncertainty in the displacement is $\Delta x \geq \lambda/2\pi$. Thus the molecular velocity inferred from the Doppler shift is the mean velocity over a displacement $\sim\lambda/2\pi$.

If collisions are infrequent, the velocity is constant over the time intervals required to travel $\lambda/2\pi$ and the observed frequency shifts will reflect the Maxwellian velocity distribution of the molecules. However, as the pressure increases and collisions become more frequent the molecule will on average travel less than $\lambda/2\pi$ between collisions. This reduces the mean velocity component sampled by the Doppler shift, which reduces the width and changes the shape of the Doppler-broadened component of the line. At high enough pressures, the mean velocity approaches zero and the Doppler component of the line entirely disappears.

The commonly-used line shape to describe the combination of pressure broadening and Dicke narrowing is the Galatry profile [129], though several other profiles have also been proposed. The Galatry profile is [129]

$$G = \frac{1}{\sqrt{\pi}} \mathrm{Re} \int_0^\infty \left(-ixt - yt + \frac{1 - zt - e^{-zt}}{2z^2} \right) dt \tag{19}$$

where $x = (v - v_0)/2\Delta v_D$, $y = \Delta v_P/(2P\Delta v_D)$, $z = \eta/(2\Delta v_D)$, and η is the Dicke narrowing coefficient. Dicke narrowing is not often seen in the laboratory since the reduction of the

Doppler width is usually masked by the much larger increase in Lorentz width from pressure broadening. The narrowing is most apparent when the broadening is anomalously small, such as for widely-spaced rotational states of light molecules with nonpolar perturbers [95]. The best way to determine if Dicke narrowing is significant in an experimentally-measured line is to examine the residuals from a Voigt fit to the line in question. If the residuals display the characteristic trends shown in Figure 1 then Dicke narrowing is significant and a Galatry function would be a better fit to the data. If the trend in Figure 1 is not observed, either because Dicke narrowing does not occur or because the trend is masked by noise in the data, then use of the Galatry function is not warranted and the Voigt profile provides an adequate description of the data [129].

2.1.3. Line Coupling. For closely-spaced lines at high pressures, when the lines have broadened such that they appreciably overlap, the spectral lines can no longer be considered to be isolated and line coupling can occur. In this situation, inelastic collisions transfer population from one radiating state to another, effectively coupling these states. These inelastic, coupling collisions are no longer effective in broadening the line [116] since they only shift intensity from one part of the spectrum to another. Line coupling can cause significant deviations in regions of the spectrum such as the windows just beyond Q-branch heads or the microwindows between closely-spaced rotational lines; these deviations modify the lines from their isolated Voigt profiles. This becomes especially significant in remote sensing applications, in which infrared signals are often propagated in the windows or microwindows, where absorption should be low. However, the presence of line coupling can alter the absorption in these regions, leading to erroneous results if the coupling effect is not considered.
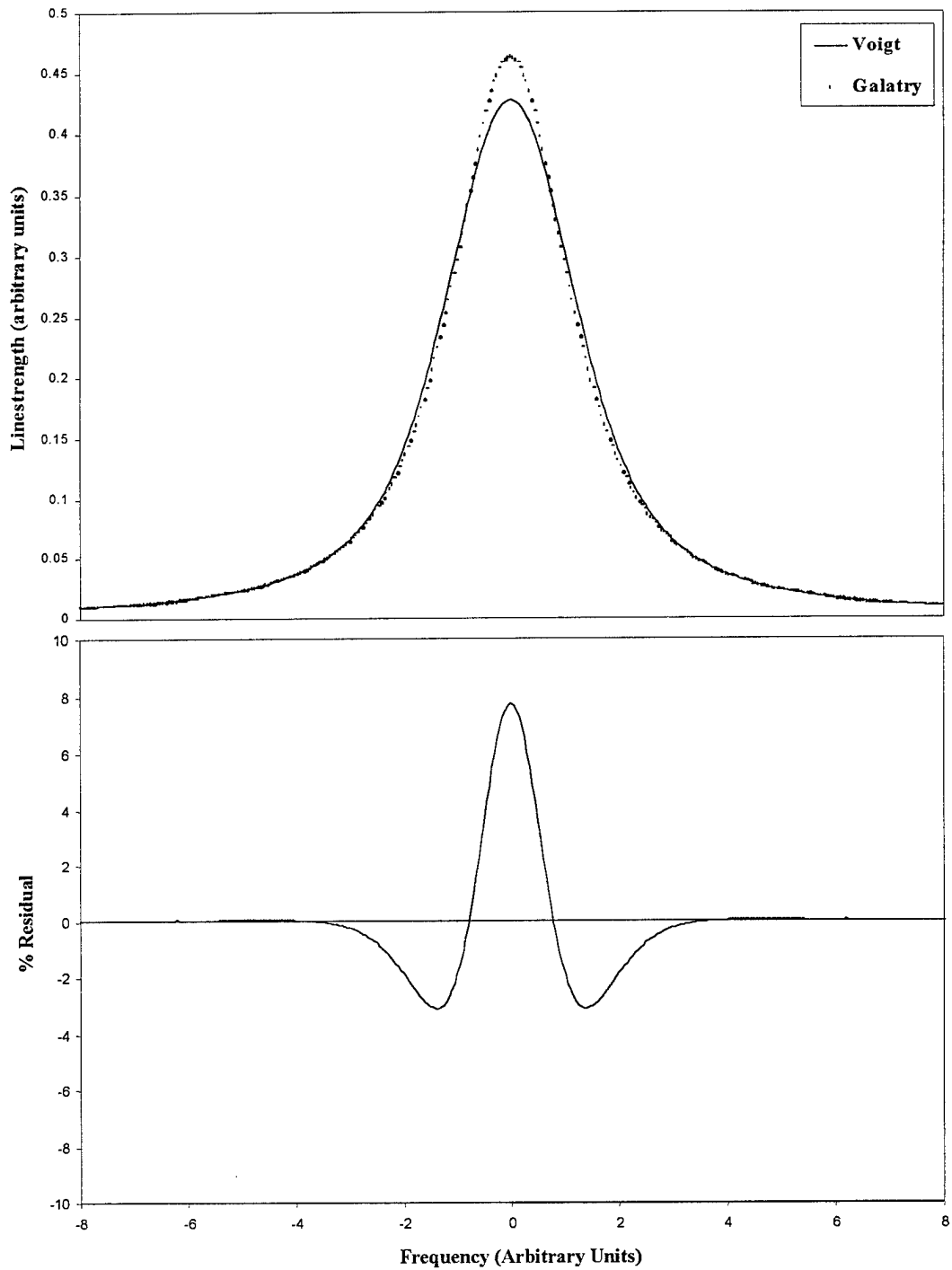
Figure 1. Comparison of the Voigt and Galatry functions. The lower curve is a plot of the difference between the two functions expressed as a percentage of the maximum value of the Galatry function. The residuals show a characteristic shape which indicates that the "data" modeled by this Voigt function has significant Dicke narrowing and would be better modeled by the Galatry function.

One can expect to observe line coupling in a spectrum when two conditions hold. First, the energy separation between consecutive rotational levels must be less than kT. Second, the frequency separation of adjacent lines must be less than or on the order of the magnitude of the linewidths.

Levy *et al.* [69] provide a good review article on line coupling. Following their development of the theory, we begin with a general expression for the spectral intensity profile at frequency v:

$$I(v) = \frac{3}{2\pi} \sum_{i,f} \rho_i \langle i | \vec{e} \cdot X | f \rangle^2 \int_{-\infty}^{\infty} dt \exp\left[\frac{i(E_f - E_i)t}{\hbar} \right] e^{-ivt} \tag{20}$$

where ρ is the density matrix of the absorbing system, $\vec{e}$ is a unit vector along the direction of the electric field of the radiation, X is the operator that couples radiation with this material system (the dipole operator for the case of infrared absorption), and i, f are initial and final states with energies E_i and E_f, respectively. Next, we make use of Liouiville formalism and apply two approximations: the impact approximation, and the approximation that the density matrix can be factored. The impact approximation assumes that the collisions are binary and are of negligibly short duration compared to the time between collisions. Factorization of the density matrix is accomplished by dividing the gas sample into a large number of identical cells and calling one cell the system while the remaining cells are the thermal bath gas. We then assume the density matrix does not include correlation between the system and bath variables, allowing the system and bath variables to be factored. After performing these simplifications, we have

$$I(v) = \frac{1}{\pi} \text{Im}\left[\sum_{k,l} \rho_k X_k X_l \langle l | (v - v_0 - iW)^{-1} | k \rangle \right] \qquad (21)$$

where ρ_k is the matrix element of the density matrix corresponding to the initial level i of

the transition giving rise to the line k, X_k is the transition moment between states i and f,

$X_k = \langle f | X | i \rangle$, $|k\rangle$ is the transition $i \rightarrow f$, $|l\rangle$ is the transition $i' \rightarrow f'$, and W is the

relaxation matrix. The elements of the relaxation matrix connect the different transitions

in the spectrum.

The elements of the relaxation matrix can be expressed as [69]

$$W_{i'f'if} = n\sigma_{i'f'if} \langle v \rangle \qquad (22)$$

where n is the number density of perturbing species, σ is the state-to-state cross section,

and $\langle v \rangle$ is the mean relative velocity. The relaxation matrix elements are complex

quantities; the real part describes the broadening cross section while the imaginary part

describes the line shifting cross section. Relaxation matrix elements can also be

expressed in terms of rate coefficients, k, since thermally-averaged rate coefficients and

cross sections are related by

$$k = \sigma \langle v \rangle \qquad (23)$$

25

Finding the elements of W thus amounts to finding the state-to-state rate constants or cross sections. The diagonal elements of the relaxation matrix, W_{kk}, represent the total removal rates from state $|k\rangle$, while the off-diagonal elements, W_{lk}, represent the state-to-state transition rates from state $|k\rangle$ to state $|l\rangle$. The diagonal elements are related to the off-diagonal elements, a relationship which will be developed in the next section. In the case that the off-diagonal elements are zero, the lines do not couple and Equation (21) reduces to the Lorentzian lineshape [69]. Thus the total removal rates determine the pressure broadening rates.

The simplest example of line coupling is the four-level system pictured in Figure 2, where $i, f, i',$ and f' represent four rotational energy levels in the molecule. Consider a molecule initially in state i and therefore able to absorb a photon v_{fi}. A collision can cause this molecule to leave state i and join a different state i'. In this new state, it is able to absorb a different photon $v_{f'i'}$. Thus, the transfer from i to i' results in a coupling between transitions $i \rightarrow f$ and $i' \rightarrow f'$. There are two paths from state i to state f: the direct path which is simply the optical transition $i \rightarrow f$ and the indirect path which is the collisional transition from i to i' plus the optical transition $i' \rightarrow f'$ plus the collisional transition from f' to f. The direct path produces the line $|k\rangle$ of frequency v_{fi}, while the indirect path gives rise to the line $|l\rangle$ of frequency $v_{f'i'}$. Similarly, there are two paths from state i' to state f'.
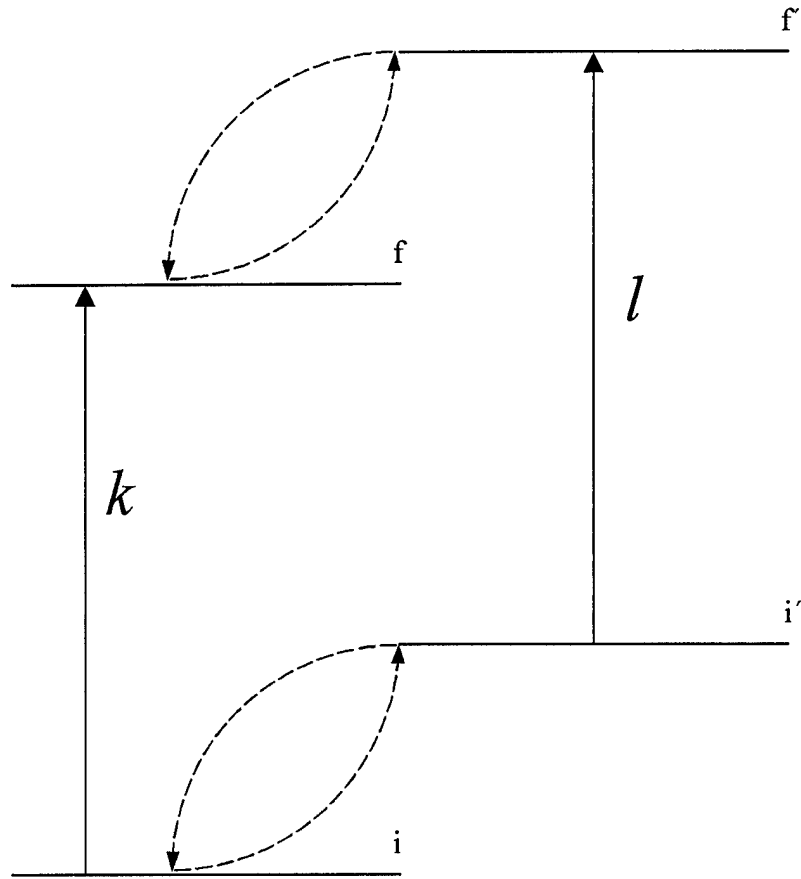
Figure 2. Line Coupling for a Four-Level System. The solid lines represent optical transitions, while the dashed arrows represent collisional transitions.

The relaxation matrix of the four-level system contains four terms:

$$W = \begin{pmatrix} W_{kk} & W_{kl} \\ W_{lk} & W_{ll} \end{pmatrix} \qquad (24)$$

The diagonal term W_{kk} represents the rate at which collisions transfer intensity from line $|k\rangle$ to all other lines in the band. The off-diagonal term W_{lk} represents the negative of the

rate at which molecules radiating in the line $|k\rangle$ leave that line to join line $|l\rangle$. Similar relations hold for W_{ll} and W_{kl}. Line coupling thus involves a transfer of population among levels. This results in the transfer of intensity from weak lines to stronger lines, which has the effect of making the line wings look sub-Lorentzian and the center of a group of overlapping lines look super-Lorentzian [69]. In a typical molecular system, the relaxation matrix can couple as many as 100 states, which leads to an $n \times n$ matrix containing up to 10^4 elements.

There are three ways to determine the cross sections or rate coefficients. The first is to start with the intermolecular potential and calculate the cross sections quantum-mechanically using scattering S-matrices. This method is generally intractable, both because of the difficulty of the calculation and because of the difficulty in finding a reliable intermolecular potential. The second way is to use an energy scaling law to decouple the dependence of the cross sections from the dynamical factors. The potential is then only required to determine the dynamics of the system. In cases where the potential is still unknown or sufficiently inaccurate, one must approximate the dynamics with a fitting law to obtain the cross sections. The third way is to begin with experimental measurements of the linewidths and use a fitting law to find the state-to-sate cross sections. Fitting laws are discussed in the next section, which more fully explores the theory of rotationally-inelastic collisions.

2.2. Rotationally-Inelastic Collisions

It is clear from the previous discussion that rotationally-inelastic (RI) collisions transfer population among rotational levels in a molecule and that this movement of

population affects the observed spectrum. The previous discussion also mentions that the off-diagonal elements of the relaxation matrix, or state-to-state rotational transfer rates, are related to the diagonal elements, or total removal rates. It was also stated that the total removal rates are equivalent to the pressure broadening rates, from which one can calculate the pressure broadening cross section. The key, then, is to determine the relationship between the diagonal and off-diagonal elements. Many researchers [18, 33, 79, 80, 97, 101, 123] contend that the diagonal and off-diagonal elements of the relaxation matrix are related by a simple sum rule which says that the total relaxation rate of state i is equal to the sum of the state-to-state rates out of state i to all final states. In its simplest form, this sum rule is expressed as

$$W_{ii} = -\sum_{f} W_{if} \tag{25}$$

or in terms of rates as

$$k_i = \sum_{f} k_{i \to f} \tag{26}$$

A more accurate sum rule for infrared transitions considers that collisions can happen in either the lower or upper level connected by the optical transition. Assuming collisions in either state have an equal effect on the total relaxation rate, the infrared sum rule is [33]

$$k_{J'' \to J'} = \frac{1}{2} \left[\sum_{J \neq J''} k_{J'' \to J} + \sum_{J \neq J'} k_{J' \to J} \right] \tag{27}$$

where the lower and upper states connected by the infrared absorption are J'' and J', respectively.

This rotationally-inelastic description of pressure broadening assumes that the possible effects of vibrational energy transfer are negligible in comparison to rotational transfer. One must also consider in the case of molecule-molecule collisions that more energy transfer pathways than just rotational-to-translational are possible, such as rotational-to-rotational transfer. However, the RI description of pressure broadening has been widely applied and has often successfully modeled the available data. Before discussing the successes and limitations of the RI description of pressure broadening, the next section will introduce the fitting laws which are used to describe rotational transfer.

2.2.1. Fitting Laws for Rotational Transfer. Several empirical equations have been proposed to describe the relationships among the off-diagonal elements of the relaxation matrix [25, 123]. These equations, called fitting laws, have been developed to describe the data gathered in state-to-state experiments with diatomic molecules. In these experiments, a particular rotational state is populated by photon absorption and the transfer of population to other rotational states under the influence of collisions is measured. This provides a direct measure of the off-diagonal elements of the matrix. Fitting laws empirically characterize all of the off-diagonal elements, for a particular initial rotational state J_i, in terms of a small number of fitting parameters. Further, for the fitting laws which follow, it has been determined [25, 123], within experimental error,

30

that the fitting parameters are independent of J_i. Thus these few fitting parameters (usually 2 to 5) can be used to describe all the off-diagonal elements of the relaxation matrix ($\sim 10^4$). Finally, if the RI description of pressure broadening is correct, these few fitting parameters can describe a fit to the diagonal elements of the relaxation matrix, as well.

When fitting state-to-state rotational transfer data, one must be sure that the results are consistent with detailed balance. Detailed balance simply says that when a reacting system reaches equilibrium the forward and reverse processes occur at the same rate. Applied to rotational transfer, this says that the collisional transfer rate from state 1 to state 2 must be in balance with the transfer rate from state 2 to state 1. Mathematically, this is expressed as [122]

$$k_{J_2 \to J_1} = k_{J_1 \to J_2} \left(\frac{2J_1 + 1}{2J_2 + 1} \right) \exp\left(\frac{E_2 - E_1}{kT} \right) \tag{28}$$

where the first term in brackets accounts for the relative degeneracies of the two levels, while the exponential term accounts for the relative population of each level for a system in thermal equilibrium. Thought of in terms of the relaxation matrix, detailed balance connects the upper triangular part of the matrix with the lower triangular part. If the fitting law used to model the rotational transfer is not itself consistent with detailed balance, the fitting law can be used to calculate the rates in one direction and the detailed balance equation above can be used to calculate the rates in the other direction.

31

Fitting laws for rotational transfer are divided into two subtypes: statistical and dynamical. In statistically-based fitting laws, the significant variable is the energy transferred in the collision. The probability for a molecule to make the collisional transition $J_i \rightarrow J_f$ depends only on the energy gap $\Delta E = | E_i - E_f |$. The energy of a rotational level is given by $E_J = hcBJ(J+1)$, where h is Planck's constant, c is the velocity of light, and B is the rotational constant of the molecule . The general form of the statistical fitting laws is [25]

$$k_{i \rightarrow f} = A T_{i \rightarrow f}^2 R(\Delta E) N_{i \rightarrow f} \qquad (29)$$

where A is a constant, $T_{i \rightarrow f}$ is proportional to the differential scattering amplitude averaged over all initial energies and solid angles and depends only on ΔE, $R(\Delta E)$ is a dimensionless translational phase space factor, and $N_{i \rightarrow f}$ is a spin degeneracy factor, which depends on the possible changes of the magnetic quantum number m during the collision. In the important case that the initial kinetic energy distribution is thermal, the translational phase space factor is [99]

$$R(\Delta E) = \Delta e^\Delta K_1(\Delta) \qquad (30)$$

where Δ is the reduced rotational energy transfer [99]:

$$\Delta = \frac{E_i - E_f}{2kT} \qquad (31)$$

and $K_1(\Delta)$ is the modified Bessel function of the first order.

The form of the spin degeneracy factor depends on whether there is any restriction on the reorientation of the projection of the rotational angular momentum vector, described by the quantum number m. For a given rotational quantum number J, the projection quantum number m has $2J+1$ allowed values, from $-J$ to J in integer steps. If there is no restriction on reorientation during the collision, then m can take all possible values and the spin degeneracy factor is given by [25]

$$N_{i \to f} = N_\Delta = 2J_f + 1 \qquad (32)$$

If reorientation is completely restricted, then $\Delta m = 0$ and the degeneracy is [25]

$$N_{i \to f} = N_0 = \frac{2J_< + 1}{2J_i + 1} \qquad (33)$$

where $J_<$ is the smaller of J_i and J_f. Finally, there is an intermediate case in which Δm is between zero and some limiting value λ, where λ is less than $2J+1$. In this case, the degeneracy factor is given by [25]

$$N_{i \to f} = N_\lambda = \frac{(2n_2 + 1)(2n_3 + 1) - \alpha(\alpha + 1)}{2J_i + 1} \qquad (34)$$

where of the three numbers $\{J_i, J_f, \lambda\}$, n_1 is the largest, n_2 is intermediate, n_3 is the smallest, and α is the greater of $(n_2 + n_3 - n_1)$ and zero.

The simplest of the statistical fitting laws, and the first proposed, is obtained by assuming an exponential dependence on ΔE. This leads to the exponential gap law (EGL): [25]

$$k_{i \to f}^{EGL} = A \exp(-\beta \, | \, \Delta E \, | \, / kT) R(\Delta E) N_{i \to f} \qquad (35)$$

where A and β are the adjustable parameters. The exponential gap law has been justified using surprisal analysis, but has in no sense been rigorously proven [25].

Another common fitting law assumes a power law dependence on ΔE. This leads to the statistical power gap (SPG) fitting law [25]:

$$k_{i \to f}^{SPG} = A \left| \frac{\Delta E}{B} \right|^{-\gamma} R(\Delta E) N_{i \to f} \qquad (36)$$

where A and γ are adjustable fitting parameters and B is the rotational constant, used to make $\Delta E/B$ dimensionless. While the use of the SPG has been more successful than using EGL in fitting rotationally-inelastic data, no firm theoretical justification has ever been given for this law.

34

A third fitting law combines the power law and exponential dependence, leading to a hybrid exponential power gap law EPGL [25]:

$$k_{i \to f}^{EPGL} = A \left| \frac{\Delta E}{B} \right|^{-\gamma} \exp(-\beta |\Delta E| / kT) R(\Delta E) N_{i \to f} \qquad (37)$$

where the law now has the three fitting parameters A, β, and γ. The EPGL was empirically proposed to try to cover a wider range of J, since SPG appears to work better for low J levels while EGL works better for higher J levels [25]. In addition to EGL, SPG, and EPGL, there are many other statistically-based fitting laws in the literature [123], with more appearing all the time.

Each of the statistically-based fitting laws can be used with any of the three degeneracies given in Equations (32), (33), and (34). The degeneracy used is indicated by appending a symbol to the name of the fitting law. For example, EGL-Δ, EGL-0, and EGL-λ correspond to the exponential gap law used with the N_Δ, N_0, and N_λ degeneracies, respectively.

In dynamically-based fitting laws for rotational transfer, the angular momentum transferred in the collision is the significant variable. These fitting laws have been derived by making certain dynamical approximations to the Schrodinger equation to solve the scattering problem. The resulting expressions for rate constants $k_{i \to f}$ involve a sum of products of angular momentum coupling coefficients and basis rate constants $k_{0 \to L}$, where L spans all rotational levels consistent with the symmetry of the active molecule.

The first dynamically-based fitting law proposed was the infinite-order sudden law (IOS) [25]:

$$k_{i \to f}^{IOS} = (2J_f + 1)\exp\left(\frac{E_{J_i} - E_{J_>}}{kT}\right)\sum_L \begin{bmatrix} J_i & J_f & L \\ 0 & 0 & 0 \end{bmatrix}^2 (2L+1)k_{0 \to L} \quad (38)$$

where $J_>$ is the greater of J_i and J_f and the first term inside the summation is a Wigner 3-J angular momentum coupling coefficient. The summation may be taken over $|J_i - J_f| \le L \le |J_i + J_f|$ with sufficient accuracy [123]. The two factors to the left of the summation guarantee detailed balance. The IOS law arises from the addition of angular momenta under the condition that the collision is sudden. A sudden collision is one in which the collision time is short compared to the rotational period of the molecule – the molecule effectively does not rotate during the collision. In a sudden collision, all angular momenta are in a plane perpendicular to the internuclear axis [25] so all the ms in the 3-J coefficient are zero.

However, Equation (38) is not yet a fitting law. To make it a fitting law, some assumptions must be made about the way the basis rate constants scale with rotational level. One common way to approximate the basis rate constants is to assume a power-law dependence [25]:

$$k_{0 \to L} = A[L(L+1)]^{-\gamma} \quad (39)$$

Together, Equations (38) and (39) make up the IOS-P fitting law with the two free

parameters A and γ. The P indicates that a power law dependence on the basis rates has

been assumed. Exponential and hybrid power-exponential dependencies have also been

used by some researchers [79]; these are indicated by appending an E or EP to the

designation of the fitting law.

In many cases, however, the collision is not sudden; the molecule rotates an

appreciable amount during a typical collision. In this case, the isolated lines are no

longer Lorentzian in the wings, since the Lorentzian lineshape was derived in the impact

limit (sudden, binary collisions). However, the deviation from Lorentzian shape in the

wings does not significantly affect the width of the line, so collision broadening can still

be modeled using the Voigt lineshape. To extend the dynamical fitting law to the case of

collisions which are not sudden, an adiabatic factor was developed [25, 117]:

$$A_L^{J_>} = \frac{1 + \left[\dfrac{(E_L - E_{L-\delta})\tau_c}{2\sqrt{6}\hbar} \right]^2}{1 + \left[\dfrac{(E_{J_>} - E_{J_>-\delta})\tau_c}{2\sqrt{6}\hbar} \right]^2} \tag{40}$$

where τ_c is the collision time, E_J is the energy of the Jth rotational level, and δ is 1 for a

heteronuclear molecule and 2 for a homonuclear molecule. The collision time τ_c is

usually expressed as [25]

$$\tau_c = \frac{l_c}{\langle v \rangle} \tag{41}$$

where $\langle v \rangle$ is the relative velocity of the collision pair and l_c is the length over which the interaction takes place. Inclusion of the adiabatic factor in the IOS law produces the energy-corrected sudden (ECS) law [25]:

$$k_{i \to f}^{ECS} = (2J_f + 1) \exp\left(\frac{E_{J_i} - E_{J_>}}{kT}\right) \sum_L \begin{bmatrix} J_i & J_f & L \\ 0 & 0 & 0 \end{bmatrix}^2 (2L+1)\left(A_L^{J_>}\right)^2 k_{0 \to L} \tag{42}$$

When the power-law approximation of Equation (39) is used for the basis rates, the resulting fitting law is called ECS-P and has the three fitting parameters A, γ, and l_c. As the collision time goes to zero, the adiabatic factor becomes 1 and the ECS law reduces to the IOS law.

While one or another of these fitting laws has successfully modeled nearly all of the available state-to-state rotational transfer data, no single law has been able to fit every data set [25]. There appears to be a trend from power law to exponential-power hybrid to exponential with decreasing mass of the collisional system [25]. The ECS model has successfully modeled more data than any other fitting law and many researchers [25, 123] have claimed that ECS is by far the best scaling law for RI data. The IOS form of ECS has been found to work better than ECS only for I_2^*+He; the small ratio of atomic mass to molecular mass makes this collision quite sudden [25].

38

An unappealing feature of these fitting laws is that the fitting parameters have little direct physical relation to the collision process. In the statistical laws, A, β, and γ have been assigned no meaning; they are simply adjustable parameters of a fit to the data. In ECS-P, however, a classical argument based on impulsive collisions relates A and γ to parameters of the intermolecular potential [25]. The argument assumes straight trajectories, impulsive collisions, and a simple long-range potential of the form

$$V(r) = C_n r^{-n} P_2(\cos\theta) \tag{43}$$

where θ is the angle between the molecular axis and the atom, P_2 is the second Legendre polynomial, and n is the order of the potential. Note the similarity between this potential and the potential of Equation (12) used in the classical broadening theory. The impulsive collision approximation assumes most of the torque applied to the molecule by the colliding atom occurs near the point of closest approach. An impulsive collision with the repulsive core of the potential, described by Equation (43), can be modeled as a collision with a hard ellipsoidal shell. This hard ellipse model will be developed further in the next section.

Through this classical argument, the fit parameter A is shown to be related to the coefficient C_n of the potential, while the fit parameter γ is related to the order of the potential n by [25]

$$\gamma = \frac{n}{n-1} \tag{44}$$

39

As stated previously, the parameter l_c is related to the collision time, though there is no way, as yet, to predict this value from the potential or the parameters of the collision partners. It thus seems that the dynamical models have an advantage over the statistical models in that the fit parameters of the dynamical models may be related to the physics of the collision, while the parameters of the statistical models are simply fitting coefficients with no special significance.

Now let's make the connection from state-to-state fitting laws back to our discussion of pressure broadening. The sum rules of Equations (25) to (27) assume that RI collisions are the dominant mechanism in pressure broadening and that all other collisional effects are negligible. Close coupling calculations indicate that the infrared sum rule of Equation (27) is in reasonable agreement with quantum-mechanical scattering calculations [47]. The sum rules, together with the fitting laws, have been successfully used to model a large body of pressure broadening data [18, 19, 23, 33, 34, 37, 67, 79, 80, 101, 123, 132]. However, different fitting laws, though they may equally fit the pressure broadening data, can predict very different state-to-state relaxation matrices.

There are several possible tests to see if pressure broadening data can be accurately described by fitting laws for RI collisions. The first, and most often used, is to measure broadening rates at low pressure and use a fitting law to model these rates and to create a relaxation matrix. This matrix can then be used to create a model of a line-coupled spectrum using Equation (21), which is then compared to an actual line coupled spectrum to check for agreement. This is a way to check that a fit to the pressure broadened data

produces a relaxation matrix which can successfully describe line coupling behavior in the same molecule at higher pressure [97]. However, various versions of EGL, SPG, and ECS have all been claimed to give the best fits to various data sets [123], so while this method lends support to the RI model of pressure broadening, it does not indicate that one fitting law is universally applicable.

A second test to see if RI collisions accurately describe total removal rate behavior is to model the imaginary part of the relaxation matrix as well as the real part, and then use the imaginary part to model the line shifting in a line-coupled spectrum. This provides an additional discriminator over just calculating the real part of the line coupling and has led to the claim [123] that ECS is the best model for Q branch line coupling and pressure broadening.

The third, and by far the most conclusive, method to see if RI collisions are the dominant mechanism in pressure broadening is to perform pressure broadening and state-to-state transfer experiment on the same optical transition of a molecule and see if a fitting law with the same fit parameters applies to both rotational transfer and pressure broadening results. However, as far as I am aware, this experiment has never been performed. This is probably because of the experimental challenges in finding a molecule and optical transition that are amenable to both kinds of experiments. This experiment would, however, provide a critical piece of information for or against the theory that RI collisions are the dominant mechanism in pressure broadening.

Along with the Q branch line coupling results which have supported the RI theory of pressure broadening, some results have pointed to inadequacies in the theory. For example, neglect of the elastic contributions is a standard and nearly universal

approximation. However, some measurements on small polyatomic molecules suggest that RI processes account for only a fraction of the linewidth and that 35-70% of the broadening may be due to elastic or other collisional mechanisms [97, 123]. Modifications to the sum rule have been proposed [80] to try to better model these possible additional collisional broadening mechanisms. With these uncertainties in mind, the RI model of collisional broadening still seems the best way to model pressure broadening of diatomic molecules by noble gas atoms.

Recently, a new state-to-state fitting law has been proposed which has some large benefits over the previous laws in that the new model has been derived from classical mechanics and the resulting fit parameters relate to the physics of the collision. The next section will present this theory and comment on its possible application to the pressure broadening problem.

2.2.2. A Classically-Derived Angular-Momentum-Based Fitting Law. Recently, McCaffery *et al.* [11, 73, 74, 75, 76, 85, 86, 87, 133] developed a theory for rotational transfer based on the classical dynamics of the conversion of linear to angular momentum during the collision. There is quite a bit of evidence which indicates that angular momentum plays the key role in rotational transfer.

First, in studies of a wide range of diatomics it was found that RT occurs with minimal reorientation of the J vector, meaning there is a propensity not to change m in a collision [74]. A consistent physical interpretation is that the relative velocity vectors, initial and final, are in a plane perpendicular to the rotational angular momentum vector of the molecule, so scattering in RT is coplanar with the plane of molecular rotation. This interpretation suggests that it is the coplanar trajectories that are effective in

42

bringing about RT. There are no energetic reasons for this preference since the *m*-states all have equal energy for a given *J*. The ECS and IOS laws, also derived from angular momentum considerations, restrict RT to the coplanar geometry via the 3-*J* symbol and indicate that an amount of angular momentum equal to the change in rotational angular momentum is simply added to that already present as though the molecule is not rotating. Thus, the ECS fitting law, which has had wide success in fitting RT data, is consistent with the angular momentum model of McCaffery *et al*.

Another piece of evidence for angular momentum control of RT probabilities is the effect on RT rates when constraints are placed on the amount of linear momentum available for conversion to angular momentum (AM). In experiments using a heavy molecule and light perturber there is a regime in which the AM limit is reached but sufficient energy remains to satisfy energy transfer requirements. The AM forbidden region exists because of the linear dependence of AM on the relative velocity, while the kinetic energy has a quadratic dependence. It has been observed [74] that beyond the region of availability of linear momentum for conversion to angular momentum, the RT rates drop faster than expected. So although there is still sufficient energy, the AM requirement dominates.

A third piece of evidence for AM control of RT comes from studies of bent triatomic molecules, in which the relationship between angular momentum and energy is more complicated than in diatomic molecules. State-to-state measurements on NH_2 show no correlation with energy change; the data cannot be fitted with exponential or power dependencies on ΔE. However, the RT rates are found to fall exponentially with magnitude of transferred AM [73, 74]. In general, the exponential or power-law behavior

43

of the RT probabilities with transferred AM is a consequence of the averaging of the angular and radial parts of the repulsive intermolecular potential under conditions of random orientation of the collision partners and a Maxwell-Boltzmann distribution of velocities [85]. Thus in the AM model, the exponential and power-gap laws, which have been found to fit a large body of RT data, have a simple physical origin. This is not apparent in the energy dependence but is a natural consequence in a calculation of the probability of angular momentum transfer.

The AM fitting law was developed as follows. In a state-resolved collisional RT experiment, the molecule is initially in a well-defined rotational state and the probability of transfer into other rotational states is measured. Since the collision results in a change of both energy and momentum, the probability of rotational transfer could depend upon both energy and angular momentum. The joint probability of a particular change in energy ΔE accompanied by a particular change in angular momentum Δl is written $P(\Delta E, \Delta l)$. Assuming that ΔE and Δl are independent [11, 74] then the probabilities $P(\Delta E)$ and $P(\Delta l)$ are independent random variables and

$$P(\Delta E, \Delta l) \cong P(\Delta E)P(\Delta l) \qquad (45)$$

This is a discrete function which is nonzero only for definite values of ΔE and integer values of Δl (since angular momentum is quantized). Conservation laws on total angular momentum and total energy must apply and these may be denoted by δ-functions which state explicitly the range over which the joint probability is nonzero.

44

The angular momentum model is characterized by an assumption that $P(\Delta l)$ is determined by the variables that control the conversion of linear to angular momentum while $P(\Delta E)$ has unit probability, within the restrictions of energy conservation. Thus, Equation (45) becomes

$$P(\Delta E, \Delta l) = P(\Delta l)\delta(E_{tot} - E'_{tot})\delta(L - L') \tag{46}$$

The task, then, is to describe $P(\Delta l)$. For visualization purposes, it useful to represent the potential using the hard ellipse model [22, 113], which embodies the impulsive, planar view of the RT process. The hard ellipse model of rotational transfer is shown in Figure 3.
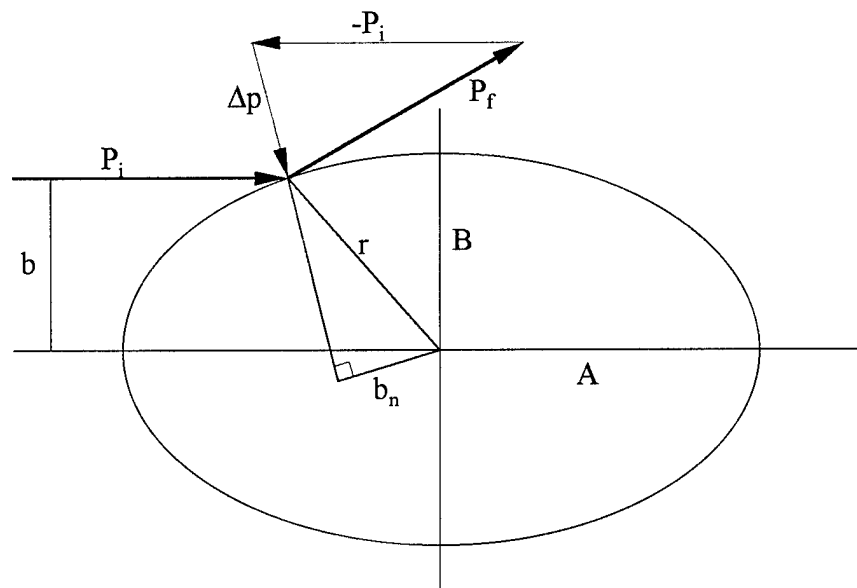
Figure 3. Hard Ellipse Model of Rotational Transfer

The classically-impulsive limit effectively assumes that RT results from interaction at the repulsive inner wall of the potential. The expression for torque is $-[dV(r,\theta)/d\theta]$, so the isotropic component, which has no variation with θ, vanishes on differentiation. Thus the component of the potential with which we are concerned in RT is the radial distribution of the repulsive anisotropy. Only at the repulsive wall does the potential vary sufficiently rapidly with θ to generate the torque required to cause appreciable RT [22].

In the classically impulsive limit, linear momentum is converted to angular momentum at a fixed distance which does not change throughout the collision. Thus, changes in l result from changes in p at radial distance r:

$$\Delta \vec{l} = \vec{r} \times \Delta \vec{p} \tag{47}$$

The magnitude of the angular momentum transferred to the ellipse is given by the product of the change in linear momentum Δp and the torque-arm or effective impact parameter r, which will be called b_n. The effective impact parameter is defined as the perpendicular distance between the center of mass of the molecule and the line of transferred momentum. In the hard ellipse model $b_n = (A - B)$, where A and B are the semi-major and semi-minor axes, respectively.

The change in linear momentum is a function of the relative collision velocity v_r, and reduced mass of the collisional system μ:

$$\Delta p = \mu v_r \tag{48}$$

46

For a collision in which the relative velocity of the system is normal to the surface of the ellipse, the magnitude of angular momentum available for transfer at the point of impact is

$$\Delta l = l = \mu v_r b_n \tag{49}$$

Since the molecule is assumed to be initially not rotating, $\Delta l = l$. Therefore, specific combinations of v_r and b_n will contribute to a particular angular momentum channel. In the hard ellipse model, the component of momentum perpendicular to the hard wall generates torque and the length of the torque arm depends strongly on the position on the ellipse that the particle strikes. For trajectories perpendicular to the hard wall, the impact parameter b and effective impact parameter b_n will be identical. There is a threshold velocity, v_{th}, at a perpendicular impact parameter, required to open each particular angular momentum channel. Higher relative velocities at less favorable impact parameters can also yield a perpendicular component equal to v_{th}.

The probability of a particular effective impact parameter b_n is $P(b_n)$. The probability $P(\Delta l) = P(l)$ of a transfer of angular momentum l is conditional upon the occurrence of a particular effective impact parameter b_n, which is written as the conditional probability $P(l|b_n)dl$. The joint probability of a particular angular momentum occurring with a particular impact parameter is obtained as a product of the two distributions, which is then averaged over all values of b_n, up to some maximum b_n^{max}, to

obtain the full probability distribution of the angular momentum available at the hard wall of the ellipse [86]:

$$P(l)dl = \int_0^{b_n^{max}} P(l \mid b_n)P(b_n)b_n db_n dl \qquad (50)$$

Thus the problem amounts to finding appropriate expressions for $P(l|b_n)$ and $P(b_n)$.

For a given value of b_n, angular momentum is a function only of relative collision velocity, so [86]

$$P(l)dl = P(v_r)\left|\frac{d}{dl}(v_r)\right| \qquad (51)$$

Thus, for a collision of an atom with the ellipse, the change in relative velocity provides the necessary impulse for the transfer of angular momentum. Application of the energy and angular momentum conservation laws for the case in which the atom is backscattered from the ellipse gives the magnitude of angular momentum transfer as [86]

$$l = \mu\left(v_r + \sqrt{v_r^2 + v_{th}^2}\right)b_n \qquad (52)$$

The threshold velocity, v_{th}, at which the rotational channel l opens is [84]

$$v_{th} = \sqrt{\frac{2\Delta E_{if}}{\mu}}$$

(53)

where ΔE_{if} is the energy gap between an initial rotational state J_i and final state J_f of the diatomic rotor. In experiments at thermal equilibrium, the relative velocity has a Maxwell-Boltzmann (MB) probability density $P(v_r)$, which is

$$P(v_r) = 4\pi \left(\frac{\mu}{2\pi kT}\right)^{3/2} v_r^2 \exp\left(-\frac{\mu v_r^2}{2kT}\right)$$

(54)

Equation (52) can be solved for v_r and substituted into Equation (51), along with the MB velocity distribution of Equation (54), to obtain an expression for $P(l|b_n)$ which is consistent with energy conservation:

$$P(l \mid b_n)dl = 4\pi \left(\frac{\mu}{2\pi kT}\right)^{3/2} \frac{v_r^2}{2\mu b_n} \exp\left(-\frac{\mu v_r^2}{2kT}\right)\left|1 - \left(\frac{\mu b_n v_{th}}{l}\right)^2\right|$$

(55)

In contrast to the expression obtained above for $P(l|b_n)$, the probability $P(b_n)$ is less readily derived and less rigorous in nature since it represents the unknown form of the radial dependence of the repulsive anisotropy of the intermolecular potential. Osborne and McCaffery fit several different functional forms to experimental state-to-state rate data and determined that the best representation of the repulsive anisotropy was found to be an inverse power relation [85, 86]:

$$P(b_n) = b_n^{-\gamma} \qquad (56)$$

where γ is a variable parameter controlling the range of the probability distribution.

Now that we have expressions for $P(b_n)$ and $P(l|b_n)$, we have a complete expression for $P(l)$ from which we can develop an expression for the probability of a particular RI state-to-state transition. For an initial rotational state J_i, the probability that a particular angular momentum l will couple to give a final state J_f may be written as $P(J_f|J_i,l)dldJ_f$. Summation over all l contributing to the transition between J_i and J_f gives the final rotational state distribution [86]

$$P(J_f|J_i)dJ_f = \int_{|J_i-J_f|}^{|J_i+J_f|} P(J_f|J_i,l) \int_0^{b_n^{max}} P(l|b_n)P(b_n)b_n db_n dl dJ_f \qquad (57)$$

where $P(J_f|J_i)$ represents the classical expression of the rotationally-inelastic transition probabilities, or rates, k_{if}. A final simplification comes from assuming a delta function $\delta(|J_i - j_f|)$ for the probability density $P(J_f|J_i,l)$. This function peaks strongly at $l = |J_i - J_f|$ and effectively restricts the collision geometry to one which is coplanar with the plane of rotation. The final expression for the state-to-state rotational relaxation rates k_{if} is [86]

$$k_{if} = P(J_f|J_i)dJ_f = C \int_0^{b_n^{max}} P(l|b_n)P(b_n)\delta(|E_{tot} - E_{tot}'|)\delta(|J_i - J_f|)b_n db_n dJ_f \qquad (58)$$

50

where C is a scaling factor having units of cm^3/sec and $P(l|b_n)$ and $P(b_n)$ are given by Equations (55) and (56), respectively. The form of Equation (55) is already consistent with energy and angular momentum conservation. Equation (58) can be used as a fitting law with three variable parameters, $\{C, b_n^{max}, \gamma\}$, and is referred to in the rest of this document as the AM fitting law of Osborne and McCaffery. Two of the fitting parameters have genuine physical significance: b_n^{max} is related to the maximum value of the repulsive anisotropy, while γ represents a measure of the steepness of the repulsive wall of the intermolecular potential.

The AM fitting law has been tested against several atom-diatom state-to-state data sets and has successfully fit the data in all cases, in many cases better than the semi-empirical fitting laws of the previous section [86]. From these fits, b_n^{max} was found to be very close to one half of the bond length (HBL) of the diatomic molecule. This indicates that the maximum angular momentum that may be transferred in a system is obtained when the reduced mass interacts with the maximum available relative velocity at a radial distance equal to one half of the bond length. Physically, this implies that the maximum anisotropy of the potential ($A - B$ in the hard ellipse model) is equal to half the diatomic bond length.

When the atom is heavier than the diatom, conservation of energy requires the maximum torque arm to be reduced, so $b_n^{max} <$ HBL [11]. On the other hand, when the diatom is heavier than the atom, angular momentum conservation is the dominant constraint. In this case the full torque arm is used and $b_n^{max} \approx$ HBL, but the number of high ΔJ channels is reduced [11]. The AM fitting law correctly models both of these cases [86].

Tests of the fitting law have found values of the fitting parameter γ, which describes the steepness of the potential, clustered in the range from 1.8 to 2.4 [86]. A classical impulsive calculation similar to that performed in the previous section for ECS-P predicts $\gamma = 2.4$ for an r^{-6} potential, with slightly smaller values for higher-order potentials [85]. The γ parameter was found to vary somewhat with collision partner for a given diatomic, but the major cause of substantial changes in rotational transfer rates was found to be the reduced mass of the collision partners [86].

Given the appealing derivation of the AM fitting law, the physical significance of the fitting parameters, and the success with which it has fit available state-to-state data, I would like to apply this model to my experimental pressure broadening data. This is only possible, however, if the fitting parameters $\{C, b_n^{max}, \gamma\}$ are independent of the initial rotational level J_i. This issue will be explored further in Chapter V of this dissertation.

2.3. Spectroscopy of the Oxygen A Band and Nitric Oxide Fundamental Band

2.3.1. The Oxygen A Band.
The oxygen molecule, O_2, is a homonuclear diatomic; this symmetry prevents the molecule from having a permanent electric dipole moment. It does, however, possess higher-order moments in the multipole expansion. The transition of interest for this research, $b^1\Sigma_g^+ \leftarrow X^3\Sigma_g^-$, is a magnetic dipole-allowed transition. The oxygen A band is a photon transition between the ground vibrational levels ($v'' = 0 \rightarrow v' = 0$) of the ground electronic state (X) and an excited electronic state (b). The total orbital angular momenta of the electrons in these states is zero, so both electronic states are Σ states. In the ground electronic state the electron spin quantum number is $S = 1$, so there are $2S + 1 = 3$ degenerate spin states, making the ground state a

triplet state, $^3\Sigma$. In the transition to the b state, one of the electron spins flips from parallel to antiparallel, so $S = 0$ and the state is a singlet state, $^1\Sigma$. The + and − superscripts and g subscript refer to symmetry properties of the electronic eigenfunctions.

Diatomic oxygen is a Hund's case (b) molecule, which means the electron spin angular momentum $\mathbf{S}$ is only weakly coupled to the internuclear axis [52]. In this case, the total angular momentum without electron spin is a good quantum number. The quantum number is designated K and may take only integer values. The total angular momentum is $\mathbf{J} = \mathbf{K} + \mathbf{S}$, where the possible values of the quantum number J run from $(K + S)$ to $|K − S|$ in integer steps.

The magnetic dipole selection rules for a Hund's case (b) diatomic molecule help describe the features in the observed A band spectrum [7, 52]. The change in total angular momentum while absorbing a photon can be $\Delta J = 0, \pm 1$ with the restriction $J = 0 \nrightarrow J = 0$. The change in K, for a $\Sigma \rightarrow \Sigma$ transition, can be $\Delta K = \pm 1$. Transitions must occur between electronic wavefunctions of the same symmetry, so only $+ \rightarrow +$ and $- \rightarrow -$ transitions are allowed. However, in the case of O_2, nuclear spin symmetry prevents the $- \rightarrow -$ transitions. Applying these selection rules to the oxygen A band results in the allowed transitions shown in Figure 4.

The transitions are labeled by P, Q, or R corresponding to $\Delta J = -1, 0,$ or $+1$, with a superscript P or R corresponding to $\Delta K = -1$ or $+1$. The spectrum of the oxygen A band thus has four allowed rotational branches, designated $^PP, ^PQ, ^RR,$ and ^RQ. The observed lines are numbered within the four branches according to the value of K''. A typical oxygen A-band spectrum is shown in Figure 5.
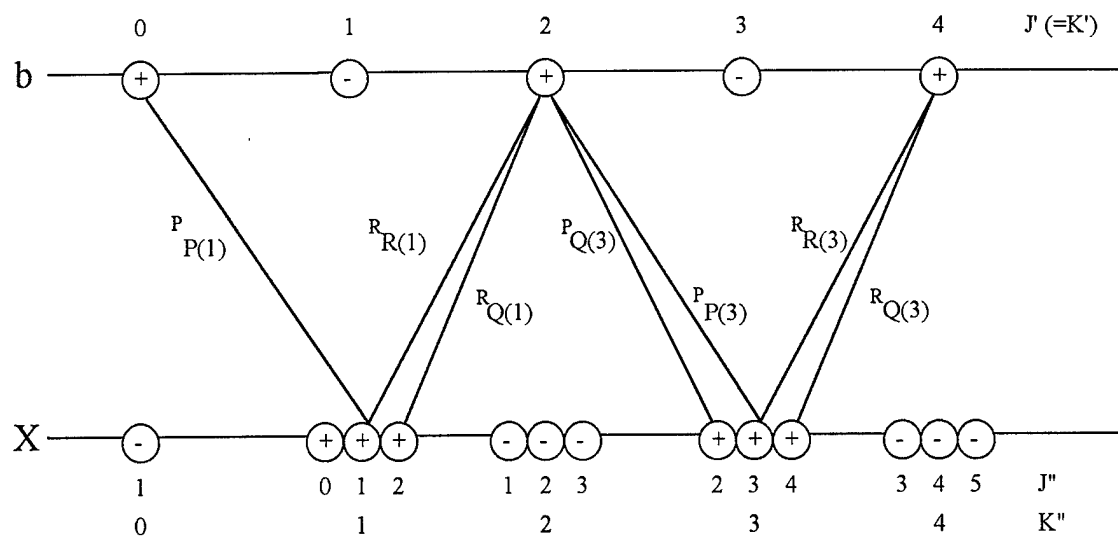
Figure 4. Allowed Transitions in the Oxygen A Band
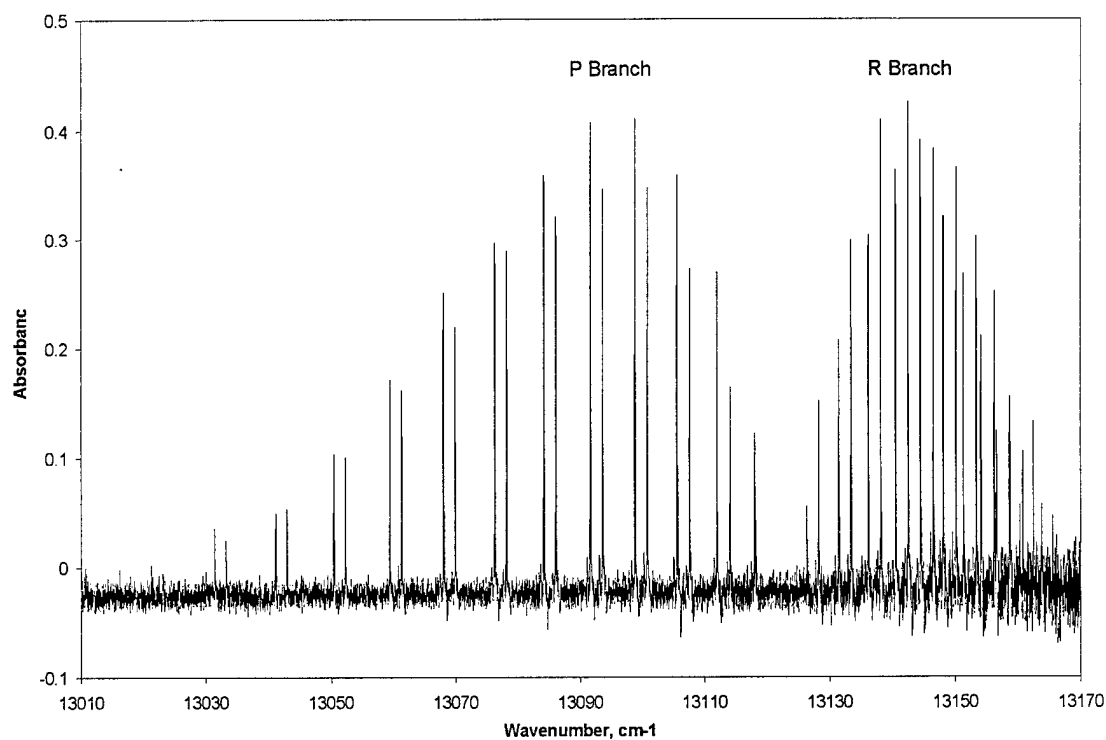
Figure 5. Typical Oxygen A Band Spectrum at Room Temperature

54

The center of the A band is at 13122 cm^{-1}, with the P branch extending to the lower wavenumber side and the R branch to the higher wavenumber side. The P branch forms pairs of lines, ^{P}P and ^{P}Q, which are separated by approximately 2 cm^{-1}. The spacing between the pairs increases from about 6 cm^{-1} at low K'' to about 10 cm^{-1} at $K'' = 12$. The R branch also forms pairs of lines, ^{R}R and ^{R}Q, which are separated by approximately 2 cm^{-1}. The R branch heads near $K'' = 29$ [91], where the spacing between the pairs decreases from about 5 cm^{-1} to less than 1 cm^{-1}.

Because the oxygen A band transition is electric dipole-forbidden, the absorption cross section is quite small. Using an Einstein A coefficient $A_{21} = 0.11$ sec^{-1} [64] and assuming a Doppler lineshape (a reasonable approximation at low pressures), the absorption cross section for a single rotational transition is 2×10^{-22} cm^2. This is 4 orders of magnitude smaller than a typical absorption cross section for an electric dipole-allowed transition.

2.3.2. The Nitric Oxide Fundamental Band. Nitric oxide is a paramagnetic molecule with nonzero nuclear spin on the nitrogen atom due to an unpaired electron. NO is the only known stable diatomic molecule with both nonzero spin and orbital angular momentum in the ground electronic state [82]. NO is a Hund's case (a) molecule, which means the electronic motion is coupled very strongly to the internuclear axis. In this case, the electronic angular momentum $\Omega = \mathbf{L} + \mathbf{S}$ is well defined, so Ω is a good quantum number. Addition with the angular momentum from nuclear rotation gives the total angular momentum, $\mathbf{J} = \Omega + \mathbf{N}$.

The nitric oxide fundamental band, which is of interest in this research, is an optical transition from the ground vibrational state to the first excited vibrational state within the electronic ground state, $(v'' = 0 \rightarrow v' = 1)$. In the ground state of nitric oxide the electron configuration is such that $\Lambda = 1$, and $S = 1/2$ because of the unpaired electron, so the ground electronic state of NO is a $^2\Pi$ state. For these values of Λ and S, the possible values of the total electronic angular momentum quantum number Ω are $\Lambda - S = 1/2$ and $\Lambda + S = 3/2$. These two Ω values are called the two magnetic substates of NO and are indicated by a subscript of the Ω value of the state label: $^2\Pi_{1/2}$ and $^2\Pi_{3/2}$. The two spin-orbit multiplets of NO are close in energy, so that both are appreciably populated at room temperature.

Since $\Lambda = 1$ for the ground state of NO, each magnetic substate is twofold degenerate: $M_L = \pm\Lambda$. These degeneracies are split by a process called Λ-doubling, which has two conflicting explanations in the literature. One explanation says the interaction between the nuclear rotation and the electronic orbital angular momentum causes a slight uncoupling of $\mathbf{L}$ from the internuclear axis, which removes the $\pm\Lambda$ degeneracy [52, 82, 121]. The second explanation says the perturbation of the ground $X^2\Pi$ state by nearby excited Σ electronic states removes the degeneracy [4, 92]. The splitting is greatest for terms with the smallest Ω [52]. As such, the Λ-doubling is ~0.01 cm^{-1} in the 1/2 substate, while it is ~0.001 cm^{-1} in the 3/2 substate [118]. The two Λ-doubled lines are labeled e and f. An energy level diagram for the NO fundamental band which shows the magnetic substates and Λ-doubled components, is shown in Figure 6, while a typical spectrum of the NO fundamental band is shown in Figure 7.
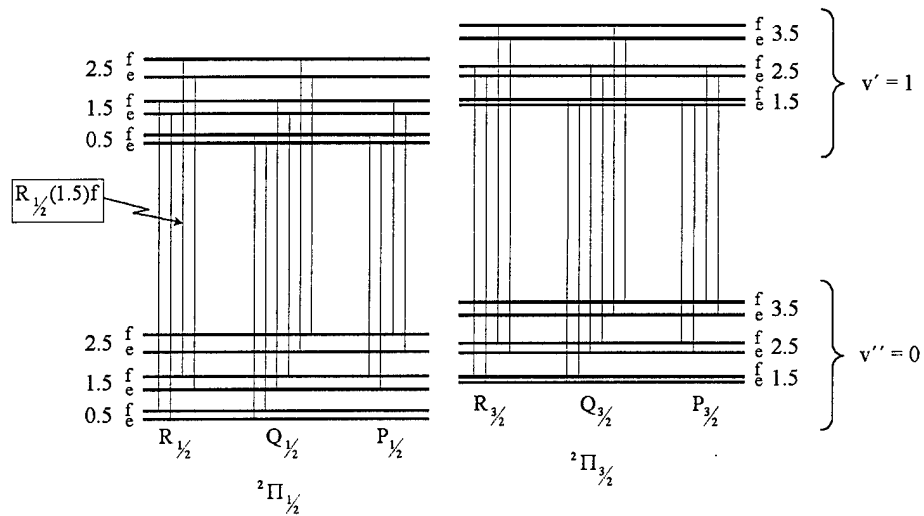
Figure 6. Energy Level Diagram of the Nitric Oxide Fundamental Band
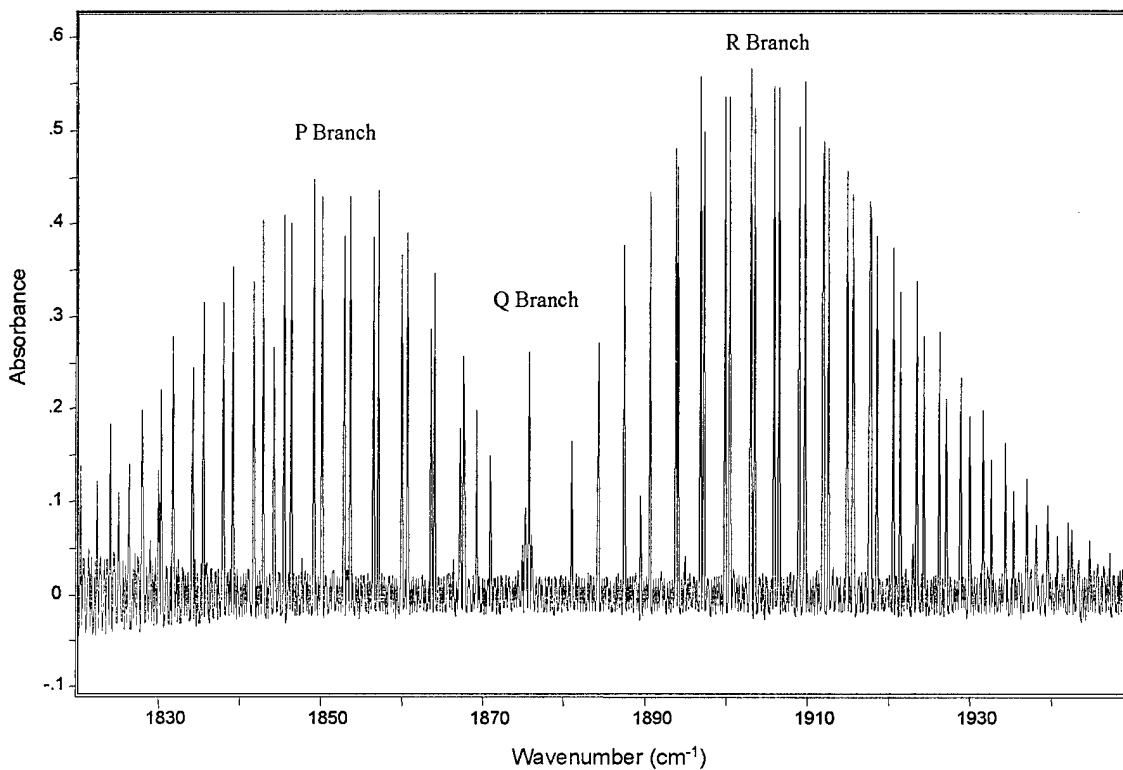
Figure 7. Typical Nitric Oxide Fundamental Band Spectrum at Room Temperature

57

The fundamental vibrational band consists of these 1/2 and 3/2 magnetic substates, each with a P, Q, and R branch corresponding to $\Delta J = -1$, 0, and +1, respectively. Lines are labeled with the branch letter, the magnetic substate, the label for the Λ-doublet component in the lower level, and the lower state rotational quantum number; see for example the $R_{1/2}(1.5)f$ line in Figure 6. Since total electronic angular momentum is half-integer and the nuclear rotation is integer, the total rotational angular momentum J has half-integer values for this molecule. The band center is at approximately 1876 cm^{-1}. The P branch extends to lower wavenumbers, while the R branch extends to higher wavenumbers. Near the band center, the frequency difference between the magnetic components is only a few hundredths of a wavenumber, but in the wings it is almost 2 cm^{-1}. The intensity of the P and R 1/2 lines, since they originate on the ground state of their doublet, are about twice as strong as the corresponding 3/2 lines [42]. Although optical transitions between the $^2\Pi_{1/2}$ and $^2\Pi_{3/2}$ subbands can occur, they are quantum-mechanically forbidden transitions with strengths $\sim 10^4$ times weaker than the corresponding strengths of the $1/2 \rightarrow 1/2$ and $3/2 \rightarrow 3/2$ transitions [2]. The Q branch sits between the P and R branches and extends to lower wavenumbers. The Λ-doublet separation in the Q branch is about twice that of the corresponding P and R branch transitions, since the Q branch transitions are $e \leftrightarrow f$, while the P and R branch transitions are $e \leftrightarrow e$ or $f \leftrightarrow f$; this is shown in Figure 6.

The rotational structure is further complicated by magnetic hyperfine structure, due to the nuclear spin of the ^{14}N nucleus [17]. The electronic magnetic moment couples the molecular momentum **J** to the nuclear spin **I**, yielding the resultant momentum **F**. At

low J, ($|m| < 2.5$), the hyperfine splitting is large enough to alter the Voigt shape of the lines. The hyperfine splitting is much smaller in the P and R branches than in the Q branch, particularly for high-J values [118].

Because the NO fundamental band transition is electric dipole-allowed, the absorption cross section is much larger than the cross section for the oxygen A band. Using an Einstein A coefficient $A_{21} = 10.78$ sec^{-1} [14] and assuming a Doppler lineshape (a reasonable approximation at low pressures), the absorption cross section for a single rotational transition is 8×10^{-18} cm^2. This is 4 orders of magnitude larger than the absorption cross section for the oxygen A band.

III. Background

Several experiments have been previously performed to study collisional effects in the oxygen A band and nitric oxide fundamental band. This chapter will briefly summarize the results of these previous studies. This will serve as a point of comparison for the results of the current study, where previous results exist, and will indicate the novelty of the current study in the cases where previous results do not exist.

Laboratory measurements of pressure broadening and line shifting are often reported as coefficients. For example, the pressure broadening coefficient is $\gamma = \Delta v / P$ where Δv is the HWHM of the line and P is the pressure. Similarly, the line shifting coefficient is $\delta = \delta v / P$ where δv is the shift of line center. A line narrowing coefficient is reported when Dicke narrowing is observed. In this document, units of these coefficients will all be expressed as cm^{-1}/torr, though other frequency/pressure units, such as cm^{-1}/atm or MHz/torr, are often seen in the literature. Errors on laboratory data will be quoted as one standard deviation $(1-\sigma)$ unless otherwise noted.

3.1. Oxygen A Band

3.1.1. Collisions with O_2, N_2, and Air.

Pressure broadening in the oxygen A band was first measured in the laboratory in 1969 by Burch and Gryvnak [27], who used a grating spectrometer to measure self- and N_2-broadening. Measurements were made for 25 lines in the P branch and it was assumed that the broadening coefficients were equal for the same J'' in the R branch. The N_2 broadening coefficients were $(6 \pm 3)\%$ larger

than the self-broadening coefficients and the coefficients decreased with increasing J. The self-broadening coefficients are graphically compared with the results of the current study in the next chapter. Oxygen A-band line positions and labels from Burch and Gryvnak are listed in Appendix A.

Also in 1969, Miller, Boese, and Giver [78] used a grating spectrometer to measure self-broadening for 19 lines in the P branch. At low J, the broadening coefficients were up to 33% less than those of Burch and Gryvnak [27], a substantial discrepancy. These self-broadening coefficients are also on the comparison graph in the next chapter. Miller *et al.* studied broadening with N_2 and found no systematic differences between self- and N_2 broadening to within experimental uncertainties.

The same researchers [43] later studied self-broadening in the B band $(v'' = 0 \rightarrow v' = 1)$ at 14500 cm^{-1}, again using a grating spectrometer. They measured from $J'' = 9$ in the R branch to $J'' = 25$ in the P branch and reported broadening coefficients which ranged from 8.29×10^{-5} cm^{-1}/torr at $J'' = 1$ to 5.53×10^{-5} cm^{-1}/torr at $J'' = 25$, with average errors of only 2%. These values fall between the two previous studies, as will be seen in the comparison graph in the next chapter. These results are significant because they have been adopted as the A-band widths in the HITRAN 96 atmospheric transmission database [56, 57, 110] and because this study was the first to measure line halfwidths directly; previous efforts calculated the broadening coefficient from the measured linestrength, assuming a Lorentzian profile.

Galkin [38] used grating spectroscopy to measure 19 lines in the P branch of the A band and 13 lines in the P branch of the B band. Broadening coefficients were calculated using curve of growth, absorption at line center, and absorption between the

lines, with discrepancies greater than 30% among the three methods. No clear set of broadening coefficients could be chosen, so these results will not be considered further. The A and B bands were found to have the same broadening coefficients to within the large experimental uncertainties of this study. Comparison of self- and N_2-broadening in the A band found N_2 broadening about 9% less efficient than self broadening.

In 1986, Ritter and Wilkerson [106, 107] used a tunable dye laser with a narrow linewidth (< 0.0001 cm^{-1}) to measure self-broadening in 54 rotational lines of the A band, with each line measured from 3 to 13 times at pressures between 30 and 800 torr. Since the resolution of this experiment was much higher than in previous grating spectroscopy experiments, a careful study of the line shapes could be performed. Lines were initially fit with Voigt profiles; however, trends in the residuals characteristic of Dicke narrowing were observed (see Figure 1), so the Galatry lineshape was used instead. Use of the Galatry instead of the Voigt only slightly changed the retrieved Lorentzian linewidths; the broadening coefficients were about 1% larger for a Galatry lineshape than for a Voigt lineshape. Self-broadening coefficients ranged from 7.89×10^{-5} cm^{-1}/torr at $J'' = 1$ to 4.74×10^{-5} cm^{-1}/torr at $J'' = 29$, with average errors of less than 1%. These results are included in the self-broadening comparison graph in the next chapter. To within the accuracy of the measurements, the pairs of lines having the same K'' in each branch were found to have the same broadening coefficient, with significant differences only occurring for $J'' < 5$, with differences increasing toward lower J''. Ritter and Wilkerson also measured air broadening for five rotational lines. Converting the results to nitrogen broadening by assuming air is 79% N_2, 20% O_2, and 1% other gases (which

were ignored), it was found that N_2-broadening coefficients were about 3.8% larger than self-broadening.

Recently, several researchers [14, 31, 63, 103, 104] have used tunable diode laser spectroscopy to measure self, N_2, and air broadening of a few lines in the oxygen A band. DeAngelis et al. [31] measured self-broadening in the ^{P}P(9) line and used a Voigt lineshape to fit the peaks. The resulting broadening coefficient was approximately twice as large as values reported by earlier researchers using grating and dye laser spectroscopy. Kauranen and Avetisov [63] measured air broadening of three lines in the R branch. Voigt lineshapes were used; however, the fit was improved by narrowing the Doppler HWHM by more than 50%. They interpreted this as an indication of Dicke narrowing. The resulting broadening coefficients were in reasonable agreement with values reported by researchers using other methods.

Bhattacharyya et al. [14] and Ray et al. [103, 104] measured self- and N_2-broadening of a few lines in the R branch. They observed the width of each line to decrease in width from 30-100 torr then increase linearly in width above 100 torr. They interpreted this as an indication of Dicke narrowing, so they used a Galatry lineshape to analyze their data. The self-broadening coefficients were in approximate agreement with the results of previous researchers; however there was no clear trend with J. The corresponding narrowing coefficients showed an increase with J and all values are substantially larger than Ritter's narrowing coefficient [107]. The N_2-broadening coefficients showed a clear decreasing trend with J but were about twice as large as those reported by other researchers, while the corresponding narrowing coefficients showed an increase with J and also showed a decrease with increasing O_2 pressure at higher J. In

general, it appears that diode laser spectroscopy does not yet offer the same high quality of results that are available from grating spectroscopy or dye laser spectroscopy.

Measurements of collision-induced line shifting have been reported much less often than pressure broadening measurements. There are two reasons for this. First, line-shifting coefficients are nearly an order of magnitude smaller than the corresponding broadening coefficients. Second, line-shifting measurements require either a very precise frequency calibration or some sort of precise reference frequency in order to measure the shifts. Broadening measurements, on the other hand, can be made on line with only a mediocre frequency calibration, as long as the frequency offset is linear and does not perturb the lineshape.

Line shifts in O_2 + air have been studied with grating spectrometers and reported to be -10.3×10^{-6} cm^{-1}/torr [3] and $-8.3\pm1.4 \times 10^{-6}$ cm^{-1}/torr [39]. The negative sign indicates that the shift is toward lower wavenumbers (a red shift) as pressure increases. These measurements found no J dependence to within measurement uncertainties. More recent measurements with a tunable dye laser [106], however, found an increase in shift with increasing J. Self-shifting coefficients varied from -2.9×10^{-6} cm^{-1}/torr for $J'' = 1$ to -8.69×10^{-6} cm^{-1}/torr for $J'' = 25$. Comparison with air-shifting found a shift coefficient ratio $\delta_{air}/\delta_{self} = 1.37$, from which one can compute the ratio of N_2 to self-shifting as $\delta_{nitrogen}/\delta_{self} = 1.73$. This indicates that N_2 shifting is much more effective than self-shifting.

3.1.2. Collisions with Other Gases. Ritter [106] used tunable dye laser spectroscopy to perform a cursory examination of broadening and shifting of oxygen by the noble gases He, Ne, Ar, Kr, and Xe. This study measured 15 rotational lines with

xenon and 13 with the other noble gases. However, only the ^{R}R(5) line was measured at a range of perturber pressures; the remaining lines were measured only at 760 torr. Precise broadening coefficients are usually determined by a linear least squares fit to a plot of Lorentzian HWHM vs. perturber pressure; this assures a linear behavior with pressure and also averages out the errors due to each individual measurement. Ritter's data, since they were computed from just a single pressure, do not have the same assurance of precision. However, they serve as a good basis of comparison for the current study. The broadening coefficients clearly show a decreasing trend with increasing J. They also indicate that the magnitude of the broadening coefficient is perturber-dependent. This will be explored further in the next chapters.

Ritter also reported pressure-induced line shifting coefficients for each line studied. The coefficients were predominately red-shifted and showed an increase with increasing J, as seen for self-shifting. However, there are some modest differences between the P-branch and R-branch shift coefficients. The R-branch coefficients, in general, were found to be smaller than the P-branch coefficients for the same J. Ritter also reported a small blue-shift (positive shift coefficients) for He and Ne from $J'' = 1$ to $J'' = 5$ in the R branch. However, the values were quite small ($< 1 \times 10^{-6}$ cm^{-1}/torr) so, depending on the magnitude of the experimental uncertainties (which were not reported), these blue-shifts may not be real. The shift coefficients also showed a clear increase with increasing perturber mass, rising in magnitude from $\sim 0.3 \times 10^{-6}$ cm^{-1}/torr for helium to $\sim 15 \times 10^{-6}$ cm^{-1}/torr for xenon at moderate values of J.

The only study of noble gas broadening in the oxygen A band which has appeared in the refereed literature is that of Biswas et $al.$ [16], who measured Ar-broadening for

three lines in the R branch, using tunable diode laser spectroscopy. While some Dicke narrowing was observed, the maximum discrepancy between a Galatry and a Voigt fit to the data was less than 5%. The resulting broadening coefficients, determined using the Galatry lineshape, were 7.17(16) for $^RR(13)$, 5.45(11) for $^RR(23)$, and 4.91(9) for $^RQ(23)$, all $\times 10^{-6}$ cm^{-1}/torr.

3.1.3. Calculations. No calculations or fitting laws have been applied to the oxygen A band in the refereed literature. However, Ritter [106] performed Anderson's-theory calculations for both self- and noble gas-broadening using available potential energy surfaces. Modifications were made to Anderson's theory to account for the two different potential curves connected by the electronic X→b transition. The resulting calculations for the noble gases, in general, matched the shape of the J-dependent trends in the broadening coefficients. The calculated result for self-broadening, however, was a poor match to the data; with the calculated results decreasing too quickly with increasing J. Ritter noticed, however that the self-broadening calculation nearly matched the Ar-broadening calculation, which has similar potential parameters. He concluded that Anderson's theory does not successfully model structured, molecular perturbers, but works well for structureless perturbers like the noble gases.

In summary, collisional effects in the oxygen A band have been studied thoroughly for self-broadening, but much less for broadening with any other perturbers. Also, no study has yet used Fourier transform spectroscopy. The current research, which uses FTS to study collisions with 10 perturbers, makes it the most complete study of the oxygen A band performed to date.

66

3.2. Nitric Oxide Fundamental Band

In contrast with the oxygen A band, many more collisional studies have been made in the nitric oxide fundamental band. The absorption cross section for the NO fundamental is about 8×10^{-18} cm^2 for a single rotational line, while the absorption cross section for a single rotational line in the oxygen A band is about 2×10^{-22} cm^2, making it much easier to perform absorption spectroscopy with nitric oxide. The reason for the large difference is that the NO fundamental band is an electric dipole-allowed transition, while the oxygen A band relies on a much weaker magnetic dipole transition. Another reason more studies have been performed in the NO fundamental is because of the interesting spectroscopy, since NO one of the few diatomic molecules with a $^2\Pi$ ground state.

Before describing the previous research in the NO fundamental, the branch-independent quantum number, m, must be introduced. A P-branch transition occurs when $\Delta J = -1$, while an R-branch transition is $\Delta J = +1$. One can develop an equation which describes the energy of a P- or R-branch transition by defining m, where $m = -J''$ for a P-branch transition and $m = J''+1$ for an R-branch transition [9]. It is often convenient to tabulate pressure-broadening values in terms of $|m|$ so P- and R-branch broadening coefficients for the same value of $|m|$ may be easily compared.

3.2.1. Collisions with NO and N_2.
Studies of the NO fundamental band pressure-broadened by N_2 have been performed extensively in the P and R branches using CO laser resonance absorption [21, 48, 105], NO resonance absorption [66], grating spectroscopy [51, 127], tunable lasers [36, 70, 81, 93, 109, 112], and Fourier transform spectroscopy [8, 58, 118, 119]. On the other hand, very little study has been made of

pressure-broadening in the Q branch of NO fundamental because the small separation between the Q branch lines requires high resolution. The only reported study of Q-branch broadening by N_2 was performed using FTS [118].

Self-broadening in the P and R branches has been studied much less than N_2 broadening, primarily because the large absorption coefficient for NO requires path lengths of less than 1 cm for studies at modest pressures. Though studied less extensively than broadening by N_2, self-broadening has also been examined by grating spectroscopy [2, 61, 131], CO laser resonance absorption [21, 40, 48, 105], tunable lasers [65, 109], and FTS [8, 58]. Self-broadening in the Q branch has been examined using CO laser resonance absorption [40] and Raman spectroscopy [69]. The NO self-broadening coefficients reported by previous researchers are important to the current research project because they are required to calculate foreign-broadening coefficients in gases which are a mix of NO and the foreign gas.

The most complete study of self-broadening in the P and R branches of the NO fundamental was performed in 1988 by Ballard *et al.* [8], so it will be summarized first and used as a basis of comparison for the results of other researchers. Ballard *et al.* used a Fourier-transform spectrometer (BOMEM DA3.002) and recorded spectra at resolutions of 0.003 or 0.005 cm^{-1}. All measurements were made above 200 torr to avoid the necessity of incorporating an instrument function into computer simulations of the measured spectra. The Voigt lineshape was used in data analysis. Ballard *et al.* assumed equal widths for the Λ components, which were not individually resolvable at the pressures used. Broadening coefficients for the 1/2 subband were found to be systematically about 1-3% less than for the 3/2 subband, an effect which was relatively

constant with J. The self-broadening coefficients of Ballard *et al.* were used for calculations in the current research project, so they are included in Appendix A.

In contrast to the results of Ballard *et al.*, early studies using grating spectroscopy [61, 131] measured only a few rotational lines. The first trend with J was reported in 1964 by James [61], who measured five lines in 1/2 substate of the R branch. The reported broadening coefficients were about 18% lower than the results of Ballard *et al.* The first systematic study of self-broadening in the NO fundamental band was made by in 1966 by Ables and Shaw [2], who measured more than 70 rotational lines in the 1/2 and 3/2 subbands. Broadening coefficients, which were determined using a curve of growth technique, were systematically about 17% less than those of Ballard *et al.*

The broadening studies using CO laser coincidence absorption generally report only a small number of rotational lines, with reported self-broadening values varying from about 10% below [40, 48] to as much as 50% above [21, 105] the values reported by Ballard *et al.* The most complete study using CO resonance absorption is that of Houdeau *et al.* [58], who measured 18 lines in the R branch and found both a J dependence and agreement to within 3% with the results of Ballard *et al.*

Studies with tunable lasers have been minimal. Rohrbeck *et al.* (1980) [109] measured five rotational lines and found no clear trend with J. The average value of the reported broadening coefficients, however, was in good agreement with the results of Ballard *et al.* Most recently, Kronfeldt *et al.* (1996) [65] measured the $R_{3/2}(25.5)$ line and reported $\gamma = 7.14(11) \times 10^{-5}$ cm^{-1}/torr, which appears to follow the same decreasing trend with J reported by Ballard *et al.*

The most comprehensive study of self-broadening in the Q branch of the NO fundamental was performed by Lempert *et al.* [68], using Raman spectroscopy. They determined *J*- and Ω-dependent pressure broadening coefficients, though the Λ doublets were not resolved. Except at the lowest *J* values, the *J* dependence was not observed. Broadening coefficients for the 3/2 subband coefficients were about 10% higher than the corresponding 1/2 subband coefficients. The only other study of self-broadening in the Q branch is that of Garside *et al.* [40], which used CO laser resonance absorption to measure two rotational lines. Pine *et al.* [95] measured five lines in the first overtone ($v = 0 \rightarrow 2$) using high-resolution tunable laser spectroscopy. The reported broadening coefficients compare favorably with those reported by Lempert *et al.* for the fundamental band. Since Q-branch self-broadening coefficients are required for calculations in this research study, the values from all three of these previous studies are included in Appendix A.

There is an added complication to determining pressure broadening coefficients for the lowest-*J* transitions in the NO fundamental. A three-fold hyperfine splitting of each rotational level is produced by magnetic dipole coupling between the nuclear spin and the unpaired electron [70]. For the lowest-*J* transitions ($J \le 3.5$), the hyperfine structure reveals itself as an asymmetry in the lineshapes because of the distribution of the hyperfine components [60, 94, 96, 118]. The hyperfine splitting diminishes in importance as the rotational quantum number increases because the intensities of the hyperfine components become concentrated in one of the hyperfine components of each of the two members of the Λ doublet.

This hyperfine splitting results in a poor symmetric fit to the line and broadening coefficients which are too large for the lowest-J lines. Spencer *et al.* [118] fit the $R_{1/2}(0.5)$ transition with a model which incorporated the hyperfine structure. This model fit each of the Λ components with five hyperfine components. The broadening coefficients within each group of five components of each Λ component were constrained to be equal to each other so that only two broadening coefficients were independently determined.

Pine *et al.* [95] reported Dicke narrowing in both self- and N_2-broadening in the first overtone ($v = 2 \leftarrow 0$) band of NO using a tunable dye laser. Collisional narrowing was most evident at intermediate pressures, 25-100 torr, where the Lorentzian and Doppler widths were comparable. However, broadening coefficients determined from the Voigt and Galatry profiles agreed to within the $\pm 2\%$ experimental error and no qualitative improvement in the fits was observed with the collisional narrowing model, so the Voigt profile was judged to be sufficient.

Because of the very small pressure shifts and the difficulties caused by the Λ-doublet structure, NO is not a good subject for accurate collisional shift measurements [95]. Only one research team has reported pressure-induced line shifting in the NO fundamental; Spencer *et al.* [118] reported N_2-induced shift coefficients of approximately -2×10^{-6} cm^{-1}/torr with large uncertainties and no clear trend with J. Pine *et al.* [95] measured the first overtone band and reported self- and N_2-induced shift coefficients of $-5.0(10) \times 10^{-6}$ cm^{-1}/torr for the 3/2 subband and $-4.7(10) \times 10^{-6}$ cm^{-1}/torr for the 1/2 subband. The slight increase of the shifts with J was smaller than the experimental

uncertainties. Frequency shifts for overtone transitions in diatomic molecules are often proportional to overtone number [118], so shifts for the fundamental band of NO should have about half the magnitude of those in the first overtone band.

3.2.2. Collisions with Other Gases. In addition to broadening with NO and N_2, broadening in the nitric oxide fundamental has been studied with the noble gases He [21, 66, 109, 131], Ar [36, 48, 51, 66, 96, 109], and Kr [48], as well as with H_2 [21, 66], CO [21], CO_2 [66], H_2O [112], and combustion gases [36] as collision partners. However, only collisions with argon have been studied systematically. Since the current research project is concerned only with broadening by the noble gases, only the noble gas results will be discussed in this section.

Four studies have been reported for helium broadening in the NO fundamental. Weber and Penner [131] used grating spectroscopy and assumed both Lorentzian lineshapes and J-independent broadening. The resulting broadening coefficient was 4.1×10^{-5} cm^{-1}/torr. Bonczyk [21] used the Zeeman effect to measure the broadening of four $|\Delta m| = 1$ components of the $R_{3/2}(1.5)$ line using a magnetic field to tune the NO lines into coincidence with a CO laser. The experiment did not resolve either the Λ doubling or the nuclear hyperfine structure. The resulting broadening coefficient for helium was 1.7×10^{-5} cm^{-1}/torr. Kunimori et al. [66] used resonance absorption from NO infrared emission to measure helium broadening. Measurements were made on the R(3.5) and R(10.5) lines with a monochromator with 2-cm^{-1} resolution, which resolved neither the magnetic nor the Λ substructure. Equal widths were assumed for the 1/2 and 3/2 lines. The results for the two rotational transitions were averaged to give the

broadening coefficient as 5.1×10^{-5} cm^{-1}/torr. Finally, Rohrbeck $et\ al.$ [109] used a tunable spin-flip Raman-laser spectrometer to measure four rotational lines. Their broadening coefficients were: $R_{1/2}(0.5) = 7.0(5)$, $P_{1/2}(1.5) = 5.6(5)$, $R_{1/2}(4.5) = 7.0(5)$, and $R_{3/2}(4.5) = 6.7(3)$, each value $\times 10^{-5}$ cm^{-1}/torr.

Only one study has reported krypton broadening in the NO fundamental. Hanson $et\ al.$ [48] measured the $R_{1/2}(18.5)$ line of NO using a coincidence absorption technique with a CO laser. The resulting broadening coefficient was 4.5×10^{-5} cm^{-1}/torr, with uncertainties up to 15%.

Early studies of argon broadening in the NO fundamental reported only a few lines, while more recent studies have been more systematic. Hanson $et\ al.$ [48] measured Ar broadening the $R_{1/2}(18.5)$ line using CO coincidence absorption, in the same study in which they measured Kr broadening. The resulting broadening coefficient was 4.7×10^{-5} cm^{-1}/torr, $\pm$ 15%, equal to their Kr result to within experimental uncertainty. Kunimori $et\ al.$ [66] used resonance absorption from NO infrared emission to measure the R(3.5) and R(10.5) lines broadened with Ar. The results were averaged and reported as 3.9×10^{-5} cm^{-1}/torr, 24% less than the result for He reported in the same study. Rohrbeck $et\ al.$ [109], at the same time they studied NO+He, reported broadening coefficients for four NO+Ar lines as: $R_{1/2}(0.5) = 7.3(3)$, $P_{1/2}(1.5) = 7.6(3)$, $R_{1/2}(4.5) = 6.8(3)$, and $R_{3/2}(4.5) = 7.5(2)$, each value $\times 10^{-5}$ cm^{-1}/torr. There were no apparent trends with J, Ω, or collision partner.

The first systematic study of argon broadening in the NO fundamental was made by Henry $et\ al.$ [51], who used grating spectroscopy to measure 14 lines in the R branch.

Their study reports the first evidence of J-dependence in noble gas broadening and the first indication anywhere for differential broadening between the magnetic substates.

Falcone et al. [36] used a tunable diode laser to measure a few lines in the P and R branches of NO+Ar. In the fits to the data, they assumed both the line strength and width were equal in each Λ doublet measured. The separation of the Λ components was held fixed for each line, using calculated values from Amiot et al. [4]. The broadening coefficients showed a decreasing trend with J, but the results displayed wide variations and there was no evidence of differential broadening between the magnetic substates.

The most comprehensive study of Ar broadening in nitric oxide was made by Pine [96], who studied the first overtone band ($v = 2\leftarrow0$) using photoacoustic spectroscopy with a tunable laser. The specific aim of the study was to measure differential broadening between the Λ doublet components in the 1/2 state. The broadening coefficients for the f symmetry components were found to be larger than for the e symmetry components by up to 6% for $J = 16.5$. This differential vanished at low J and increased with increasing J. In both the P and R branches, the stronger component, due to the lesser broadening, was the e-e vibronic symmetry transition, while the f-f transition was weaker. The observed line shapes also exhibited some Dicke narrowing. The Voigt profile was found to be a poor fit, with large systematic residuals. A better fit was obtained using a profile incorporating Dicke narrowing.

3.2.3. Line Coupling. Three research teams have reported experimental evidence of line coupling in the NO fundamental. Abels and DeBall [1] used a grating spectrometer with 0.1 cm^{-1} resolution and gas pressures up to 2 atm to measure transmittance as a function of pressure for more than 30 frequencies in the troughs

between lines. They compared these measurements to calculated transmittances for a band of Lorentzian lines using line positions, strengths, and widths from the literature and found that the experimental data indicated more absorption in the troughs (super-Lorentzian behavior) than expected from the calculated results. Deviations from Lorentzian behavior ranged from 8-25%.

Hirono and Ichikawa [55] measured the several P- and R- branch lines in the N_2-broadened NO fundamental using a grating spectrometer with 2.2 cm^{-1} resolution and gas pressures less than 1 atm. Using the EGL and EPGL fitting laws with a simple sum rule, they calculated state-to-state rate coefficients W_{jk}. They then used their coupling coefficients to calculate a band correction function [26], which is a ratio of the absorption coefficient with line mixing to the Lorentz absorption coefficient without line mixing. They found sub-Lorentzian behavior in the far wing of the R branch ($J > 20$) and super-Lorentzian behavior at lower J values. The three-parameter EPGL was found to fit better than two-parameter EGL, and the N_0 degeneracy factor produced the best of the EPGL fits. However, even the EPGL-0 fitting law produced relatively poor fits to the observed broadening coefficients, which casts some doubt on the line coupling conclusions.

Lempert et al. [68] measured self-broadened Q-branch spectra of NO in the range from 150-750 torr using Raman spectroscopy with a resolution of 0.0007 cm^{-1}. From these measurements, they determined J- and Ω-dependent pressure broadening coefficients, which are included in Appendix A. Modeling their spectrum at 620 torr using a sum of Lorentzians and their experimentally-determined broadening coefficients, they saw recognizable effects of line coupling: a slight super-Lorentzian behavior in the troughs between lines and a noticeable sub-Lorentzian drop-off at the bandhead.

75

To improve the model of the self-broadened Q branch they used the EPGL-0 fitting law. In addition to the pure J-changing collisions modeled by the EPGL-0 law, they proposed two additional fitting laws to account for pure spin-flip ($\Delta\Omega$) transitions and combined ΔJ and $\Delta\Omega$ transitions. These additional fitting laws are

$$k_{J'-1 \leftarrow J}^{1/2 \leftarrow 3/2} = k_0 \tag{59}$$

for pure spin-flip transitions, and

$$k_{J' \leftarrow J}^{1/2 \leftarrow 3/2} = S k_{J'+1 \leftarrow J}^{3/2 \leftarrow 3/2} \tag{60}$$

for combined J- and Ω-changing collisions. The EPGL-0 law was applied to the 1/2 and 3/2 substates separately, allowing the scaling parameter A to vary between the substates but forcing β and γ to be the same. This scheme produced six fitting parameters: $A_{3/2}$, $x = A_{1/2}/A_{3/2}$, β, γ, k_0, and S. A large spin-flipping probability ($S = 0.7$) reproduced the observed spectrum considerably better than a small one. The authors mentioned that RT rates are expected to be larger for transitions with $\Delta J =$ even with $\Delta J =$ odd, but did not indicate how this was handled in the modeling procedure.

The resulting relaxation matrix qualitatively reproduced the state-to-state data of Sudbo and Loy [124] and modeled the observed collisionally-narrowed Q-branch spectrum quite well, in contrast to the poor fits of Hirono and Ichikawa obtained by

considering *J*-changing collisions alone. This indicates that spin-changing collisions are a relatively important mechanism in nitric oxide.

Pine *et al.* [95] applied the fitting procedure of Lempert *et al.* to P- and R- branch self- and N_2-broadened data. They obtained good fits to the broadening data and also found spin-flipping transitions to be a significant mechanism. They used the spin-flipping transitions to explain the differential broadening between the 1/2 and 3/2 substates.

IV. Experiment

4.1. Fourier Transform Spectroscopy

All absorption spectra in this research project were acquired using a BOMEM DA8.002 Fourier Transform Spectrometer (FTS) with a maximum resolution of 0.004 cm^{-1}. The DA8 is a Michelson-type interferometer, in which the incoming light source is divided by a beamsplitter into two paths, one fixed and one variable. Light reflects from a mirror at the end of each path, is recombined at the beamsplitter, and then passes through a gas absorption cell on its way to a detector. The mirror in the variable path moves, varying the optical path difference (OPD) from zero to some maximum. Since the light travels down and back through each path, the maximum OPD is twice the distance traveled by the mirror. The resolution of the spectrometer, using the Rayleigh criterion in which the maximum of one peak occurs at the first zero of a second peak, is determined by the maximum OPD between the two paths in the interferometer. For an unapodized interferogram, the resolution (in wavenumbers, cm^{-1}) is

$$R = \frac{1}{L} \tag{61}$$

where L is the maximum OPD, in centimeters [10]. The Fourier transform spectrometer uses a broadband light source to illuminate the sample. Spectral information is determined from the interferogram, or interference pattern, which is formed by

recombination of the light from the two paths of the interferometer. The interferogram is converted to a spectrum through a mathematical Fourier transform [10].

There are three significant effects of the FTS instrument on the recorded spectral lineshapes: finite resolution, aperture effect, and asymmetry. In the standard definition of the Fourier transform, the interferogram is integrated from zero to infinity to produce the spectrum. The spectrometer, however, only records spectra from zero to the maximum OPD, so the Fourier transform must be performed over these more limited bounds. This is equivalent to the multiplication of an infinite interferogram with a rectangle function of unit height and length L. The result of this convolution in frequency space is a sinc function with a HWHM given by $1.2067/L$ [10, 88]. This sinc function is the instrument lineshape (ILS) for an unapodized interferogram with finite resolution. Apodization literally means, "having no feet." The sinc function has large sidelobes, or secondary maxima, which may be reduced by multiplying the interferogram with a function other than a rectangle, such as a triangle [10, 88]. These apodization functions reduce the sidelobes, but they also increase the width of the central maximum, effectively degrading the resolution. Since the shape of the recorded spectral lines is of primary importance in this research project, all interferograms were unapodized to minimize the effect of the instrument lineshape.

A second effect of the instrument on the recorded spectrum is the so-called "aperture effect." This is a degradation of the resolution caused by the imperfect collimation of the incoming light through an aperture of finite diameter, which allows off-axis rays with path lengths different from the on-axis path. The spectrum of a monochromatic source through an aperture of finite diameter is given by [10, 120]:

79

$$B_{exp}(\sigma) = \frac{1}{2} \int_{-\infty}^{\infty} \text{sinc}\left(\frac{\Omega \sigma_0 \delta}{2}\right) \exp\left[i2\pi\sigma_0\delta\left(1 - \frac{\Omega}{4\pi}\right)\right] \exp(-i2\pi\sigma\delta)d\delta \qquad (62)$$

where Ω is the solid angle due to the finite source and σ_0 is the frequency of the source. The resulting spectrum is a rectangle that starts at σ_0 and extends toward lower wavenumbers. The halfwidth of this aperture effect rectangle is [10]

$$\delta\sigma_{HW} = \frac{\sigma_0\Omega}{4\pi} \qquad (63)$$

The solid angle can be expressed as [10]

$$\Omega = \frac{\pi h^2}{4F^2} \qquad (64)$$

where h is the diameter of the circular aperture and F is the focal length of the collimating mirror in the spectrometer. Combining these last two equations, the half-width of the aperture effect rectangle, or "aperture effect" is

$$\delta\sigma_{HW} = \frac{\sigma_0 h^2}{16F^2} \qquad (65)$$

80

A third instrument effect, which can perturb the spectrum, is asymmetry due to phase error. An asymmetric interferogram results when there is an error in the zero path difference (ZPD) location [88]. The Bomem FTS takes a low-resolution two-sided scan called a phase file before each data run to try to locate, by symmetry, the ZPD and minimize this phase error. However, this location is not always perfect. The FTS samples discrete points in the interferogram a distance β apart. The center of the interferogram may be improperly located because the sampled point of maximum intensity may not be exactly at the ZPD. This displacement causes an asymmetric distortion in the resulting spectral line. For a Lorentzian line of the form [10]

$$L(\sigma) = \frac{A\,\Delta v}{(\sigma - \sigma_0)^2 + \Delta v^2} \tag{66}$$

the asymmetric distortion produced by phase error is [10]

$$B_c(\sigma) = L(\sigma)\exp(2\pi\beta\Delta v)\left[\cos(2\pi\sigma_0\beta) + \left(\frac{\sigma_0 - \sigma}{\Delta v}\right)\sin(2\pi\sigma_0\beta)\right] \tag{67}$$

The deviation from ZPD falls in the range $\beta\sigma_0 \leq 1/4$. A value of $\beta = 0$ corresponds to a symmetric Lorentzian line. A Lorentzian line with and without phase error is shown in Figure 8. As the figure shows, the phase error produces a peak in the spectrum which is not only asymmetric, but which is also shifted in frequency.
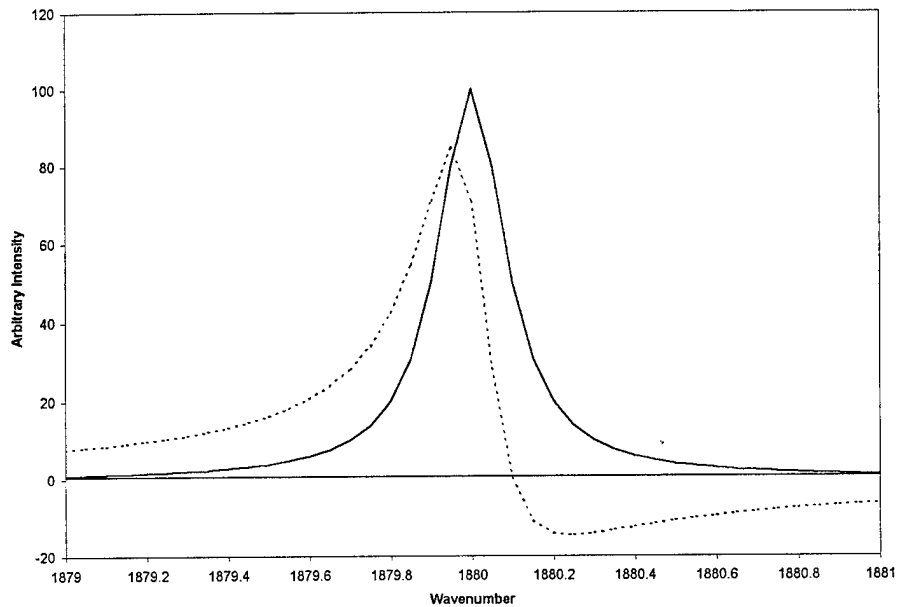
Figure 8. Asymmetric Distortion Due to Phase Error. Solid line is symmetric
Lorentzian, dashed line is asymmetry with $\beta\sigma_0 = 1/8$.

Further, since the asymmetry is a function of Lorentzian HWHM, the phase error

produces a distortion that depends on pressure – high-pressure (wider) lines are more

shifted than low-pressure (narrower) lines. This is shown in Figure 9.

The actual spectral line produced by FTS is a convolution of the actual physical

shape of the line (Voigt) with these three instrument effects. To precisely determine

lineshapes, either these instrument effects must be accurately modeled or the instrument

effects must be much less significant than the physical lineshape, making their

contributions negligible.

The next sections describe the experimental data acquisition and determination of

both qualitative and quantitative effects of collisions on the rotational lines in the oxygen

A band and nitric oxide fundamental band. Section 4.2 discusses the oxygen A-band
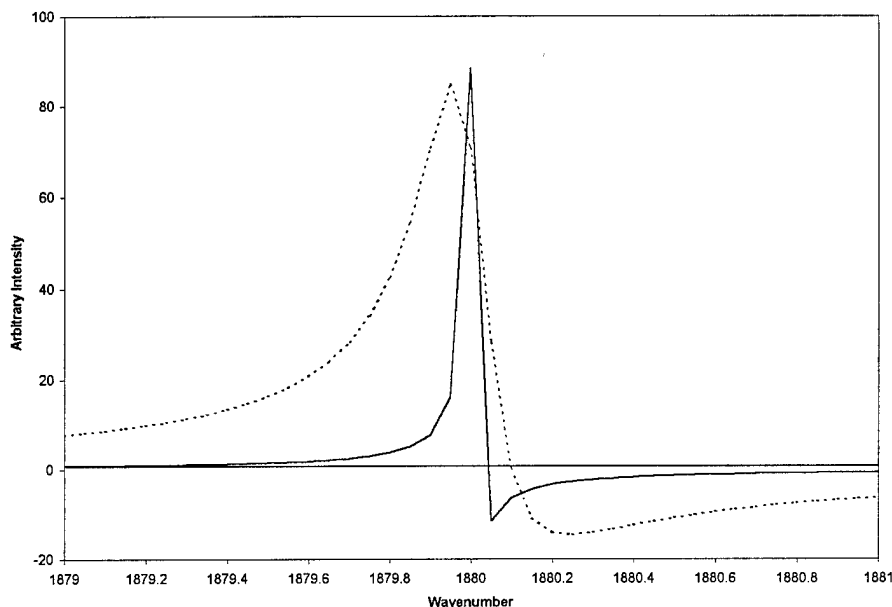
Figure 9. Asymmetric Distortion Due to Phase Error. Both lines have $\beta\sigma_0 = 1/8$. Solid line has Lorentzian HWHM = 0.008 cm^{-1}, while dashed line has Lorentzian HWHM = 0.1 cm^{-1}.

experiment, while Section 4.3 describes the experiment on the nitric oxide fundamental band. Oxygen results include line broadening coefficients for O_2 with He, Ne, Ar, Kr, Xe, O_2, N_2, CO, CO_2 and SF_6, as well as pressure-induced line shifting coefficients for O_2 with Xe. The nitric oxide results include line broadening coefficients in the P and R branches for NO with the five noble gases. The Q branch was also examined for NO with argon. These Q-branch results include quantitative broadening coefficients and qualitative indication of line coupling at high pressure.

4.2. The Oxygen A Band

4.2.1. Experimental Conditions. All absorption spectra for the oxygen A band were acquired using the Bomem components in Table 1.

Table 1. Bomem Components for Spectroscopy in the Oxygen A Band

Component	Type	Spectral Range, cm^{-1}
Light source:	Quartz lamp	2000-25000
Beamsplitter:	Quartz visible, IMB2100L	4000-25000
Detector:	Silicon avalanche, IPH5700L	9000-20000

These components restricted the spectral range to 9000-20000 cm^{-1}. To further restrict the range, a 1-inch diameter band-pass filter was placed just after the light source. The filter was an Oriel #57290, with a center frequency of 13046 cm^{-1} and a FWHM of 170 cm^{-1} ($\lambda = 766.5$ nm, $\Delta\lambda = 10$ nm). Along with the band-pass filter, limits on the acquisition bandwidth were set in the Bomem control software. The lower and upper limits set in this manner were $S_N = 12950$ cm^{-1} and $S_X = 13200$ cm^{-1}, for a bandwidth of 250 cm^{-1}. Setting a restrictive bandwidth in the software rejects components in the interferogram with frequencies above and below the cutoffs, improving signal-to-noise. The absorption spectrum of the oxygen A band, superimposed on the band-pass filter response curve and limited by the bandwidth set in the acquisition software, is shown in Figure 10.

The filter adequately captures the P branch, which starts at 13122 cm^{-1} and proceeds to lower wavenumbers. However, the R branch is located almost entirely below the half-maximum of the filter response curve. The signal-to-noise ratio (S/N) decreases as the spectral lines become further from the maximum intensity of the filter, so the S/N will be worse in the R branch than in the P branch.
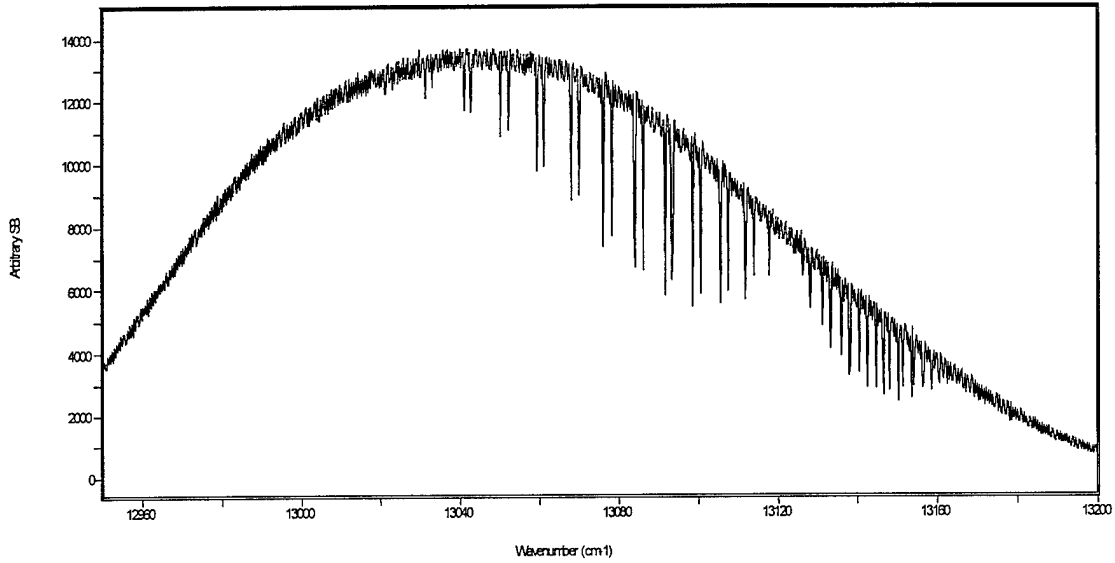
Figure 10. Oxygen A Band Spectrum Superimposed on Band-Pass
Filter Response Curve

After the band-pass filter, the incoming light passes through an aperture, which

restricts the cone of rays incident on the collimating mirror. The divergence of the

collimated beam is related to the precision of the OPD obtained, which places a limit on

maximum OPD, and thus on the attainable spectral resolution. The aperture diameter is

related to the resolution R by [88]:

$$D_{aperture} = 2f\sqrt{\frac{R}{S_X}} \qquad (68)$$

where S_X is the maximum recorded frequency and $f = 12.75$ inches is the focal length of

the input collimating mirror. The minimum aperture diameter is 0.5 mm, which would

allow a maximum resolution of 0.008 cm^{-1} for $S_X = 13200$ cm^{-1}. The next smallest

aperture diameter is 1.0 mm, which drops the resolution to 0.032 cm^{-1} for the same S_X.

Because the absorption coefficient of the oxygen A band is very small, a long

path is required for appreciable absorption. The long path was achieved by using a

White-type multipass cell with 10-meter path length (Bomem IPG9800L). Light enters

the cell and is reflected from mirrors at either end of the cell, traversing the cell 40 times

before exiting and proceeding to the detector. Unfortunately, the multiple reflections

from the mirrors introduced both losses of signal intensity and aberrations in the beam.

The resulting S/N at the detector was unacceptable with a 0.5-mm aperture but was

satisfactory with a 1.0-mm aperture. Thus, a 1.0-mm aperture, with a resulting resolution

of 0.032 cm^{-1}, was used for the majority of the oxygen A band measurements. A small

number of scans at 0.020 and 0.010 cm^{-1} were performed to look for evidence of Dicke

narrowing, but these scans were not used in the determination of the line broadening

coefficients.

Spectra were recorded at several pressures for each broadening gas. For each

spectrum, several scans were co-added, or averaged, to improve S/N, under the

assumption that random noise will tend to average out. A scan is a single translation of

the moving mirror from zero path difference (ZPD) to the maximum OPD. The response

time of the silicon avalanche detector requires the mirror to move at 0.15 cm/s, so each

scan at 0.032 cm^{-1} takes about 2.4 minutes. S/N improvement goes as the square root of

the number of co-adds, so improving S/N by increasing the number of scans can proceed

only so far before the time cost becomes prohibitive. Reasonable S/N ratios, greater than

10 near J_{max} and decreasing to 2-3 at low and high J, were achieved for runs of 100 scans, which took about 4 hours of acquisition time.

The strength of each line in the absorption spectrum increases linearly with oxygen pressure. Thus, in the case of self-broadening, S/N improves with increasing oxygen pressure. However, in foreign-gas broadening studies, the oxygen pressure was generally held constant as the bath gas pressure was increased. In this case the line has the same strength but is broadened with increasing pressure, decreasing the peak intensity of the line and reducing the S/N ratio. For this reason, spectra at high foreign gas pressures were often recorded with 400 scans to approximately double the S/N ratio. These 400-scan runs took about 16 hours to acquire, which is approaching the practical upper limit of acquisition time.

An additional reason to improve the S/N ratios for the highest-pressure spectra has to do with the procedure for determining broadening coefficients. The Lorentzian HWHM component of the spectral line should be linear in pressure and should be zero at zero pressure. (The latter is achieved in foreign-broadened spectra by subtracting the contribution to the width due to self-broadening.) The broadening coefficient can be determined from the slope of a plot of Lorentzian HWHM vs. bath gas pressure. Since we expect zero broadening at zero pressure, the y-intercept can be constrained to zero. This causes the data at the highest pressures to have the largest effect on the determination of the slope of the line. For this reason, high-precision data is especially important in the highest-pressure scans. The gas pressures and numbers of scans for each broadening gas are listed in Appendix B. All gas pressures were measured on MKS Baratron temperature-stabilized manometers.

87

4.2.2. Analysis. After acquiring the absorption spectra, the first step in analyzing the data was the removal of the band-pass filter response curve. To do this, spectra of the filter response curve were recorded with the gas cell evacuated. These background spectra were then ratioed against the sample spectra using Beer's law:

$$\frac{I(x)}{I_0} = \exp\left(-\frac{P\sigma x}{kT}\right)$$
(69)

where P is pressure, σ is the absorption cross section, x is the path length in the absorber, k is Boltzmann's constant, and T is temperature. I_0 and $I(x)$ are background and sample intensities at each frequency. The y-axis of the calculated absorbance spectrum is $-\ln(I(x)/I_0)$, which is equal to minus the argument of the exponential in Beer's law. A typical absorbance spectrum is shown in Figure 11. The increase in baseline noise at high wavenumbers is a result of the decreasing intensity of the filter response curve, which is centered at 13046 cm^{-1}.

The next step is to analyze, individually, each rotational line that has a reasonable S/N ratio. For each oxygen spectrum 42 lines were analyzed, 21 in each branch. This was performed using the Peak Fit software package by Jandel, which uses the Levenburg-Marquardt nonlinear least squares fitting algorithm [12]. Each peak was fit using a Voigt function of the form [89]:
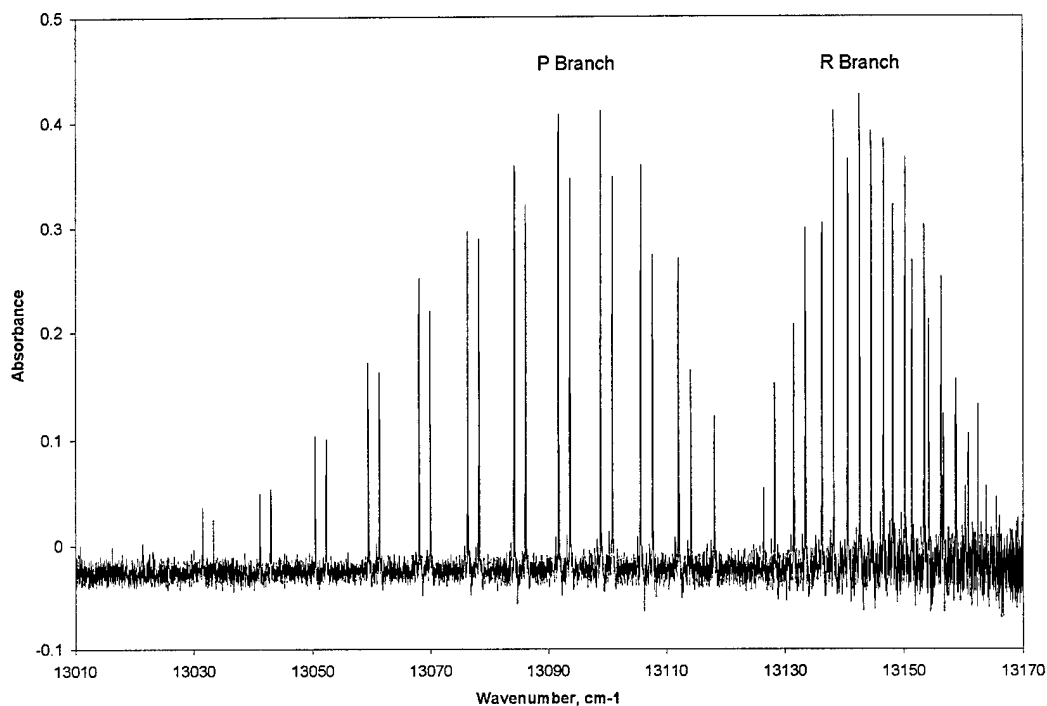
Figure 11. Typical Absorbance Spectrum of the Oxygen A Band
(300 torr O_2, 100 scans at 0.032 cm^{-1} resolution)

$$y = \frac{a_0}{a_2\sqrt{2\pi}} \int_{-\infty}^{\infty} \frac{\exp(-t^2)dt}{\dfrac{a_3^2}{2a_2^2} + \left(\dfrac{x - a_1}{a_2\sqrt{2}} - t\right)^2} \qquad (70)$$

where a_0 is the area parameter, a_1 is the line center position, a_2 is the Gaussian standard

deviation, a_3 is the Lorentzian HWHM, and x is the frequency variable. The actual area

under the Voigt profile, found by convolving the normalized Gaussian and Lorentzian

lineshapes [62] and comparing them to the Peak Fit equation, is

89

$$area = \frac{a_0 a_2 \pi \sqrt{2}}{a_3} \tag{71}$$

which is a function of the Gaussian and Lorentzian width components as well as the area parameter. The Gaussian standard deviation is related to the Gaussian HWHM by [12, 49]

$$\Delta v_D^{HWHM} = a_2 \sqrt{2\ln 2} \tag{72}$$

In addition to the four variables in the Voigt equation, Peak Fit includes two additional variables for the slope and intercept of a linear baseline. Thus a Voigt fit to a single peak, with no constraints, has six free parameters.

Large uncertainties were produced in the Gaussian and Lorentzian width parameters when both were allowed to vary while fitting the rotational lines. The fits were greatly improved by constraining the Gaussian width to be equal to the computed Doppler width of the oxygen A band transition at room temperature, which is $\Delta v_D = 0.014$ cm^{-1}. For each peak, the residuals were examined for deviations characteristic of Dicke narrowing. These deviations, however, were never observed, so the Voigt lineshape was used throughout the analysis of the oxygen A band. A typical Voigt fit to a single rotational line in oxygen, together with the residuals, is shown in Figure 12.

Because of the low S/N ratio and the closely spaced rotational lines near the bandhead, a slightly different analysis method was used for the four lines $J'' = 18-21$ in
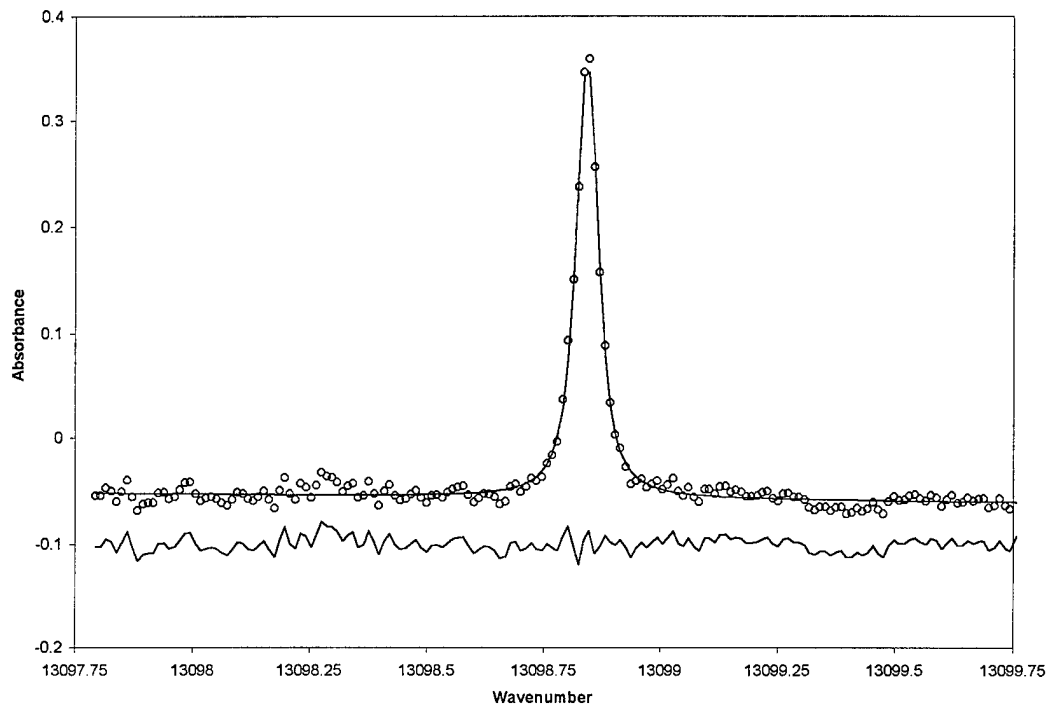
Figure 12. Voigt Fit to a Rotational Line in the Oxygen A Band. This is the ^{P}P(7) line of a self-broadened spectrum at 300 torr. The residuals (lower trace) have been offset by −0.1.

the R branch. The pair of lines $J'' = 18$ and 19 are significantly overlapped at all pressures, while the pair of lines $J'' = 20$ and 21 are very closely spaced and of very low S/N. These two pairs of lines were analyzed forcing the $J'' = 18$ and 19 widths to be equal and the $J'' = 20$ and 21 widths to be equal. This removed one parameter from the fit and consequently reduced the uncertainties on the width values. The constraint of equal widths is not absolutely correct, but is a justifiable approximation since any differences in width should be well within the experimental uncertainties.

91

After determining the Lorentzian HWHM of each peak, the broadening coefficients were found by plotting the Lorentzian HWHM vs. bath gas pressure for each of the 42 peaks. The slope of a linear least-squares fit to this data is the broadening coefficient in units of cm^{-1}/torr. Data for several peaks were fit using a linear fit of the form $y = a + bx$. However, it was found that the y-intercept, expressed by the fit parameter a, averaged to zero over fits to several peaks. Since no systematic effects were found in the y-intercept value, a zero-intercept line of the form $y = bx$ was used for all fits. This is more appealing on physical grounds since zero pressure broadening is expected at zero pressure, and also produces much better error statistics by reducing linear fit from two variables to one variable. Each Lorentzian HWHM data point was weighted by its measurement error, using the standard convention: weight = 1/error^2. A typical width vs. pressure fit to a self-broadened oxygen A-band peak is shown in Figure 13.

Bhattacharyya *et al.* [14] observed a decrease in peak width vs. pressure from 30-100 torr for self-broadening in the oxygen A band, which they interpreted as evidence of Dicke narrowing. The current research project examined several spectra in the 30-100 torr region, at resolutions of 0.032 and 0.020 cm^{-1} but found no deviations from linear pressure broadening. This is shown in Figure 13. Since neither the decrease in width from 30-100 torr or the deviations in the peak residuals characteristic of Dicke narrowing were observed, one must conclude that there is no evidence of Dicke narrowing in the oxygen A-band spectra of the current study.
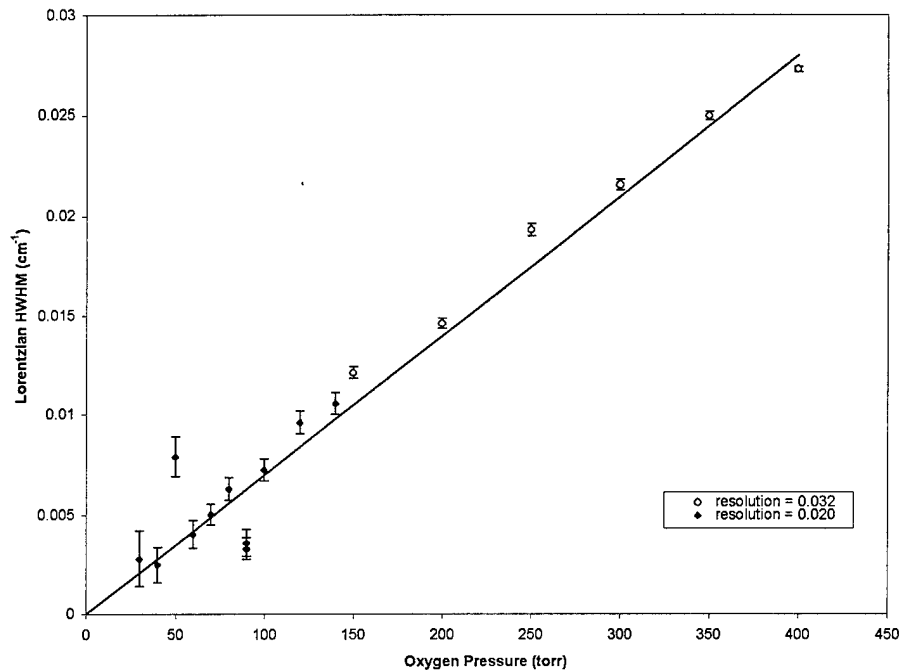
Figure 13. Linear Least Squares Fit to Lorentzian HWHM as a Function of Pressure. The slope of this plot is the broadening coefficient for this transition. This data is for the self-broadened $^PQ(9)$ transition of the oxygen A band.

Broadening coefficients for foreign-gas broadening in the oxygen A band were determined in a similar manner. In order to perform a zero-intercept fit for the foreign-gas-broadened spectra, the contribution due to self-broadening had to be removed. This was done using the self-broadening coefficients determined in this study. A typical plot of foreign-broadened Lorentzian widths vs. pressure is shown in Figure 14.

Before concluding that the pressure-broadened linewidths from Peak Fit can indeed be used to determine the broadening coefficients, it is important to consider the possible effects of the FTS instrument on these measurements. The three effects which could perturb the measured spectral line from its theoretical Voigt shape, as discussed previously, are the instrument lineshape, aperture effect, and asymmetry caused by phase

errors. The measured peaks are actually a convolution of the Voigt lineshape with these three instrument effects. The question that must be answered is whether the instrument effects, which cannot be modeled in Peak Fit, have a significant effect on the measured Lorentzian linewidths.
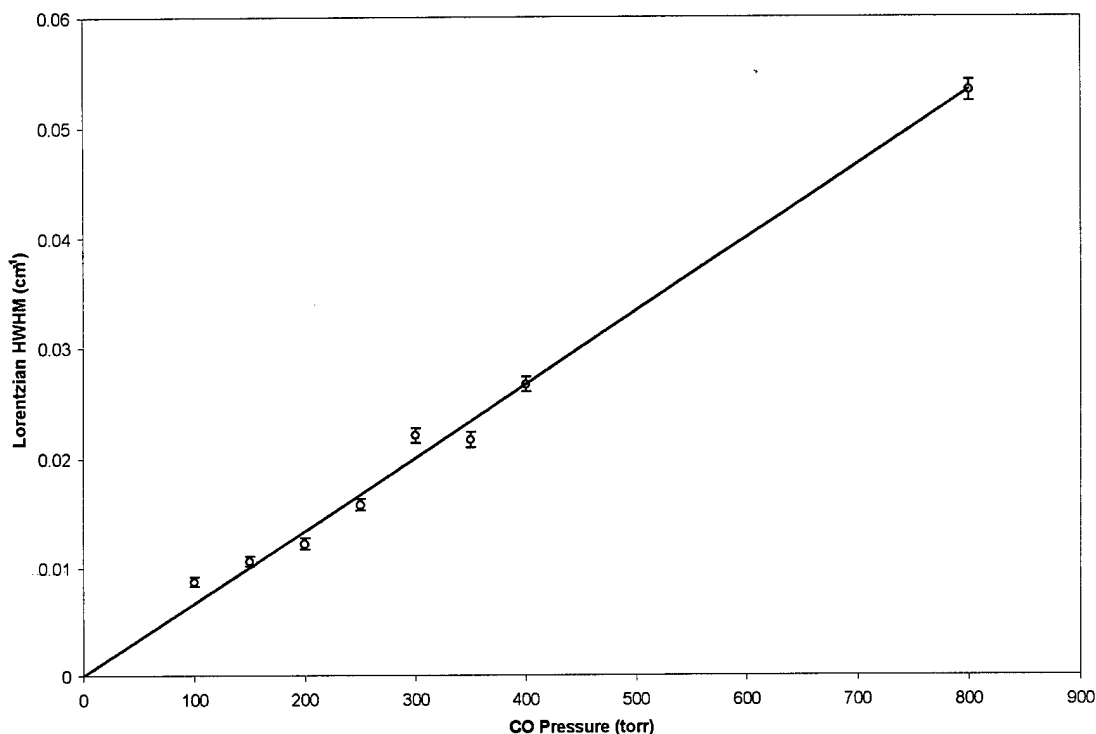
Figure 14. Linear Least Squares Fit to Lorentzian HWHM as a Function of Pressure for Oxygen Broadened with Carbon Monoxide. The slope of this plot is the broadening coefficient for this transition. This data is for the $^PQ(13)$ transition of the oxygen A band.

Since Peak Fit cannot model these instrument effects, a subset of the data was modeled using the DUDV program provided by Hawkins [50]. This program uses the DUD (Doesn't Use Derivatives) nonlinear least squares algorithm of Ralston and Jennrich [102] and is able to model a Voigt line convolved with instrument effects.

94

DUDV requires a transmittance file rather than absorbance file. The transmittance file is simply a ratio of the spectrum to a background scan: $T = I(x)/I_0$. The Doppler width is calculated and held constant in each fit, just like in the Peak Fit analysis.

DUDV can simultaneously fit up to 31 peaks. For each peak in the fit, accurate starting guesses must be provided for line strength ($\times 10^{-20}$ cm^{-1}/cm^{-2} molecule), Lorentzian HWHM at 1 atm (cm^{-1}/atm), and line position (cm^{-1}). The starting guesses for strength and width came from Ritter and Wilkerson [107], while the line center positions came from Burch and Gryvnak [27]. In addition to the three parameters for each peak, DUDV has three background parameters: a constant offset, a linear term (slope), and a quadratic term. For small spectral ranges with a good ratio between the spectrum and the background file, the constant offset term is often the only one needed. Finally, the DUDV program has three parameters to model the instrument effects: the maximum OPD (cm), which determines the width of the ILS, the aperture effect (cm), and the asymmetry due to phase error.

To quantify the instrument effects on the measured spectra, all 21 lines in the O_2-O_2 P branch were fit using DUDV and compared to the results from Peak Fit. For the oxygen A-band measurements, $\sigma_0 = 13120$ cm^{-1}, $h = 0.1$ cm, and $F = 32.385$ cm, so the aperture effect parameter is $\delta\sigma_{HW} = 0.00782$ cm^{-1}. The resolution for these measurements was 0.032 cm^{-1}, so the maximum OPD parameter is 31.25 cm. The asymmetry was found to be zero for all but the 400 torr O_2 spectrum. Asymmetry reduced the peak widths by an average of 0.85% over the best-fit symmetric peaks, which reduced the broadening coefficients by an average 1.1%. A typical DUDV fit is shown in Figure 15. The model that considers instrument effects produces broadening coefficients

95

which are an average of $3.2 \pm 3.5\%$ larger than the model which does not consider these effects. The difference is systematic but is not statistically significant, since the error in the broadening coefficients is on the order of 3% as well. Thus the Peak Fit results for oxygen self-broadening are not significantly perturbed by instrument effects.
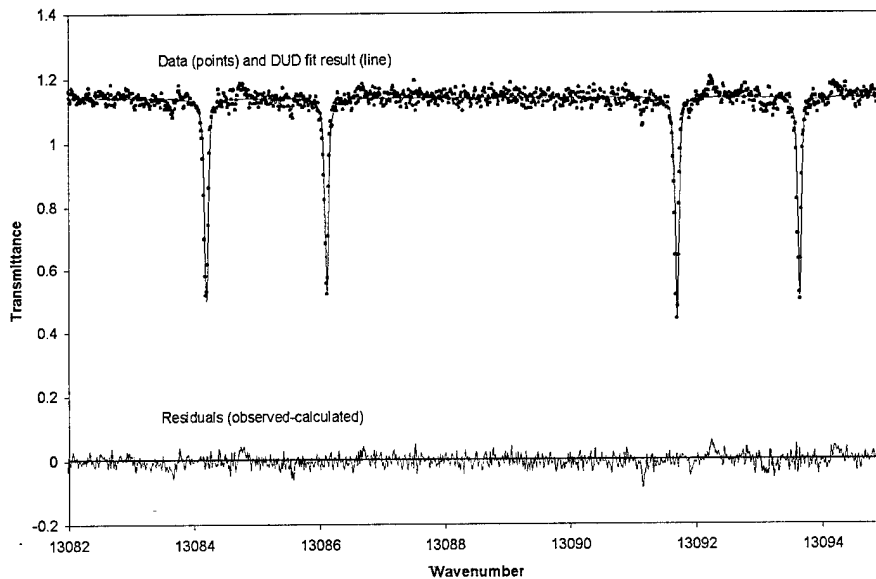
Figure 15. Oxygen Self-Broadening Modeled with DUDV, which Considers Instrument Effects. These are the $^{P}P(11)$, $^{P}Q(11)$, $^{P}P(9)$, and $^{P}P(9)$ lines of a self-broadened spectrum at 300 torr.

The fits for the J'' = 6-13 lines in the P branch of the O_2-He data were also analyzed to see if the instrument lineshape affected the foreign-broadened spectra differently from the self-broadened spectra. The asymmetry was again found to be zero for all but the 400-torr He spectrum, where a small asymmetry correction improved the fit. The best fit with asymmetric peaks reduced the widths of the peaks by an average of 10% over the best-fit symmetric peaks. The corresponding reduction in the broadening

coefficients, however, was only 1-2%. For these eight lines, there was no systematic difference between the fits with and without instrument effects. The fit which considered instrument effects varied from 1.39% higher to 5.77% lower than the fit without instrument effects, with an average difference of $-1.8 \pm 6.3\%$. This is, again, not statistically significant, so the Peak Fit results for oxygen foreign broadening are not significantly perturbed by instrument effects.

4.2.3. Results. Since the instrument effects were found to be insignificant, the Lorentzian widths determined by Peak Fit were used to determine all broadening coefficients for the oxygen A band. This study considered oxygen broadened with O_2, He, Ne, Ar, Kr, Xe, N_2, CO, CO_2, and SF_6. The self-broadening coefficients from the current study are graphed together with the results of previous researchers in Figure 16.

As shown in Figure 16, the oxygen self-broadening coefficients determined in this study fall well within the range of coefficients determined by previous researchers using other measurement techniques. Indeed, the broadening coefficients of the current study are nearly identical to those of Giver *et al.* [43], which are the broadening coefficients currently used in the HITRAN 96 atmospheric transmission database [56, 57, 110]. Since self-broadening coefficients in the oxygen A band have been previously reported, the purpose of the self-broadening study was to lend confidence to the data acquisition and analysis procedures. This is important since the results from the current study are the only measurements using FTS. The close agreement with the HITRAN broadening coefficients indicates that FTS is a useful tool for broadening coefficient measurements and that the analysis methods of this study are indeed correct. In fact, the careful

97

measurements and analysis performed in the current study have produced results of higher precision and higher confidence than any of the previous studies.
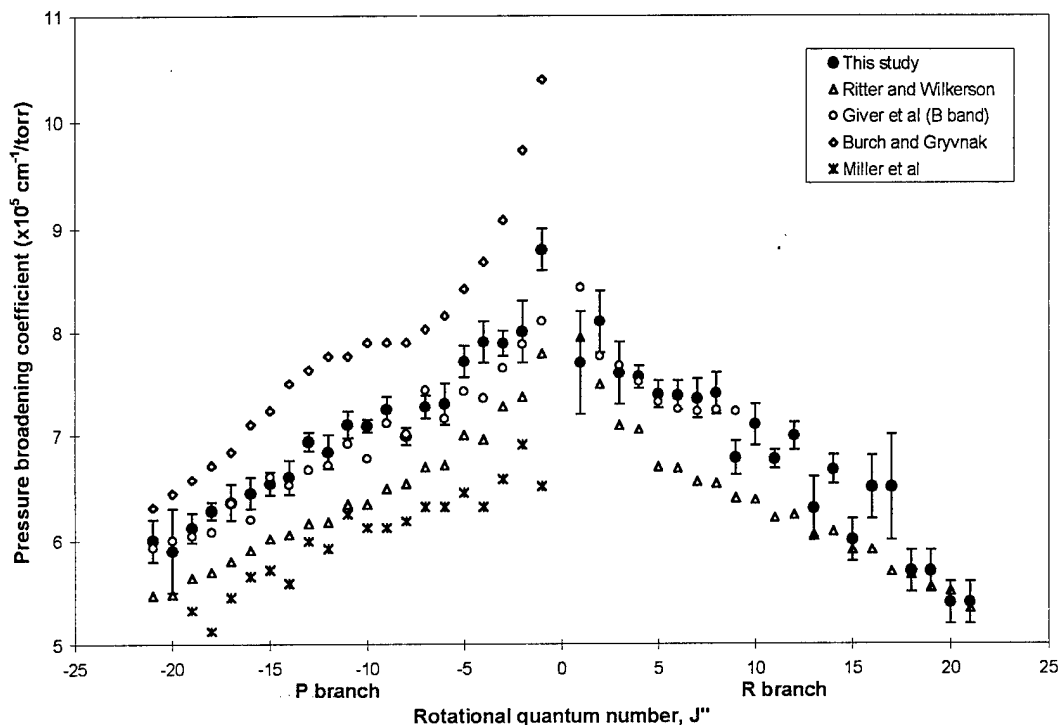
Figure 16. Oxygen Self-Broadening Coefficients vs. J'': Results of this Research and Comparison with Results of Previous Researchers. References are: Ritter and Wilkerson [107], Giver et al. [43], Burch and Gryvnak [27], Miller et al. [78].

Figures 17 through 21 show the oxygen A band broadened with the noble gases.

Riter [106] previously reported broadening coefficients for oxygen in collision with noble gas atoms. He used a tunable dye laser to measure the Lorentzian HWHM at one atmosphere of bath gas and assumed a linear trend with pressure (using a zero intercept) to determine his reported coefficients. In all cases, Ritter's reported results fall within the

error bars of the results from the current, more rigorous, study, lending credibility to Ritter's results.

Figures 22 through 25 show oxygen broadened with the molecules N_2, CO, CO_2, and SF_6. Of the five molecular broadening gases (including O_2), SF_6 causes the most broadening, while N_2 causes the least. CO_2, for the most part, appears to broaden more than CO, but the values are close and occasionally the trend is reversed. Broadening coefficients for oxygen with all ten perturbers are listed in Tables 2 and 3. The data in Tables 2 and 3 is quoted with 1-σ statistical errors, which are expressed in parentheses following each value and are to be interpreted as the uncertainty in the last significant figure.
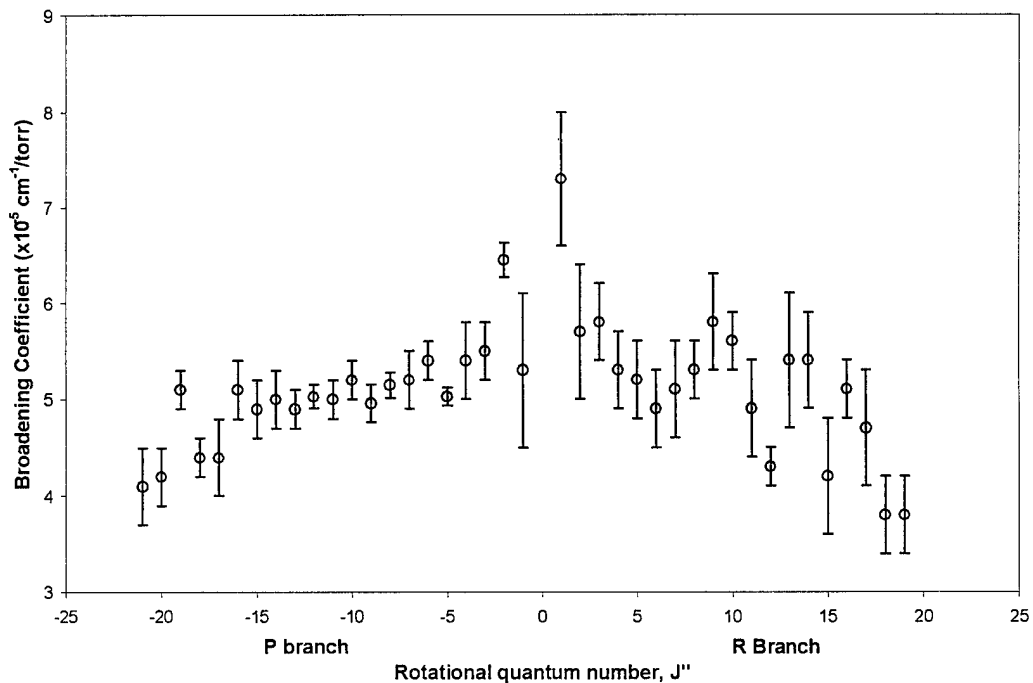
Figure 17. Broadening Coefficients for Oxygen Broadened with Helium
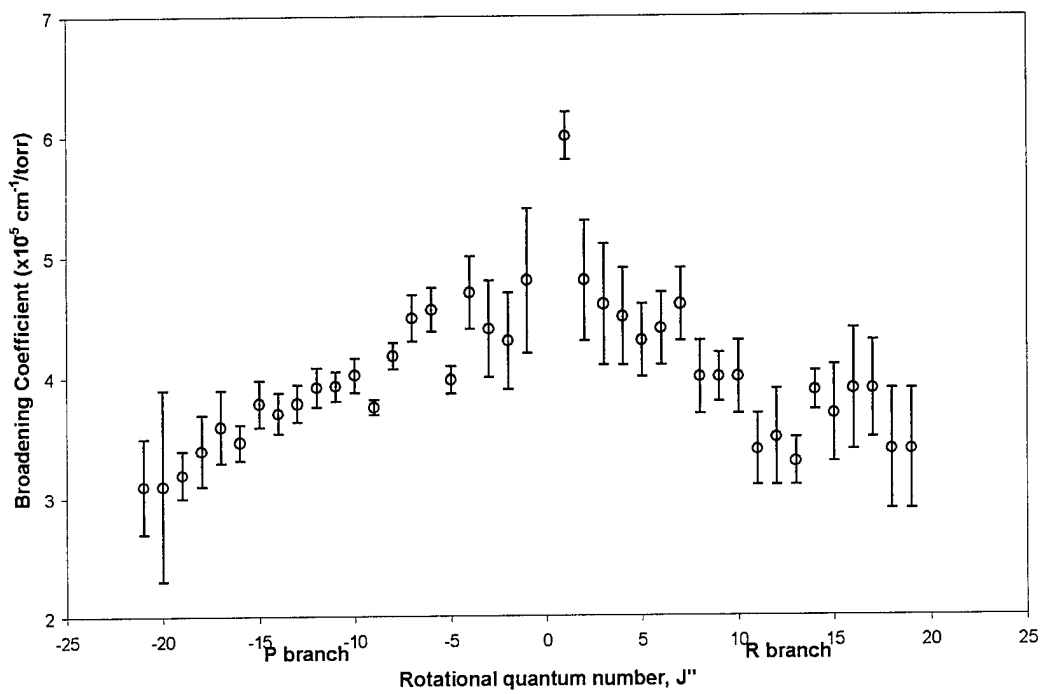
Figure 18. Broadening Coefficients for Oxygen Broadened with Neon
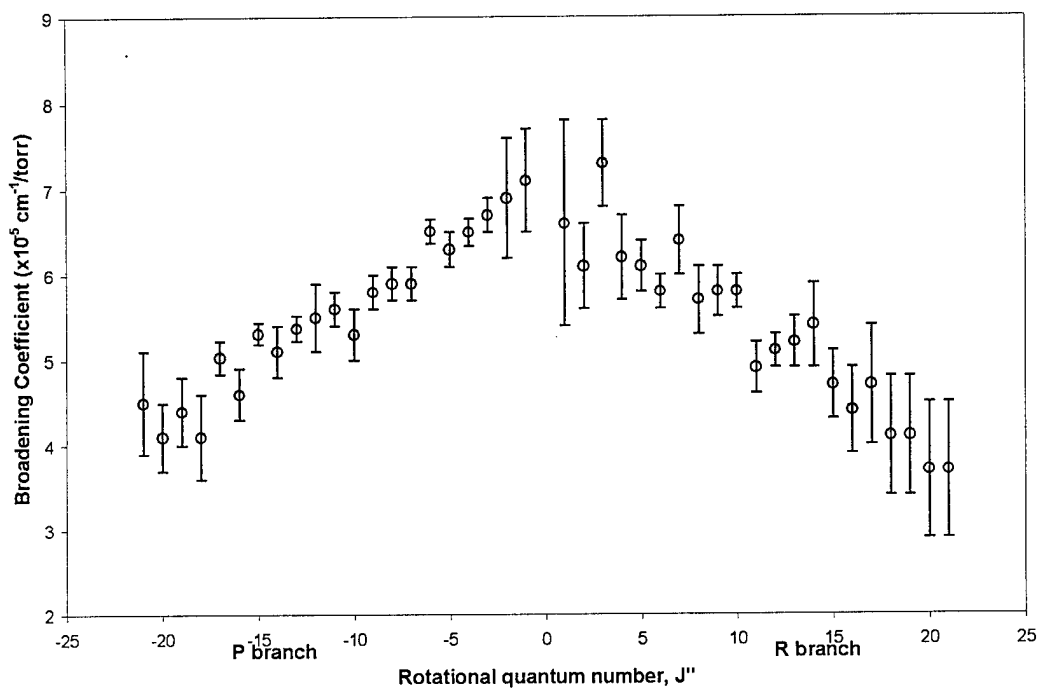
Figure 19. Broadening Coefficients for Oxygen Broadened with Argon

100
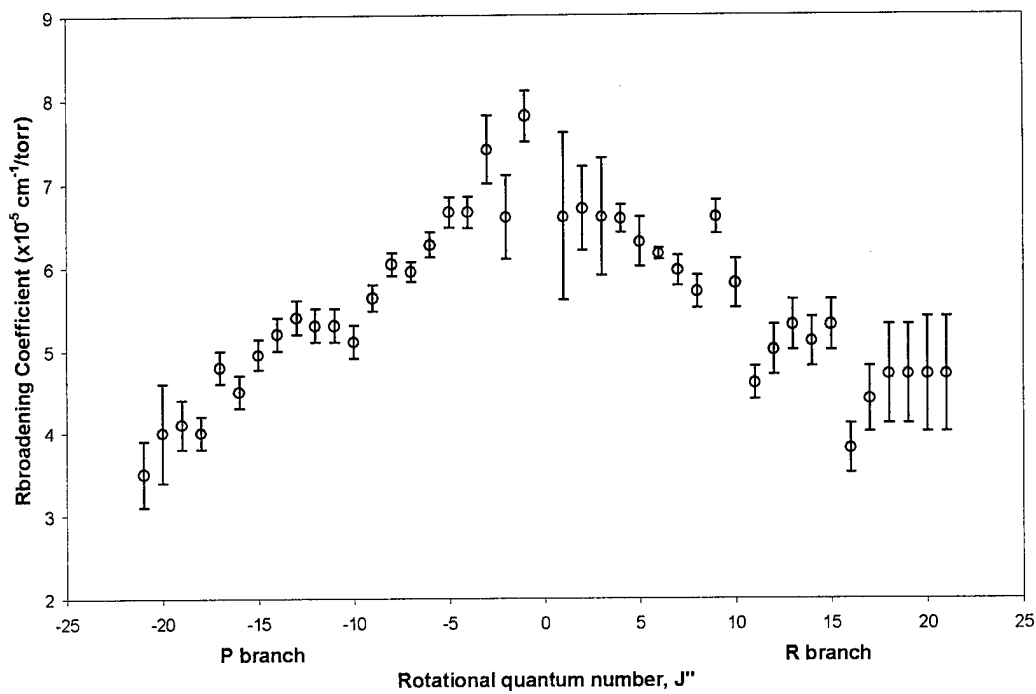
Figure 20. Broadening Coefficients for Oxygen Broadened with Krypton
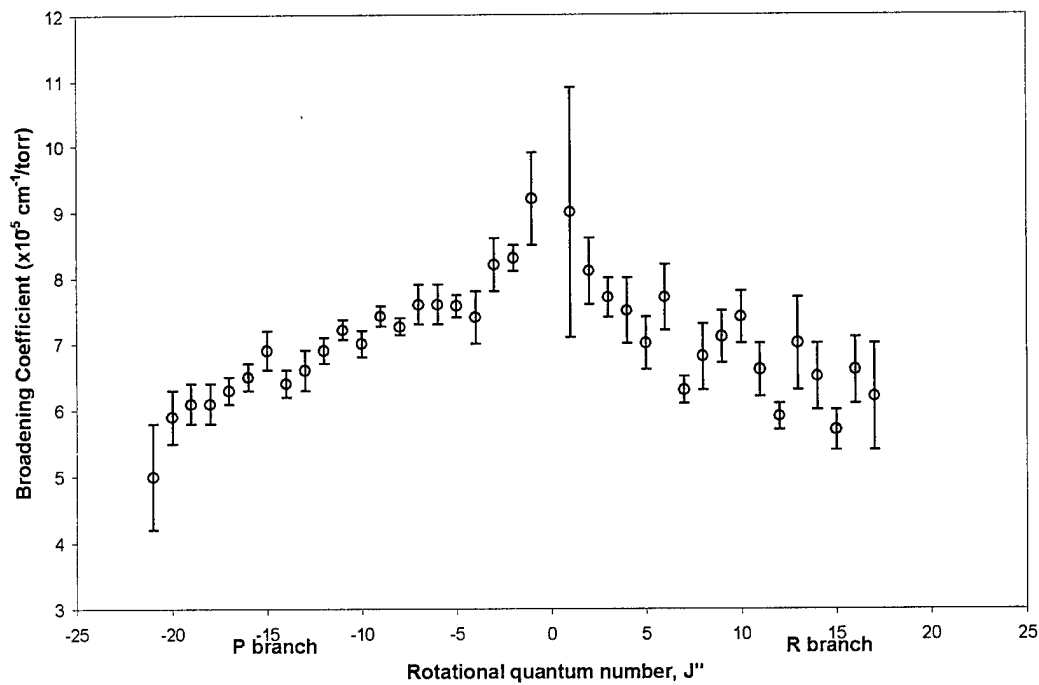
Figure 21. Broadening Coefficients for Oxygen Broadened with Xenon

101
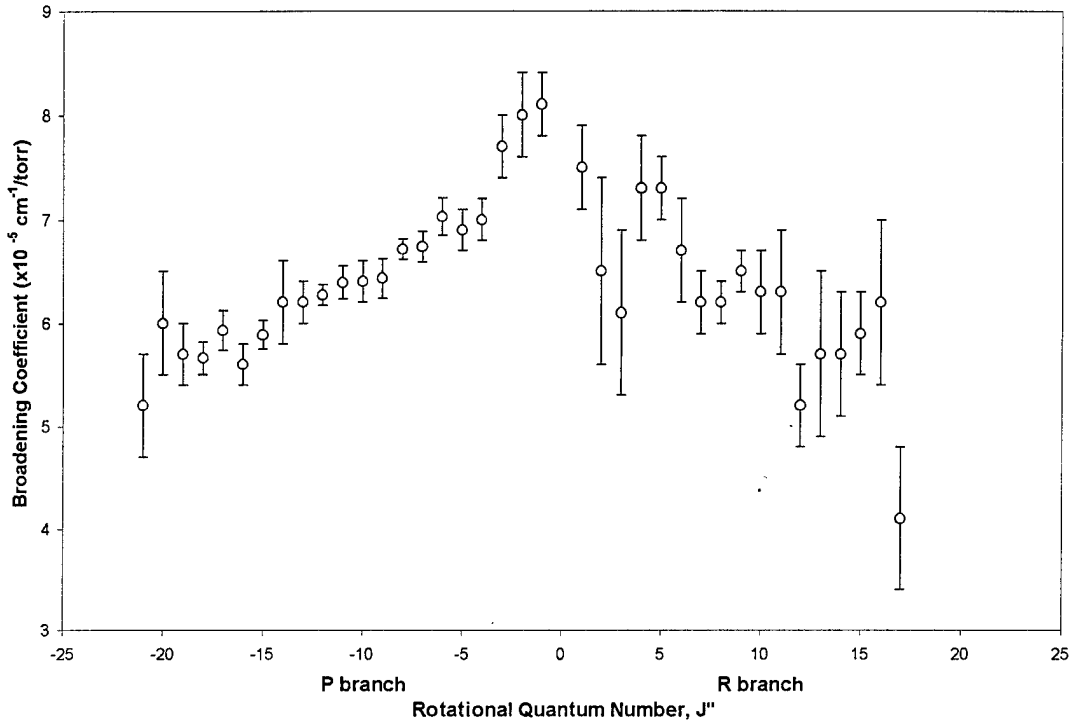
Figure 22. Broadening Coefficients for Oxygen Broadened with Nitrogen (N_2)
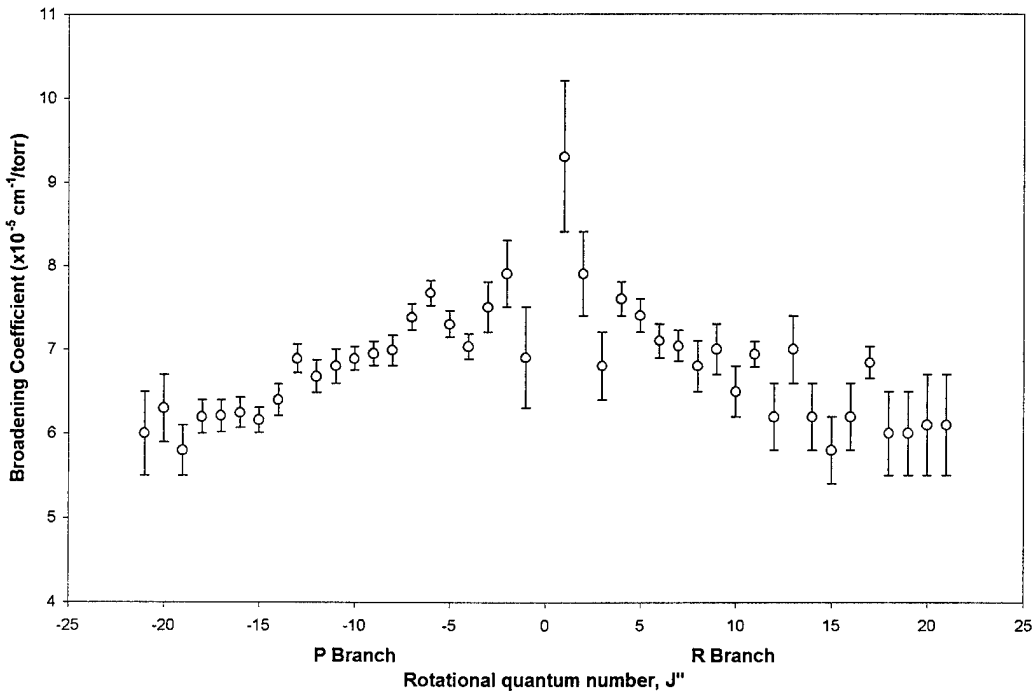
Figure 23. Broadening Coefficients for Oxygen Broadened with Carbon Monoxide (CO)
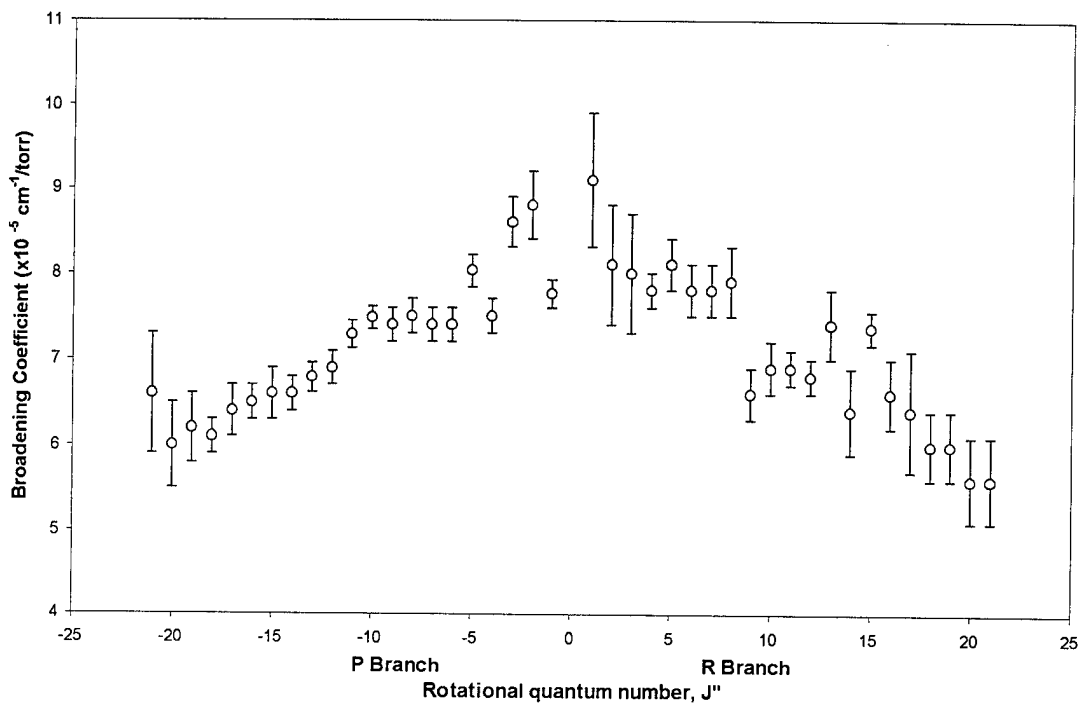
Figure 24. Broadening Coefficients for Oxygen Broadened with Carbon Dioxide (CO_2)
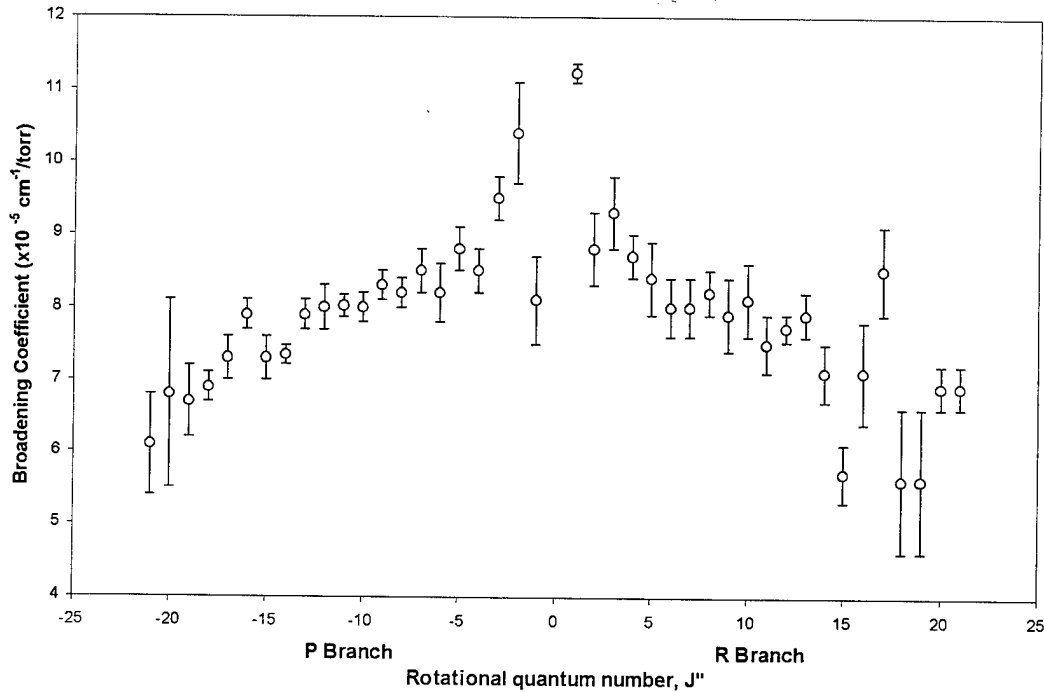
Figure 25. Broadening Coefficients for Oxygen Broadened with Sulfur Hexafluoride (SF_6)

Table 2. O_2+Noble Gas Broadening Coefficients ($\times 10^{-5}$ cm^{-1}/torr)

J''	Label	He	Ne	Ar	Kr	Xe
21	$^PP(21)$	4.1(4)	3.1(4)	4.5(6)	3.5(4)	5.0(8)
20	$^PQ(21)$	4.2(3)	3.1(8)	4.1(4)	4.0(6)	5.9(4)
19	$^PP(19)$	5.1(2)	3.2(2)	4.4(4)	4.1(3)	6.1(3)
18	$^PQ(19)$	4.4(2)	3.4(3)	4.1(5)	4.0(2)	6.1(3)
17	$^PP(17)$	4.4(4)	3.6(3)	5.03(19)	4.8(2)	6.3(2)
16	$^PQ(17)$	5.1(3)	3.50(15)	4.6(3)	4.5(2)	6.5(2)
15	$^PP(15)$	4.9(3)	3.79(19)	5.31(13)	4.95(18)	6.9(3)
14	$^PQ(15)$	5.0(3)	3.71(17)	5.1(3)	5.2(2)	6.4(2)
13	$^PP(13)$	4.9(2)	3.79(15)	5.37(15)	5.4(2)	6.6(3)
12	$^PQ(13)$	5.03(12)	3.92(16)	5.5(4)	5.3(2)	6.9(2)
11	$^PP(11)$	5.0(2)	3.93(12)	5.6(2)	5.3(2)	7.21(15)
10	$^PQ(11)$	5.2(2)	4.02(14)	5.3(3)	5.1(2)	7.0(2)
9	$^PP(9)$	4.96(19)	3.76(6)	5.8(2)	5.63(16)	7.42(15)
8	$^PQ(9)$	5.15(13)	4.18(11)	5.9(2)	6.04(14)	7.26(13)
7	$^PP(7)$	5.2(3)	4.49(19)	5.9(2)	5.95(12)	7.6(3)
6	$^PQ(7)$	5.4(2)	4.56(18)	6.51(14)	6.27(15)	7.6(3)
5	$^PP(5)$	5.03(9)	3.98(11)	6.3(2)	6.66(18)	7.57(17)
4	$^PQ(5)$	5.4(4)	4.7(3)	6.50(16)	6.66(19)	7.4(4)
3	$^PP(3)$	5.5(3)	4.4(4)	6.7(2)	7.4(4)	8.2(4)
2	$^PQ(3)$	6.45(18)	4.3(4)	6.9(7)	6.6(5)	8.3(2)
1	$^PP(1)$	5.3(8)	4.8(6)	7.1(6)	7.8(3)	9.2(7)
1	$^RR(1)$	7.3(7)	6.0(2)	6.6(12)	6.6(10)	9.0(19)
2	$^RQ(1)$	5.7(7)	4.8(5)	6.1(5)	6.7(5)	8.1(5)
3	$^RR(3)$	5.8(4)	4.6(5)	7.3(5)	6.6(7)	7.7(3)
4	$^RQ(3)$	5.3(4)	4.5(4)	6.2(5)	6.58(17)	7.5(5)
5	$^RR(5)$	5.2(4)	4.3(3)	6.1(3)	6.3(3)	7.0(4)
6	$^RQ(5)$	4.9(4)	4.4(3)	5.8(2)	6.16(7)	7.7(5)
7	$^RR(7)$	5.1(5)	4.6(3)	6.4(4)	5.96(18)	6.3(2)
8	$^RQ(7)$	5.3(3)	4.0(3)	5.7(4)	5.7(2)	6.8(5)
9	$^RR(9)$	5.8(5)	4.0(2)	5.8(3)	6.6(2)	7.1(4)
10	$^RQ(9)$	5.6(3)	4.0(3)	5.8(2)	5.8(3)	7.4(4)
11	$^RR(11)$	4.9(5)	3.4(3)	4.9(3)	4.6(2)	6.6(4)
12	$^RQ(11)$	4.3(2)	3.5(4)	5.1(2)	5.0(3)	5.9(2)
13	$^RR(13)$	5.4(7)	3.3(2)	5.2(3)	5.3(3)	7.0(7)
14	$^RQ(13)$	5.4(5)	3.89(16)	5.4(5)	5.1(3)	6.5(5)
15	$^RR(15)$	4.2(6)	3.7(4)	4.7(4)	5.3(3)	5.7(3)
16	$^RQ(15)$	5.1(3)	3.9(5)	4.4(5)	3.8(3)	6.6(5)
17	$^RR(17)$	4.7(6)	3.9(4)	4.7(7)	4.4(4)	6.2(8)
18	$^RQ(17)$	3.8(4)	3.4(5)	4.1(7)	4.7(6)	
19	$^RR(19)$	3.8(4)	3.4(5)	4.1(7)	4.7(6)	
20	$^RQ(19)$			3.7(8)	4.7(7)	
21	$^RR(21)$			3.7(8)	4.7(7)	

104

Table 3. O_2+Molecular Gas Broadening Coefficients ($\times$ 10^{-5} cm^{-1}/torr)

J''	Label	O_2	N_2	CO	CO_2	SF_6
21	$^PP(21)$	6.0(2)	5.2(5)	6.0(5)	6.6(7)	6.1(7)
20	$^PQ(21)$	5.9(4)	6.0(5)	6.3(4)	6.0(5)	6.8(13)
19	$^PP(19)$	6.12(14)	5.7(3)	5.8(3)	6.2(4)	6.7(5)
18	$^PQ(19)$	6.28(8)	5.66(16)	6.2(2)	6.1(2)	6.9(2)
17	$^PP(17)$	6.36(17)	5.93(19)	6.21(19)	6.4(3)	7.3(3)
16	$^PQ(17)$	6.45(15)	5.6(2)	6.25(18)	6.5(2)	7.9(2)
15	$^PP(15)$	6.54(11)	5.89(14)	6.16(15)	6.6(3)	7.3(3)
14	$^PQ(15)$	6.60(16)	6.2(4)	6.40(19)	6.6(2)	7.35(13)
13	$^PP(13)$	6.94(9)	6.2(2)	6.89(17)	6.79(17)	7.9(2)
12	$^PQ(13)$	6.84(16)	6.27(10)	6.68(19)	6.90(19)	8.0(3)
11	$^PP(11)$	7.10(13)	6.39(16)	6.8(2)	7.29(16)	8.02(15)
10	$^PQ(11)$	7.09(6)	6.4(2)	6.89(14)	7.48(13)	8.0(2)
9	$^PP(9)$	7.25(12)	6.43(19)	6.95(14)	7.4(2)	8.3(2)
8	$^PQ(9)$	6.99(8)	6.71(10)	6.99(18)	7.5(2)	8.2(2)
7	$^PP(7)$	7.27(11)	6.74(15)	7.38(16)	7.4(2)	8.5(3)
6	$^PQ(7)$	7.3(2)	7.03(18)	7.67(15)	7.4(2)	8.2(4)
5	$^PP(5)$	7.71(15)	6.9(2)	7.30(16)	8.03(19)	8.8(3)
4	$^PQ(5)$	7.9(2)	7.0(2)	7.03(15)	7.5(2)	8.5(3)
3	$^PP(3)$	7.89(12)	7.7(3)	7.5(3)	8.6(3)	9.5(3)
2	$^PQ(3)$	8.0(3)	8.0(4)	7.9(4)	8.8(4)	10.4(7)
1	$^PP(1)$	8.8(2)	8.1(3)	6.9(6)	7.76(16)	8.1(6)
1	$^RR(1)$	7.7(5)	7.5(4)	9.3(9)	9.1(8)	11.23(13)
2	$^RQ(1)$	8.1(3)	6.5(9)	7.9(5)	8.1(7)	8.8(5)
3	$^RR(3)$	7.6(3)	6.1(8)	6.8(4)	8.0(7)	9.3(5)
4	$^RQ(3)$	7.56(11)	7.3(5)	7.6(2)	7.8(2)	8.7(3)
5	$^RR(5)$	7.39(13)	7.3(3)	7.4(2)	8.1(3)	8.4(5)
6	$^RQ(5)$	7.38(14)	6.7(5)	7.1(2)	7.8(3)	8.0(4)
7	$^RR(7)$	7.35(19)	6.2(3)	7.04(18)	7.8(3)	8.0(4)
8	$^RQ(7)$	7.4(2)	6.2(2)	6.8(3)	7.9(4)	8.2(3)
9	$^RR(9)$	6.78(16)	6.5(2)	7.0(3)	6.6(3)	7.9(5)
10	$^RQ(9)$	7.1(2)	6.3(4)	6.5(3)	6.9(3)	8.1(5)
11	$^RR(11)$	6.77(9)	6.3(6)	6.94(15)	6.9(2)	7.5(4)
12	$^RQ(11)$	6.99(13)	5.2(4)	6.2(4)	6.8(2)	7.72(19)
13	$^RR(13)$	6.3(3)	5.7(8)	7.0(4)	7.4(4)	7.9(3)
14	$^RQ(13)$	6.67(14)	5.7(6)	6.2(4)	6.4(5)	7.1(4)
15	$^RR(15)$	6.0(2)	5.9(4)	5.8(4)	7.36(19)	5.7(4)
16	$^RQ(15)$	6.5(3)	6.2(8)	6.2(4)	6.6(4)	7.1(7)
17	$^RR(17)$	6.5(5)	4.1(7)	6.84(19)	6.4(7)	8.5(6)
18	$^RQ(17)$	5.7(2)		6.0(5)	6.0(4)	5.6(10)
19	$^RR(19)$	5.7(2)		6.0(5)	6.0(4)	5.6(10)
20	$^RQ(19)$	5.4(2)		6.1(6)	5.6(5)	6.9(3)
21	$^RR(21)$	5.4(2)		6.1(6)	5.6(5)	6.9(3)

105

The broadening coefficients reported in Tables 2 and 3 are given with $1-\sigma$ statistical errors, as estimated by the least-squares fit, on the order of 3% near the center of each branch and increasing to about 10% for the less-intense lines at high and low J''. Possible sources of systematic error, such as instrument lineshape effects and filter transmission effects have been carefully taken into account, so the quoted statistical errors should be the true measure of uncertainty in these results.

While no previous researcher has reported a full set of broadening coefficients for O_2+N_2, several researchers have measured a few lines of oxygen broadened with either N_2 or air and have indicated the effectiveness of N_2 broadening relative to self-broadening. Using the data from Table 3, the current study has found that N_2 is on average $9.6 \pm 6.0\%$ less effective than self-broadening. The results of previous researchers are in Table 4.

Table 4. Effectiveness of O_2-N_2 Broadening Relative to O_2 Self-Broadening as Reported by Other Researchers

O_2-N_2 broadening relative to O_2-O_2 (%)	Researchers
−9	Galkin [38]
same	Miller et al. [78]
+3.8	Ritter and Wilkerson [106, 107]
+6 ± 3	Burch and Gryvnak [27]

The results of the current study are in agreement with those of Galkin [38], but in disagreement with other researchers. The current results are more likely to be correct than the previous results because 38 lines broadened with both O_2 and N_2 were measured and compared, while previous researchers measured only a few N_2- or air-broadened

lines. The current research result also makes physical sense. Oxygen and nitrogen have similar masses, but resonant inelastic rotation-rotation (RR) transfers, in addition to RT transfers, can occur in self-broadening since the absorber and perturber have the same energy level structure. In nitrogen, the energy levels are not identical so RR transitions are unlikely and RT will dominate. The additional open channels in self-broadening can be expected to cause more broadening than a molecule of similar mass without the RR channels.

Finally, compare the broadening coefficients from this study to those reported in the literature for O_2, N_2, air, and He, as measured by tunable diode lasers, which were presented in the previous chapter. The single self-broadened coefficient reported by DeAngelis [31] is 73% larger than the current result. Of the six self-broadened measurements reported by Ray *et al.* [103, 104], two of the values are 10% higher than the current results, while the other four values are more than 40% higher than the current results. The four N_2-broadened values reported by Ray *et al.* [104] are all more than 110% larger than the current results. The three air-broadened values reported by Kauranen and Avetisov [63] agree with the calculated air-broadened values of the current study to better than 2%. Finally, the three O_2-He measurements of Biswas *et al.* [16], which are the only noble-gas broadened results which have been published in the refereed literature, are systematically larger than the results of the current study by more than 30%. It appears that use of diode laser spectroscopy to determine pressure broadening needs more refinement, in contrast with tunable dye lasers, FTS, and grating spectroscopy, which have all demonstrated the ability to produce accurate broadening coefficients.

In addition to line broadening, an attempt was made to quantify pressure-induced line shifting coefficients in the oxygen A band. The slope of a plot of line position vs. perturber pressure gives the line shifting coefficient. The peak position is one of the free parameters in the Voigt fit to each rotational line, so peak positions, with uncertainties, are determined at the same time as Lorentzian widths. For the position vs. pressure fit, the linear equation with unknown intercept, $y = a + bx$, was used. A fit to the data for a rotational line in the O_2+Xe spectrum is shown in Figure 26.
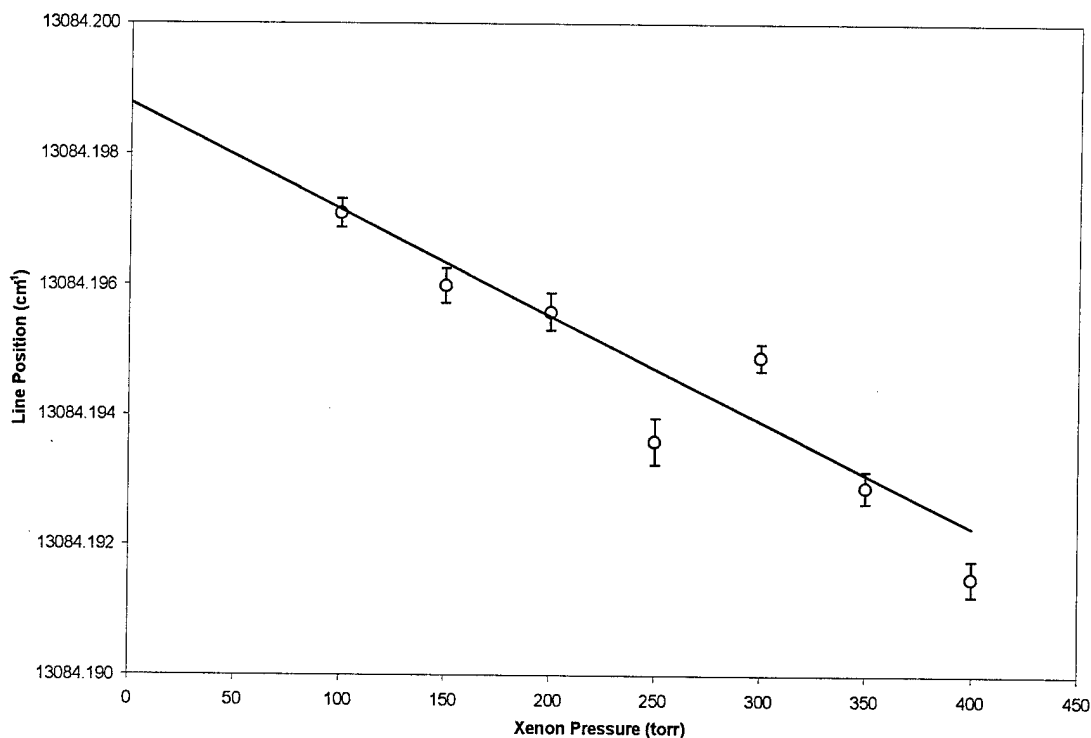
Figure 26. Line Shifting in the $^PP(11)$ Line of O_2+Xe. The slope of this line is the pressure-induced line shifting coefficient.

Line shifting coefficients were determined for 21 lines in the P branch for O_2+Xe. The R branch data was not analyzed because of the closer line spacings and relatively poor S/N. The 21 line shifting coefficients are listed in Table 5 and graphed vs. J'' in Figure 27. Table 5 also compares the results of this study to those of Ritter [106], which are the only previous measurements of line shifting in the oxygen A band for collisions with the noble gases.

Table 5. Pressure-Induced Line Shifting Coefficients for O_2+Xe with Comparison Data from Ritter [106]. (all values are $\times 10^{-6}$ cm^{-1}/torr)

J''	Label	This Research	Ritter
1	$^PP(1)$	−6(12)	−6.74
2	$^PQ(3)$	−19(12)	−11.13
3	$^PP(3)$	−15(5)	−12.78
4	$^PQ(5)$	−12(8)	−12.62
5	$^PP(5)$	−13(4)	−13.95
6	$^PQ(7)$	−19(5)	−14.74
7	$^PP(7)$	−11(8)	−15.26
8	$^PQ(9)$	−18(5)	
9	$^PP(9)$	−17(6)	−17.11
10	$^PQ(11)$	−22(5)	
11	$^PP(11)$	−16(3)	−19.87
12	$^PQ(13)$	−27(6)	−21.84
13	$^PP(13)$	−30(5)	
14	$^PQ(15)$	−16(7)	
15	$^PP(15)$	−29(5)	
16	$^PQ(17)$	−24(8)	
17	$^PP(17)$	−33(5)	
18	$^PQ(19)$	−35(7)	
19	$^PP(19)$	−40(9)	
20	$^PQ(21)$	−37(11)	
21	$^PP(21)$	−54(10)	

Ritter's results are in good agreement with the values from the current study to within the experimental uncertainties, but these uncertainties are quite large compared to the
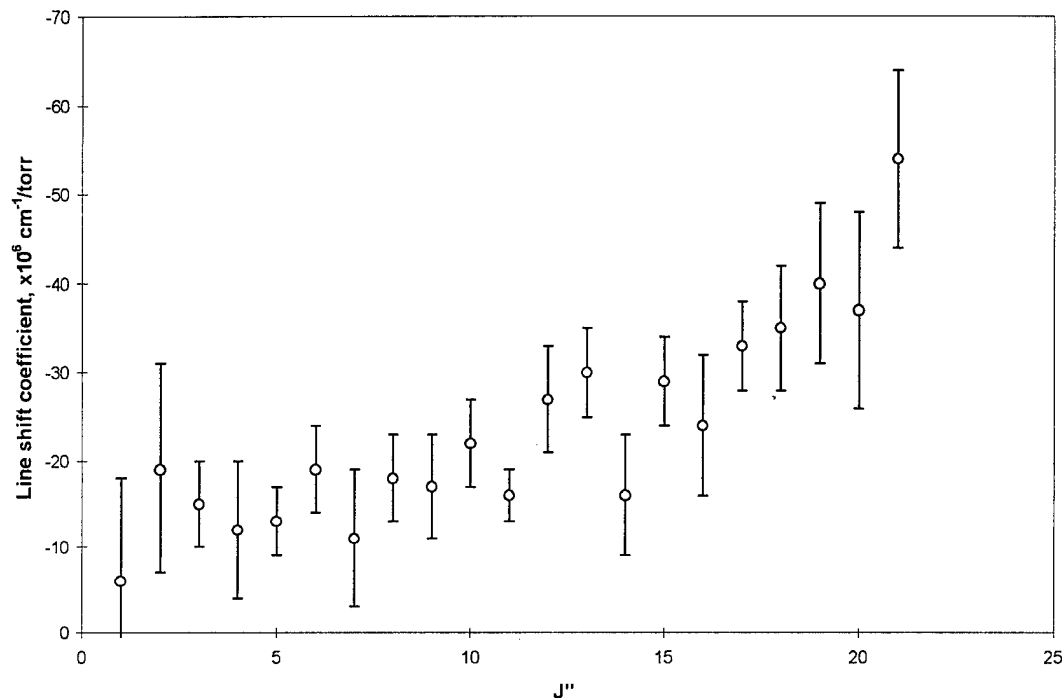
Figure 27. Pressure-Induced Line Shifting Coefficients vs. J'' in the P Branch of O_2+Xe

pressure broadening coefficients determined form the same spectra. The average error in

the O_2+Xe shifting coefficients reported here is 40%, compared to 5.7% for the O_2+Xe

broadening coefficients. The shifting coefficients themselves are about 66% smaller than

the broadening coefficients, which is the primary cause of the larger uncertainties. In

spite of the large uncertainties, some trends are apparent. The shifting coefficients are all

negative, which indicates that the pressure-induced shift moves the line toward lower

wavenumbers (red shift) with increasing pressure. There is also clearly an increasing

shift with increasing J, in contrast to broadening which decreases with increasing J. A

likely cause of line shifting is the distortion of the electron cloud of the molecule during

the collision. This distortion alters the potential energy surfaces, which changes the

energy spacing between the levels connected by the photon transition. The red shift indicates that the levels move closer together in energy during the collision. The increase in shifting with increasing J'' may occur because increasing rotation causes increasing centrifugal distortion in the molecule; a distortion which may further enhance the distortion caused by collisions.

According to Ritter [106], xenon causes the largest shift of the gases studied. From Ritter's data, the average shifts of the P branch lines, as a percentage of the average O_2+Xe shifts, are: 0.5% for He, 5% for Ne, 60% for Ar, 85% for Kr, and 40% for O_2. The current study attempted to determine the shift coefficients for O_2+O_2 but the uncertainties were too large to obtain meaningful results. Because of the large uncertainties in the O_2+Xe results and the very large uncertainties in the attempt to quantify the O_2+O_2 shifts, line shifting in the oxygen A band was not studied any further.

4.3 The Nitric Oxide Fundamental Band

4.3.1. Experimental Conditions. The nitric oxide fundamental band, since it is further in the infrared than the oxygen A band, required a different configuration of the Bomem Fourier transform spectrometer. Absorption spectra for the NO fundamental were acquired using the Bomem components in Table 6.

Table 6. Bomem Components for Spectroscopy in the Nitric Oxide Fundamental Band

Component	Type	Spectral Range, cm^{-1}
Light source:	Globar	200-10000
Beamsplitter (1):	CaF_2 (IMB2200L)	1200-8500
Beamsplitter (2):	KBr (IPB0900L)	450-4000
Detector:	MCT (IPH4400L)	400-5000

There are two beamsplitters listed because two different researchers collected the data. Cornicelli used the CaF_2 beamsplitter and an instrument resolution of 0.004 cm^{-1} to record several spectra, which are reported in reference [30]. For the study reported here, a KBr beamsplitter was used because of its better transmission at the frequencies of interest. Spectra were also acquired at the slightly reduced resolution of 0.005 cm^{-1}, since a problem with the instrument prevented data acquisition at 0.004 cm^{-1}. In each case, a one-inch-diameter band-pass filter, #NO5230-8, with a center frequency of 1886 cm^{-1} and a FWHM of 116.3 cm^{-1} was placed just after the light source. Along with the band-pass filter, limits on the acquisition were set in the software. The lower and upper limits used by Cornicelli were $S_N = 1800$ cm^{-1} and $S_X = 2000$ cm^{-1}, while the new data was acquired using the more restrictive $S_N = 1800$ cm^{-1} and $S_X = 1950$ cm^{-1}. The absorption spectrum of the NO fundamental, superimposed on the band-pass filter response curve and limited by the more restrictive bandwidth set in the acquisition software, is shown in Figure 28. The filter produces data with high S/N for lines from $J'' = 0.5$ to 19.5 in the R branch, but P-branch data quality diminishes beyond about beyond about $J'' = 5.5$.

The sample cell for the NO work was a 10-cm long single-pass cell with CaF_2 windows at either end. Since the NO fundamental transition is dipole-allowed, the absorption coefficient is much higher than for the oxygen A-band transition and a multi-pass cell is no longer required. Indeed, in the absence of buffer gas, the spectral lines in the NO fundamental saturate at about 1 torr of NO for the 10-cm cell. Since the cell is single-pass, the optical aberrations, which degraded the quality of the beam exiting the

cell in the oxygen experiment, are no longer present. This allowed adequate illumination

of the MCT detector with a 0.5-mm source aperture, which permitted using the Fourier

transform spectrometer at high resolutions of 0.004 and 0.005 cm^{-1}.

Figure 28. Nitric Oxide Fundamental Band Spectrum Superimposed on Band-Pass Filter
Response Curve for Filter Centered at 1886 cm^{-1}

Spectra were recorded for NO in collisions with the noble gases He, Ne, Ar, Kr,

and Xe. Cornicelli's spectra were acquired at 0.5 torr of NO, 0.004 cm^{-1} resolution, and

32 or 100 scans. The new measurements are limited to 0.005 cm^{-1} resolution because of

an instability in the instrument. To improve the S/N ratio, the nitric oxide pressure was

increased in the cell as bath gas pressures were increased and all runs included 100 co-

added scans. The response time of the MCT detector requires a mirror scan speed of 0.5

cm/sec, so a 100-scan run at 0.005 cm^{-1} takes about 7.5 hours, while a 100-scan run at

0.004 cm^{-1} takes about 9.5 hours. Further improvements in S/N by increasing the

number of co-adds would be time-prohibitive. The gas mixtures, number of scans, and resolution of each measurement of the NO fundamental are listed in Appendix B.

4.3.2. Analysis. The analysis of the NO spectra, because of the Λ-doublet structure, is much more complicated than the analysis of the oxygen A band. The spectra were analyzed following a method outlined by Spencer *et al.* [118, 119], who studied N_2 broadening of the NO fundamental using a Fourier-transform spectrometer with 0.0064 cm^{-1} resolution. For transitions involving the 3/2 substate, the Λ splitting was not resolved for any of the pressures and transitions studied. In this case, the separations between line centers of the e and f components were fixed to values calculated from literature values of the line positions [118] (reproduced in Appendix C), while the widths and intensities were adjusted with the constraint that the e and f pairs be held equal. Thus for the 3/2 subband, only one set of unique line parameters was obtained for each Λ doublet pair.

For the 1/2 substate, the doublets were usually resolvable for pressures less than about 150 torr. In this case, the line centers and broadening coefficients were allowed to vary independently with the constraint that the intensities of the e and f components be equal [44]. Thus the analysis of a pair of resolved lines in the 1/2 subband produces unique positions and widths for each line, but each line shares a common strength parameter. For cases in which the 1/2 lines were not resolvable, the pair of lines were analyzed using the method outlined above for the unresolved 3/2 lines. At low J, the spacing between the 1/2 and 3/2 substates is small enough that both doublets had to be fit simultaneously at the higher pressures.

114

As with the oxygen spectra, the first step in analyzing the data was the removal of

the band-pass filter response curve and creation of an absorbance spectrum. A typical

absorbance spectrum is shown in Figure 29. The increase in noise at low wavenumbers
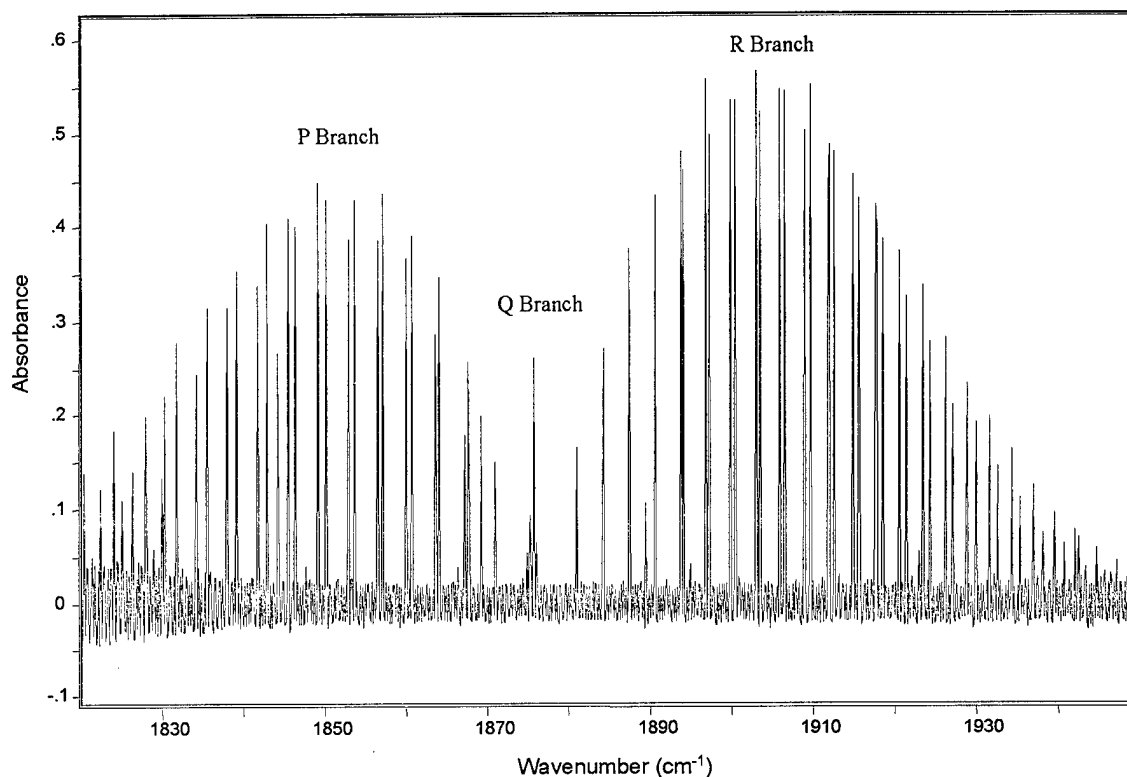
Figure 29. Typical Absorbance Spectrum of the Nitric Oxide Fundamental Band
(0.5 torr NO broadened with 10 torr Ar, 32 scans at 0.004 cm^{-1} resolution)

was a result of the decreasing intensity of the filter response curve, which was centered at

1886 cm^{-1}. There are a few contaminant lines in this spectrum, presumably from water

vapor. A good atlas of the spectrum, such as that presented in Appendix C, helps to

differentiate between the NO and contaminant lines. In cases where the contaminant

115

peaks were close enough to the NO peaks to perturb the fits, the contaminant peaks were modeled as well in order to remove any possible effects.

The next step was to analyze each Λ doublet with a reasonable S/N. For each spectrum, lines were analyzed from $J'' = 0.5$ to 19.5 in the R branch and from $J'' = 1.5$ to 13.5 in the P branch. Because of the magnetic substate splitting, this produced a total of 39 Λ doublets in the R branch and 25 doublets in the P branch. (The Q branch lines were analyzed only for NO+Ar; this work will be presented in Section 4.3.4.) Fits were again performed using the Voigt function in Peak Fit. However, the Voigt could not be implemented directly; special user-defined functions were created to model the peaks with the constraints described previously.

The Doppler widths were again constrained to calculated values to further reduce the number of free parameters in the fit. However, for NO, instead of using a single value for the Doppler width for each line in the spectrum, a frequency-dependent Doppler width parameter was calculated for each line. These calculated values, expressed as the Gaussian standard deviation, are listed in Appendix C. The Doppler HWHM changes by about $\pm 3\%$ from its value at the center of the fundamental band (0.0021 cm^{-1}). The Doppler width of the O_2 A band, in contrast, varies by only about $\pm 1\%$ from its band center value of 0.014 cm^{-1}, so the use of a constant value for the Doppler HWHM in the oxygen analysis introduces a negligible error.

The asymmetry due to phase error proved to be significant for most of the NO spectra. As a result, the asymmetry had to be modeled in the user-defined functions to achieve a good fit to the spectral lines. To model the asymmetry, Bell's asymmetry function, Equation (67), was used with a Voigt instead of a Lorentzian for the symmetric

116

part of the function. This asymmetry function introduces the additional fitting parameter β. In the user-defined functions, each Λ doublet was fit with a single value of β. Fits to typical peaks in the 1/2 and 3/2 substates are shown in Figures 30 and 31, while the parameters for these two fits are listed in Table 7.
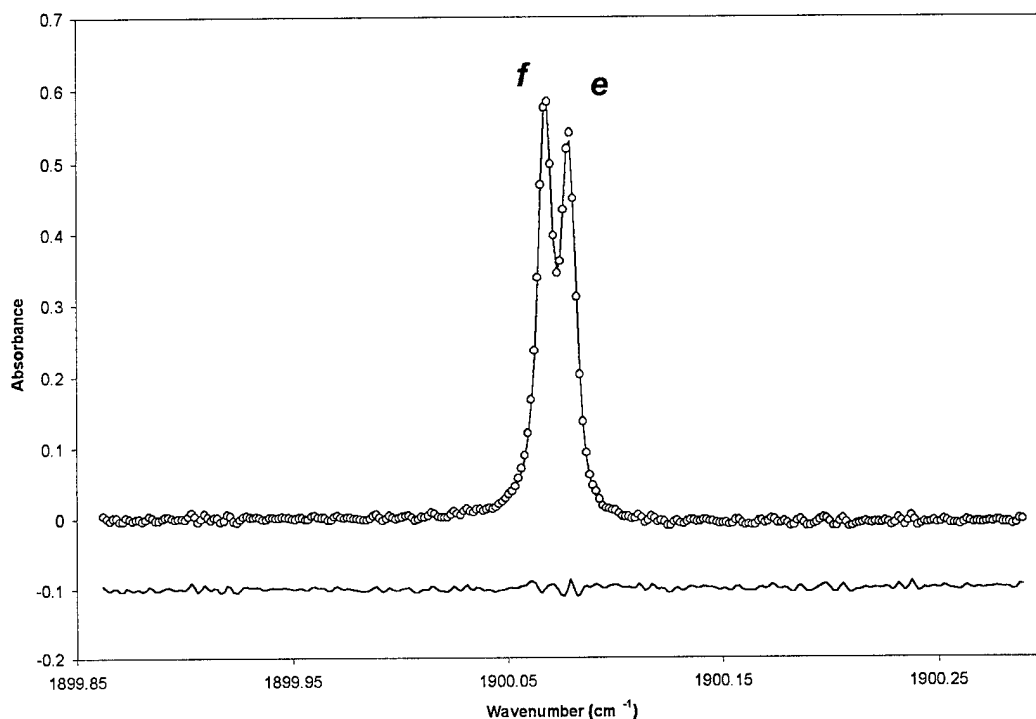
Figure 30. Fit to the $J'' = 6.5$, $\Omega = 1/2$ Resolved Λ Doublet in the NO Fundamental for a Spectrum with 2.0 Torr NO and 50 Torr Ne. Residuals (lower trace) have been offset by -0.1. Asymmetry due to phase error has been modeled. Peaks constrained to have equal areas, Doppler widths, and asymmetry parameters; peak positions and Lorentzian widths are determined separately for each peak. In this fit, the Lorentzian HWHM of the e peak is $10.6 \pm 0.5\%$ larger than for the f peak, indicating the possibility of differential broadening between the Λ doublets.

117
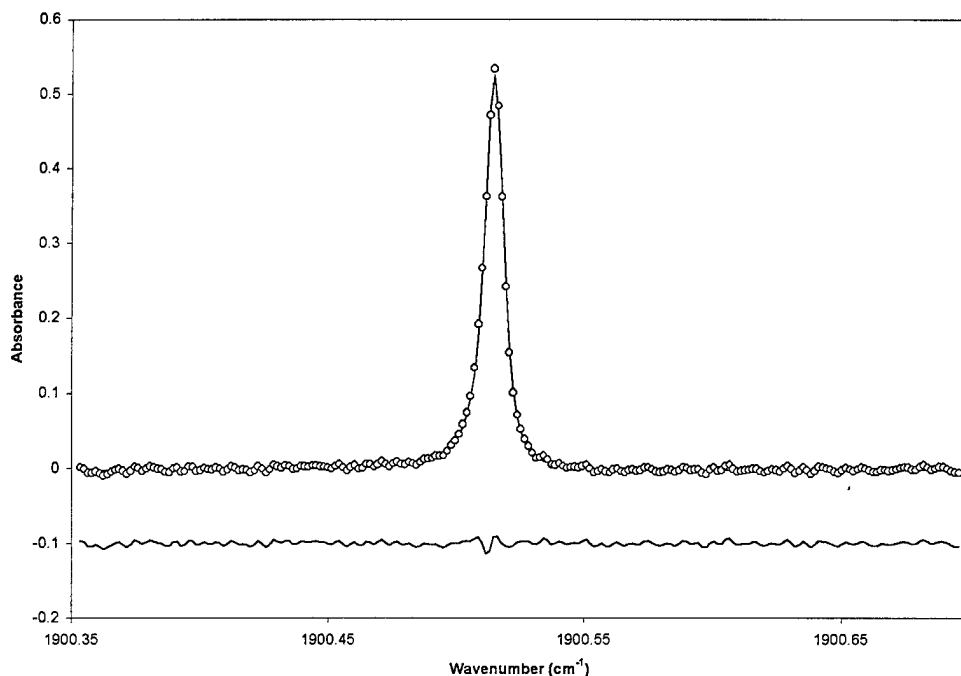
Figure 31. Fit to the $J'' = 6.5$, $\Omega = 3/2$ Unresolved Λ Doublet in the NO Fundamental for a Spectrum with 2.0 Torr NO and 50 Torr Ne. Residuals (lower trace) have been offset by -0.1. Asymmetry due to phase error has been modeled. Peak separation is fixed. Doublet peaks constrained to have equal areas, Doppler widths, Lorentzian Widths, and asymmetry parameters. The fit thus determines only one unique area, Lorentzian HWHM, asymmetry, and position parameter.

Table 7. Parameters of the Fits to the R(6.5) lines of 2.0 Torr NO with 50 Torr Ne Shown in Figures 30 and 31. Errors (1-σ) are in parentheses.

Peak	Fixed Doppler HWHM (cm^{-1})	Area Parameter	Doublet Peak Separation (cm^{-1})	Lorentzian HWHM of e peak (cm^{-1})	Lorentzian HWHM of f peak (cm^{-1})	Asymmetry Parameter ($\times$ 10^{-6} cm)
R$_{1/2}$(6.5)	0.0021	0.006082 (8)	0.01104 (2)	0.003123 (12)	0.002825 (11)	4.09(12)
R$_{3/2}$(6.5)	0.0021	0.003344 (6)	0.00078	0.003269 (12)	0.003269 (12)	9.0(3)

Several trends are apparent from these two figures and the accompanying table. First, the intensity of the 1/2 peaks are about twice that of the 3/2 peaks with the same J''. Next, the separation of the Λ doublets in the 1/2 substate is about an order of magnitude more than the separation in the 3/2 substate. Third, the Lorentzian width of the e peak of the resolved 1/2 doublet is $10.6 \pm 0.5\%$ larger than the width of the f peak, indicating a differential broadening between the Λ doublets in the 1/2 substate. Fourth, the Lorentzian width of the 3/2 peaks is $9.9 \pm 0.7\%$ larger than the average width of the 1/2 peaks, indicating a differential broadening between the magnetic substates. Finally, the asymmetry parameters from the two fits differ by more than a factor of 2. This is not the expected result; the asymmetry parameter should be nearly the same for two lines spaced so close in frequency. Errors in the asymmetry parameter may contribute to uncertainties in the retrieved width parameters. However, the fits have been greatly improved by the inclusion of the asymmetry effect.

After finding the widths of all the peaks in each spectrum, broadening coefficients were determined from a linear least squares fit to a plot of the Lorentzian HWHM vs. bath gas pressure. Broadening coefficients were determined separately in all cases for the 1/2 and 3/2 magnetic substates. However, broadening coefficients were determined individually for the e and f doublet peaks of the 1/2 substate only for collisions with Ne and Ar, since a systematic differential broadening between the Λ-doublet components was generally not observed. Early in the analysis of the data, a careful look at the lines from $R_{1/2}(6.5)$ to $R_{1/2}(10.5)$ for NO+Ar was performed to see if there was any difference in broadening coefficients for the e and f lines. These lines are well-resolved in the spectra for argon pressures less than 80 torr. It was found that the e and f lines of the 1/2

.

119

substate broadened the same to within experimental uncertainties. Thus, for the remainder of the analysis, the 1/2 e and f components were considered to have the same width. This held true for all lines except for those in the P and R branches of NO+Ne and in the P branch of NO+Ar. In these two exceptional cases, the S/N was very good and the differential broadening between the Λ-doublet components was clearly apparent.

To determine the broadening due to the noble gases, the broadening due to the nitric oxide in the cell had to be subtracted from the measured Lorentzian widths. To do this, the self-broadening coefficients were fixed to values determined by Ballard et al. [8], which are included at Appendix A. A typical fit to the Lorentzian HWHM vs. pressure is shown in Figure 32.

Because the $R_{1/2}(1.5)$ and $R_{3/2}(1.5)$ lines are strongly overlapped, and because Ballard et al. do not provide self-broadening coefficients for these lines (also because of the overlap), no broadening coefficients are reported for these lines. For all lines analyzed, the characteristic residuals of Dicke narrowing were never observed, and the plots of width vs. pressure always increased linearly with pressure, so Dicke narrowing was not observable in these spectra and the Voigt function was used for all fits.

Before accepting the broadening coefficients determined by the Peak Fit procedure described above, instrument effects had to be analyzed. This was done using DUDV, just as for the oxygen measurements. However, for the more complicated spectrum of the NO fundamental, line positions, widths, and intensities had to be constrained in the same way they were in the Peak Fit analysis. The instrument effect parameters are also different for these fits, since the resolution and aperture have changed from the oxygen measurements. For the nitric oxide fundamental band measurements,

$\sigma_0 = 1876 \text{ cm}^{-1}$, $h = 0.05$ cm, and $F = 32.385$ cm, so the aperture effect parameter is

$\delta\sigma_{HW} = 0.000279 \text{ cm}^{-1}$. For spectra acquired at 0.004 cm^{-1} resolution, the maximum

OPD is 250 cm, while for spectra acquired at 0.005 cm^{-1} resolution, the maximum OPD

is 200 cm. The asymmetry parameter must be determined from a fit to each spectrum.
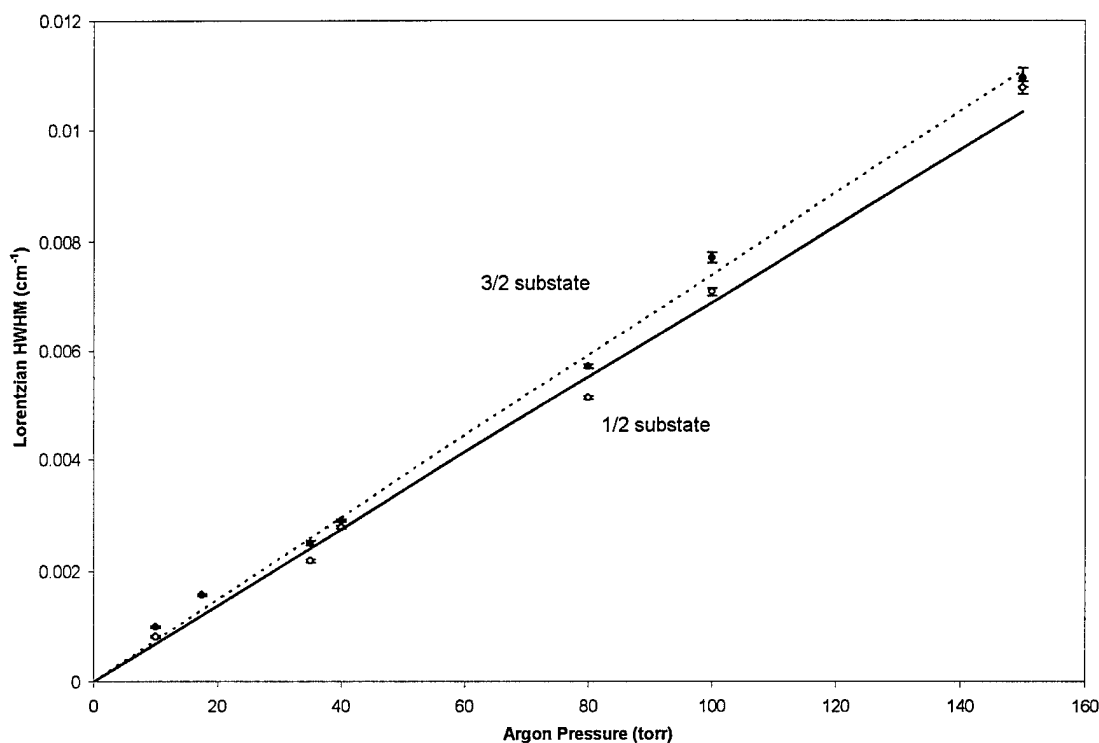
Figure 32. Linear Least Squares Fit to Lorentzian HWHM as a Function of Bath Gas
Pressure. This data is for the R(6.5) lines of NO+Ar. The slopes of these lines are the
broadening coefficients. The broadening coefficients determined from this fit are
$\gamma_{1/2} = 6.9(3)$ and $\gamma_{3/2} = 7.4(2)$, each in units of $\times 10^{-5} \text{ cm}^{-5}/\text{torr}$. This data indicates that
the 3/2 substate for this transition broadens $7 \pm 5\%$ more than the 1/2 substate.

To examine the instrument effects in the NO data, DUDV fits were performed on

the six doublets between $J'' = 6.5$ and 8.5 in the R branch of NO+Xe. Accurate initial

guesses are required for the parameters of the fit. Initial guesses for line positions came

from Spencer *et al.* [118], while broadening coefficients and line strengths came from

Ballard *et al.* [8]. A typical DUDV fit to the NO data is shown in Figure 33.
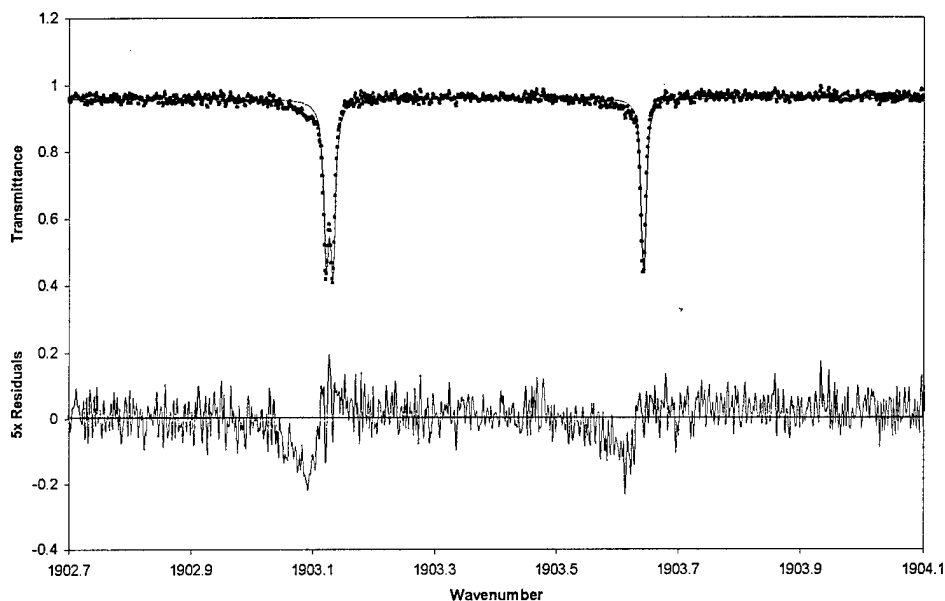
Figure 33. DUDV Fit to J" = 7.5 in the R branch of 0.5 Torr NO with 40 Torr Xe. Residuals have been multiplied by a factor of five to better show discrepancies in fit.

The DUDV results indicate that a fit that considers the instrument effects

increases the broadening coefficients an average of 5 ± 4% over a fit that does not

consider the ILS and aperture effects. However, as Figure 33 shows, the DUDV fits did

not model the asymmetry as accurately as Peak Fit. Furthermore, the DUDV results

show no indication of differential broadening between the magnetic substates, while the

Peak Fit results for the same lines clearly show this differential broadening. It appears

that DUDV does not model the asymmetry as well as Peak Fit and that this difficulty with

the asymmetry may be a primary cause of the different retrieved broadening coefficients.

Since the difference in the broadening coefficients between the fits with and without

instrument effects is small, and since there is some question about the quality of the

DUDV results, it was concluded that instrument effects were not a significant issue in the NO data set. The results from Peak Fit will therefore be used to determine the broadening coefficients.

4.3.3. Results. A plot of the NO+Ar broadening coefficients is shown in Figure 34. The data shows a distinct asymmetry between the P and R branches above $J'' = 5.5$, with the broadening coefficients in the P branch "hooking" upward above this value. Examination of the broadening coefficients for the other four noble gases also showed this asymmetry. Since the broadening coefficients in the P and R branches are expected to be symmetric, an instrumental cause for the observed asymmetry was suspected. It was determined that the P-branch lines above $J'' = 5.5$ occur in a part of the band-pass filter response curve which is rapidly decreasing in intensity. To see if the filter was the
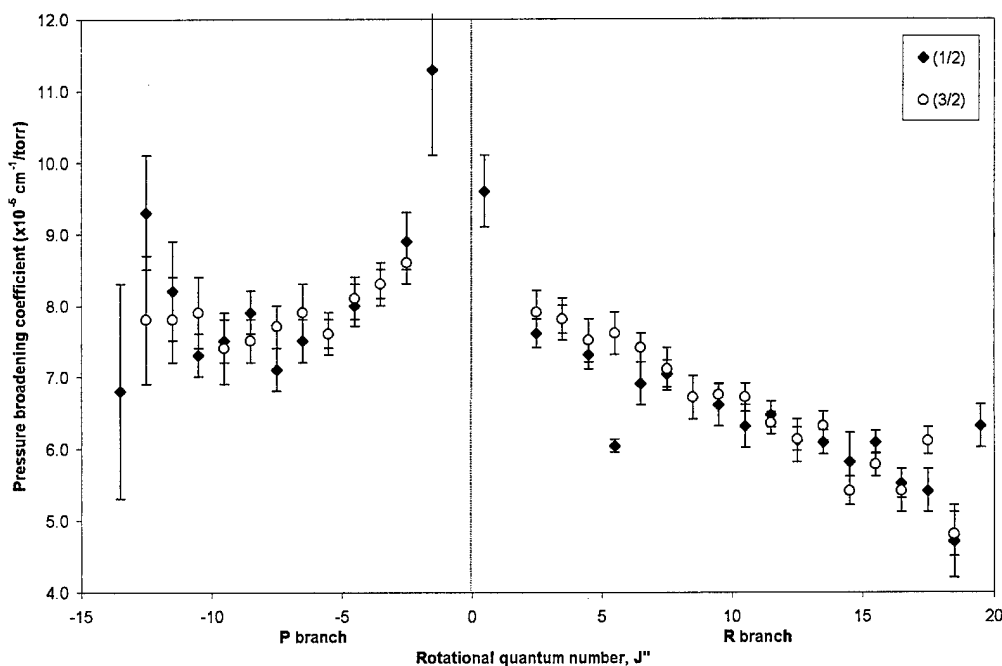
Figure 34. Broadening Coefficients vs. J'' for NO+Ar for Data Acquired with the Band-Pass Filter Centered at 1886 cm^{-1}

problem, spectra of NO+Ar were measured again, this time using a filter centered on the

P branch. The new band-pass filter, Infrared Optical Products #BP5420-400 is centered

at 1840 cm^{-1} and has a FWHM of 160 cm^{-1}. The NO+Ar spectrum superimposed on this

new band-pass filter is shown in Figure 35. Four new NO+Ar spectra were acquired with

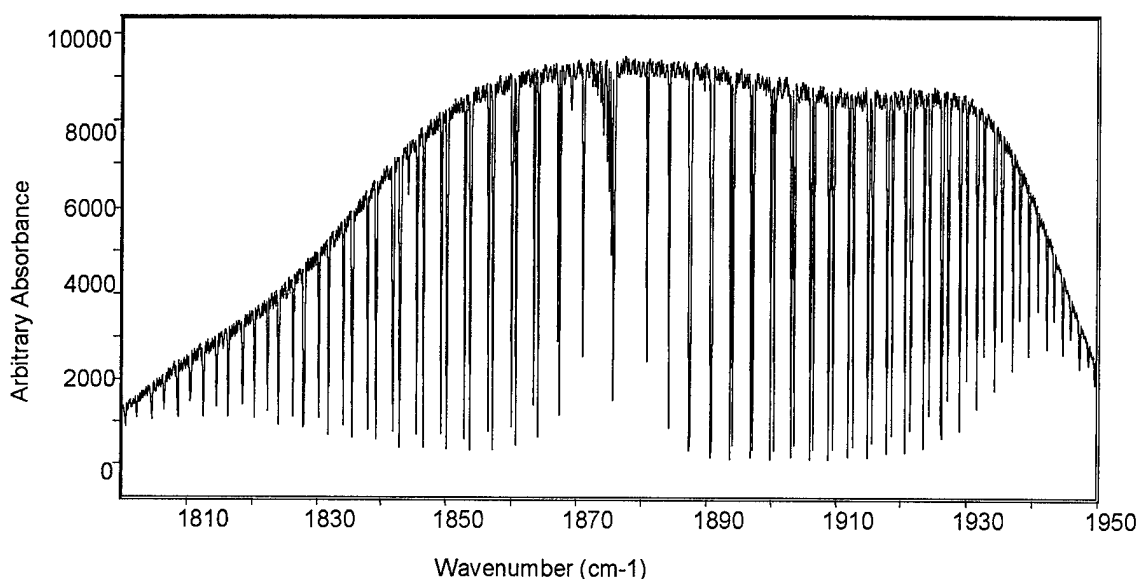the new filter. The experimental conditions for these new measurements are listed in

Appendix B.
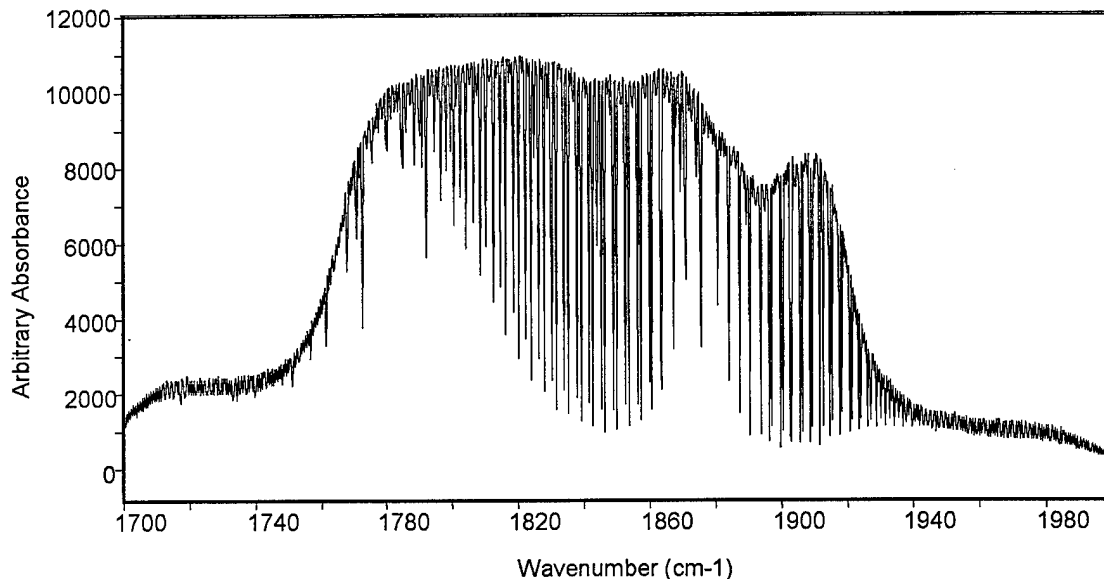
Figure 35. Nitric Oxide Fundamental Band Spectrum Superimposed on Band-Pass Filter
Response Curve for Filter Centered at 1840 cm^{-1}

Using the data from these four new spectra with the new filter, the broadening

coefficients in the P branch of NO+Ar were determined again. These new broadening

coefficients are compared to the old coefficients in Figure 36.
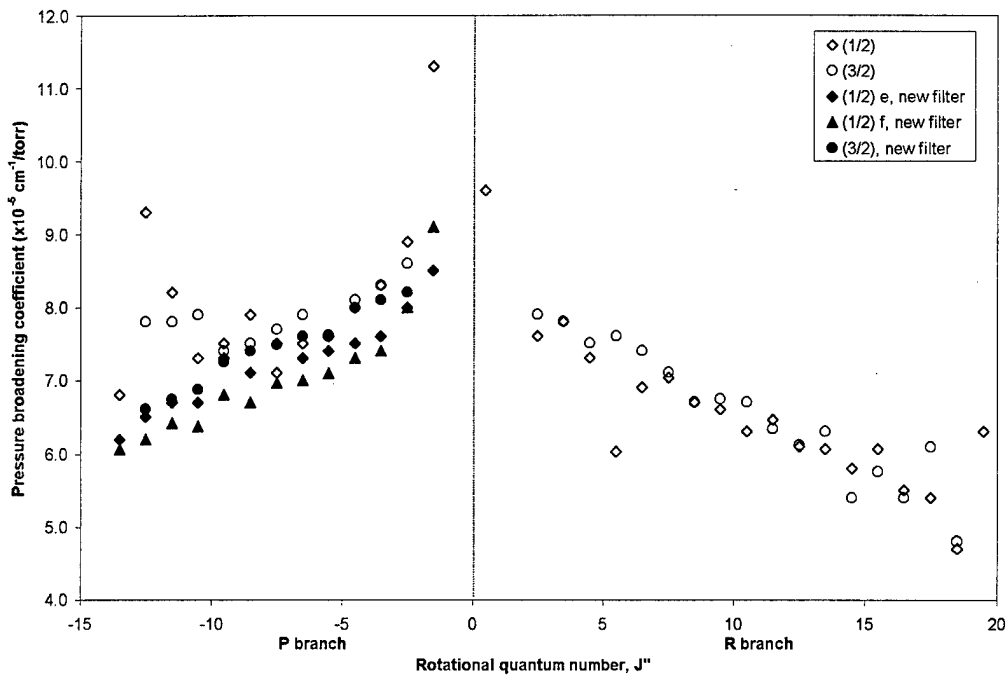
Figure 36. Broadening Coefficients vs. J" Acquired with a Band-Pass Filter Centered at
1886 cm^{-1} ("Old Filter") and with a Different Band-Pass Filter Centered at 1840 cm^{-1}
("New Filter")

As Figure 36 shows, the P-branch broadening coefficients determined using the

new filter are now symmetric with the broadening coefficients in the R branch.

Assuming symmetry between the branches, data for $J" > 5.5$ in the P branch of NO

broadened with the other four noble gases was discarded rather than measuring each of

these gases again with the new band-pass filter. The broadening coefficients for the nitric

oxide fundamental band broadened with the noble gases He, Ne, Ar, Kr, and Xe are

graphed vs. $J"$ in Figures 37 to 41 and listed in Tables 8 and 9.

The broadening coefficients reported in Tables 8 and 9 are given with 1-σ

statistical errors. These statistical errors are on the order of 4% near the center of each

branch and increase to about 10% for the less-intense lines at high and low $J"$. Possible

sources of systematic error, such as instrument lineshape effects and filter transmission effects have been carefully taken into account, so the quoted statistical errors should be a good measure of uncertainty in these results.
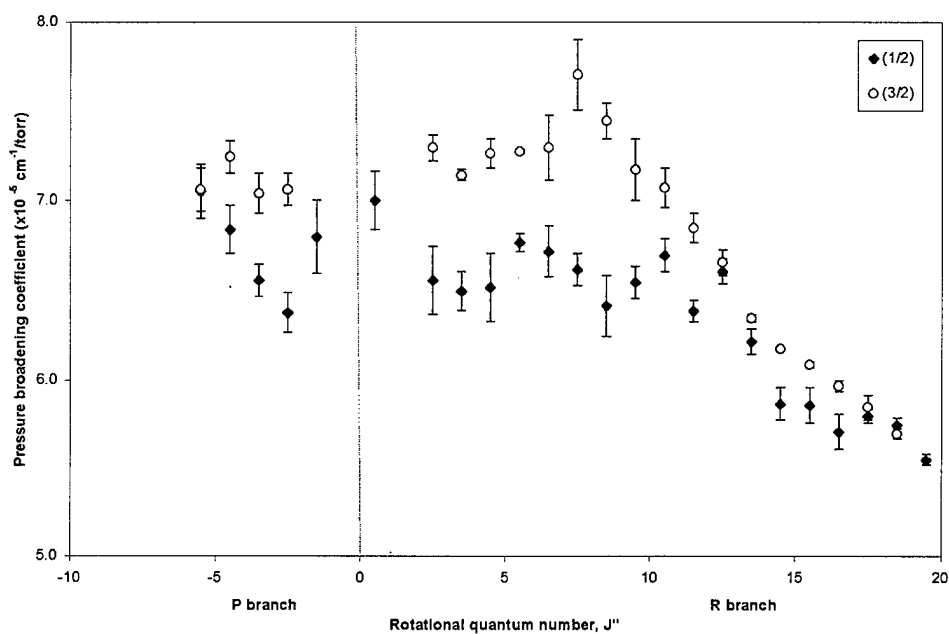
Figure 37. The Nitric Oxide Fundamental Band Broadened with Helium
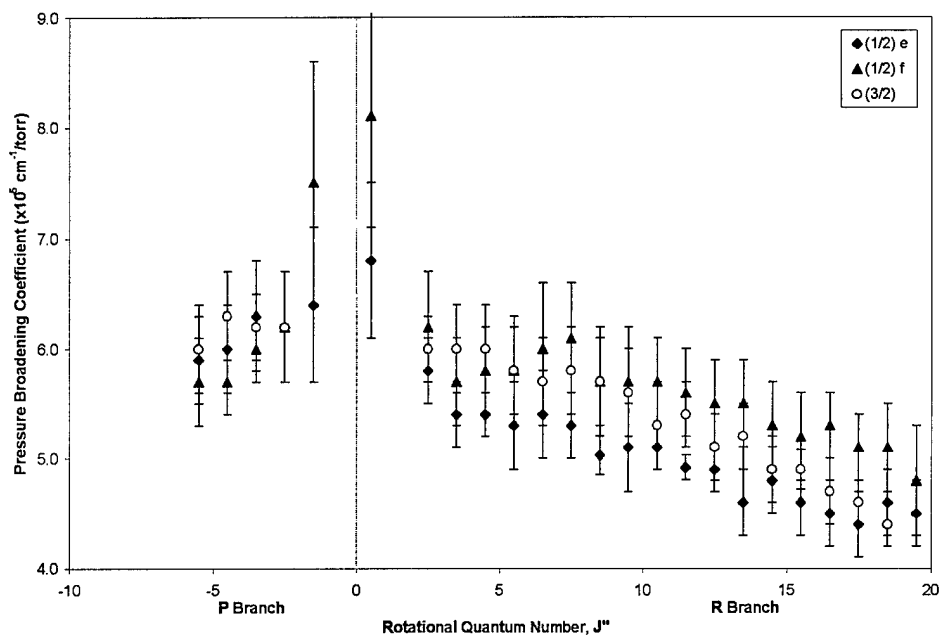
Figure 38. The Nitric Oxide Fundamental Band Broadened with Ne. Differential broadening between the Λ doublet components in the 1/2 subband was observed.
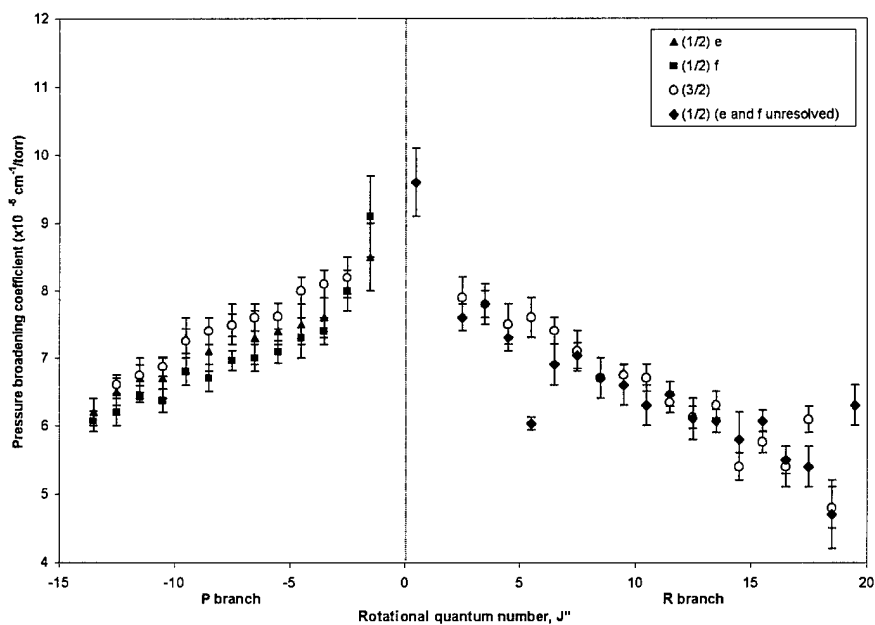
Figure 39. The Nitric Oxide Fundamental Band Broadened with Ar. The band-pass filter centered at 1840 cm^{-1} was used for the P branch, while the filter centered at 1886 cm^{-1} was used for the R branch. Differential broadening between the Λ-doublet components in the 1/2 subband was resolvable in the new P-branch data.

127
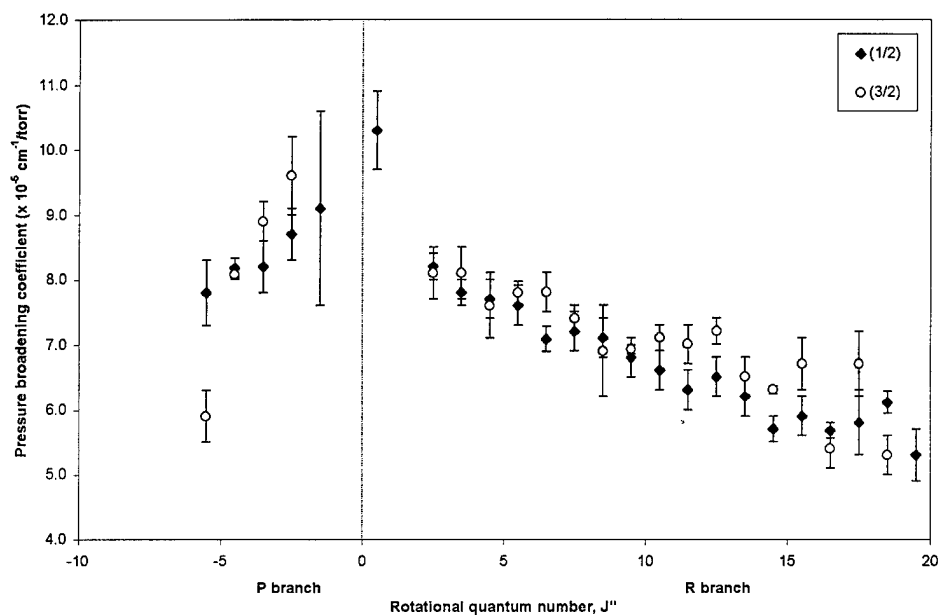
Figure 40. The Nitric Oxide Fundamental Band Broadened with Kr
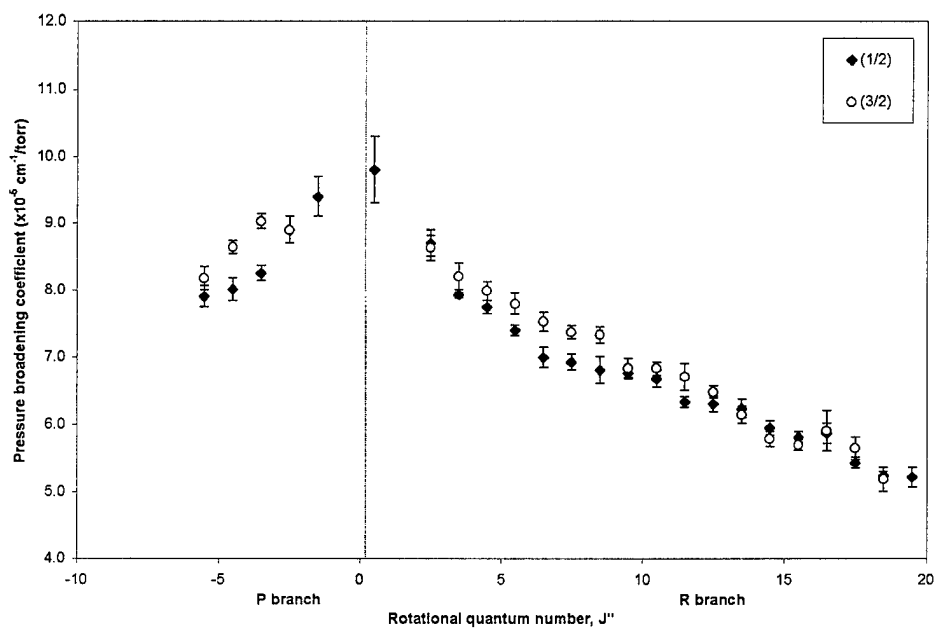
Figure 41. The Nitric Oxide Fundamental Band Broadened with Xe

128

Table 8. NO+Noble Gas Broadening Coefficients, $\Omega = 1/2$ Substate of the NO Fundamental Band. Differential broadening is reported between the e and f Λ-doublet components with neon and in the P-branch with argon. (all values are $\times\ 10^{-5}$ cm^{-1}/torr)

Label	He	Ne (e)	Ne (f)	Ar (e)	Ar (f)	Kr	Xe
P(13.5)				6.2(2)	6.07(15)		
P(12.5)				6.5(2)	6.2(2)		
P(11.5)				6.7(3)	6.42(7)		
P(10.5)				6.7(3)	6.37(17)		
P(9.5)				7.3(3)	6.8(2)		
P(8.5)				7.1(3)	6.7(2)		
P(7.5)				7.5(3)	6.96(15)		
P(6.5)				7.3(4)	7.0(2)		
P(5.5)	7.05(15)	5.9(4)	5.7(4)	7.4(2)	7.09(17)	7.8(5)	7.90(16)
P(4.5)	6.84(13)	6.0(4)	5.7(3)	7.5(3)	7.3(3)	8.18(15)	8.01(17)
P(3.5)	6.56(9)	6.3(5)	6.0(3)	7.6(3)	7.4(2)	8.2(4)	8.25(11)
P(2.5)	6.38(11)	6.2(5)	6.2(5)	8.0(3)	8.0(3)	8.7(4)	8.9(2)
P(1.5)	6.8(2)	6.4(7)	7.5(11)	8.5(5)	9.1(6)	9.1(15)	9.4(3)
R(0.5)	7.00(16)	6.8(7)	8.1(10)	9.6(5)		10.3(6)	9.8(5)
R(1.5)							
R(2.5)	6.56(19)	5.8(3)	6.2(5)	7.6(2)		8.2(2)	8.7(2)
R(3.5)	6.50(11)	5.4(3)	5.7(4)	7.8(2)		7.8(2)	7.92(4)
R(4.5)	6.52(19)	5.4(2)	5.8(4)	7.3(2)		7.7(3)	7.74(10)
R(5.5)	6.77(5)	5.3(4)	5.8(5)	6.03(9)		7.6(3)	7.39(8)
R(6.5)	6.72(14)	5.4(4)	6.0(6)	6.9(3)		7.08(19)	6.99(15)
R(7.5)	6.62(9)	5.3(3)	6.1(5)	7.03(19)		7.2(3)	6.92(12)
R(8.5)	6.42(17)	5.03(18)	5.7(5)	6.7(3)		7.1(3)	6.8(2)
R(9.5)	6.55(9)	5.1(4)	5.7(5)	6.6(3)		6.8(3)	6.76(9)
R(10.5)	6.70(9)	5.1(2)	5.7(4)	6.3(3)		6.6(3)	6.67(12)
R(11.5)	6.39(6)	4.92(11)	5.6(4)	6.46(18)		6.3(3)	6.33(8)
R(12.5)	6.61(7)	4.9(2)	5.5(4)	6.1(3)		6.5(3)	6.30(12)
R(13.5)	6.22(7)	4.6(3)	5.5(4)	6.07(17)		6.2(3)	6.23(14)
R(14.5)	5.87(9)	4.8(3)	5.3(4)	5.8(4)		5.7(2)	5.94(11)
R(15.5)	5.86(10)	4.6(3)	5.2(4)	6.07(16)		5.9(3)	5.81(8)
R(16.5)	5.71(10)	4.5(3)	5.3(3)	5.5(2)		5.68(12)	5.86(15)
R(17.5)	5.80(4)	4.4(3)	5.1(3)	5.4(3)		5.8(5)	5.42(8)
R(18.5)	5.75(4)	4.6(3)	5.1(4)	4.7(5)		6.11(17)	5.23(6)
R(19.5)	5.55(3)	4.5(3)	4.8(5)	6.3(3)		5.3(4)	5.21(15)

Table 9. NO+Noble Gas Broadening Coefficients, Ω = 3/2 Substate of the NO Fundamental Band. (All values are $\times\ 10^{-5}\ cm^{-1}$/torr)

Label	He	Ne	Ar	Kr	Xe
P(12.5)			6.61(14)		
P(11.5)			6.74(15)		
P(10.5)			6.87(14)		
P(9.5)			7.25(18)		
P(8.5)			7.4(2)		
P(7.5)			7.49(17)		
P(6.5)			7.6(2)		
P(5.5)	7.06(12)	6.0(4)	7.62(19)	5.9(4)	8.17(17)
P(4.5)	7.24(9)	6.3(4)	8.0(2)	8.08(7)	8.64(10)
P(3.5)	7.04(11)	6.2(3)	8.1(2)	8.9(3)	9.03(11)
P(2.5)	7.06(9)	6.2(5)	8.2(3)	9.6(6)	8.9(2)
R(2.5)	7.29(7)	6.0(3)	7.9(3)	8.1(4)	8.63(19)
R(3.5)	7.14(3)	6.0(4)	7.8(3)	8.1(4)	8.2(2)
R(4.5)	7.26(8)	6.0(4)	7.5(3)	7.6(5)	7.98(14)
R(5.5)	7.270(13)	5.8(4)	7.6(3)	7.79(18)	7.79(16)
R(6.5)	7.29(18)	5.7(4)	7.4(2)	7.8(3)	7.52(14)
R(7.5)	7.7(2)	5.8(4)	7.1(3)	7.4(2)	7.36(10)
R(8.5)	7.44(10)	5.7(4)	6.7(3)	6.9(7)	7.32(12)
R(9.5)	7.17(17)	5.6(4)	6.74(15)	6.92(7)	6.83(14)
R(10.5)	7.07(11)	5.3(4)	6.7(2)	7.1(2)	6.82(10)
R(11.5)	6.85(8)	5.4(3)	6.34(15)	7.0(3)	6.7(2)
R(12.5)	6.66(7)	5.1(3)	6.12(16)	7.2(2)	6.48(9)
R(13.5)	6.35(2)	5.2(3)	6.3(2)	6.5(3)	6.14(13)
R(14.5)	6.181(7)	4.9(3)	5.4(2)	6.30(6)	5.78(11)
R(15.5)	6.090(18)	4.90(18)	5.76(16)	6.7(4)	5.69(8)
R(16.5)	5.97(3)	4.7(3)	5.4(3)	5.4(3)	5.9(3)
R(17.5)	5.85(7)	4.6(2)	6.09(19)	6.7(5)	5.64(17)
R(18.5)	5.7(3)	4.4(2)	4.8(3)	5.3(3)	5.18(18)

Now compare these NO + noble gas broadening results with those reported by previous researchers. There are no previous results for NO broadened with Ne or Xe. The only previous result for NO broadened with Kr is that of Hanson et al. [48], who

measured just the $R_{1/2}(18.5)$ line and reported a value 26% smaller than the value found

in the current study. There have been four previous studies of NO broadened with He.

These values are compared with results from the current study in Table 10.

Table 10. NO+He Broadening Coefficients ($\times 10^{-5}$ cm^{-1}/torr) from Previous
Researchers Compared to Results of Current Study

Researcher(s)	Line	Reported Broadening Coefficient	Compared to Results of Current Study
Webber and Penner [131]	no J-dependence	4.1	−35%
Bonczyk [21]	$R_{3/2}(1.5)$	1.7	−77%
Kunimori et al. [66]	avg. of R(3.5), R(10.5)	5.1	−22%
Rohrbeck et al. [109]	$R_{1/2}(0.5)$	7.0(5)	$0 \pm 7\%$
	$P_{1/2}(1.5)$	5.6(5)	$-18 \pm 9\%$
	$R_{1/2}(4.5)$	7.0(5)	$+7 \pm 8\%$
	$R_{3/2}(4.5)$	6.7(3)	$-8 \pm 5\%$

The early researchers [21, 109, 131] reported results which are between 22 and 77%

lower than the results of the current study. More recently, however, Rohrbeck et al.

[109] used a tunable laser and measured four lines which nearly match the results of the

current study to within experimental error.

By far, the majority of previous work in NO broadened with the noble gases has

been performed with argon. Five previous research groups have reported broadening

coefficients for NO+Ar in the fundamental band, and two of these studies have been

reasonably systematic, J-dependent investigations. In addition, a very comprehensive

study was performed for NO+Ar in the first overtone. The results of these six previous

efforts are graphically compared to the results of the current study in Figure 42. In an

131

effort to simplify the diagram, any differential broadening between Λ doublets or magnetic substates have been averaged together to give a single coefficient for each J.
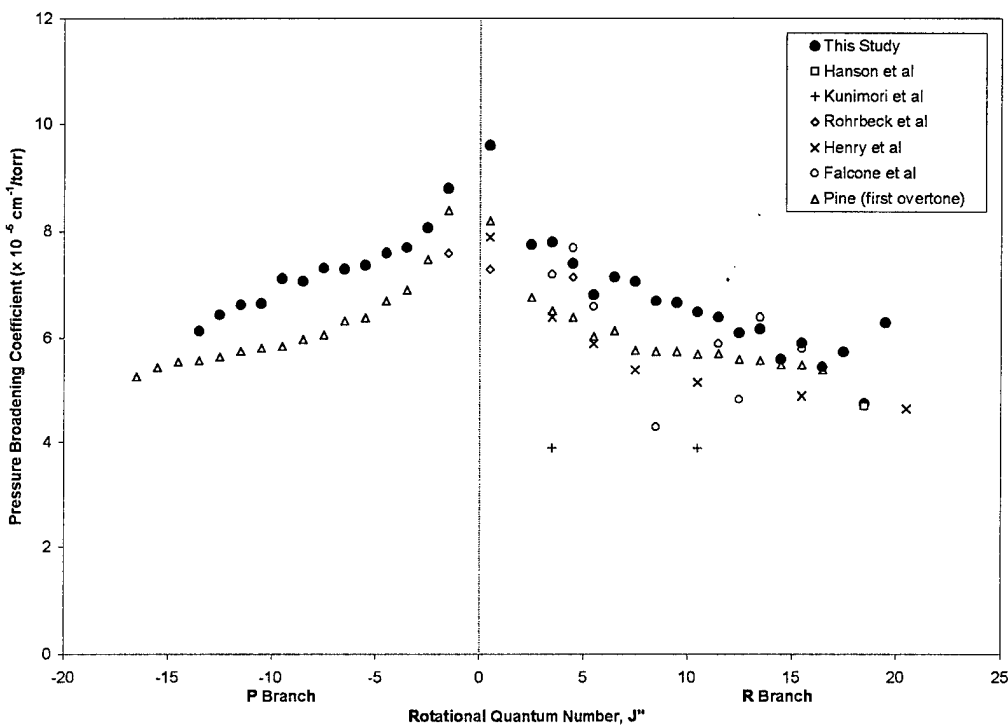
Figure 42. Nitric Oxide Broadened with Argon: Comparison with Results of Previous Researchers. References are: Hanson *et al.* [48], Kunimori *et al.* [66], Rohrbeck *et al.* [109], Henry *et al.* [51], Falcone *et al.* [36], and Pine [96].

The broadening coefficients from the three previous less-than-systematic studies are compared to the results of this study in Table 11. The results of Kunimori *et al.* [66] show the largest discrepancy with the results of the current study. There is some doubt as to the accuracy of their reported results, since their NO+Ar broadening coefficient is 24% less than their NO+He broadening coefficient, contrary to the expected increase in broadening with increasing perturber mass. The results of Hanson *et al.* [48] and

Rohrbeck *et al.* [109] come much closer to matching the results of the current study to within experimental uncertainties.

Table 11. NO+Ar Broadening Coefficients ($\times\ 10^{-5}\ cm^{-1}$/torr) from Previous Researchers Compared to Results of Current Study

Researcher(s)	Line	Reported Broadening Coefficient	Compared to Results of Current Study
Hanson *et al.* [48]	$R_{1/2}(18.5)$	4.7(7)	$0 \pm 18\%$
Kunimori *et al.* [66]	avg. of R(3.5), R(10.5)	3.9	-45%
Rohrbeck *et al.* [109]	$R_{1/2}(0.5)$	7.3(3)	$-24 \pm 7\%$
	$P_{1/2}(1.5)$	7.6(3)	$-14 \pm 10\%$
	$R_{1/2}(4.5)$	6.8(3)	$-7 \pm 5\%$
	$R_{3/2}(4.5)$	7.5(2)	$0 \pm 4\%$

To compare the results of the current research project with those of the previous systematic studies, two in the fundamental band and one in the first overtone, the average NO+Ar broadening coefficients were computed for each study. The comparison between these averages and the average broadening coefficient from the current study are in Table 12. The results of these three previous studies are systematically less than the results of the present research. These discrepancies are not large, though they are larger than the experimental uncertainty of the current study. The average uncertainty in the NO+Ar results of the current study is $\pm$ 6%, the average uncertainty in Pine's [96] results is $\pm$ 1.4%, and no uncertainties are given for the other two studies. The J-dependent trend of the results of Falcone *et al.* [36] is a good match to the trend in the data from the current study, while the results of Henry *et al.* [51] and Pine [96] appear to indicate a steeper decrease with increasing J.

133

Table 12. Systematic Studies NO+Ar Broadening from Previous Researchers
Compared to Results of Current Study

Researcher(s)	Number of Measurements	Compared to Average from Current Study
Henry *et al.* [51]	14	−18%
Falcone *et al.* [36]	10	−9%
Pine [96] (first overtone)	64	−12%

The next topic to consider is the magnitude of the observed differential

broadening, both between the magnetic substates and between the 1/2 Λ doublets. A

definite difference in broadening was observed between the 1/2 and 3/2 magnetic

substates for collisions with all five noble gases. These observed differences, together

with all known quantitative reports of magnetic substate differential broadening from the

literature, are listed in Table 13.

Table 13. Differential Broadening Between the Ω = 1/2 and 3/2 Magnetic Substates of
Nitric Oxide: Results from Current Study and Literature Results

Results from Current Study		Literature Results		
Collision Partner	$\gamma_{3/2} > \gamma_{1/2}$ (%)	Collision Partner	$\gamma_{3/2} > \gamma_{1/2}$ (%)	Reference
He	7 ± 2	NO	1 to 3	[8]
Ne	3 ± 7		7	[95] (Q branch)
Ar	3 ± 4		10	[68] (1st overtone)
Kr	5 ± 6	N_2	3.8 ± 1.8	[118]
Xe	3 ± 3		7	[68] (1st overtone)
		Ar	12	[51]

The trend in the results is that the broadening coefficients for the 3/2 substate are an

average of about 4% larger than the coefficients for the 1/2 substate, although only the

NO+He difference is larger than the experimental uncertainty. There are no observed

trends with perturber or J, and the effect appears to be symmetric in both the P and R

branches. A look at the values for differential broadening reported by previous

researchers indicates similar trends. A possible physical mechanism for this differential

broadening will be described in the next chapter.

Some evidence of differential broadening between the e and f components of the 1/2

Λ doublets was also observed. These observations, together with all known quantitative

reports of Λ doublet differential broadening from the literature, are listed in Table 14.

Table 14. Differential Broadening Between the Λ Doublet Components of the 1/2
Magnetic Substate of Nitric Oxide: Results from Current Study and Literature Results
(He results from $J'' = 5.5$ in a single spectrum)

Results from Current Study			Literature Results		
Collision Partner	P Branch $\gamma_e > \gamma_f$ (%)	R Branch $\gamma_f > \gamma_e$ (%)	Collision Partner	P,R Branches $\gamma_f > \gamma_e$ (%)	Reference
He	8 ± 4	18 ± 5	N_2	2 ± 3	[118]
Ne	3 ± 10	11 ± 10		4.4	[119]
Ar	3 ± 5	$-$	Ar	6	[96] (1st overtone)
Kr	$-$	$-$			
Xe	$-$	$-$			

In Table 14, the He results come from just the two $J'' = 5.5$ peaks in a single

spectrum. These two peaks are shown in Figure 43. The Ne P-branch results exclude the

$P_{1/2}(1.5)$ lines since they appear to have been affected by nuclear hyperfine splitting. The

Ne R-branch and Ar P-branch results include all measured data. No systematic trends
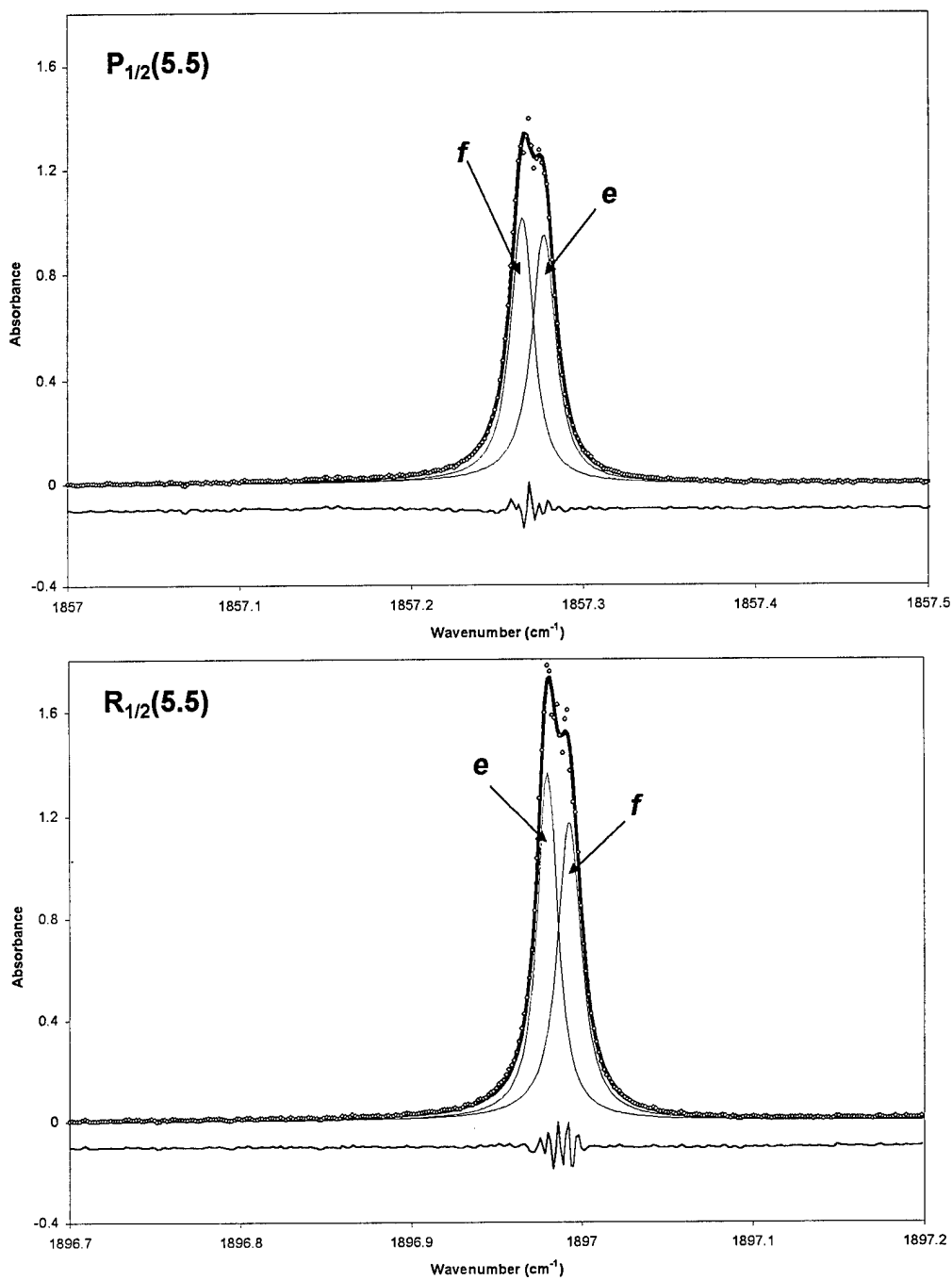
Figure 43. Evidence of Differential Broadening Between the Λ-Doublet Peaks, with Opposite Trends in P and R Branches (5 Torr NO with 100 Torr He)

were observed for Kr, Xe, and the R-branch of Ar. The trend in the current results is that the *e* component broadens an average of 4% more than the *f* component in the P branch, while the *f* component broadens an average of 15% more than the *e* component in the R branch. The literature results, on the other hand, indicate that the *f* component broadens an average of 4% more than the *e* component in the both branches. Figure 43 shows the $P_{1/2}(5.5)$ and $R_{1/2}(5.5)$ lines for a spectrum of NO+He.

Figure 43 demonstrates the observed reversal of differential broadening between the P- and R-branch Λ doublets. The Λ-doublet components of each peak have equal strengths, so the differences in peak heights are due to differences in width. In each case, the peak on the higher wavenumber side is the wider of the two peaks. This figure also demonstrates the larger observed differential broadening in the R branch than in the P branch. Asymmetry due to phase error has been modeled in the fits to these peaks, so the observed asymmetry is not due to instrumental effects. However, it is difficult to propose a good explanation for the observed differences between the two branches.

While some evidence of differential broadening between the Λ-doublet components was observed for some of the spectra in the current study, the results were not conclusive. Apparent systematic differences were only observed with three of the five noble gas collision partners and the error bars of the two Λ-doublet components overlapped in most cases. The FTS instrument does not really have the resolution to definitively measure such a fine effect. To truly resolve the differential broadening between the Λ-doublet components, one would need to use a narrow-line tunable laser to record several spectra with bath gas pressures less than 80 torr. It is also possible that the effect itself disappears above 80 torr.

One can also observe in Figure 43 that the residuals from the fits are 2-4 times larger in the peaks than in the baseline. This indicates that the fitting function is not correct. Asymmetry appears to have been modeled correctly because there are no observed asymmetric trends in the baseline near the peaks. The DUDV program indicates that the instrument line width and aperture effect are not significant perturbations on the measured lines. A careful look at the resolved tips of the peaks indicates that the data is a little bit narrower than the fit. This apparent non-Lorentzian narrowing may be due to either Dicke narrowing or line coupling between the Λ doublets. Since the large residuals are concentrated between the peaks rather than uniformly on each side of each peak, line coupling is a more likely explanation than Dicke narrowing. The spectrum of Figure 43 has exceptionally good S/N; these subtle deviations in the fit were less pronounced or unobservable in the other spectra.

In addition to line broadening, an attempt was made to measure pressure-induced line shifting in NO but the shifting was not quantifiable. Difficulties included the complex spectroscopy of NO, the change in line position caused by the phase error, and a possible change in the frequency calibration of the spectrometer between data acquired by Cornicelli and data acquired for this study.

4.3.4. Line Broadening and Line Coupling in the Q Branch. In addition to the study of pressure broadening the P and R branches of the NO fundamental, the Q branch was studied in collisions with argon. The object of this part of the experiment was to determine quantitative broadening coefficients for several lines in the Q branch at pressures low enough that the lines were still isolated, then to increase the pressure and show qualitatively that the Q branch exhibits deviations from Lorentzian behavior

characteristic of line coupling. Several NO+Ar spectra have already been acquired for analysis of the P and R branches. Seven of the best spectra were chosen for the Q-branch analysis; these spectra are listed in Appendix B.

Because the lines in the Q branch are so close together, the entire branch must be fit simultaneously. The Peak Fit program is not suited to simultaneous fits of multiple lines with many constraints on the fitting parameters. However, the DUDV program was designed for just such applications, so the DUDV program was used to determine the NO+Ar line widths in each of the seven spectra analyzed. DUDV can simultaneously analyze a maximum of 31 lines. To help select the lines that would be modeled, the HITRAN 96 database [56] was used to generate a plot of the locations and intensities of the first 40 Q-branch lines. This plot is shown in Figure 44.

Several things are apparent from this plot. First, the 3/2 lines are more intense than the 1/2 lines, in contrast to the P and R branches where the 1/2 lines were about twice as intense as the 3/2 lines. Next, the Λ doublets for both magnetic substates are more separated than they were in the P and R branches, and this separation rapidly increases with increasing J. A look at the energy level diagram of the NO fundamental in Figure 6 shows the reason for this increased separation. In each vibrational manifold, the e-parity level of each Λ-doubled rotational level is lower in energy than the f-parity level. P and R branches connect states of equal parity, while the Q-branch transitions connect states of opposite parity. This causes the large and rapidly increasing separation between the Q-branch Λ-doublet peaks. Finally, note that there are several overlaps or near overlaps with lines in the 1/2 and 3/2 substates. Thus, to accurately model some of the intense 3/2 lines, the nearby 1/2

139
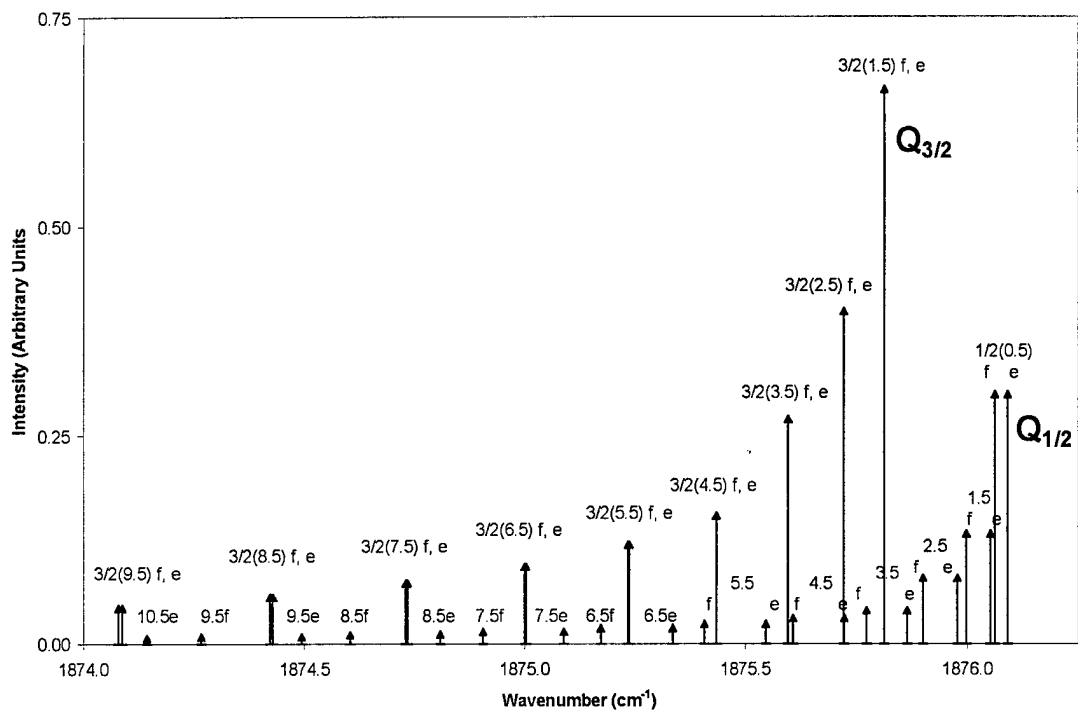
Figure 44. Strengths and Positions of Several Lines in the Q Branch of the NO Fundamental

lines must also be modeled, even if the peaks are not apparent in the spectrum. Based on Figure 44, it was decided to analyze $J'' = 1.5$ to 8.5 in the 3/2 substate and $J'' = 0.5$ to 6.5 in the 1/2 substate. Because each line is Λ-doubled, this is a total of 30 peaks, which is about as many as DUDV can handle in a simultaneous fit.

With three parameters for each line plus three parameters for the instrument effects and three more for the baseline, the potential number of free parameters in the fit is 96. To improve the quality of the results, as many parameters as possible were constrained using literature values for strengths and positions. Using data from the HITRAN database [56] and from Spencer *et al.* [118], the following constraints were imposed:

(1) equal strengths for each Λ-doublet pair,

(2) equal widths for each Λ-doublet pair,

(3) fixed separation between each Λ-doublet pair,

(4) all strengths ratioed to the strength of the $Q_{1/2}(1.5)$ lines,

(5) fixed location of each f-parity peak relative $Q_{3/2}(1.5)$, and

(6) widths of $Q_{1/2}(4.5)$, (5.5), and (6.5) ratioed to $Q_{1/2}(3.5)$ using self-broadened
values from Lempert *et al.* [68] (listed in Appendix A). This approximation helps
account for weak, overlapped lines and minimizes errors in the larger lines
nearby.

In addition to the constraints on the lines, the number of free parameters for the
background and instrument effects were also reduced. For the background, only the
constant and linear terms were used; the quadratic term was set to zero. For the
instrument parameters, the maximum OPD and aperture effect were fixed at calculated
values. The asymmetry was set to zero for two reasons. First, there were little or no
visually-apparent asymmetries in the Q-branch spectra. Second, and of more practical
importance, the run-time and DUDV code would be unacceptably long with the
asymmetry parameter allowed to vary for a spectrum of this complexity. With these
constraints, there are only 16 free parameters in the fit; a significant reduction. The free
parameters include one line position, one line strength, two baseline parameters (slope
and intercept), and 12 line widths.

The next challenge in the Q-branch fits was removal of channel spectra. A
channel spectrum is a sinusoidal oscillation in the baseline caused by etalon effects due to

surface reflections in the spectrometer. To remove the channel spectrum, it must be characterized so it can be mathematically subtracted. To characterize the channel spectrum, a section of the oscillating baseline was fit using the function

$$y = a + b\sin[c(x+d)] \tag{73}$$

where a is a linear offset from zero, b is the amplitude of the channel spectrum sine wave, c is the wavelength of the sine wave, and d is a phase factor. After fitting the channel spectrum, it was subtracted from the spectrum of the Q branch. A Q-branch spectrum before and after removal of the channel spectrum is shown in Figure 45.

With the channel spectrum removed and the constraints implemented, each Q-branch spectrum was fit using DUDV. A typical low-pressure fit to the NO+Ar Q branch is shown in Figure 46. After each of the seven NO+Ar spectra were fit using DUDV, the effects of self-broadening were subtracted from the measured widths using the self-broadening coefficients of Lempert *et al.* [68] (listed in Appendix A). A linear least-squares fit with a zero intercept was then performed to the width vs. pressure data as for all previous pressure broadening determinations. One of these fits is shown in Figure 47. The resulting broadening coefficients are listed in Table 15 and graphed vs. J in Figure 48.
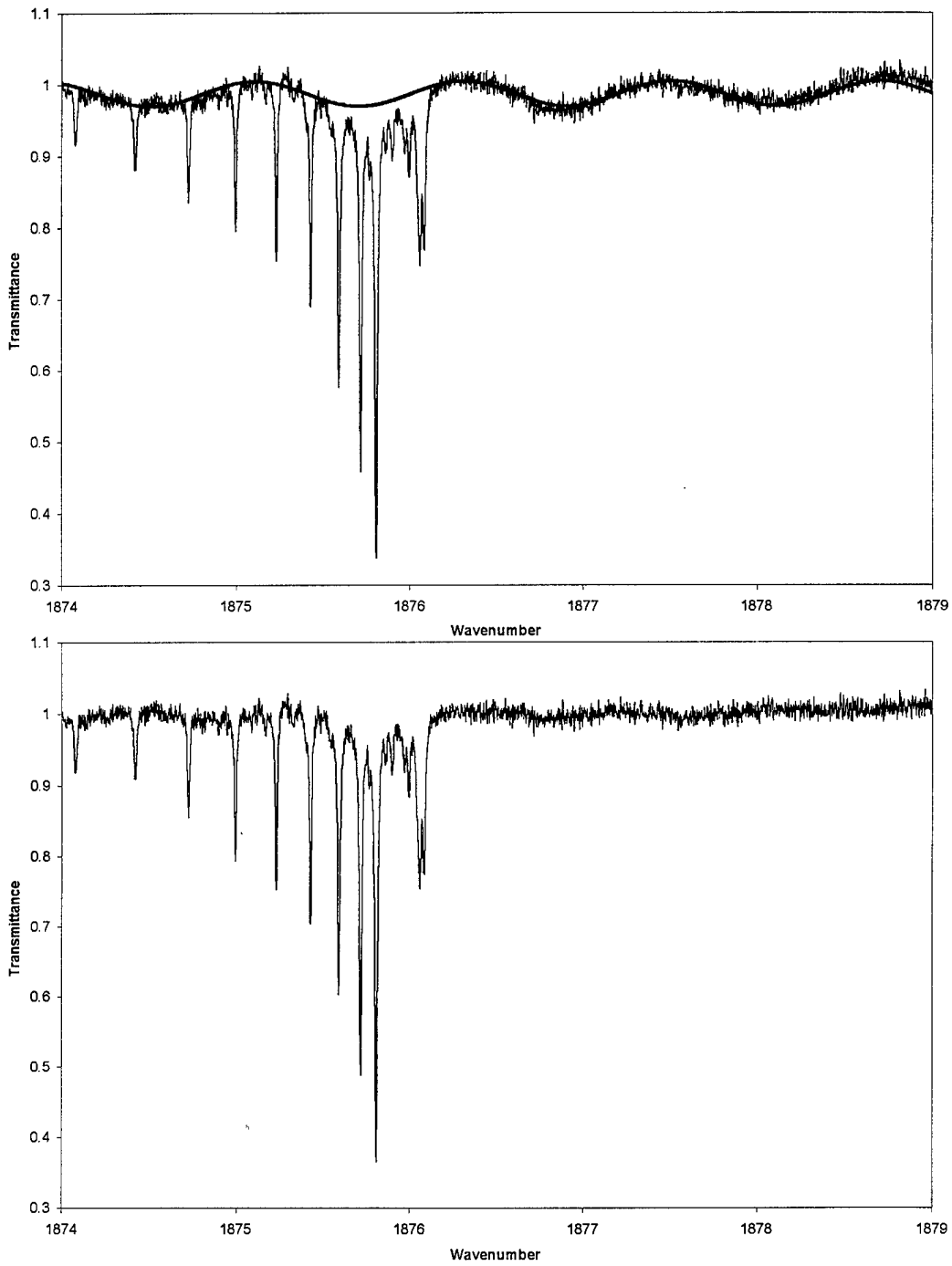
Figure 45. The Q Branch of the NO Fundamental Before and After Mathematical Subtraction of Channel Spectrum; Upper Trace Shows the Fit to the Channel Spectrum
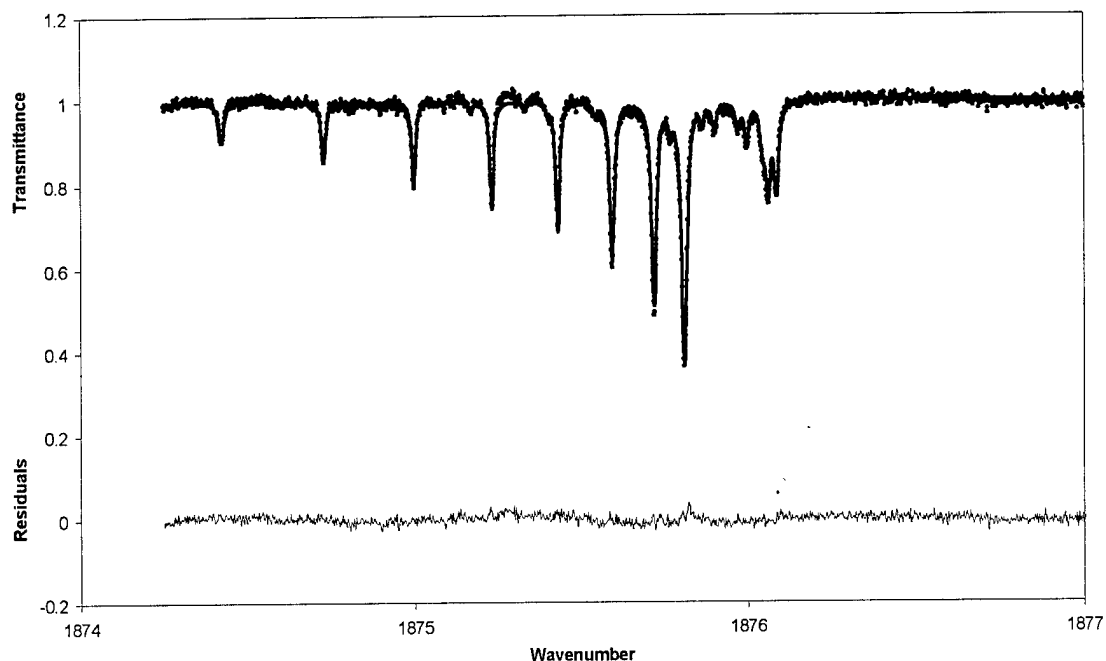
Figure 46. DUDV Simultaneous Fit to 30 Lines in the Q Branch of the NO Fundamental; this Spectrum is 2.5 Torr NO Broadened with 75 Torr Ar
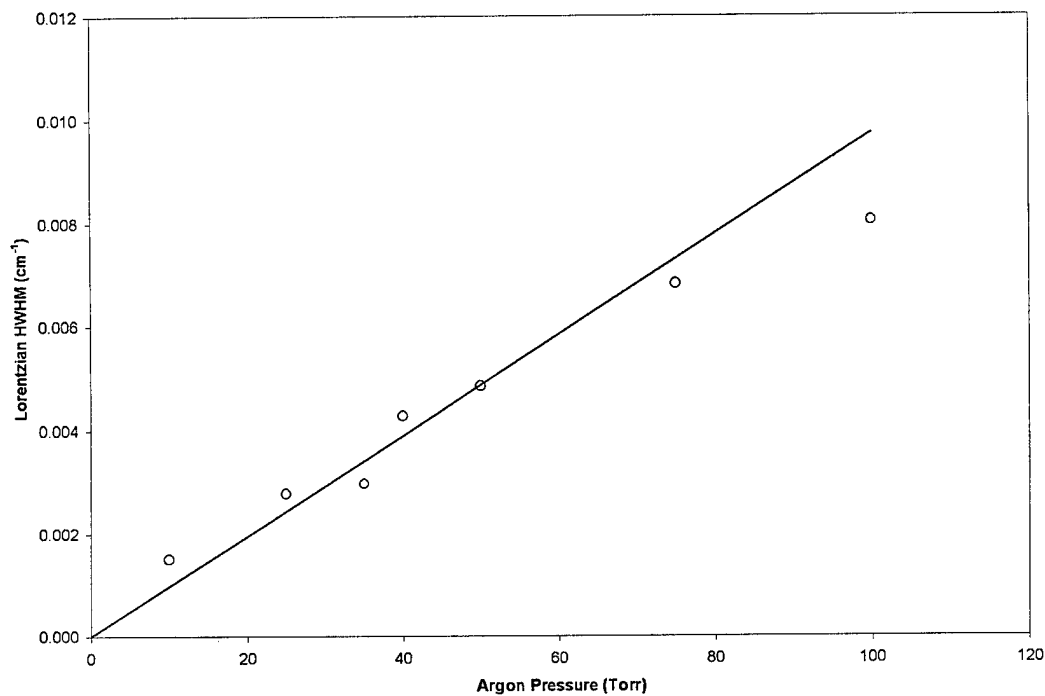
Figure 47. Linear Least-Squares Fit to the Widths $Q_{3/2}(1.5)$ Lines as a Function of Argon Pressure for the NO Fundamental Band (1-σ error bars are smaller than the data points)

144

Table 15. Broadening Coefficients for the Q Branch of the Nitric Oxide Fundamental Band for Collisions with Argon (coefficients are $\times 10^{-5}$ cm^{-1}/torr)

J	Broadening Coefficient, $\Omega = 1/2$	Broadening Coefficient, $\Omega = 3/2$
0.5	10.4(5)	
1.5	9.5(2)	9.7(6)
2.5	9.1(2)	8.6(4)
3.5	8.0(7)	8.3(3)
4.5	8.0(7)	7.65(19)
5.5	7.8(7)	7.1(2)
6.5	7.6(7)	7.4(4)
7.5		7.4(4)
8.5		7.6(5)
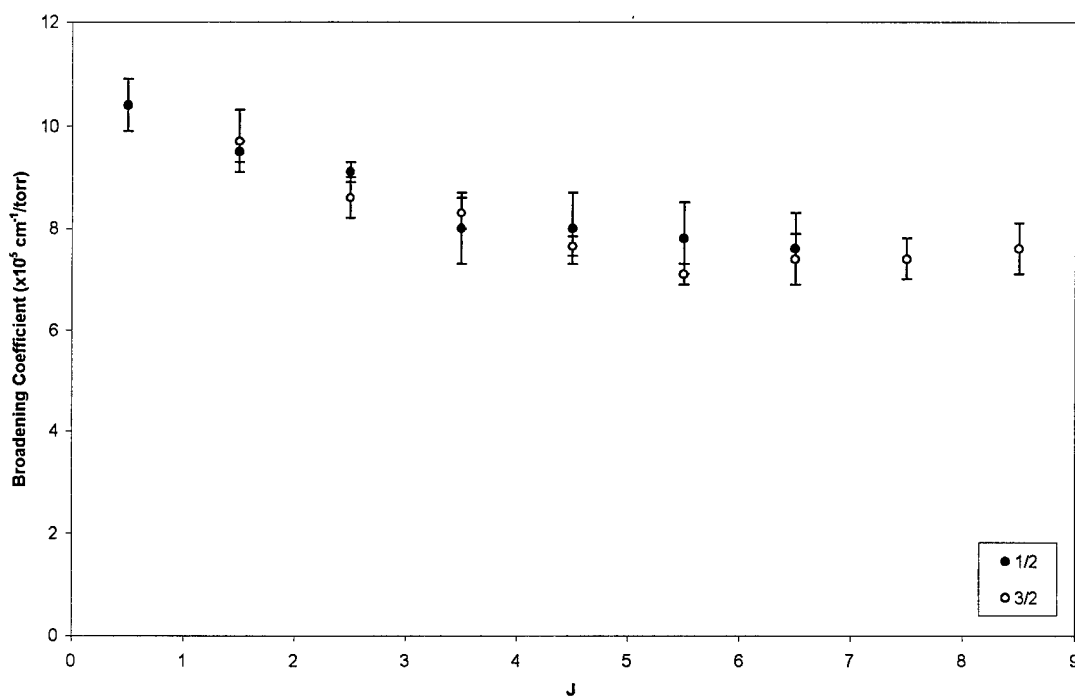
Figure 48. NO+Ar Q-Branch Broadening Coefficients vs. J

The broadening coefficients in the Q branch show a decrease with increasing J, just as for the P and R branches. There is no discernible differential broadening between

145

the magnetic substates. As stated previously, the widths of the $J = 4.5$, 5.5, and 6.5 lines in the 1/2 subband were fixed relative to the width of the $J = 3.5$ line, with the ratios between the widths set according to the ratios between the self-broadened widths reported by Lempert et al. [68]. Thus the broadening coefficients for the $J = 3.5$ to 6.5 lines in the 1/2 subband have not been independently determined in the current study but are fixed to ratios determined by previous researchers.

With the NO+Ar broadening coefficients determined for the Q branch, a high-pressure spectrum could be acquired to look for deviations from sum-of-Lorentzians behavior characteristic of line coupling. Because high pressures were required for this part of the experiment, the 10-cm long glass cell with CaF_2 windows glued to each end was no longer appropriate. Instead, a 10-cm long stainless steel cell with 4-mm thick ZnSe windows clamped to each end was used. This new cell was rated to a maximum pressure of 2800 torr (3.7 atmospheres). The other spectrometer components were the same as for my previous NO measurements.

The spectrum acquired for the line coupling study consisted of 40 torr NO with 860 torr Ar. The run was 100 co-adds at 0.005 cm^{-1} resolution using the band-pass filter centered at 1840 cm^{-1}. Additional spectra were acquired at higher pressures, up to 2800 torr total cell pressure, but scans above 900 torr total cell pressure had no resolved features in the Q branch. This made the analysis much more difficult so results from these higher-pressure spectra will not be reported.

Because of the large peak widths in the 900 torr spectrum, there were no baseline regions in the spectrum suitable for identifying and analyzing any channel spectra which were present. Thus, any channel spectra which may be present have not been removed.

146

Also, because the baseline is difficult to find in this spectrum, the best way to properly set the baseline in the fit was to use a weighted average of the baseline parameters from the four other Q-branch spectra taken with the same instrument setup (same filter, detector, scan parameters, etc.).

Next, since line coupling is manifested as deviations from Lorentzian broadening, the values of the peak widths were locked to values calculated from the pressure broadening coefficients determined at lower pressures. With the baseline and width parameters constrained as described (and the other constraints as described for the pressure broadening work) there were only 2 remaining free parameters in this fit, the strength and position of the $Q_{3/2}(1.5)$ line. Both Voigt and Lorentzian lineshapes were tried but there was no difference in the results. At high pressure, one expects Dicke narrowing to have reduced the Doppler width to nearly zero, leaving the line almost entirely Lorentzian. However, even without considering Dicke narrowing, the Lorentzian HWHM is much, much larger than the Doppler width at high pressures, making the Doppler portion insignificant to the fit. The fit to the Q branch at 900 torr total pressure is shown in Figure 49.

Two features in Figure 49 are very characteristic of line coupling in a Q branch. The first is the narrowing of the Q branch at the bandhead, shown at the right of the figure where the data returns to 100% transmittance faster than the sum-of-Lorentzians fit. The second indicative feature is the deviation between the 1/2 and 3/2 substates, near 1876 cm^{-1}. There is less absorption in the data than modeled by the sum-of-Lorentzians fit, indicating that the $Q_{1/2}$ lines are collapsing into a single feature near 1876.1 cm^{-1},

147
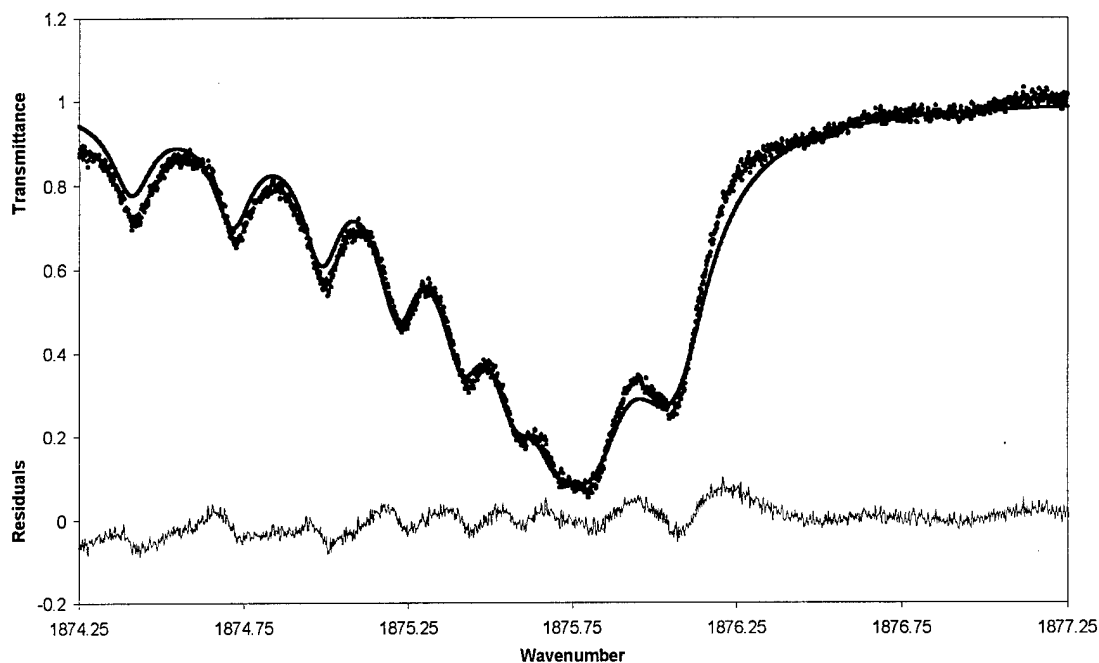
Figure 49. DUDV Fit to the Q Branch of the NO Fundamental at 900 Torr Total Pressure Showing Deviations from Lorentzian Behavior Characteristic of Line Coupling

while the $Q_{3/2}$ lines are collapsing into a feature near 1875.75 cm^{-1}, leaving a gap in between. There are several other minor deviations from Lorentzian behavior toward higher J, which are best indicated in the residuals. The quality of the fit deteriorates at the left where contributions from higher-J lines not included in the fit start to become significant. Previous evidence of line coupling in the Q branch of the NO fundamental has been reported only for self-broadening measured by Raman spectroscopy [68]. The results of the current study thus represent three "firsts": this is the first line coupling result in NO reported by infrared spectroscopy, it is the first result reported in NO using FTS, and it is the first foreign-broadened line coupling result in NO.

As a final experiment, cell pressures were raised to values as high as 2800 torr to look for evidence of line coupling in the P branch, but deviations from sum-of-Lorentzians behavior characteristic of line coupling were not conclusively observed. Any line coupling behavior in the P and R branches must be observed at pressures greater than 2800 torr.

V. Analysis and Interpretation

A large number of pressure-broadening coefficients were reported in the previous chapter. Coefficients were reported for several initial rotational states of two different diatomic molecules perturbed by a wide range of collision partners. In this chapter, two different pressure-broadening theories will be applied to this large body of experimental data to see to what extent the laboratory observations are consistent with the theoretical descriptions. The first theoretical model assumes that all broadening collisions are elastic, while the second model assumes all broadening collisions are rotationally inelastic. The elastic-collision model used in this chapter is Weisskopf's theory, which was presented in Chapter II. The inelastic-collision description of pressure broadening is explored by applying several semi-empirical, rotationally-inelastic fitting laws to the O_2 broadening data. These fitting laws were also described in Chapter II. Finally, the experimentally-determined O_2+noble-gas broadening data is used to explore the state-to-state, angular-momentum-based, inelastic-collision model of Osborne and McCaffery [86] (also presented in Chapter II).

5.1. Pressure Broadening Cross Sections vs. $|m|$

The first step in the physical interpretation of the broadening data is the conversion of this data from broadening coefficients vs. J to broadening cross sections vs. $|m|$. There are several advantages to this conversion. The conversion from J to $|m|$ averages two data points for most values of $|m|$, which produces a data set with less variability and smaller error bars. The conversion from coefficient to cross section is

$$\sigma = \frac{\gamma\, kT}{\langle v \rangle} \tag{74}$$

where $\langle v \rangle$ is the relative velocity of the two collision partners. The conversion to cross section thus corrects the data for different perturbers for their different relative velocities, allowing the exploration of other parameters which may influence broadening.

For NO, the conversion from J'' to $|m|$ is straightforward: $m = -J''$ for the P branch and $m = J'' + 1$ for the R branch. Thus two values, one from each branch, are averaged for each $|m|$. The conversion is a little bit different for O_2. The rotational quantum number without spin, K'', determines the energy level spacing. Thus $m = -K''$ for the P branch and $m = K'' + 1$ for the R branch. There are two values of J'', angular momentum with spin, for each K'', so two broadening coefficients vs. J'' are averaged for each m. Additionally, since only odd values of K'' produce allowed transitions, the P branch produces only odd values of $|m|$, while the R branch produces only even values of $|m|$.

Before "folding" the P- and R-branch data into a single set of data vs. $|m|$, the data was studied for any evidence of differences in the broadening coefficients between the P and R branches. Using the $|m|$ parameter, the self-broadening coefficients for the oxygen A band were plotted. This plot is shown in Figure 50. The $|m|$ convention appears reasonable – the P-branch (odd $|m|$) and R-branch (even $|m|$) values interleave nicely with no apparent systematic differences to within experimental uncertainties. Also, the values with non-zero electron spin (^{P}Q and ^{R}Q) are not systematically different from the values

without spin (^{P}P and ^{R}R) for the same $|m|$. This indicates that the broadening mechanism is not appreciably effected by the spin of the electrons.
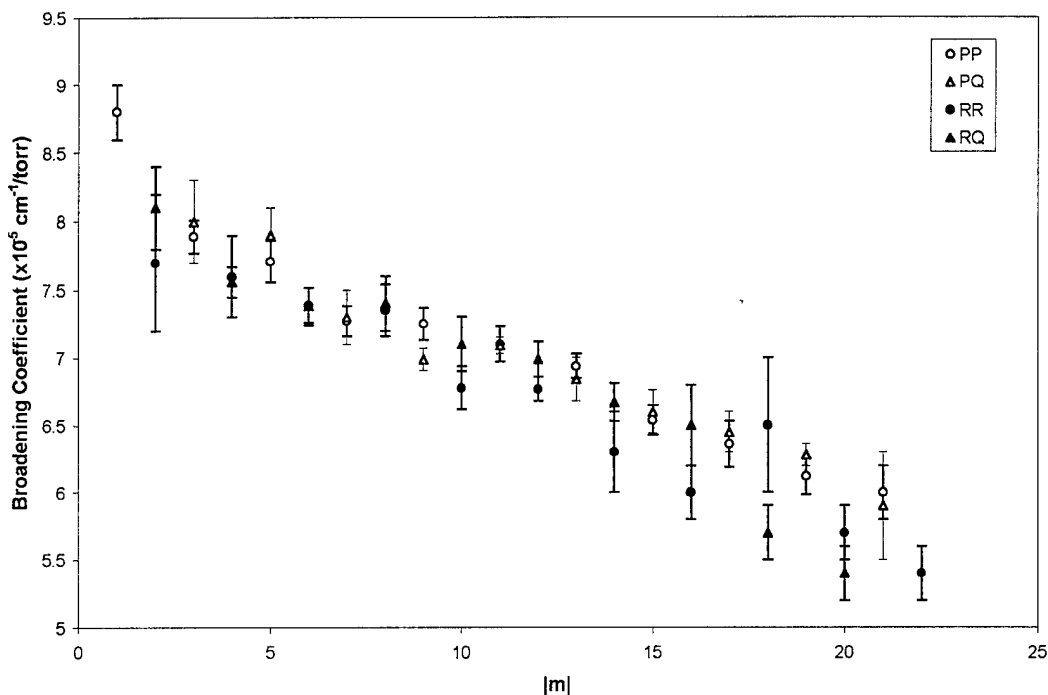
Figure 50. Oxygen A-Band Self-Broadening Coefficients vs. $|m|$

The same check was performed with NO broadened with argon, averaging the observed differential broadening between the 1/2 Λ doublets in the P branch for clarity. This plot is shown in Figure 51. As with the oxygen data, there appears to be no systematic differences between the P- and R-branch data to within experimental uncertainties, so the $|m|$ convention again appears reasonable.

Before applying the elastic and inelastic collision models, a look at the cross sections and some of the physical parameters of the collision partners provides some insight into the broadening mechanism. The O_2 and NO broadening cross sections,

152
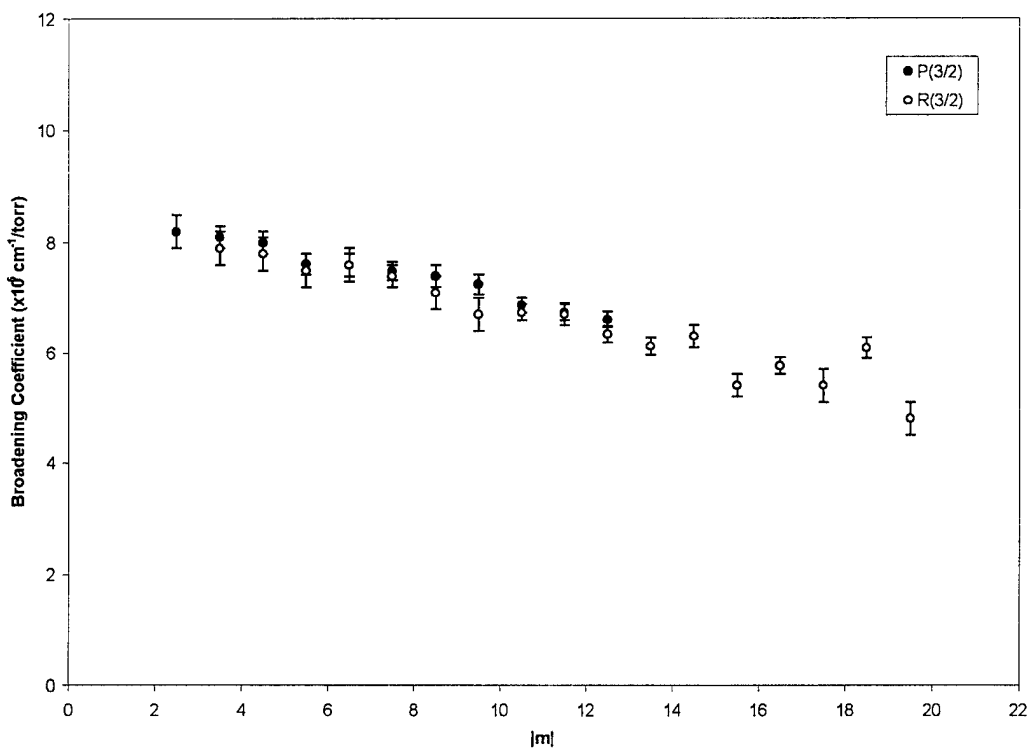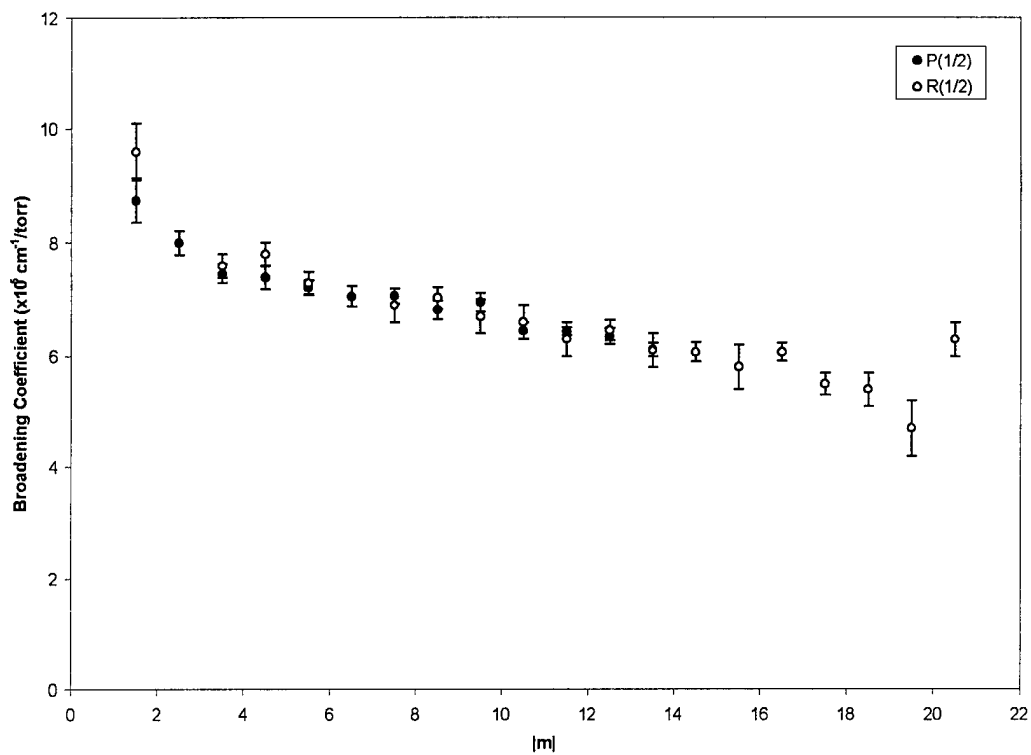
Figure 51. NO+Ar Broadening Coefficients vs. |m|

calculated from the broadening coefficients reported in the previous chapter, are graphed in Figures 52 to 55. The cross sections are tabulated vs. $|m|$ in Appendix D.
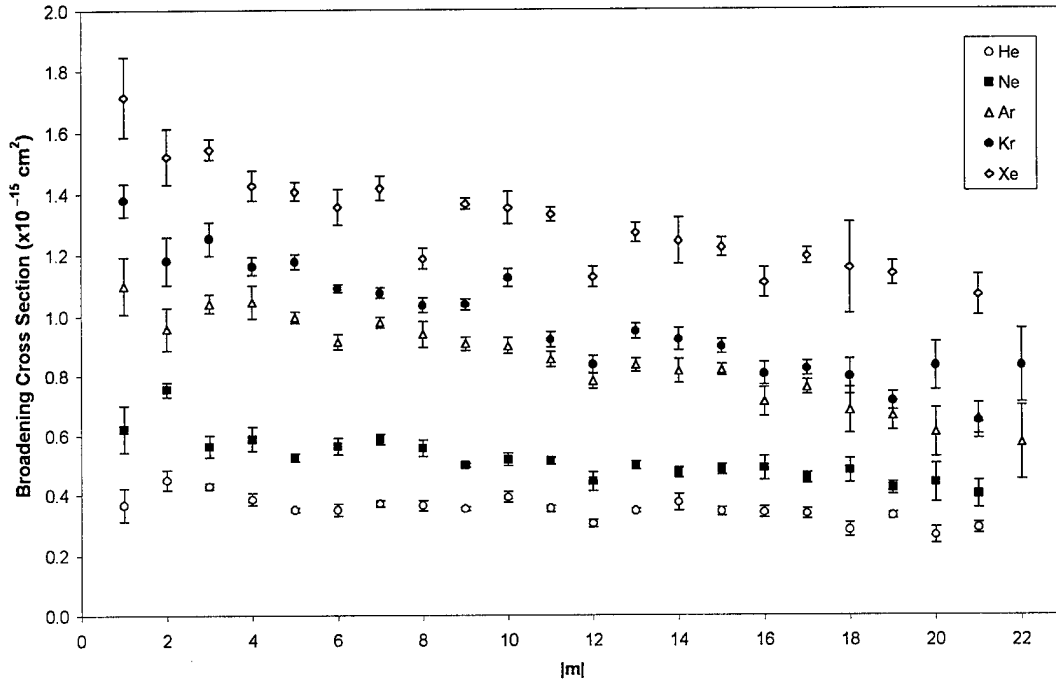
Figure 52. O_2+Noble Gas Broadening Cross Sections
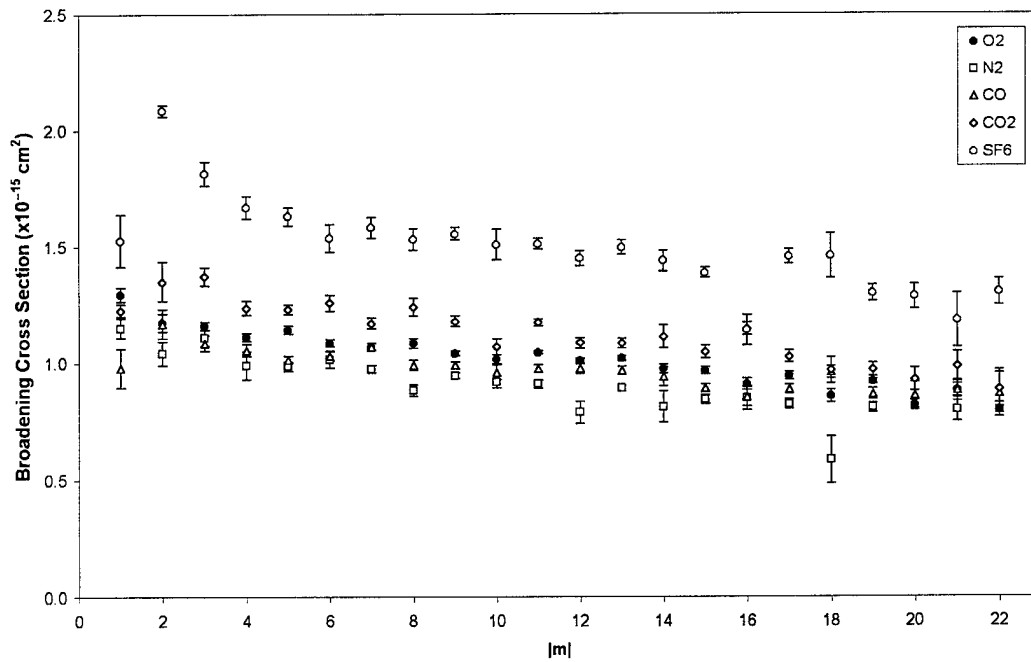
Figure 53. O_2+Molecule Broadening Cross Sections

154
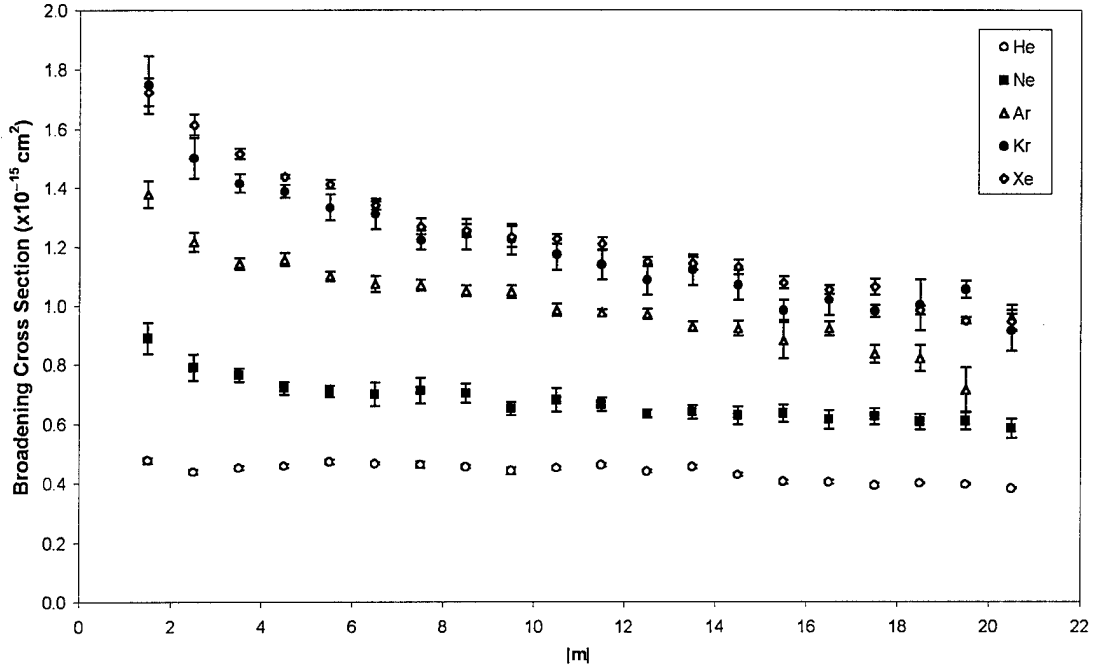
Figure 54. NO+Noble Gas Broadening Cross Sections, $\Omega = 1/2$ Magnetic Substate
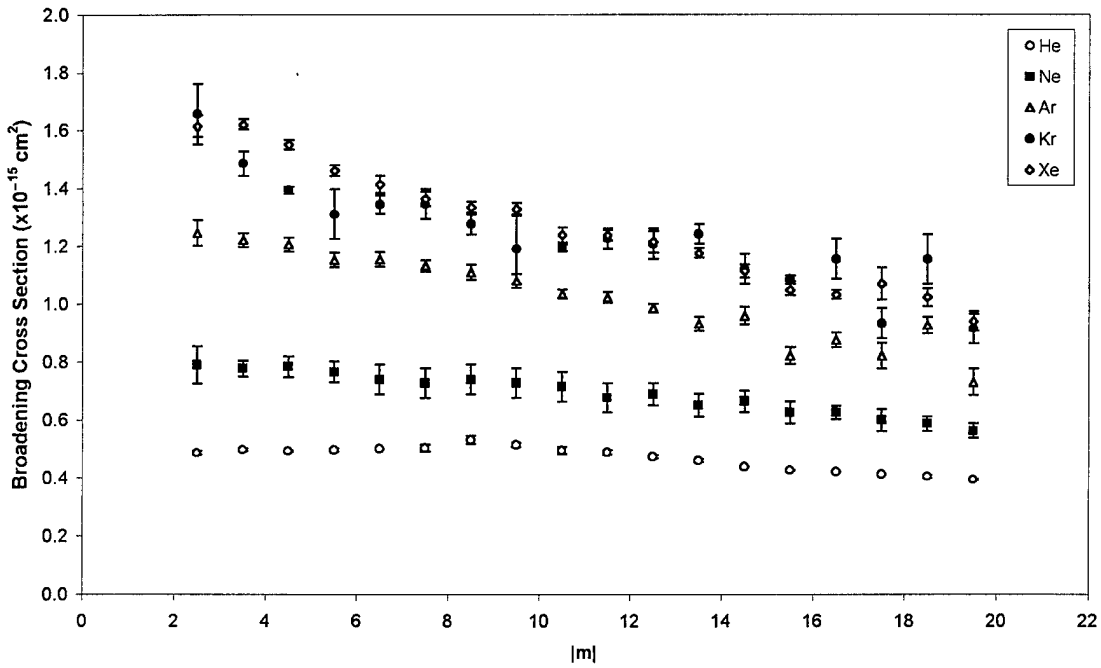
Figure 55. NO+Noble Gas Broadening Cross Sections, $\Omega = 3/2$ Magnetic Substate

155

The O_2+noble gas broadening cross sections are smallest for helium and largest for xenon, with the other three noble gases falling in between in the order they appear on the periodic table. Pressure broadening in the O_2 A band thus clearly depends on one or more physical properties of the perturbing species. Parameters which appear in the broadening theories include perturber mass, permanent electric multipole moments, and the ability of the perturber to be polarized in an electric field ("polarizability"). The noble gas atoms have no permanent electric multipole moments, so the only significant parameters are the masses and polarizabilities. These parameters are listed in Table 16.

Table 16. Physical Parameters of the Noble Gases

Noble Gas	Mass (amu) [90]	Polarizability (Å^3) [130]
He	4.00260	0.204956
Ne	20.179	0.3956
Ar	39.948	1.6411
Kr	83.80	2.4844
Xe	131.30	4.044

In the O_2+molecules broadening cross section plot, SF_6 clearly broadens O_2 more than the other molecular collision partners. The other four molecules, listed in order of increasing broadening effectiveness, are N_2, CO, O_2, and CO_2. The molecular perturbers possess internal rotational and vibrational structure and electric multipole moments in addition to the parameters which characterize the noble gases. The physical parameters of these five molecules are listed in Table 17.

Table 17. Physical Parameters of the Five Molecules Used in the O_2 Pressure Broadening Experiments (Molecules Listed in Order of Increasing Broadening Cross Section)

Molecule	Mass (amu) [90]	Polarizability (Å^3) [130]	Dipole Moment ($\times 10^{-18}$ esu cm) [130]	Quadrupole Moment ($\times 10^{-26}$ esu cm^2)
N_2	28.0134	1.7403	–	1.4 [127]
CO	28.0104	1.95	0.112	2.84 [46]
O_2	31.9988	1.5812	–	0.4 [127]
CO_2	44.0098	2.911	–	4.48 [59]
SF_6	146.0504	6.54	–	–

Only one of the five molecular collision partners, CO, has a non-zero dipole moment, while all but SF_6 have non-zero quadrupole moments. SF_6 has no non-zero multipole moments below the hexadecapolar term [59]. However, the presence of the dipole moment in CO does not seem especially significant, since the O_2+CO broadening cross sections are not much different from the O_2+N_2 and O_2+O_2 cross sections, in which no electric dipole moments are involved.

The O_2+SF_6 cross sections are the largest of all, even though SF_6 has no low-order multipole moments. The primary differences between SF_6 and the other collision partners are the very large values of mass and polarizability. Looking at the oxygen A band broadened with all ten collision partners, mass and polarizability of the perturber appear to be the two physical parameters which change the magnitude of the broadening cross section for different collision partners. The permanent electric multipole moments and internal structure of the molecular perturbers does not appear to be very significant to the broadening mechanism.

Now let's look at the NO fundamental band broadened by the noble gases to see what additional insights may be gained. The NO broadening cross sections increase with increasing mass of the noble gas atom, just as for pressure broadening in oxygen. Two interesting features are observed in Figures 54 and 55. First, xenon does not broaden NO substantially more than krypton, in contrast with the O_2 cross sections where there was a noticeable difference. Second, the NO+He trend vs. $|m|$ differs from every other collision pair studied in this research project. Instead of decreasing uniformly with increasing $|m|$, the NO+He broadening cross sections remain approximately constant at low $|m|$, then decrease with increasing $|m|$ above $|m| = 7.5$.

The differences between O_2 and NO broadened with the noble gases further helps us to understand the broadening mechanisms involved. These cross sections are compared in Table 18.

Table 18. O_2+Noble Gas and NO+Noble Gas Broadening Cross Sections Compared

Noble Gas	Comparisons (%)	
	$NO_{1/2} - O_2$	$NO_{3/2} - O_2$
He	+24	+32
Ne	+30	+32
Ar	+17	+18
Kr	+20	+24
Xe	−6.2	−4.0

With the exception of xenon, the noble gases broaden NO an average of 25% more than O_2. The slope of the broadening cross section vs. $|m|$ plot is approximately equal for O_2 and NO broadened with the same noble gas, with the NO trend just a bit steeper. This is shown in the argon broadening data in Figure 56.

158
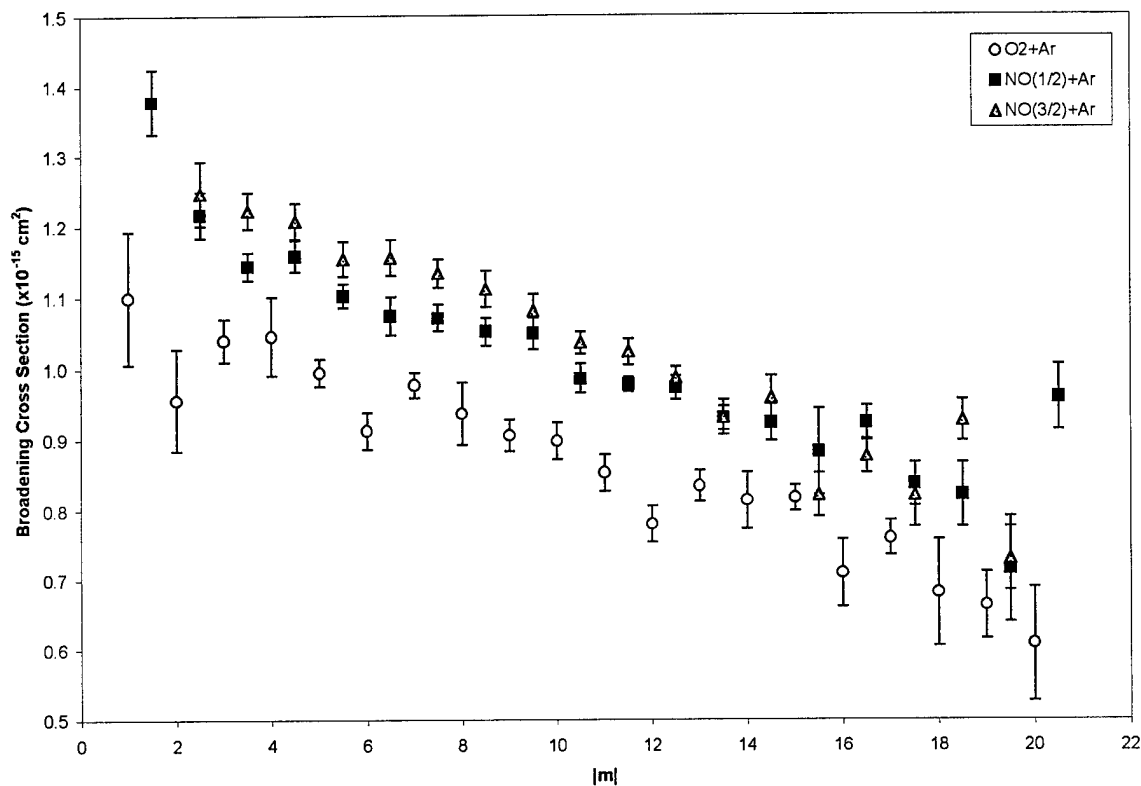
Figure 56. Graphical Comparison of O_2 and NO Broadened with Argon

The differences between the O_2 and NO noble gas broadening coefficients should be explicable by one or more physical properties of the two molecules. Several physical properties of O_2 and NO are listed in Table 19. The most significant difference is that NO possesses a non-zero electric dipole moment and a large electric quadrupole moment compared to O_2. This makes the intermolecular potentials for NO stronger than the corresponding potentials for O_2 and is likely the primary reason for the larger NO broadening cross sections. NO has larger rotational constants than O_2, meaning that adjacent rotational energy levels are further apart for NO than for O_2. The slightly steeper drop-off of the broadening cross sections with $|m|$ for NO is probably due to the

159

larger rotational constants, since the increasing separation at high rotational quantum numbers would tend to inhibit rotational transfer out of the higher rotational levels. In general, the decrease in broadening cross section with increasing rotational quantum number is caused by the increased spacing between rotational levels as J increases. The increased spacing between levels results in a smaller probability of inelastic RT transfer out of that J level. The reduced probability of inelastic RT transfer reduces the broadening cross section, indicating that the inelastic mechanism is an important factor in pressure broadening in molecules.

Table 19. Comparison of Several Physical Parameters of O_2 and NO

	O_2 A Band	NO Fundamental Band
mass (amu)	31.9988 [90]	30.0061 [90]
radius (Å)	1.75 [54]	1.75 [54]
polarizability (Å^3)	1.5812 [130]	1.74 [127]
dipole moment ($\times 10^{-18}$ esu cm)	–	0.159 [127]
quadrupole moment ($\times 10^{-26}$ esu cm^2)	0.4 [127]	2.4 [127]
photon transition	electronic	vibrational
lower state rotational constant, B'' (cm^{-1})	1.44566 [52]	1.6961359 [92]
upper state rotational constant, B' (cm^{-1})	1.40041 [52]	1.6785671 [92]

5.2. Application of Classical Elastic Theory to O_2 Broadening Cross Sections

The next step in interpreting the O_2 and NO broadening cross section data is to apply existing physical models to the data. I will first use the elastic broadening model, which was discussed in Chapter II. The key relationship from the theory is Equation (16), which relates the broadening cross section to the multipole moment or polarizability of the perturber, the reduced mass of the collision pair, and the order of the intermolecular potential. Based on the observations in Section 5.1, the polarizability of the perturber appears to be more significant than any non-zero multipole moments. Thus, for this application the elastic broadening theory, polarizability will be used to characterize each perturber and any non-zero multipole moments will be neglected. In this case, Equation (16) becomes

$$\sigma_b = C\alpha_B^{\left(\frac{2}{n-1}\right)}\mu^{\left(\frac{1}{n-1}\right)} \tag{75}$$

where σ_b is the broadening cross section, α_B is the polarizability of the perturber, μ is the reduced mass of the collision pair, n is the order of the r^{-n} intermolecular potential, and C is a collection of constants which depends only on the absorbing molecule and is independent of the perturber.

To apply the classical model of Weisskopf to the data from this research project, a three-dimensional non-linear least squares software routine was used to fit the broadening cross sections, plotted simultaneously vs. both polarizability and reduced mass, with C and n as the variable parameters of the fit. Because Weisskopf's model was derived for

161

atomic broadening, it has no provisions to describe the effect of molecular rotation. Thus, a separate fit had to be generated for each $|m|$. Four sets of fits were generated: one for oxygen with all ten perturber gases, a second for oxygen with just the five noble gases, a third for the 1/2 substate of NO with the noble gases, and a fourth for 3/2 substate of NO with the noble gases. A 3-D plot of a typical oxygen data set is shown in Figure 57. The figure clearly shows the simultaneous trends with reduced mass and polarizability.
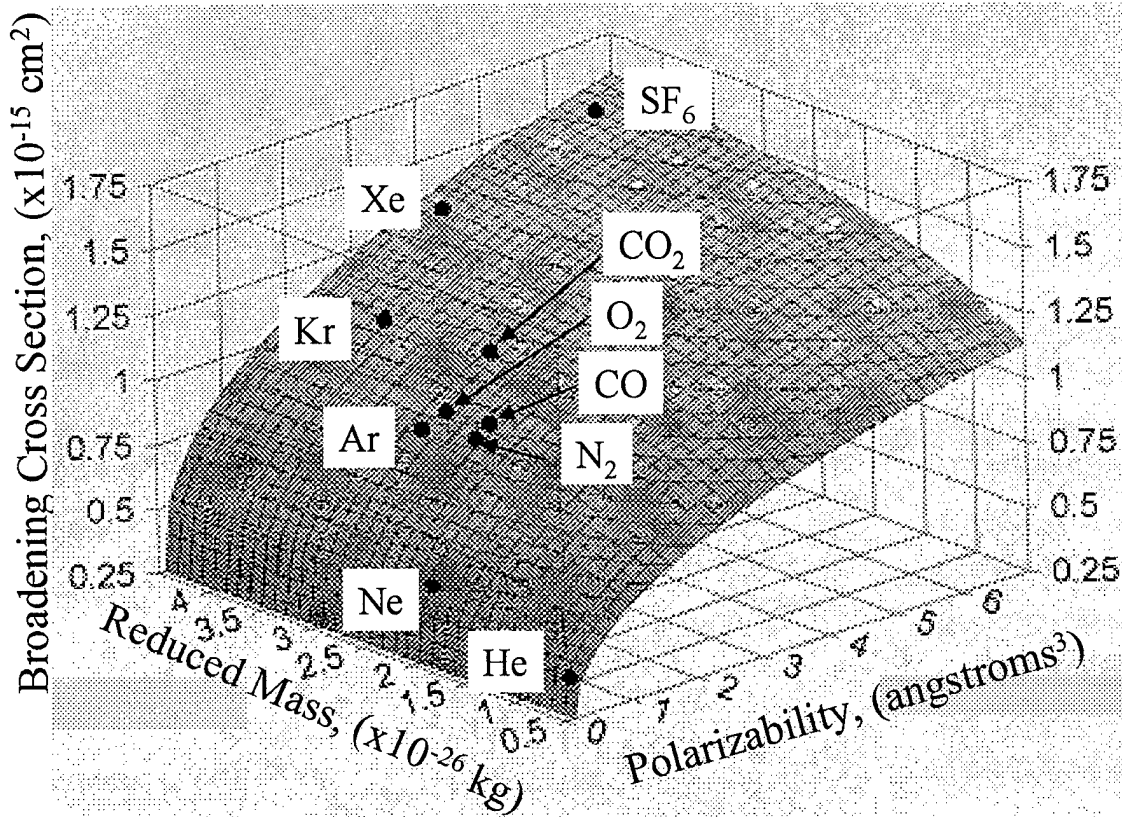
Figure 57. A 3-D Plot of the O_2 Broadening Cross Sections vs. Polarizability of the Perturber and Reduced Mass of the Collision Pair; This Plot is $|m| = 10$

The 3-D fits to these data sets using Equation (74) produced surfaces with power-law behavior. Deviations of individual data points from the calculated fits were generally less than 10%. The overall quality of the fits was very good; most had an r^2 correlation coefficient value of greater than 0.9, where a value of 1.0 indicates a perfect fit. The non-linear least squares fits returned values, with associated uncertainties, for the two free parameters n and C. Plots of n and C vs. $|m|$ for oxygen broadened with all ten collisions partners are shown in Figure 58.

The value of the fit parameter n appears to be independent of J and has an average value of 7.11 ± 0.12. Since n is supposed to indicate the order of the intermolecular potential, this value indicates an r^{-7} potential, which is the order of a quadrupole-induced dipole potential. Since O_2 has no permanent dipole moment, but does have a permanent quadrupole moment, it is reasonable to expect the O_2 quadrupole moment to interact via the polarizability of the perturber species to induce a dipole in the perturber. Thus, this value of n makes physical sense.

The value of the fit parameter C starts around 0.9 at low J and decreases about 40% by $J = 22$. The shape is very similar to the J-dependence of the cross sections, indicating that the J-dependence is showing up in C, even though the elastic broadening theory has no J-dependence built into it. The important observation from this application of Weisskopf's theory is that an elastic theory based only on the mass and polarizability of the perturbers correctly indicates the order of the intermolecular potential. At the very least, this shows that molecular pressure broadening cross sections follow a power-law behavior with respect to the mass and polarizability of the perturbers.
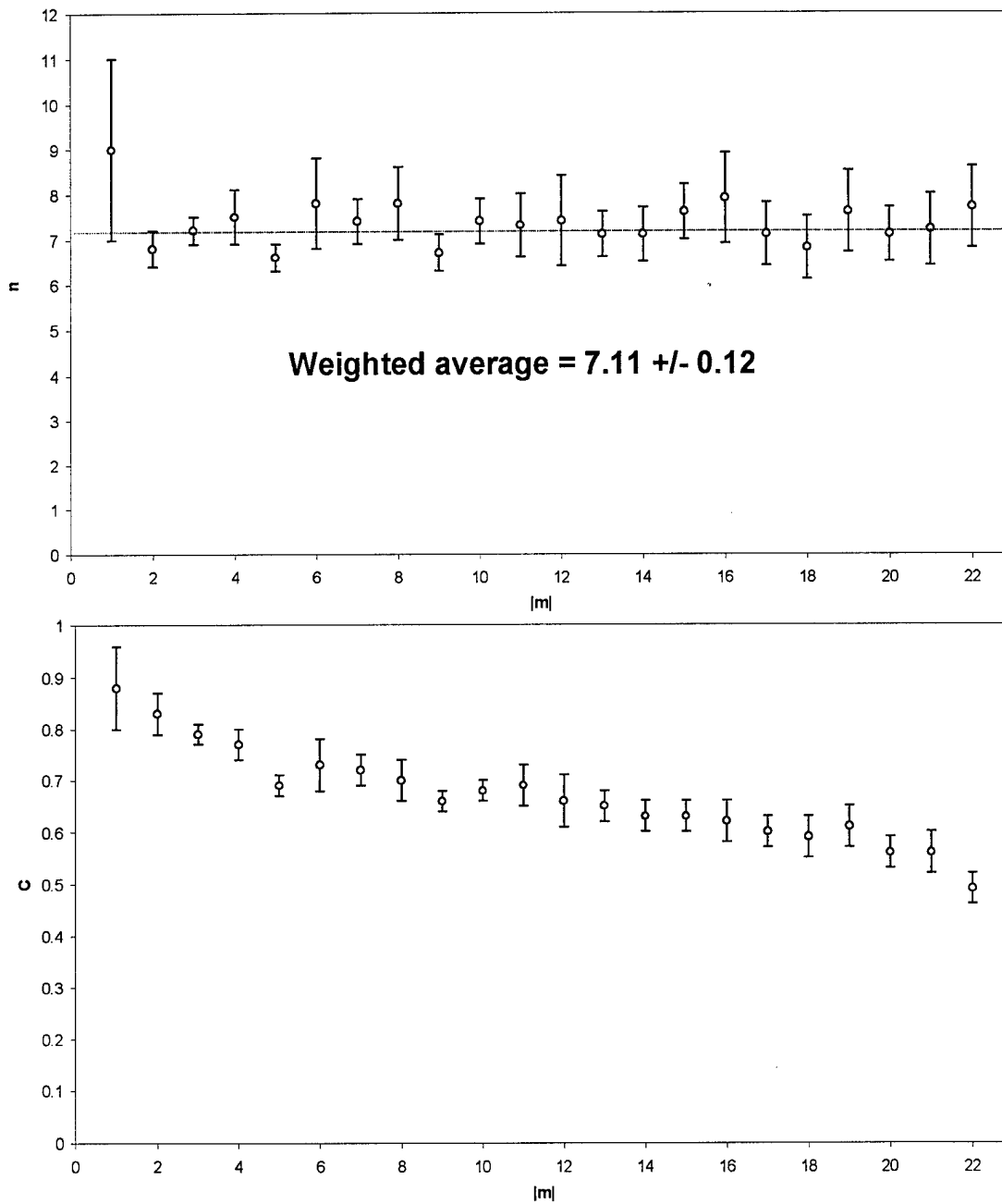
Figure 58. Fit Parameters n and C from the Classical Elastic Broadening Theory for O_2
Broadened with Ten Different Collision Partners

The classical elastic theory was also applied to oxygen broadened with just the noble gases to see if the noble gas and molecular broadeners behaved any differently. Plots of n and C for this case are shown in Figure 59.
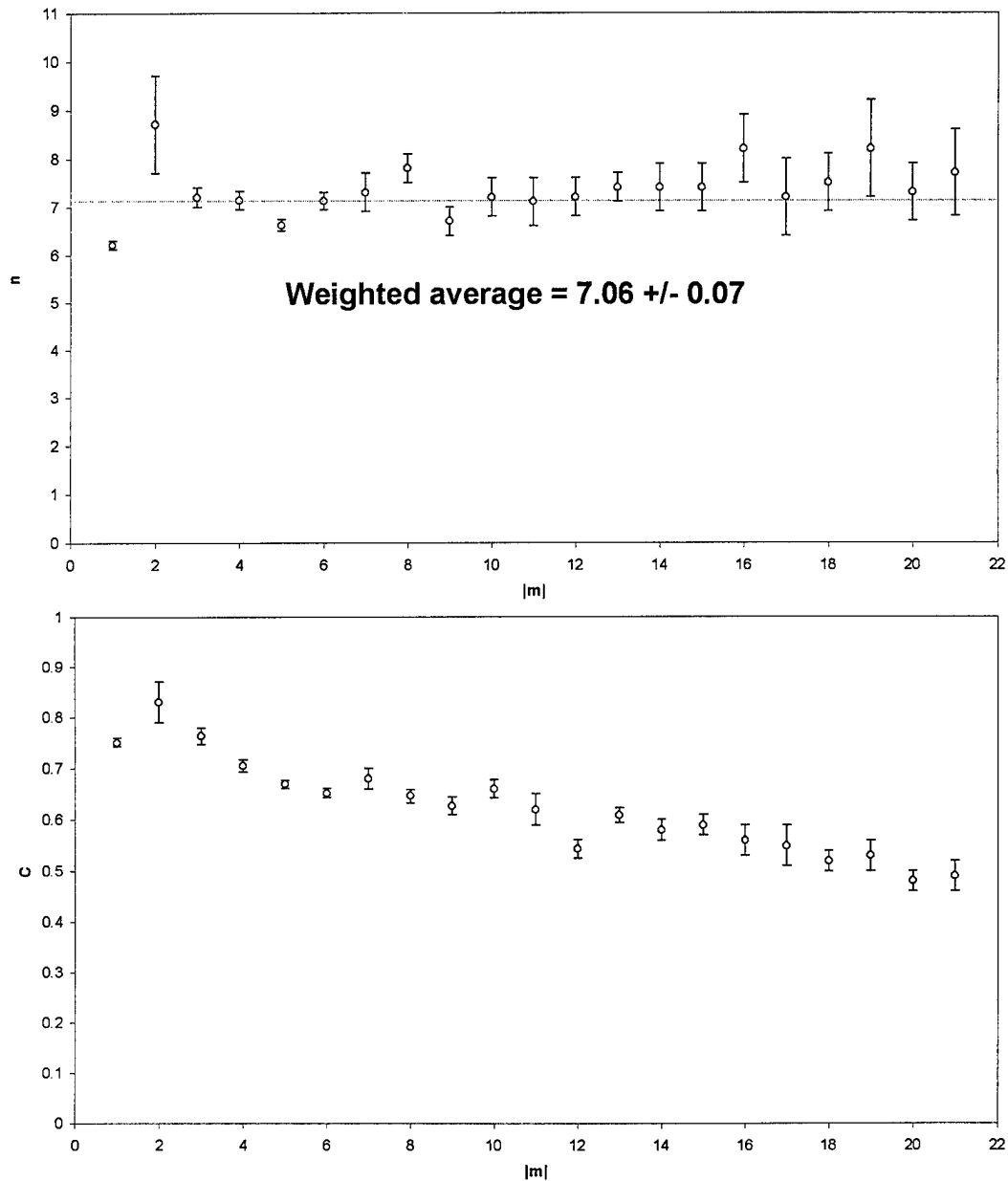
Figure 59. Fit Parameters n and C from the Classical Elastic Broadening Theory for O_2 Broadened with Five Noble Gases

The trends from the fit to just the noble gas broadeners are the same as the trends from the fits to the five noble gases plus five molecular gases. The n parameter still appears reasonably constant with J and has an average value of 7.06 ± 0.07, which is again consistent with an r^{-7} potential. The degree-of-fit indicator is slightly better, with most fits having $r^2 > 0.95$.

Next, the classical broadening theory was applied to the NO broadening cross sections. Values of the two fit parameters are graphed in Figure 60 for the 1/2 substate and in Figure 61 for the 3/2 substate. The average degree-of-fit values for the 1/2 and 3/2 substates of NO are both generally greater than 0.98, which indicates very high quality fits. Figures 60 and 61 show that the fitting parameter C again decreases with increasing J. However the n parameter also appears to be J-dependent for the NO fundamental band. For both magnetic substates, n starts near 7.0 for low J and then rises to values as high as 10 or 11 at $J'' = 20.5$. Since NO has a permanent dipole moment, one might expect the intermolecular potential between NO and the noble gases to be a dipole-induced dipole, which is an r^{-6} potential. However, Hirschfelder *et al.* [54] indicate that the quadrupole moment is the more important term in pressure broadening, which would lead to an r^{-7} intermolecular potential. This is consistent with the observed values of n only for low J.
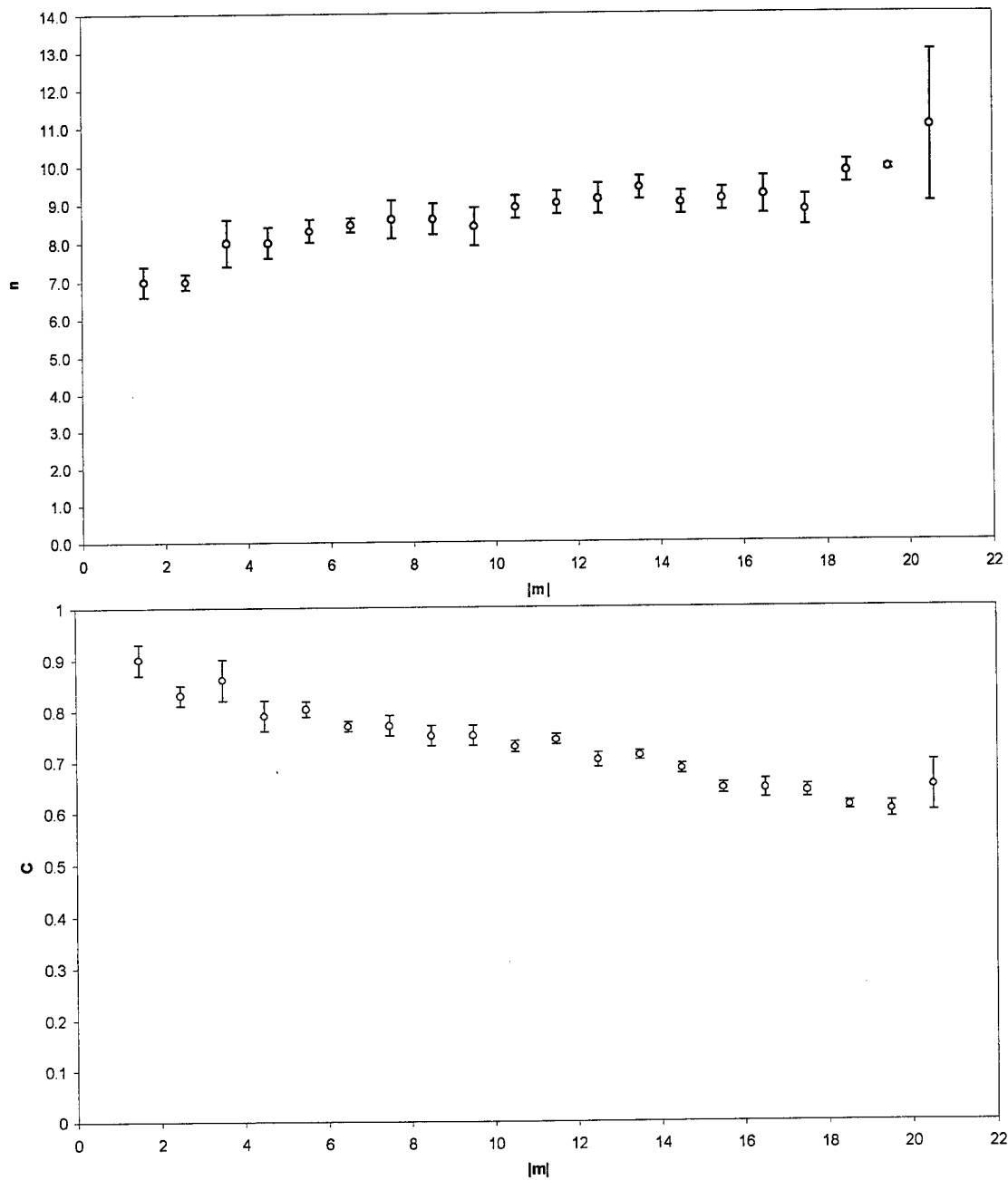
Figure 60. Fit Parameters *n* and *C* from the Classical Elastic Broadening Theory for the 1/2 Magnetic Substate of NO Broadened with Five Noble Gases

167
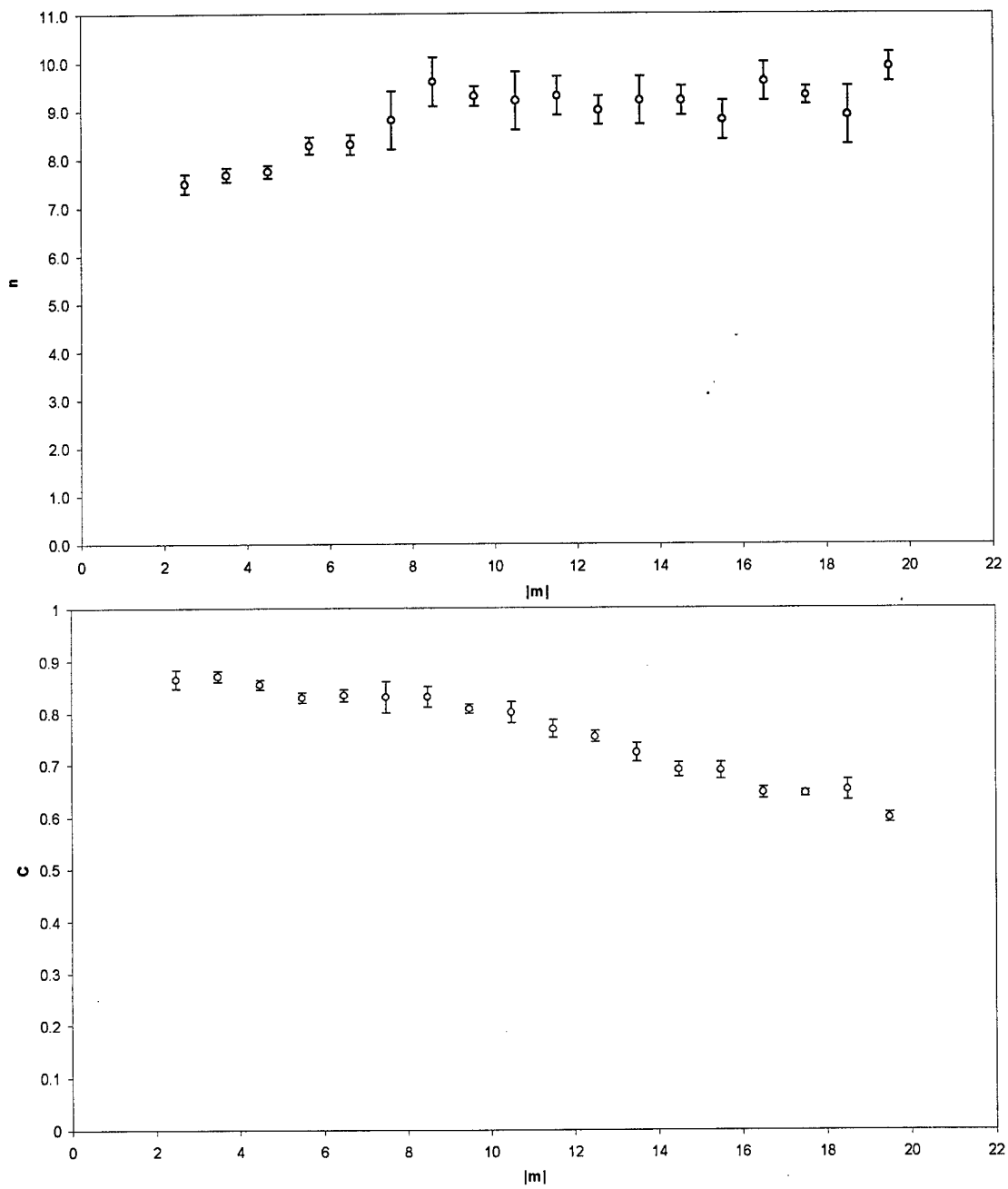
Figure 61. Fit Parameters *n* and *C* from the Classical Elastic Broadening Theory for the 3/2 Magnetic Substate of NO Broadened with Five Noble Gases

168

The increasing value of n with increasing J may mean one of two things. First, it may indicate an actual physical change in the intermolecular potential with J. Nitric oxide is a heteronuclear molecule with definite "plus" and "minus" ends. At low J these separate ends would be very apparent to an approaching noble gas atom. However, as J increases, the NO molecule spins faster. This would tend to average out the anisotropy of the NO molecule as seen by an approaching atom. This averaging could cause the force on the atom to be felt at shorter range as J increases, which is the same as saying n increases as J increases. On the other hand, this may simply point out the shortcomings of trying to apply a classical elastic broadening theory to the case of pressure broadening in molecules, which is generally believed to be dominated by inelastic processes. The failure of the theory may also be due to the assumed spherically-symmetric form of the intermolecular potential. The actual potential for a diatomic molecule is angle-dependent, so the approximation of spherical symmetry may be unwarranted.

Whether or not the classical elastic broadening theory is sufficient to describe pressure broadening in molecules, the O_2 and NO data both clearly indicate that the magnitude of the broadening cross sections depends on polarizability and reduced mass. This indicates that mass and polarizability of the perturber are definitely factors in the mechanism which governs the collision.

Another useful feature of the elastic-collision theory is its ability to describe difference potentials. The "difference potential" is simply the difference in potential energy between a collision complex in the upper and lower states connected by the photon transition. For example, a collision between a ground-state $O_2(X)$ molecule and a Xe atom is described by an interaction potential. A collision between an excited-state

169

$O_2(b)$ molecule and a Xe atom has a different potential. In each case, the Xe atom perturbs the O_2 electronic potential curve. The two O_2 potential curves are, in general, shifted differently, causing a shift in the position of a spectral line caused by a photon transition between the two states. The energy difference between the two potential curves, expressed as a function of the distance between the O_2 molecule and the Xe atom, is the difference potential. Difference potentials are usually expressed using a Lennard-Jones potential [53]:

$$V(r) = \frac{\left(C_{12}^{upper} - C_{12}^{lower}\right)}{r^{12}} - \frac{\left(C_6^{upper} - C_6^{lower}\right)}{r^6} = C_{12}r^{-12} - C_6 r^{-6} \tag{76}$$

where r is the separation between the collision partners and C_6 and C_{12} are two constants which describe the shape of the potential; C_{12} describes the hard repulsive wall, while C_6 describes the attractive well.

The elastic-collision theory predicts that the C_6 and C_{12} coefficients of the difference potential can be found from the ratio between the shifting and broadening coefficients [53]. First, the broadening coefficient, γ, and the shifting coefficient, β, are expressed as [53]

$$\gamma = 2\left(\frac{3\pi}{8}\right)^{2/5} N \langle v \rangle^{3/5} \left(\frac{C_6}{\hbar}\right)^{2/5} B(\alpha) \tag{77}$$

$$\beta = \left(\frac{3\pi}{8}\right)^{2/5} N\langle v\rangle^{3/5} \left(\frac{C_6}{\hbar}\right)^{2/5} S(\alpha) \tag{78}$$

where N is the number density of the perturbing species and $\langle v\rangle$ is the mean relative velocity between the collision partners. The functions $S(\alpha)$ and $B(\alpha)$ are given by [53]

$$S(\alpha) = \int_0^\infty x\sin\left(\alpha x^{-11} - x^{-5}\right)dx \tag{79}$$

$$B(\alpha) = \int_0^\infty x\sin^2\left\{\frac{1}{2}\left(\alpha x^{-11} - x^{-5}\right)\right\}dx \tag{80}$$

where α is expressed as [53]

$$\alpha = \frac{C_{12}63\pi}{256}\left(\frac{8}{C_6 3\pi}\right)^{11/5}\left(\hbar\langle v\rangle\right)^{6/5} \tag{81}$$

The C_6 and C_{12} coefficients are found using the following procedure. First, compute the ratio of the shifting and broadening coefficients, β/γ. Next compute the ratio $S(\alpha)/2B(\alpha)$ and find the value of α for which $S(\alpha)/2B(\alpha) = \beta/\gamma$. With a value of α, values can be determined for $S(\alpha)$ and $B(\alpha)$, using equations (79) and (80). These values can then be used in either Equation (77) or (78) to find C_6. With values for C_6 and α,

equation (81) can be used to find C_{12}. The coefficients C_6 and C_{12} can then be used in equation (76) to plot the difference potential.

In this research project, shifting coefficients were measured for O_2+Xe, so the difference potentials for the O_2+Xe collision complex can be computed using the elastic theory. Remember that the elastic theory was developed for atom-atom collisions; to my knowledge, this theory has not previously been used to calculate difference potentials for pressure broadening in molecules. For a molecular absorber, there are different broadening and shifting coefficients for each initial rotational level, which produces a different value of the ratio β/γ for each $|m|$. The β/γ ratios for O_2+Xe are plotted in Figure 62. The broadening and shifting coefficients for these ratios come from the data presented previously in Tables 2 and 5.
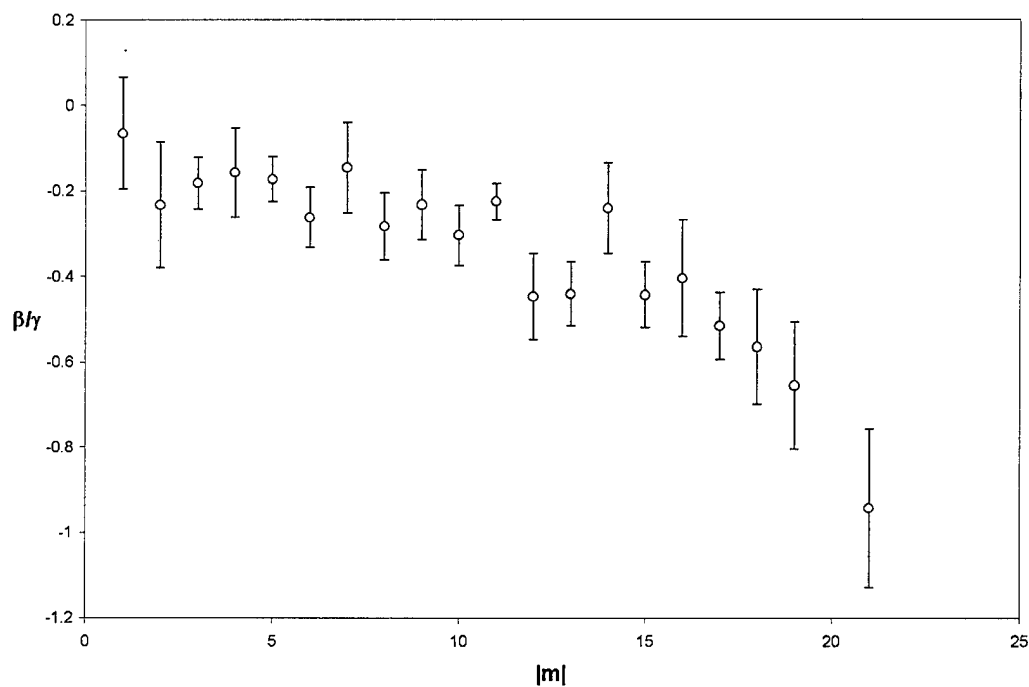
Figure 62. Ratio of β/γ, as a function of $|m|$, for O_2+Xe

The values of the β/γ ratio decrease with increasing initial rotational level. There is no ratio for $|m| = 20$ because a broadening coefficient was not determined for this rotational level. The β/γ ratio values were then each compared to the ratio $S(\alpha)/2B(\alpha)$ to determine a value of α for each $|m|$. Unambiguous values of α were found for all values of $|m|$ except $|m| = 19$ and $|m| = 21$. For these cases, the value of the β/γ ratio is in a part of the $S(\alpha)/2B(\alpha)$ curve where α can have multiple values. In these cases, values of α were limited to the range from 0.16 to 10.0, which is in the non-oscillatory part of the $S(\alpha)/2B(\alpha)$ function. The values of α were then used with Equations (77) and (81) to find the C_6 and C_{12} coefficients for each initial rotational level. Values of α, C_6, and C_{12} are listed in Table 20.

Table 20. Values of α, C_6, and C_{12} for the O_2+Xe Difference Potentials

$|m|$	α (unitless)	C_6 (eV Å^6)	C_{12} ($\times 10^6$ eV Å^{12})
1	2.78	12.92	13.70
2	1.43	13.92	8.34
3	1.71	13.08	8.68
4	1.88	10.20	5.50
5	1.77	10.16	5.15
6	1.31	10.96	4.51
7	1.97	9.77	5.24
8	1.23	8.16	2.21
9	1.44	10.63	4.62
10	1.16	11.65	4.55
11	1.48	9.78	3.95
12	0.80	8.92	1.74
13	0.81	11.95	3.37
14	1.40	8.52	2.77
15	0.81	10.87	2.72
16	0.89	8.13	1.58
17	0.68	11.07	2.40
18	0.61	10.69	2.00
19	0.51	10.99	1.76
21	0.28	10.17	0.83

The C_6 and C_{12} coefficients are graphed vs. initial rotational level in Figure 63. The C_6 (repulsive) coefficients decrease slowly with increasing initial molecular rotation, while the C_{12} (attractive) coefficients decrease more rapidly.
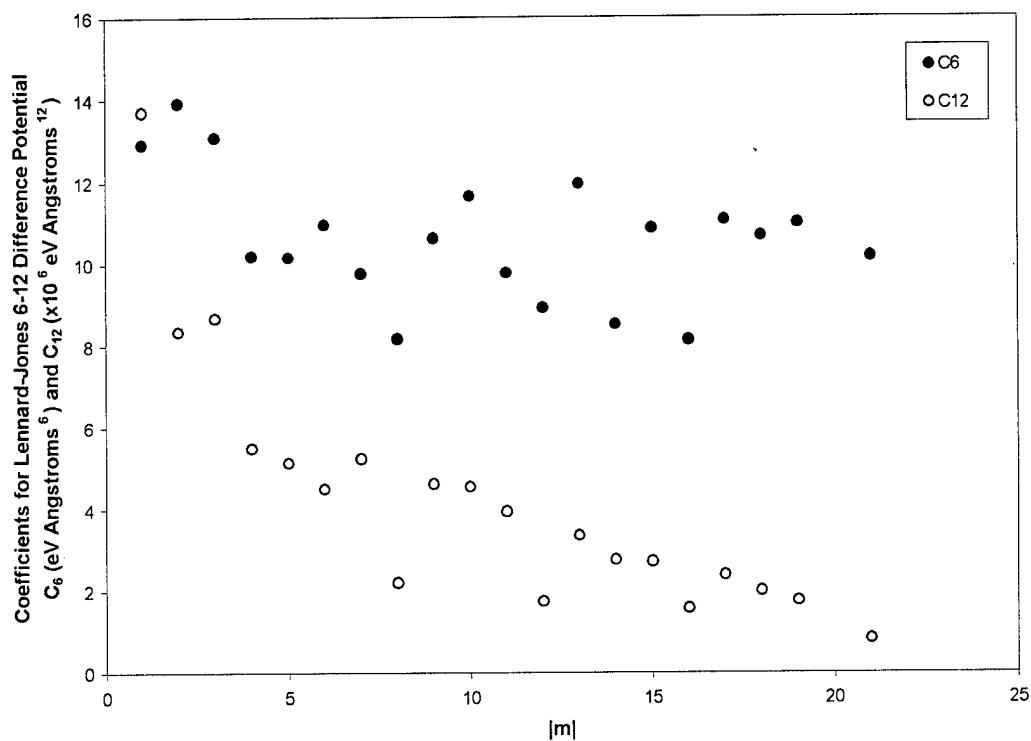
Figure 63. Coefficients for O_2+Xe Difference Potential.

Finally, difference potentials were determined from the C_6 and C_{12} coefficients using Equation (76). Difference potentials for five different initial rotational levels for the O_2+Xe collision complex for the X→b transition in oxygen are graphed in Figure 64.
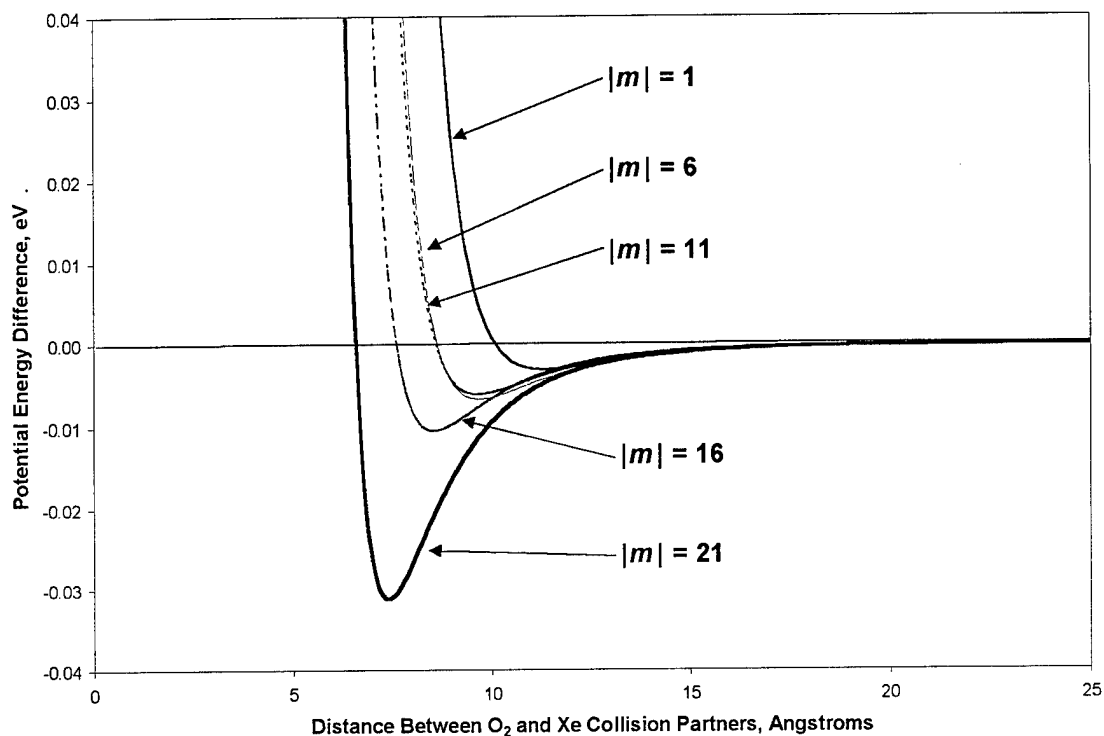
Figure 64. Difference Potentials for O_2+Xe for Five Different Initial Rotational States of the Oxygen Molecule

Two rotationally-dependent effects are observed in the difference potentials of Figure 64. First, the attractive well becomes deeper with increasing $|m|$. Second, the hard repulsive wall occurs at decreasing separation distances with increasing $|m|$. According to the angular-momentum-based, inelastic-collision theory of Osborne and McCaffery [86], the atom-molecule collision occurs at the hard repulsive wall of the potential. If the collision occurs at the repulsive wall, then Figure 64 indicates that the impact parameter decreases with increasing J''. This relationship between increasing molecular rotation and decreasing impact parameter will be discussed further in a later section of this chapter.

175

5.3. Application of Inelastic RT Fitting Laws to O_2 Broadening Cross Sections

In the previous section, an elastic pressure broadening model was applied to the measured broadening cross sections to see to what extent an elastic-collision theory could describe the observed behavior. In this section, several state-to-state RT fitting laws are applied to the O_2 data to see to what extent inelastic-collision theories can describe the observed broadening behavior. The fitting laws, described in Chapter II, were coded in Mathematica [72]; a typical model is included in Appendix E. A total of ten fitting law models were created, eight based on energy transfer and two on angular momentum transfer.

The energy-based models were forms of the EGL, SPG, and hybrid EPGL fitting laws combined with the different degeneracy expressions. The eight combinations of basic fitting law and degeneracy are indicated in Table 21.

Table 21. The Eight Combinations of Basic Energy-Based RT Fitting Laws and Degeneracy Expressions Used to Model the Data

Energy-Based RT Fitting Laws	Degeneracy Expressions		
	N_0	N_Δ	N_λ
EGL	X	X	X
SPG	X	X	X
EPGL	X	X	

The EGL and SPG laws, when used with either the N_0 or N_Δ degeneracy, have only two free fitting parameters. The N_λ degeneracy expression introduces an additional fitting parameter, so EGL-λ and SPG-λ are three-parameter fits. The hybrid EPGL-0 and

176

EPGL-Δ laws each have three fit parameters. Use of the N_λ degeneracy with EPGL produces a law with four parameters, which is more free parameters than the data can reasonably support (based on the number of data points and the size of the uncertainties), so the EPGL-λ law was not used.

The two angular-momentum-based models used in this study were the IOS-P and ECS-P fitting laws. These laws were implemented in Mathematica in the same way as the energy-based fitting laws. IOS-P has two free fitting parameters, while ECS-P has three. Although several researchers claim to obtain better fits with the ECS-EP than with ECS-P [25, 80, 123], the EP model adds a fourth free parameter, which was considered too many free parameters for the data, so the EP form was not developed. The other possibility, the ECS-E law, was not developed because it has generally been reported to be much less successful than either ECS-P or ECS-EP for fitting laboratory data [25].

The computer model which was developed to calculate the fitting laws requires three physical parameters: the temperature, the reduced mass of the collision pair, and the rotational constant, B, for oxygen. All pressure-broadening experiments in this study were performed at ambient room temperature, so 296 K was used as the temperature parameter. The reduced mass for each collision pair was computed from the atomic and molecular masses in Tables 16 and 17. The ground state B value was used for all O_2 fits, since there was no simple way to include both upper and lower state B values in the model. Since collisions are occurring in both electronic states, it would be preferable to include both rotational constants. However, the upper-state B value is only 3.1% smaller than the ground state value, so the discrepancies introduced by using B'' for both electronic states should be negligible.

The fitting-law computer code first computes the state-to-state rotational transfer rates using the specified fitting law. The model calculates the rates out of each initial state, where the initial states ran from $J_i = 1$ to 22 in integer steps. State-to-state rates were calculated using the selection rule $\Delta J =$ even, which is always obeyed for rotationally-inelastic collisional transitions involving homonuclear diatomic molecules. This results from the inability of RI collisions to change the nuclear spin symmetry of the molecule [25]. The model calculates both upward ($J_f > J_i$) and downward ($J_f < J_i$) rates out of each initial state. Upward rates were calculated up to the state $J_f = J_i + 30$, while downward rates were calculated to $J_f = 0$ or 1, depending on whether J_i was even or odd.

Each of the ten models was checked to see if it satisfied detailed balance. To do this, the code was modified so that only the upward rates were calculated directly from the fitting law. The downward rates were calculated by detailed balance, using Equation (28). The rates calculated from detailed balance were then compared to the rates found directly from the fitting law. It was found that every fitting law was consistent with detailed balance except for the two energy-based laws which used the N_λ degeneracy factor. This calls into question the physical validity of the N_λ degeneracy expression. Since detailed balance is a physical requirement, the EGL-λ and SPG-λ fitting laws were modeled using the modified form of the code in which the upward rates were calculated by the fitting law while the downward rates were calculated by detailed balance.

Once the state-to-state rates were calculated, the total removal rates out of each initial state were found using the sum rule of Equation (27). The total removal rates k_i were then converted to broadening cross sections σ_i by dividing the rates by the relative

average velocity. To perform the fits in Mathematica, an interpolating function over the discrete points σ_i was created. The fits were then performed using Mathematica's Levenberg-Marquardt weighted nonlinear least-squares routine.

The fitting routine returned best-fit values for each free parameter but could not calculate uncertainties for these parameters because of limitations in the analysis software. These best-fit values were then used to compute a best-fit broadening cross section σ_{calc} for each J_i. The fit was then plotted together with the experimental values of the broadening cross sections to provide a visual indication of the quality of the fit. In addition, three goodness-of-fit statistics were calculated. These statistics provide an indication of whether or not a particular fitting law is a good match to the data and also allow the different fitting laws to be quantitatively compared.

Several quantities are useful in describing how well a fitting law works or in determining which of a number of fitting laws best models the data. Reduced chi-squared is the standard measure of whether the fit agrees with the data to within error. Chi-squared, χ^2, is the sum of the squares of the relative deviations (difference between fit and data), each divided by its associated error. Reduced chi-squared divides χ^2 by ν, the number of data points less the number of free parameters. The relation for reduced chi-squared is [24]

$$\frac{\chi^2}{\nu} = \frac{1}{\nu} \sum_i \left(\frac{y_i^{data} - y_i^{fit}}{\sigma_i^{data}} \right)^2 \tag{82}$$

179

A reduced chi-squared near 1 indicates a fit to within error, while a reduced chi-squared much larger than 1 indicates an inadequate fit [126].

However, there is a drawback to using reduced chi-squared as the only measure of goodness of fit. For example, two experiments, one with small error bars and the other with large error bars on the data, may each return a reduced chi-squared near 1. The experiment with the smaller error bars is clearly the more precise verification of the fit, but reduced chi-squared alone does not reflect this. For this reason, Brunner and Pritchard [24, 25] defined a weighted RMS fractional deviation to describe the quality of the fit, independent of the quality of the data, and a weighted RMS fractional error to describe the quality of the data, independent of the fit. The RMS fractional deviation is [24]

$$
D = \sqrt{\frac{\sum_i \left(\frac{y_i^{data}}{\sigma_i^{data}}\right)^2 \left(\frac{y_i^{data} - y_i^{fit}}{y_i^{data}}\right)^2}{\sum_i \left(\frac{y_i^{data}}{\sigma_i^{data}}\right)^2}}
\tag{83}
$$

while the RMS fractional error is [24]

$$
E = \sqrt{\frac{\sum_i \left(\frac{y_i^{data}}{\sigma_i^{data}}\right)^2 \left(\frac{\sigma_i^{data}}{y_i^{data}}\right)^2}{\sum_i \left(\frac{y_i^{data}}{\sigma_i^{data}}\right)^2}} = \sqrt{\frac{1}{\sum_i \left(\frac{y_i^{data}}{\sigma_i^{data}}\right)^2}}
\tag{84}
$$

The RMS fractional deviation and RMS fractional error are related to the reduced chi-squared by [24]

$$\frac{\chi^2}{v} = \frac{N}{v}\left(\frac{D}{E}\right)^2 \tag{85}$$

where N is the number of measurements. Thus D and E allow independent checks of the quality of the data and the fit to the data, while D and E together can reproduce the reduced chi-squared, which is the standard check to see if the fit agrees with the data "to within errors." Taken together, χ^2/v, D, and E helped determine the applicability of the inelastic RT fitting laws for the O_2 broadening data and helped select a best fit from among the many models.

To validate the Mathematica implementation of the state-to-state RT fitting laws, the SPG-λ model was used to replicate a fit to state-to-state data reported in the literature by Dexheimer et $al.$ [35]. The data set chosen for the validation was for I_2^*+He, $J_i = 81$. Using the values for the fit parameters $\{A, \gamma, \lambda\}$ given in the paper, the Mathematica implementation of the SPG-λ fitting law accurately reproduced the fit shown in their paper. The validation fit to the data is shown in Figure 65. Not only does Figure 65 show that the state-to-state fitting laws have been implemented correctly, it shows that calculating the upward rates directly and calculating the corresponding downward rates by detailed balance is the correct way to use the N_λ degeneracy expression.

The energy-based fitting-law models run in about fifteen minutes, while the angular-momentum-based models take eight to nine hours to run on a 200 MHz Pentium

181
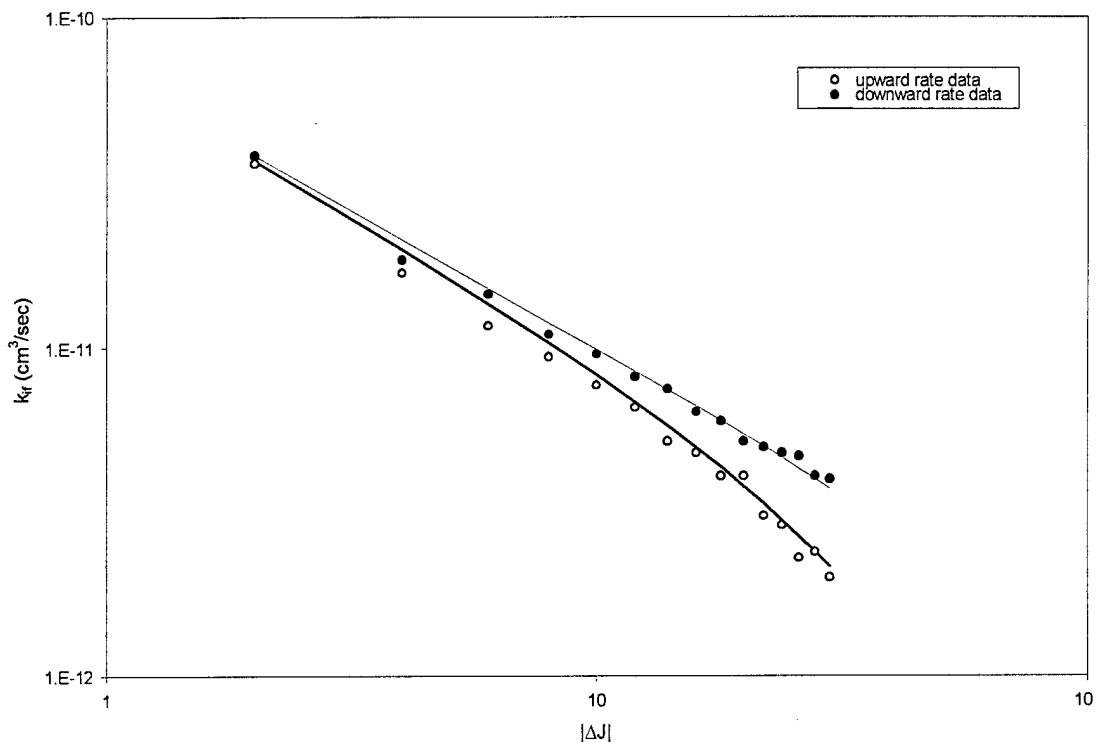
Figure 65. Validation of the Mathematica Implementation of RT Fitting Laws. This plot shows the I_2^*+Xe, J_i = 81 data from Dexheimer et al. [35] (points) fit with the SPG-λ fitting law created by the Mathematica code developed in the current study (lines), using the three fitting parameters specified by Dexheimer et al.

PC. To reduce this run time, an approximation to the ECS-P model suggested by Smith and Pritchard [117] was implemented. The approximation eliminates the computation of the many 3-J symbols, which Smith and Pritchard identify as a major contributor to long run times for the ECS-P fitting law. The Mathematica implementation of this ECS-P approximation is included in Appendix F. The exact and approximate ECS-P fits are compared to the data and to one another in Figure 66. Both fits match the data very well
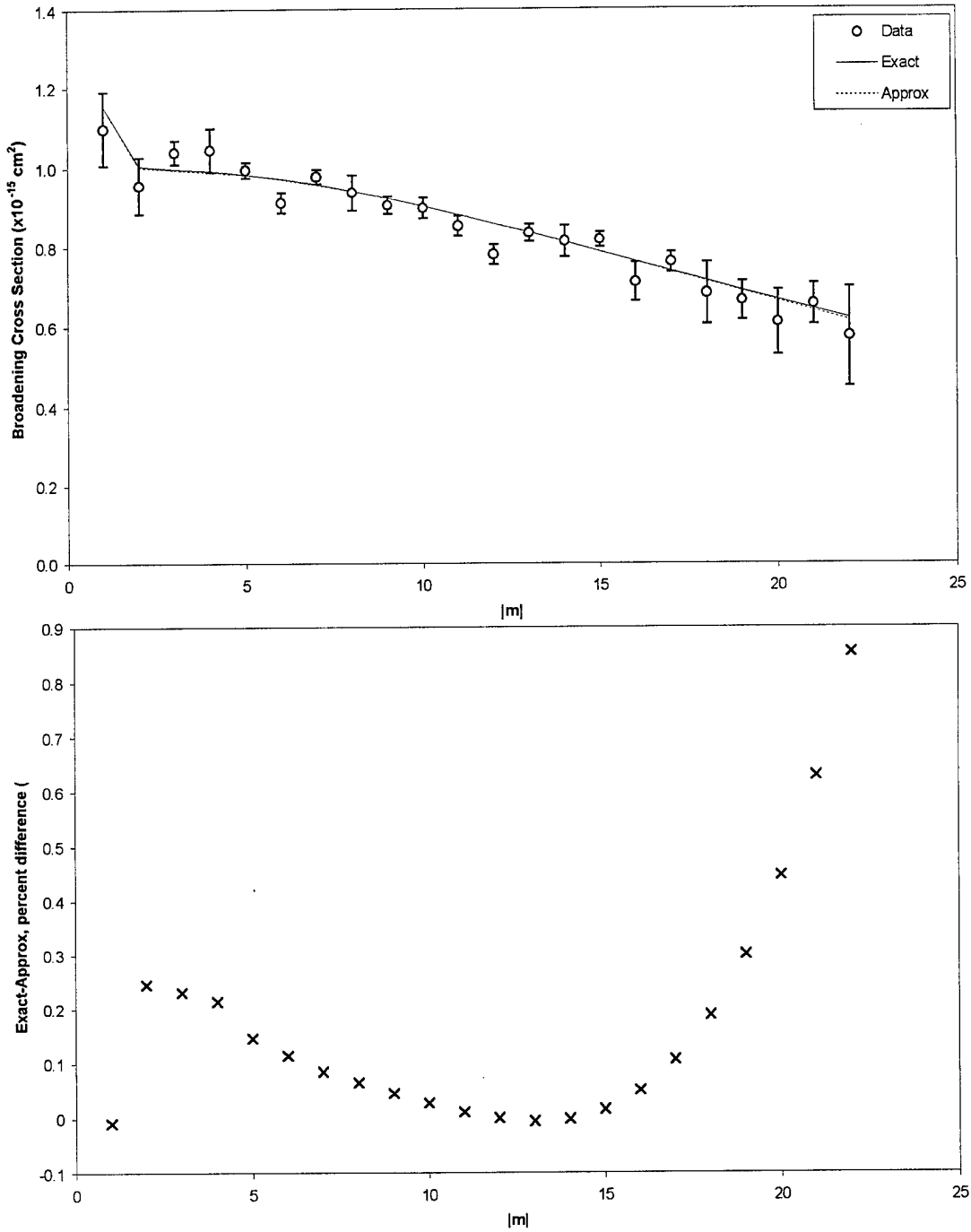
Figure 66. Graphical Comparison of the Exact and Approximate ECS-P Fitting Law Fit to O_2+Ar: the Top Plot Shows Both Laws Fit to the Data, Showing Nearly Identical Fits, while the Bottom Plot Shows the Percent Difference Between the Exact and Approximate Fits, which Remains Below 1%

and the fits are nearly indistinguishable. The largest discrepancy between the exact and

approximate fits is less than 1%, much less than the uncertainty in the experimental data.

The fitting parameters, goodness-of-fit, and run time for the exact and approximate

ECS-P models are compared in Table 22. For an almost one-third savings in computer

time, the fit parameters and quality of the fit differ by less than 5%. The most significant

discrepancy caused by the approximation is the 5% underestimation of l_c, which is a

systematic problem with the approximation mentioned by Smith and Pritchard.

However, this is an acceptably small discrepancy for the associated decrease in run time.

Table 22. Comparison of Fitting Parameters, Reduced Chi-Squared, and Run Time for
the Exact and Approximate ECS-P Fitting Law

Parameter	Exact ECS-P	Approx. ECS-P	Difference (%)
A ($\times 10^{-12}$ cm^2)	71.3	69.8	−2.1
l_c (Å)	0.766	0.727	−5.1
γ	1.18	1.17	−0.85
χ^2/ν	1.27	1.29	+1.6
Run Time (hours)	8.7	6.2	−29

Based on this comparison, the approximation to the ECS-P model was used in place of

the exact expression for all other fits.

Following the validation of the fitting-law codes and the implementation of the

ECS-P approximation, all ten RT models were fit to the O_2+Ar broadening cross sections.

The fits are plotted with the data in Figures 67 to 70.
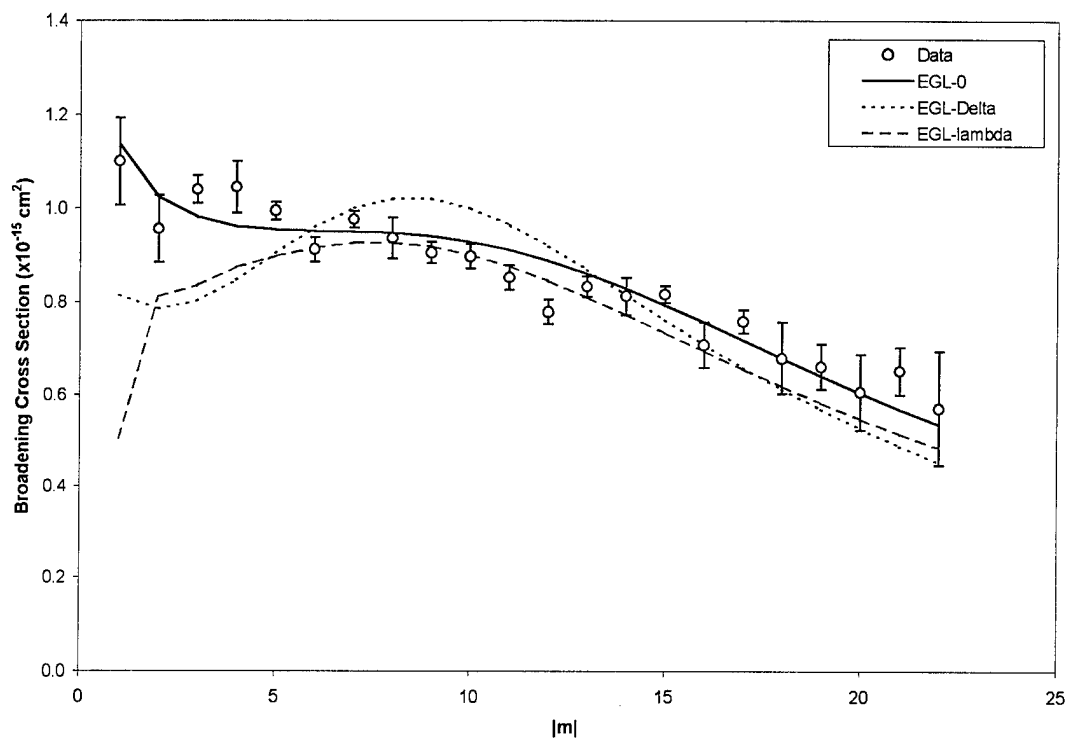
Figure 67. EGL Fits to O_2+Ar Broadening Cross Sections

As Figure 67 indicates, the EGL-0 law is the only acceptable EGL fit. The EGL-Δ and EGL-λ laws are both somewhat reasonable fits at high initial rotational quantum numbers, but fail for low J_i. The sharp drop-off of the N_λ degeneracy factor at low J_i has been reported previously in fits to pressure broadening data [55].
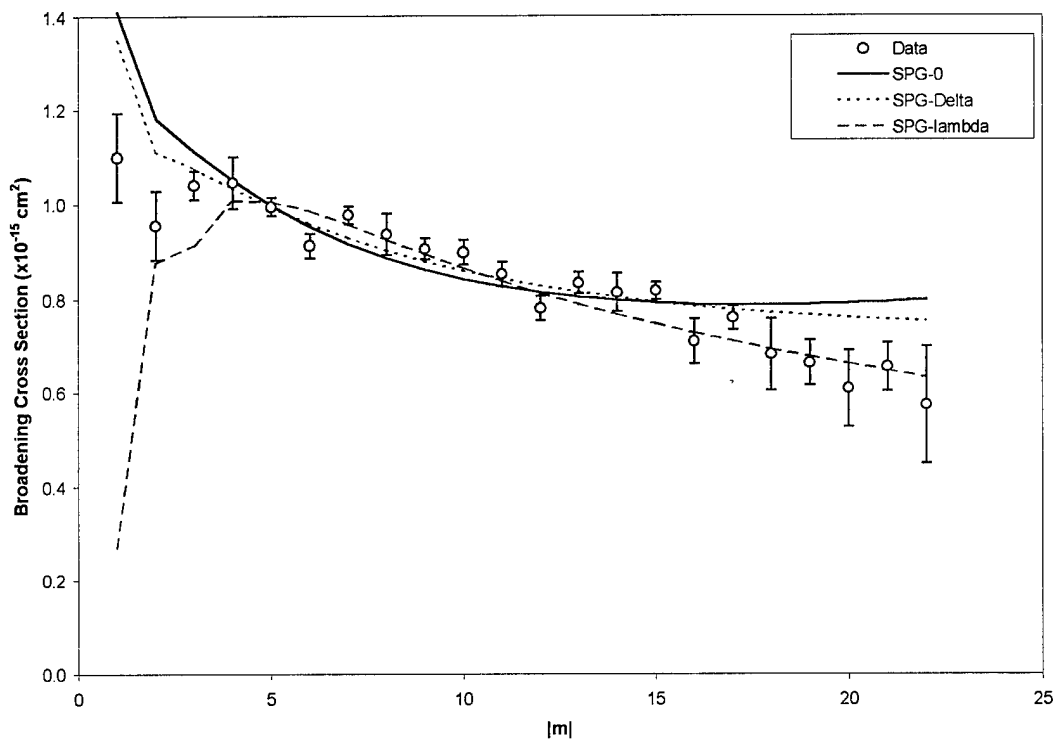
Figure 68. SPG Fits to O_2+Ar Broadening Cross Sections

Figure 68 indicates that the SPG-0 and SPG-Δ laws both produce reasonable fits to the data, although they both overestimate the broadening a bit at both low and high J_i, while underestimating the broadening at intermediate values of the initial rotational quantum number. The SPG-λ law produces the best SPG fit to this data for $J_i \geq 4$, but fails for low J_i in the same manner as the EGL-λ law. Overall, the SPG-Δ produces the best fit to this data set.
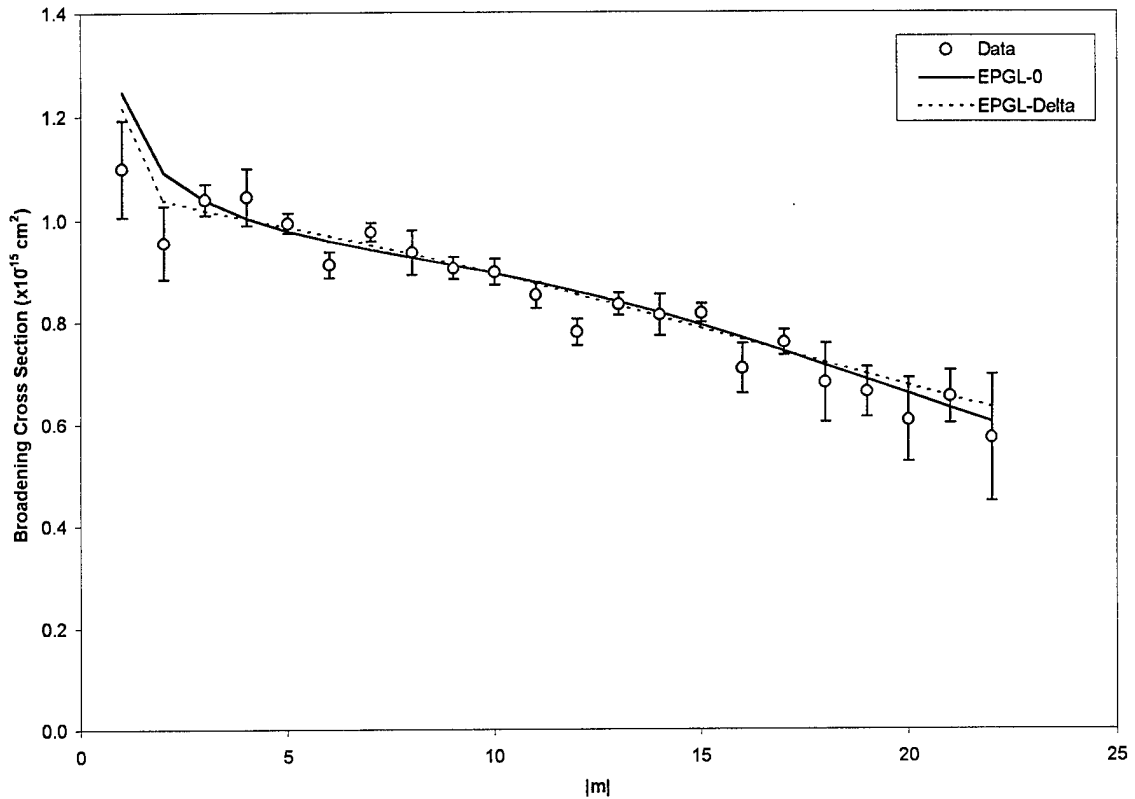
Figure 69. EPGL Fits to O_2+Ar Broadening Cross Sections

Figure 69 shows that the EPGL-0 and EPGL-Δ laws both produce very good fits

and are nearly indistinguishable from one another. The form of the degeneracy factor

seems to matter little to the shape of the EPGL fit, though the fitting parameters have

very different values for the two degeneracy factors. The EPGL law is a hybrid

exponential/power law fit, so it combines the best fitting features of each of the two

previous models. However, it is not possible to say whether the EPGL law produces a

better fit because it more accurately represents the physics or simply because it has an

additional free parameter in the fit.
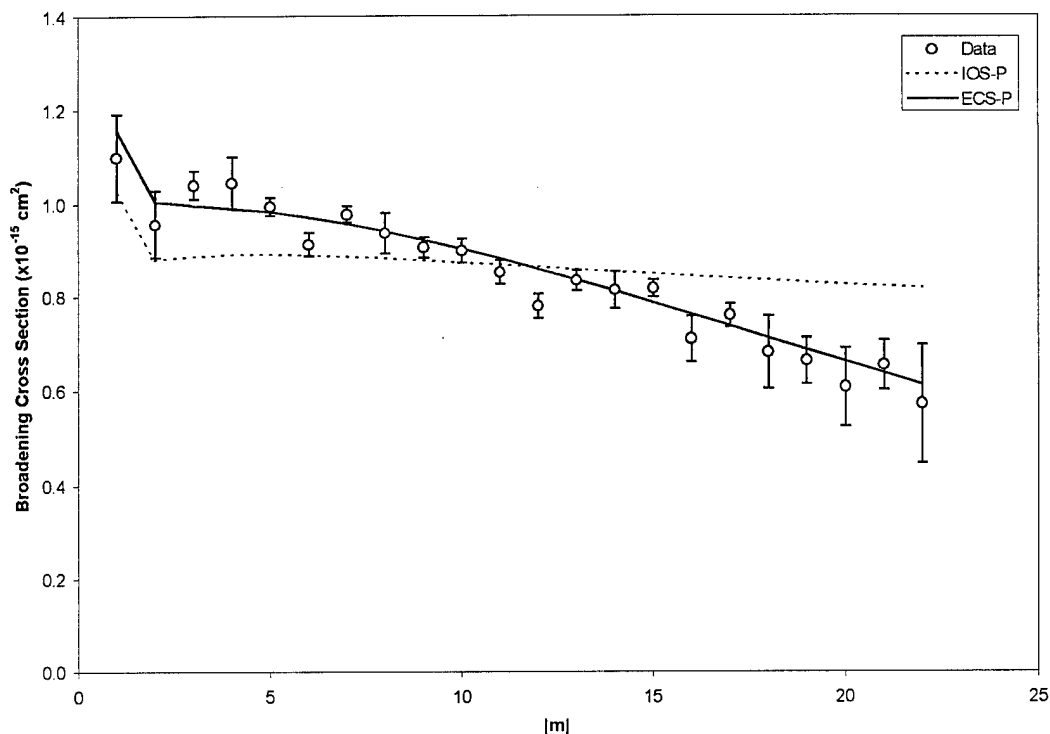
Figure 70. IOS-P and ECS-P Fits to O_2+Ar Broadening Cross Sections

Figure 70 shows the two angular-momentum-based fitting laws. The IOS-P law clearly fails to match the data, while the ECS-P law produces a very good fit. This is not unexpected, since IOS is only predicted to work when the perturber is much lighter than the absorber, which is not the case for O_2+Ar. Heavier collision pairs have slower relative velocities which means that the perturber remains near the absorber longer, long enough that the collisions are no longer "sudden." The failure of the IOS-P law indicates that the sudden approximation, in which the molecule does not rotate during the collisional interaction, may be a poor approximation for oxygen broadened with argon. The failure of the IOS-P law, then, might serve as a test of the impact approximation and

188

a warning to look for deviations from the Lorentzian lineshape in the corresponding spectra. The interaction time is explored further later in this section.

The fitting parameters and fit statistics from these ten models are listed in Table 23. There are large variations in the fitting parameters based on the law and degeneracy factor chosen. The parameter values in Table 23 demonstrate how the choice of model affects the magnitude of the fitting parameters, even though several models may provide "good" fits. The fitting parameters thus appear to have no universal physical meaning across all the models, even though many models share the same exponential or power-law mathematical components.

Table 23. Fitting Parameters and Fit Statistics for O_2+Ar Broadening Cross Sections Fit with Ten RT Fitting Laws (The RMS Fractional Error in the O_2+Ar Data is $E = 3.32\%$)

Law	Fitting Parameters					Fit Statistics		
	A $(\times 10^{-12}\ cm^2)$	β	γ	λ	l_c (Å)	χ^2/ν	D (%)	Rank
EGL-0	24.6	1.41				2.41	4.92	4
EGL-λ	2.62	1.58		4.33		10.87	10.18	9
EGL-Δ	3.40	3.98				12.79	11.33	10
SPG-0	140		0.62			4.37	6.62	6
SPG-λ	26.4		0.79	5.17		7.58	7.32	7
SPG-Δ	134		1.37			2.62	5.13	5
EPGL-0	53.5	0.80	0.27			1.42	3.69	3
EPGL-Δ	70.2	0.69	1.13			1.22	3.41	1
IOS-P	97.3		1.34			8.70	9.34	8
ECS-P	71.3		1.18		0.77	1.27	3.49	2

The last column of Table 23 rank-orders the ten fits based on the reduced chi-squared values, with a lower-numbered rank indicating a better fit. Based on these fit statistics and on the observed fits in Figures 67 to 70, the IOS-P, EGL-Δ, EGL-λ, and

SPG-λ were determined to be poor fits and were not used on any of the other data sets. The remaining six fits were applied to the rest of the oxygen data sets. Based on the fit statistics for each of these six fitting laws fit applied to the ten O_2 data sets, the EPGL-0, EPGL-Δ, and ECS-P laws produced the best fits to the data sets as a whole, with average reduced chi-squared values of 3.61, 3.77, and 3.99, respectively. In contrast, the SPG-Δ fits had an average reduced chi-squared of 5.34, while the EGL-0 and SPG-0 fits had average reduced chi-squared values of 8.09 and 8.52, respectively. To try to prevent overwhelming the reader with information, the remainder of this section will concentrate on the best energy-based fitting law (EPGL-0) and the best angular-momentum-based fitting law (ECS-P). Details of the other four fits and the comparison of the fit statistics for all six fitting laws are in Appendix G. The EPGL-0 and ECS-P fits to the ten O_2+perturber data sets are graphed in Figures 71 and 72.

In each case, the EPGL-0 fits are steeper than the ECS-P fits at low J_i. The ECS-P fits appear to drop steeply from $J_i = 1$ to 2, then decrease slowly for higher values of J_i with a slope which appears to steepen with increasing J_i. The behavior of the EPGL-0 fits is less consistent; some are predominantly power-law in character (Ne, SF_6) while other display more exponential-law behavior (Ar, O_2, CO_2). There are no apparent perturber-dependent reasons for the different behaviors, which indicates that while the EPGL-0 law may be a convenient way to describe the data, it does not appear to provide any clear information on the underlying collisional interactions.
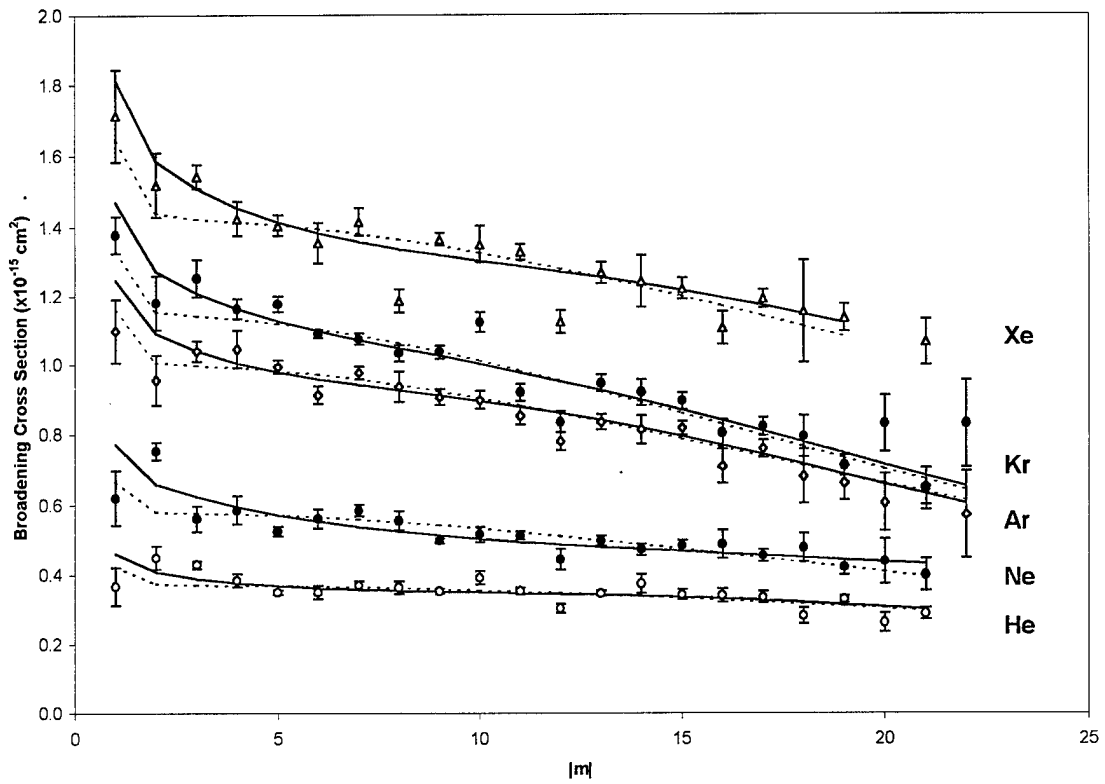
Figure 71. O_2+Noble Gas Broadening Cross Sections Fit with the EPGL-0 (Solid Lines)
and ECS-P (Dashed Lines) Rotationally-Inelastic Fitting Laws
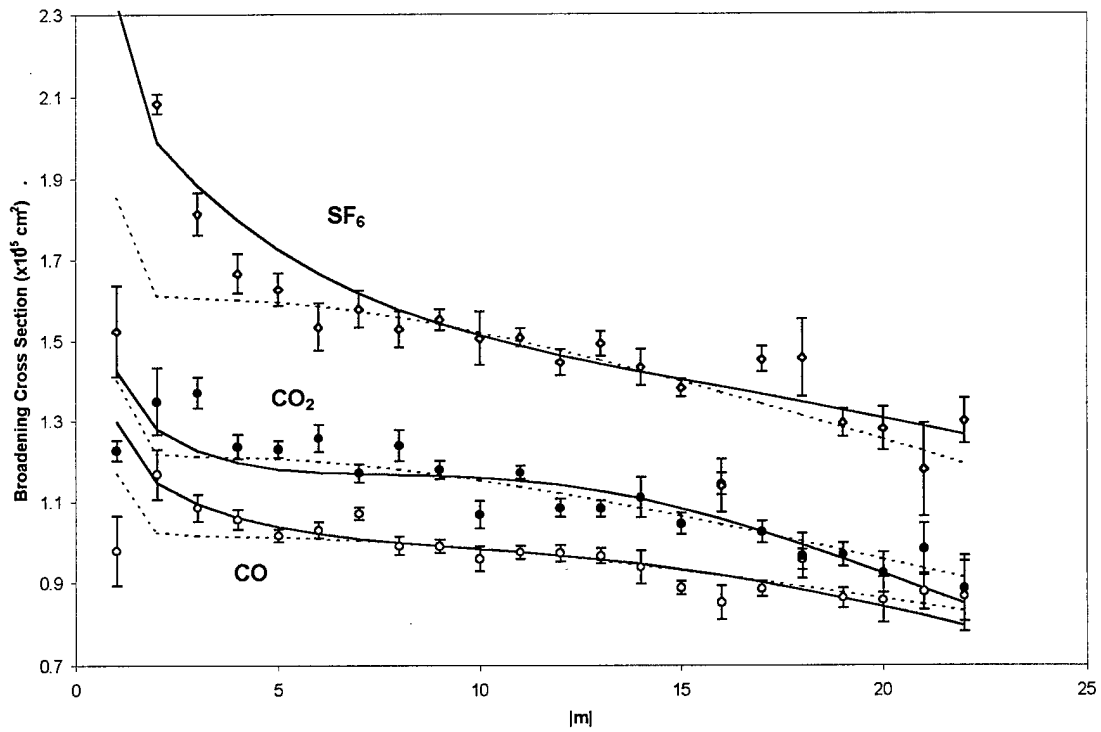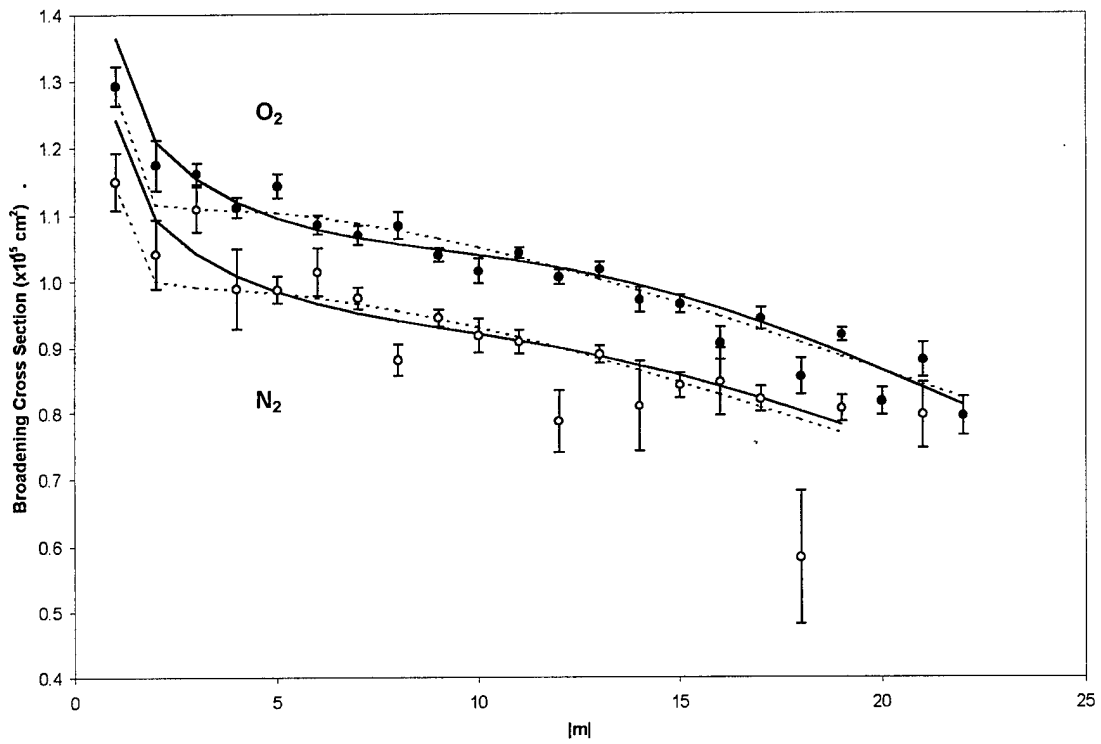
Figure 72. O_2+Molecule Broadening Cross Sections Fit with the EPGL-0 (Solid Lines)
and ECS-P (Dashed Lines) Rotationally-Inelastic Fitting Laws

The fitting parameters and statistics for the EPGL-0 fits to the O_2 data set are listed in Table 24.

Table 24. Results of EPGL-0 Fits to O_2 A Band Broadening Cross Sections
with Ten Different Perturbers

Collision Partner	A ($\times 10^{-12}$ cm^2)	β	γ	χ^2/ν	Fit Quality, D (%)	Data Quality, E (%)
He	39.8	0.52	0.27	3.10	5.65	3.46
Ne	64.9	0.27	0.48	3.59	6.03	3.44
Ar	53.5	0.80	0.27	1.42	3.69	3.32
Kr	66.7	0.77	0.33	3.38	4.20	2.49
Xe	70.8	0.52	0.33	4.21	4.87	2.59
N_2	55.7	0.61	0.28	2.32	3.46	2.48
CO	54.5	0.57	0.26	2.69	3.57	2.34
O_2	52.7	0.65	0.24	2.81	2.26	1.45
CO_2	36.6	0.89	0.11	6.01	5.54	2.43
SF_6	136	0.29	0.48	6.60	5.42	2.27

From the relative magnitudes of the β and γ parameters, one can identify fits which are more power-like or exponential-like in character. For example, the parameters for broadening by Ne and SF_6 have γ (power law) values which are larger than their β (exponential law) values, which indicates the predominant power-law character of the fits. On the other hand, CO_2 has a β value which is much larger than its γ parameter, indicating a fit which is very exponential in character. The remaining seven perturbers also have fits which are more exponential than power-law in character, though less so than CO_2.

This is, to my knowledge, the first time inelastic RT fitting laws have been applied to pressure broadening of a molecule with a large number of different perturbers. As such, this study provides an important opportunity to search for physical significance

193

in the fitting parameters. To look for systematic trends in the fitting parameters which might relate to the physical parameters of the perturbers, each of the thee fitting parameters was graphed vs. the reduced mass of the collision pair. Reduced mass was chosen as a convenient physical parameter of the perturber; its use should demonstrate the presence of any perturber-dependent trends. The EPGL-0 fitting parameter plots vs. reduced mass are shown in Figures 73 to 75.
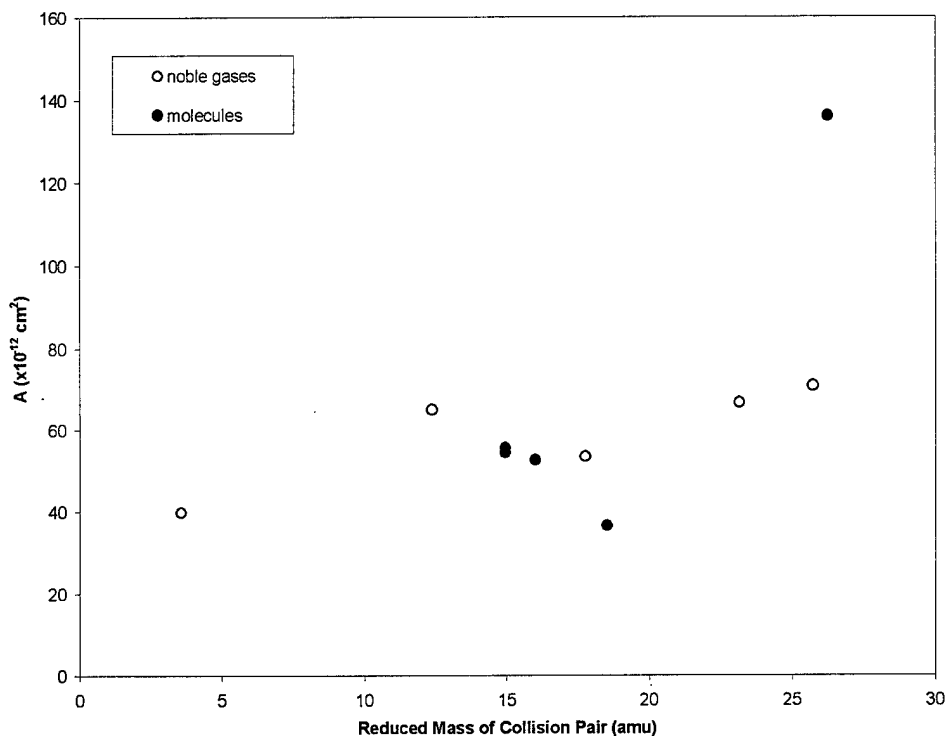
Figure 73. EPGL-0 Fitting Parameter A (the Scaling Parameter) vs. Reduced Mass of Collision Pair

Figure 73 shows no definite perturber-dependent trends with the scaling parameter A; the values appear to be either slightly increasing with mass or constant with

a wide variability. There is also no clear difference in the values of the scaling parameter between the noble gas and molecular perturbers.
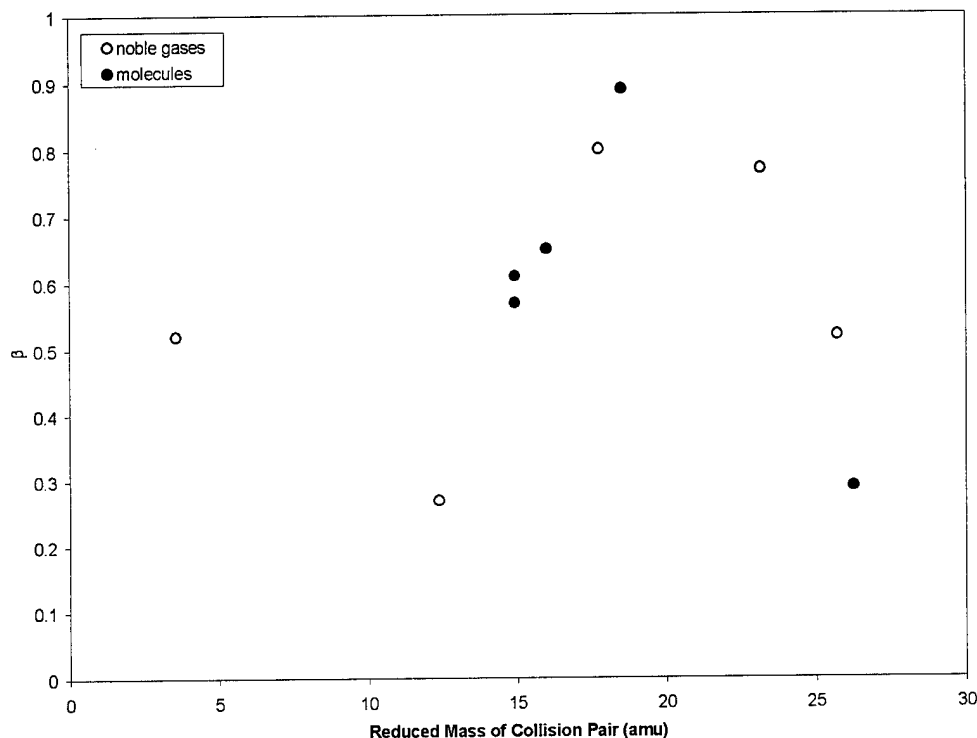
Figure 74. EPGL-0 Fitting Parameter β (the Exponential-Law Parameter) vs. Reduced Mass of the Collision Pair

Figure 74 shows no discernable perturber-dependent trends with the exponential-law parameter β. There is again no clear difference in the values of the parameter between the noble gas and molecular perturbers. Based on fits to several state-to-state data sets, Brunner and Pritchard [25] claim that the β parameter depends only on the absorber and not on the perturber. The results of the current study, though widely scattered, are consistent with a constant value of β for all perturbers.
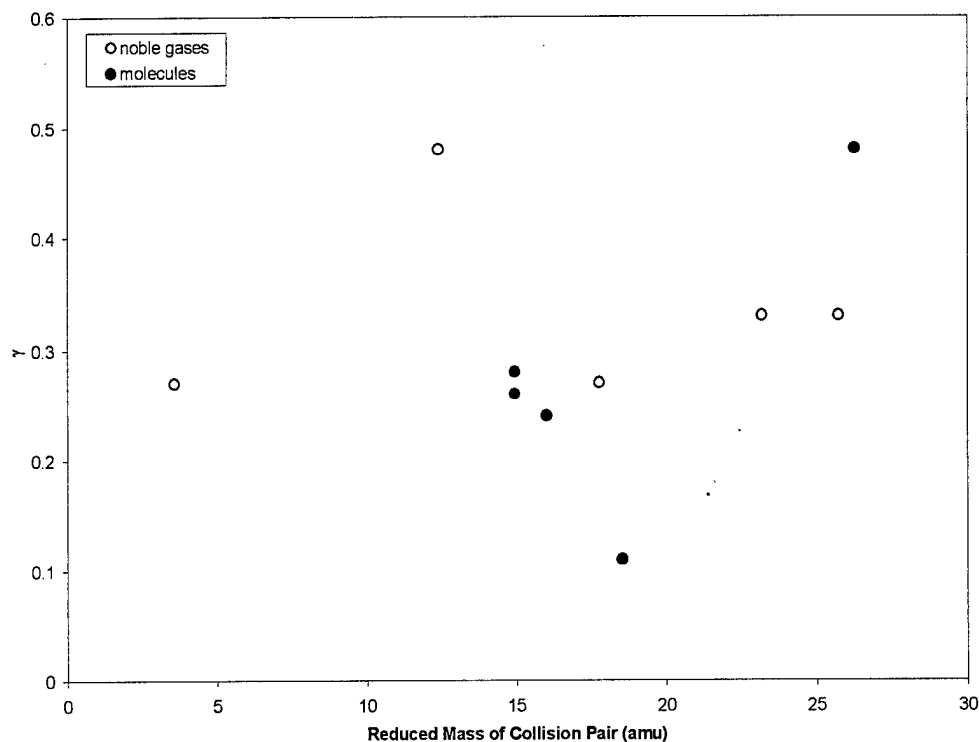
Figure 75. EPGL-0 Fitting Parameter γ (the Power-Law Parameter)
vs. Reduced Mass of the Collision Pair

Figure 75 shows no discernable perturber-dependent trends with the power-law

parameter γ. Once again, there is no clear difference in the values of the fitting parameter

between the noble gas and molecular perturbers. One must conclude that the fitting

parameters of the EPGL-0 law do not correlate to any physical properties of the

perturbing atoms or molecules. As such, the EPGL-0 fitting law says little about the

physics of the collisional interactions. It simply indicates that the observed pressure

broadening cross sections can be adequately described by a mathematical model which is

based on inelastic collisions effecting a transfer of energy with a probability of transfer

based in an exponential/power hybrid manner on the energy-spacing between the rotational levels.

In contrast with the energy-based EPGL-0 model, the angular-momentum-based ECS-P model displays several trends in the fitting parameters which may be related to the physics of the interaction. The fitting parameters and statistics for the ECS-P fits to the O_2 data set are listed in Table 25.

Table 25. Results of ECS-P Fits to O_2 A Band Broadening Cross Sections
with Ten Different Perturbers

Collision Partner	A ($\times 10^{-12}$ cm^2)	l_c (Å)	γ	χ^2/ν	Fit Quality, D (%)	Data Quality, E (%)
He	41.0	1.28	1.05	4.10	6.50	3.46
Ne	48.0	0.79	1.17	7.62	8.78	3.44
Ar	66.6	0.74	1.15	1.29	3.50	3.32
Kr	65.1	0.73	1.14	3.74	4.42	2.49
Xe	64.9	0.56	1.08	5.43	5.53	2.59
N_2	63.4	0.68	1.11	2.82	3.82	2.48
CO	62.9	0.53	1.10	2.85	3.68	2.34
O_2	77.0	0.59	1.15	3.26	2.44	1.45
CO_2	79.9	0.52	1.16	4.79	4.95	2.43
SF_6	90.0	0.45	1.16	32.18	11.96	2.27

Each of the three fitting parameters is graphed vs. the reduced mass of the collision pair in Figures 76 to 78. Figure 76 shows that the value of γ, which is the power-law parameter, is nearly constant for each perturber over a large range of reduced masses. Furthermore, the constant value is very close to 1.17, which is indicated by the dashed line in the figure. The impulsive classical description of the ECS-P model, described in Chapter 2, predicts that γ is related to the order of the inverse-power
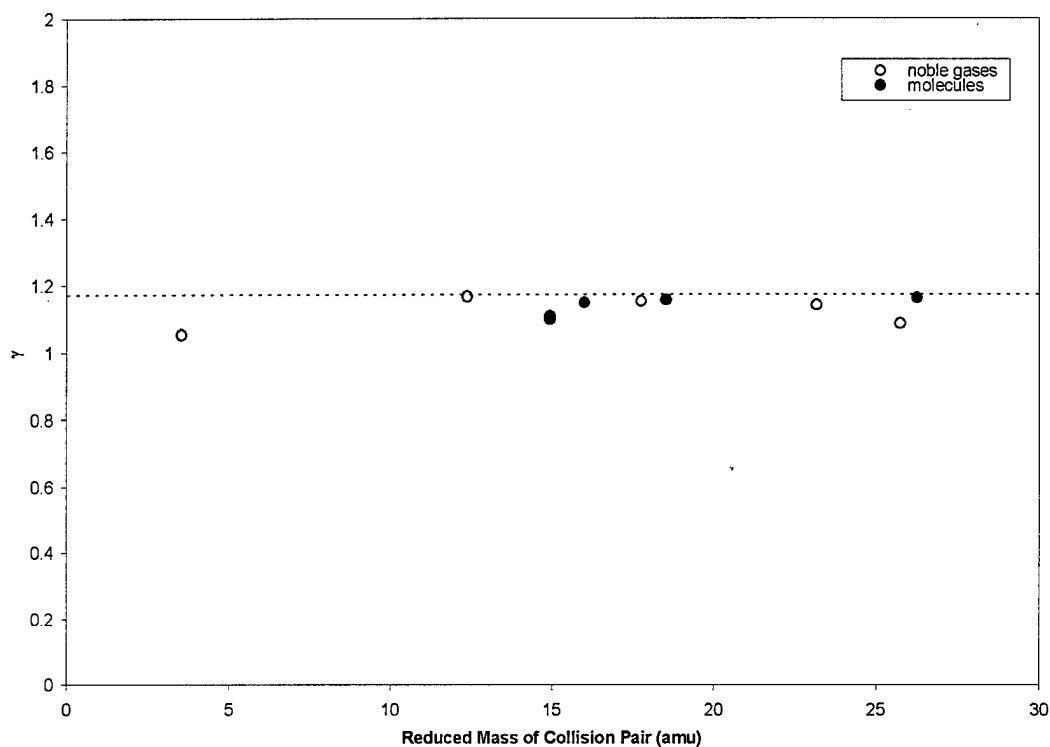
Figure 76. ECS-P Fitting Parameter γ vs. Reduced Mass of Collision Pair. Dashed line is $\gamma = 1.17$, corresponding to an r^{-7} potential in the impulsive classical limit.

intermolecular potential by $\gamma = n/(n-1)$. The values of γ for several possible r^{-n} potentials are listed in Table 26.

Table 26. Impulsive-Classical Predictions of the Value of the ECS-P Fitting Parameter γ for Several Possible r^{-n} Intermolecular Potentials

Potential	Order, n	ECS-P parameter γ
dipole-dipole	3	1.50
dipole-quadrupole	4	1.33
quadrupole-quadrupole	5	1.25
dipole-induced dipole	6	1.20
quadrupole-induced dipole	7	1.17

198

The results of the fits of O_2 with the ten perturbers gave values of γ between 1.05 and 1.17, which is largely consistent with the expected r^{-7} quadrupole-induced dipole potential. The molecules are not noticeably different from the noble gases, indicating that the molecules also interact predominantly via their polarizabilities, rather than their electric multipole moments. Brunner and Pritchard [25] performed ECS-P fits to several state-to-state data sets and found the value of γ to be relatively constant between 0.911 and 1.38, which is consistent with the ECS-P pressure broadening fits of the current study.
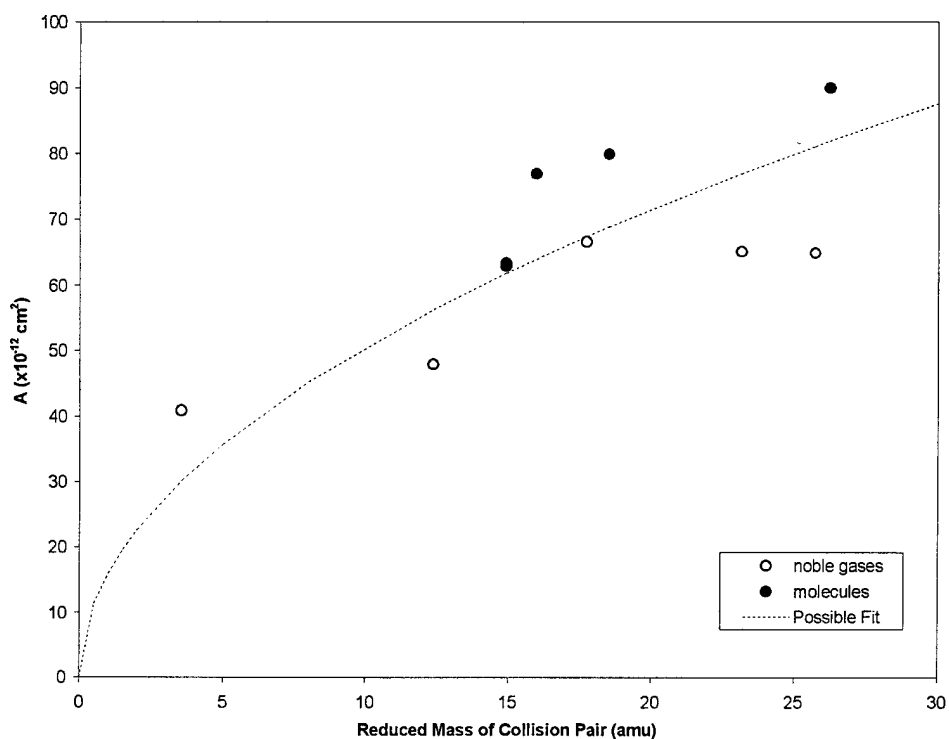
Figure 77. ECS-P Fitting Parameter A vs. Reduced Mass of Collision Pair. Dashed line is $A = 16\sqrt{\mu}$, indicating a possible trend.

199

Figure 77 clearly shows an increasing trend in the ECS-P scaling parameter A with increasing reduced mass. The angular-momentum-based picture of pressure broadening relates broadening to the momentum transferred in the collision, $l = \mu\langle v\rangle b$. Since the average velocity is related to reduced mass by $\langle v\rangle \propto 1/\sqrt{\mu}$, the transferred momentum is related to the reduced mass of the system by $l \propto \sqrt{\mu}$. The dashed line in Figure 77 corresponds to a least-squares fit to the data with the equation $y = a\sqrt{x}$. The fit finds $a = 16$, with a goodness-of-fit $r^2 = 0.49$. While this is not a conclusive fit to the data, it indicates a possible explanation for the observed trend which is consistent with the physics of momentum transfer.
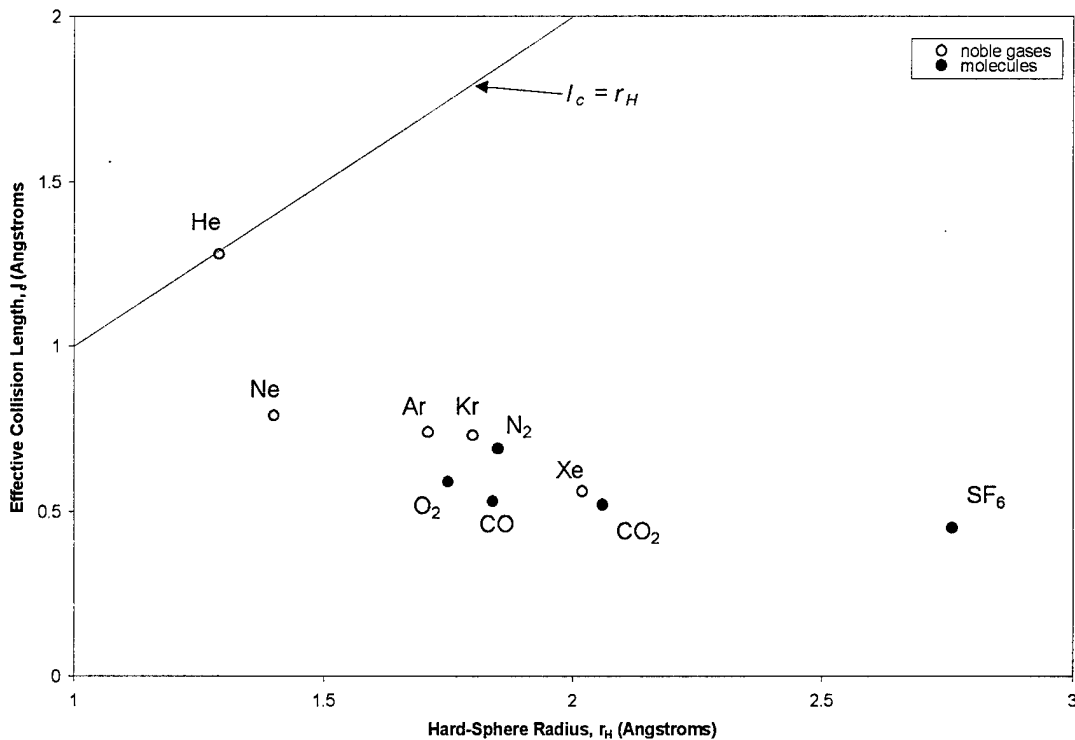
Figure 78. ECS-P Fitting Parameter l_c, the Effective Collision Length, Plotted vs. the Hard-Sphere Radius of the Perturber. With the exception of He, $l_c < r_H$ for all perturbers.

200

Figure 78 shows no certain perturber-dependent trends with the characteristic

interaction length, l_c; the values appear to either decrease slightly or remain constant with

increasing mass. Based on fits to state-to-state data, Brunner and Pritchard [25] claim l_c

depends on the absorbing molecule but not on the perturber, an observation which is

consistent with the results of the current study. Figure 78 gives some idea of the

magnitude of this interaction length parameter. Millot [79] indicates that l_c may be

approximated by the hard sphere radius, which would generally produce an increasing l_c

with increasing mass. The solid line in Figure 78 shows the line at which l_c equals the

hard sphere radius, r_H. Only He falls on this line; the interaction lengths for the other

nine perturbers are less than the corresponding hard sphere radii. The results of the

current study are thus more in agreement with the observations of Brunner and Pritchard

[25] than with Millot [79].

For an additional investigation of the l_c parameter, the interaction length may be

converted to an interaction time by the relation $\tau_c = l_c / \langle v \rangle$. Collision time is graphed vs.

reduced mass in Figure 79. The IOS fitting law ($\tau_c = 0$) is predicted to work well for

light collision pairs but to fail with increasing system mass, so one expects some kind of

increase in τ_c with increasing mass. The noble gases from helium to krypton show a

slight increasing trend, though xenon deviates. The collision times for the molecular

perturbers seem to be fairly flat with reduced mass and appear to be uniformly a bit lower

than the noble gases. The observation of increasing interaction times with increasing

mass agrees with the observations of Millot [79], who says the interaction time decreases

201
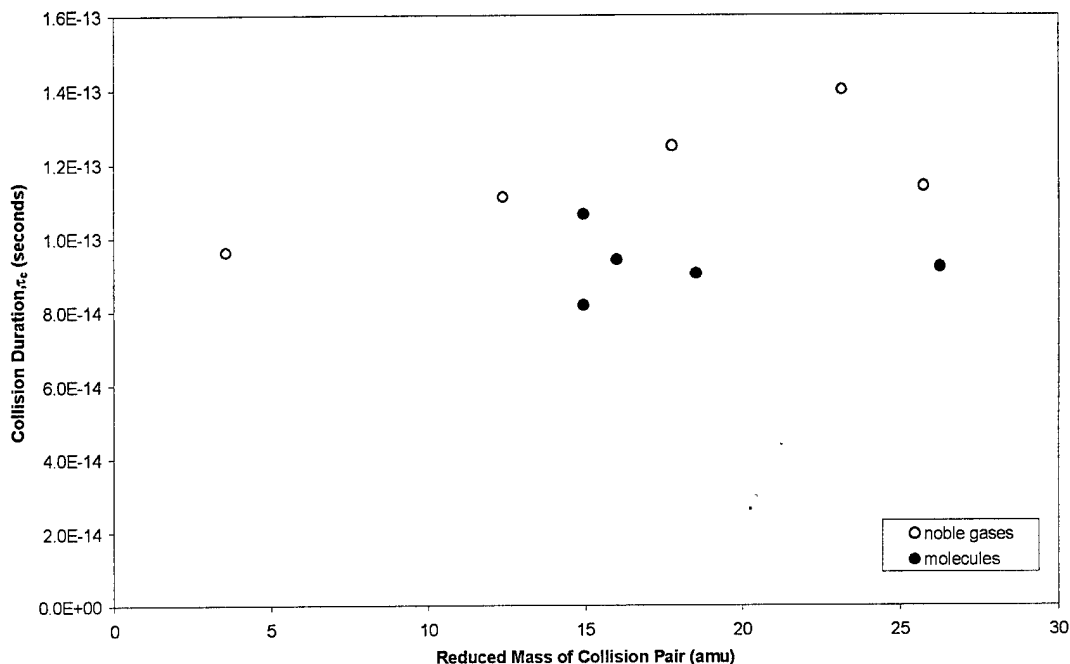
Figure 79. Collision Duration vs. Reduced Mass of Collision Pair, Calculated from ECS-P Fitting Parameter l_c

with increasing kinetic energy. Thus for light systems the IOS law becomes more appropriate, while for heavy systems, which have lower kinetic energy, the sudden approximation becomes less accurate. Boulet and Boissoles [23] say that with a light perturber like He, short range forces are dominant through head-on collisions corresponding to very short duration τ_c of about 0.05 picoseconds. The observed interaction time for O_2+He from the current study is 0.096 picoseconds, which is certainly of the same order.

A collision is considered "sudden" if the molecule effectively does not rotate during the interaction. The angular frequency of a rotating diatomic molecule is [79]

$$\omega_{J \to J-\Delta} = 2\pi cB[J(J+1) - (J-\Delta)(J-\Delta+1)] \tag{86}$$

where $\Delta = 2$ for a homonuclear molecule like O_2. The rotation of the molecule, in radians, during the collision is then given by [79]

$$\tau_J = \frac{\omega_{J \to J-\Delta}}{2} \tau_c \tag{87}$$

The average collision time for the ten collision partners used in this study is found to be 0.11 picoseconds. The rotation of the O_2 molecule during this interaction time, found from Equations (86) and (87), is plotted vs. initial rotational level in Figure 80.
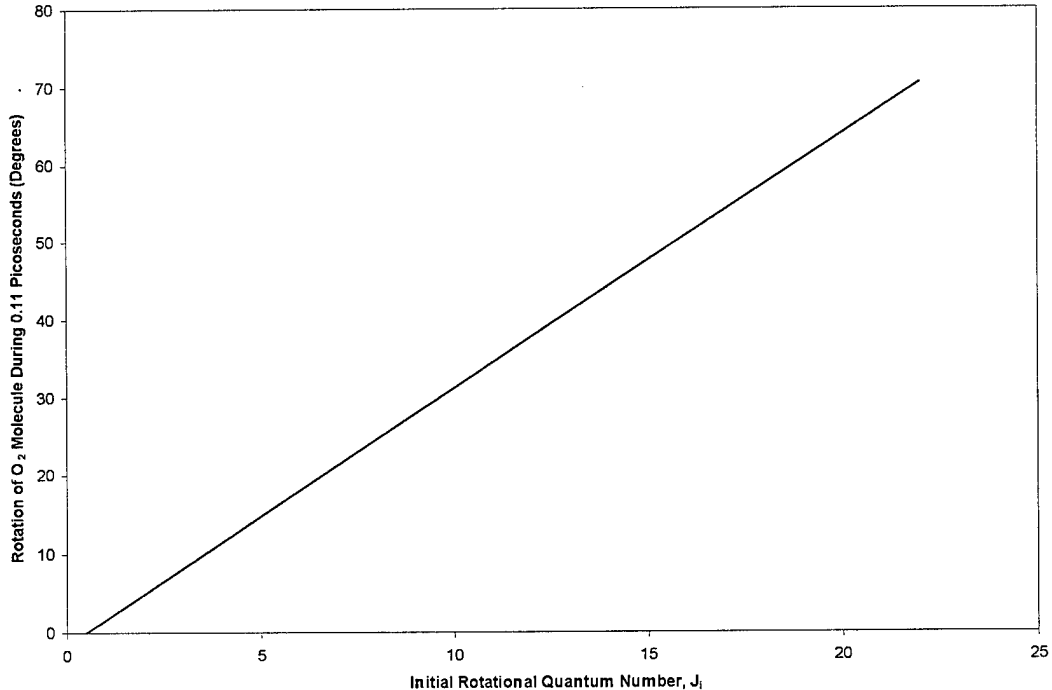
Figure 80. Rotation of the O_2 Molecule as a Function of Initial Rotational Quantum Number for an Average Collisional Interaction Time of 0.11 Picoseconds

203

The O_2 molecule makes almost a quarter rotation by $J_i = 22$, definitely not a "sudden" collision. This indicates why the IOS-P law performed so poorly on the O_2+Ar data set.

Overall, while the EPGL-0 and ECS-P fitting laws both produced good fits to the O_2 broadening cross sections, only the ECS-P law seems to have any physical significance to its fitting parameters. The ECS-P law further provides a possible indication of a relationship between the magnitude of the scaling parameter and the square root of the reduced mass; a relationship which is consistent with an inelastic angular-momentum transfer mechanism for pressure broadening.

No similar indication of an energy-dependent mechanism was discovered in the analysis of the energy-based EPGL-0 fits, which lends some support to the theory that momentum transfer, rather than energy transfer, is the governing mechanism in the behavior of rotationally-inelastic collisions. The ECS law has been identified by many researchers [25, 123] as the best model for fitting rotationally-inelastic, state-to-state data. While the current study generally found the EPGL laws to have slightly better fit statistics than ECS-P, the benefits offered by the possible physical relevance of the fitting parameters suggest that ECS-P is the best semi-empirical inelastic RT model for fitting pressure broadening data.

Now compare the results of the inelastic fits to the oxygen data set from this section with the elastic model in the previous section. Both the elastic model and the inelastic ECS-P law produce results consistent with an r^{-7} quadrupole-induced dipole potential for perturbers interacting with O_2. However, while the inelastic models fit the broadening cross sections for all the initial rotational levels simultaneously, the elastic model must be fit to each J_i individually. This is because the elastic model makes no

predictions about dependence of the cross sections on initial rotational level, while the inelastic models all account for this dependence. It was pointed out however, that the scaling term in the elastic model, when graphed vs. J_i, showed the same shape as the average J_i dependence of the cross sections. Thus the collection of "constants" which were collected together to form the scaling parameter might be able to be analyzed to find a quantifiable J_i-dependent mechanism.

In general, one expects both elastic and inelastic collision to take place. The question is which mechanism dominates the interactions. Most researchers assume that the proportion of elastic collisions is effectively negligible. Millot $et\ al.$ [80] lend some quantitative support to this argument in the case of pressure broadening in O_2. Millot et $al.$ measured the Q Branch of O_2, in collisions with O_2 and N_2, by Raman scattering from the $^3\Sigma_g^-$ ground state. The resulting broadening coefficients were fit with forms of the EGL and ECS fitting laws, using a sum rule which considered elastic vibrational dephasing collisions and elastic reorientational collisions ($\Delta m \neq 0$) as well as inelastic RT collisions. The researchers claimed pure vibrational dephasing was negligible for oxygen collisions, while the average reorientational component was $\leq 5\%$ of the total linewidth. Thus pressure broadening in O_2 should be able to be modeled using an inelastic RT collision theory with a fair degree of accuracy.

In any case, it is safe to assume that elastic and inelastic collisions both occur in the bath gas and that each type of collision acts to broaden the spectral line. Application of the elastic theory of Weisskopf indicates that some elastic pressure broadening is occurring, but the elastic theory does not account for the J-dependent trends in the data. The inelastic models are able to match the J-dependent trends in the data, indicating that

the J-dependence is the result of inelastic collisions. However, inelastic collisions are not the whole story. The inelastic fitting laws should be expected to match the trend but not the absolute magnitude of the broadening coefficient, since some of the broadening is the result of elastic collisions. The fitting laws are able to match the magnitude as well as the trend because the scaling coefficient on the inelastic fitting laws must contain a J-independent elastic component.

Inelastic RT fits were not performed on the NO data collected in this research because of the additional complications resulting from the complex spectroscopy of NO fundamental band. As pointed out be Lempert *et al.* [68] and discussed in Chapter III, in addition to modeling the rates for pure rotational transfer, one must model the rates for pure spin-flipping collisions ($1/2 \leftrightarrow 3/2$) and for combined spin-flipping and rotational collisions. The resulting fitting laws require six free parameters, which are more degrees of freedom than I believe the data warrants. In addition, NO is heteronuclear, which means that the ΔJ = even state-to-state selection rule is no longer applicable. However, since NO is "almost homonuclear", there is still apparently a propensity for ΔJ = even transitions to have larger rates than ΔJ = odd transitions [6, 115]. The ratio between the even and odd rates, however, appears to vary with perturber and with J_i in an as-yet unpredictable way, making it very difficult to model in a case like the current research when only the total removal rates are available.

The application of the state-to-state fitting laws to the experimental pressure-broadening data has assumed that the collisions which cause broadening are purely inelastic, in contrast with Weisskopf's theory which assumed that the collisions which cause broadening are purely elastic. The inelastic-collision, state-to-state fitting laws

have been applied to molecular pressure-broadening data by previous researchers [37, 97, 101, 123], while the elastic theory has not, to my knowledge, been applied previously to molecules. Steinfeld *et al.*, in a review article on fitting laws, state that "neglect of the elastic contributions is a standard and early universally made approximation [123]." Neglecting elastic collisions is justified if (a) the majority of collisions with diatomic molecules are inelastic or (b) inelastic collisions are much more effective at broadening than elastic collisions.

To explore the effect of elastic collisions on the state-to-state fitting laws, the EGL-0 computer model was modified to permit a constant elastic-collision component in the broadening cross sections. The constant elastic component was expressed as a percent of the broadening cross section of the highest-J level. For example, the broadening cross section for O_2+Ar, $J_i = 22$, is 5.7×10^{-14} cm^2. A 10%-elastic component, then, considered 5.7×10^{-15} cm^2 of the broadening cross section for each J_i to be due to elastic collisions, while the remainder was due to inelastic collisions. The constant elastic-component model was chosen as a rough, easy-to-model approximation to the actual (unknown) elastic/inelastic partition. The EGL-0 law was then used to fit the O_2+Ar broadening cross section data for four different cases, with constant elastic components of 0% (purely inelastic), 10%, 50%, and 100% of the $J_i = 22$ cross section. These four fits are shown in Figure 81.
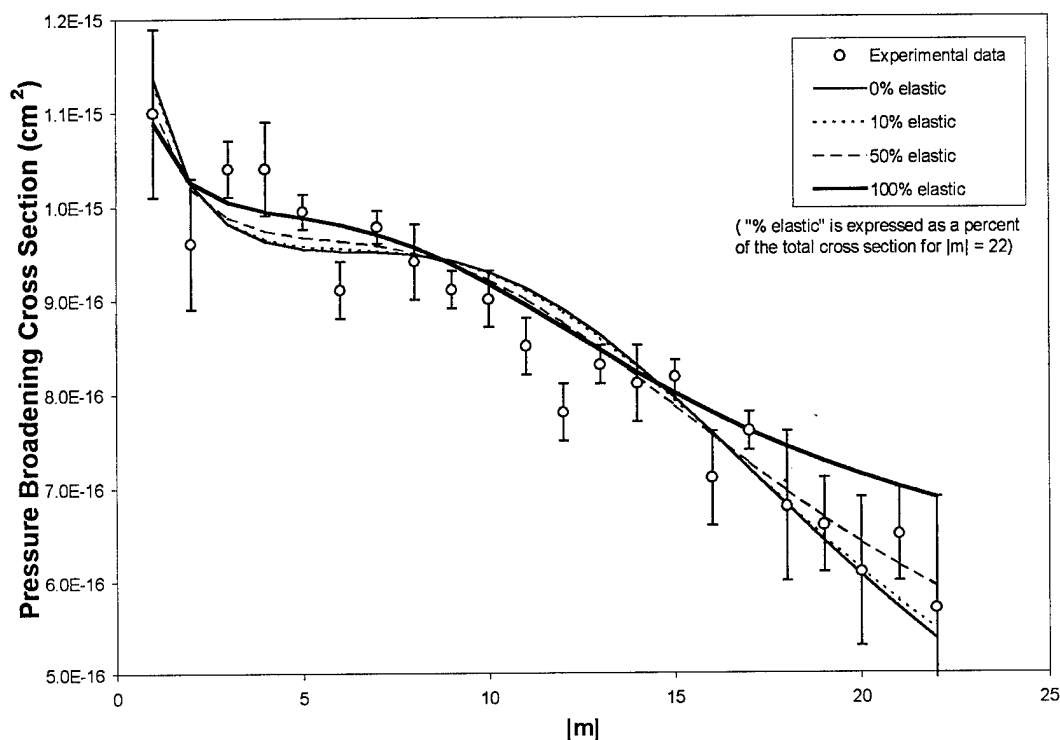
Figure 81. EGL-0 Fits to O_2+Ar Broadening Cross Sections for the Case of Purely-Inelastic Collisions and for Three Constant Elastic-Collision Components

Figure 81 shows that the fitting EGL-0 fitting law provides nearly identical fits for the purely-inelastic and 10% elastic cases; the values of the EGL-0 function at each $|m|$ differ by an average of only 0.4% for the purely-inelastic and the 10%-elastic cases. The differences become more pronounced for larger elastic components, rising to 2.3% for the 50%-elastic case and 6.4% for 100%-elastic case. However, all four fits to the data pass through the majority of the error bars and have reduced-chi-squared values between 1.59 and 2.41. Thus the EGL-0 law is able to fit the data well under drastically different assumptions of elastic/inelastic partitioning. This indicates that the state-to-state

fitting laws can be used with confidence on pressure-broadening data if the elastic contribution is either known or negligible.

The values of the fit parameters and the reduced-chi-squared values for each case are listed in Table 27.

Table 27. Fit Parameters and Reduced-Chi-Squared Values for EGL-0 Fits to the O_2+Ar Broadening Cross Sections Under Four Different Elastic/Inelastic-Collision Assumptions

Elastic-collision component	A ($\times 10^{-12}$ cm^2)	β	χ^2/ν
0% (purely inelastic)	24.5	1.41	2.41
10%	23.5	1.46	2.27
50%	19.6	1.75	1.75
100%	15.2	2.59	1.59

The values of the A and β fit parameters differ by an average of 3.8% between the purely-inelastic and 10% elastic cases. The difference rises to 22% for 50% elastic and 61% for 100% elastic. This indicates that the value of the A and β fit parameters depends on the elastic/inelastic partition. All values reported previously in this chapter assumed that broadening collisions were 100% inelastic. This brief exploration using the EGL-0 model indicates that the reported A and β values remain fairly constant for small elastic contributions to the pressure-broadening cross sections, but A and β begin to change significantly for large elastic contributions to the pressure-broadening cross sections. This brief exploration of the effect of broadening due to elastic collisions on the validity of the state-to-state fitting-law results reported previously in this chapter depend on the elastic component being negligible, on the order of 10% of the $J_i = 22$ broadening cross section.

The results of this study cannot definitively say whether pressure broadening is primarily caused be elastic or inelastic collisions. The inelastic, angular-momentum-transfer theory provides an appealing picture of the collisional process and provides a way to explain the J-dependence of the broadening cross sections. On the other hand, the elastic theory also demonstrated some successes in predicting the order of the intermolecular potential and describing the difference potentials. Furthermore, the elastic theory shows that the rotational behavior of the molecule, which influences the angular part of the intermolecular potential and alters the shape of the difference potential, may also be a mechanism to explain the J-dependence in the broadening cross sections. The current, almost universally-accepted view of molecular pressure broadening held by other researchers in this field is that inelastic collisions are the dominant mechanism. It is the belief of this researcher that inelastic collisions indeed determine the J-dependence of the broadening cross sections. However, elastic collisions may also contribute in some non-negligible way to the broadening cross sections. The elastic component may well be J-dependent; molecules in lower rotational states have energy levels which are more closely spaced, increasing the chances of a collision being inelastic. Molecules in higher rotational states, however, have energy levels which are spaced further apart, decreasing the chances of a collision being inelastic. The elastic/inelastic collision issue is a key area for further study.

5.4. Applicability of AM Fitting Law to O_2+Noble Gas Broadening Cross Sections

The final analysis performed in this study was an examination of the applicability of the AM fitting law of Osborne and McCaffery [86] to pressure broadening data. The

AM fitting law, described in Chapter II, was developed to fit rotationally-inelastic state-to-state rate data. Like the IOS and ECS laws, the AM fitting law was developed using angular-momentum transfer as the governing mechanism in rotationally-inelastic collision rates. However, unlike semi-empirical IOS and ECS laws, the AM fitting law was derived from first principles using the physics of classical momentum transfer. Osborne and McCaffery thus claim that the three fitting parameters $\{C, b_n^{max}, \gamma\}$ have direct physical significance, rather than the implied possible physical significance of the three ECS-P fitting parameters $\{A, \gamma, l_c\}$.

This study marks the first time the AM fitting law has been examined for its applicability to pressure broadening rate data. The semi-empirical fitting laws of the previous section were all able to be used to model total removal rate data because it had been shown by previous researchers [25, 123] in fits to state-to-state rates that the fitting parameters were all independent of initial rotational level. The three fitting parameters of the AM fitting law, however, have not been previously examined for the presence or absence of a J_i dependence. The first step in this exploration, then, was to analyze the J_i dependence of these fitting parameters.

There are physical reasons to expect that the fitting parameters for the AM fitting law may not be constant with J_i. The scaling parameter C is said to be related to the total removal rate. Since the total removal rate has been clearly shown to have a J_i dependence, one can expect C to have a dependence as well. The upper bound on the integral, b_n^{max}, is a measure of the maximum anisotropy of the potential and has been found to be related to the half-bond length of the diatomic, to a good approximation. At least two physical mechanisms may change this value. On one hand, as the diatom spins

faster, one expects centrifugal distortion to slightly increase the length of the bond, which would increase b_n^{max} with increasing J_i. On the other hand, as the diatom spins faster, the anisotropy may be averaged out since the perturber will see several degrees of rotation of the diatomic during the collisional interaction. Thus the approaching perturber may see a potential which is less angle-dependent, decreasing b_n^{max} with increasing J_i. It would be interesting if this is the observed effect, since the AM model was derived in the sudden approximation in which the diatomic does not rotate during the collision. Finally, the parameter γ represents the steepness of the potential. This parameter has been likened to the impulsive classical behavior of the γ parameter in the ECS-P law, in which the value of γ is related to the order of the intermolecular potential, independent of J_i. Thus there is reason to expect that C and b_n^{max} have some dependence on J_i, while γ does not.

Before the J_i dependence could be explored, however, the AM fitting law had to be coded and validated. Like the semi-empirical inelastic fitting laws of the previous section, the AM fitting law was coded using Mathematica; a typical example of the model is included in Appendix H. The code implements Equation (58) of Chapter II, together with the required additional equations from Chapter II which describe the probability density functions and the conservation of momentum and energy. Like the previous models, the AM fitting law model uses the Levenberg-Marquardt nonlinear least squares routine. Unlike the previous models, the AM fitting law is purely a state-to state model which calculates upward rates out of a single initial rotational quantum number. The AM fitting law has never been used to calculate downward rates, so it is unknown whether the predictions of this model are consistent with detailed balance. Because of the complexity of the integral calculations in the model, the AM fitting law code requires

about two hours to run on a 200 MHz Pentium PC, even though it is calculating a much smaller subset of the problems calculated in the total-removal-rate models of the previous section.

After creating the AM fitting law in Mathematica, it was validated by producing a fit to the I_2^*+Xe, $J_i = 41$ state-to-state rates reported by Dexheimer *et al.* [35]. This same data set was fit by Osborne and McCaffery [86] to test their version of the AM fitting law. Three different fits to this data were performed:

(1) a weighted fit with b_n^{max} and γ fixed to the values reported by Osborne and McCaffery, allowing only the scaling parameter C to vary,

(2) a weighted fit with all three parameters allowed to vary,

(3) a non-weighted fit with all three parameters allowed to vary.

The three fits are graphed vs. the data in Figure 82 and the resulting fitting parameters from the different methods are compared to the values from Osborne and McCaffery in Table 28.

The weighted fit with b_n^{max} and γ constrained is meant to replicate the fit reported by Osborne and McCaffery, permitting a comparison with the two unconstrained fits. The fit could not be replicated with the C parameter constrained as well, because this produced a fit which was much lower than the data. The scaling parameter C is supposed to include a normalization of the probability density integrals which Osborne (private communication) [84] indicates is not yet correct as reported in the literature and is still being studied.
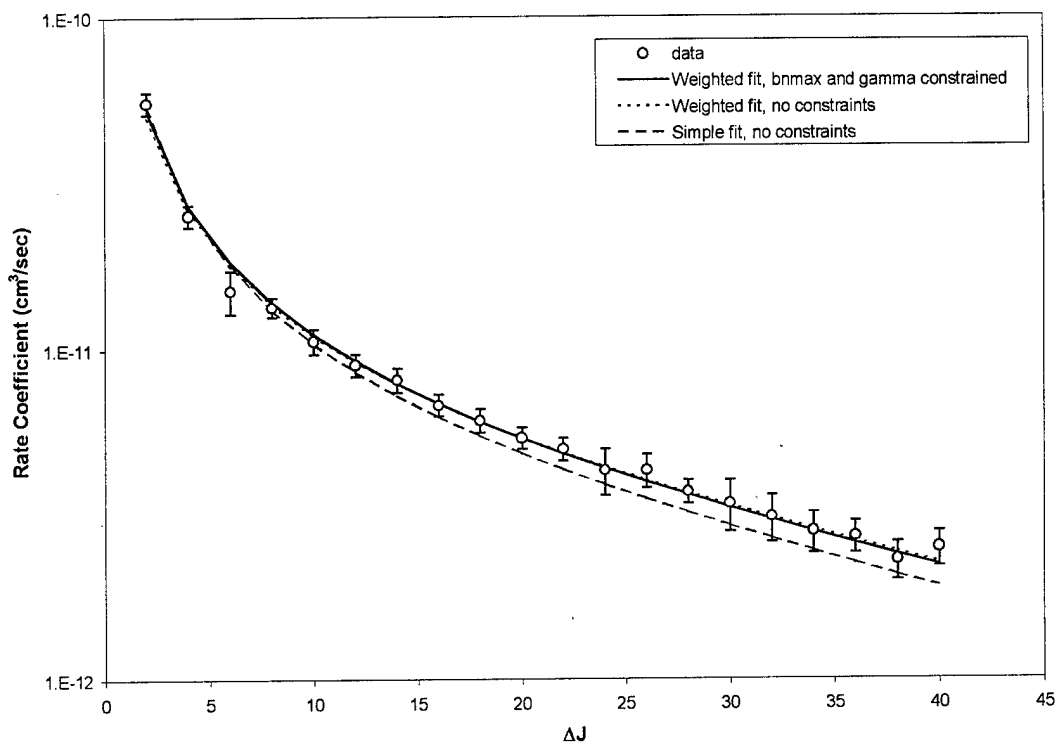
Figure 82. I_2^*+Xe, J_i = 41 Data from Dexheimer *et al.* [35] Fit with the AM Fitting Law in Three Different Ways

Table 28. Values of Fitting Parameters and Reduced Chi-Squared for Three Different Fits to the I_2^*+Xe, J_i = 41 Data of Dexheimer *et al.* [35] Compared to the Fit Reported by Osborne and McCaffery (OM) [86]

	C ($\times 10^{-13}$ cm^3/s)	b_n^{max} (Å)	γ	χ^2/ν
Reported values from OM	2079	1.63	1.94	0.37
Weighted fit with b_n^{max} and γ fixed to MO values	3888	1.63 (fixed)	1.94 (fixed)	0.37
Difference from OM	+87%	–	–	–
Weighted fit with no constraints	6173	1.60	1.92	0.32
Difference from OM	+197%	−1.8%	−1.0%	−14%
Simple fit with no constraints	998	1.64	2.00	N/A
Difference from OM	−52%	+0.6%	+3.1%	–

214

The weighted fit with no constraints matches the fit of Osborne and McCaffery (represented by the weighted fit with b_n^{max} and γ constrained) to better than 5%, while the non-weighted fit with no constraints has discrepancies of up to 14%, with the worst deviations occurring at large ΔJ where the magnitudes of the rates are small. Thus, a weighted nonlinear least-squares fit is required. As Table 28 indicates, the weighted fit with no constraints produces values for b_n^{max} and γ which are less than 2% different from the values reported by Osborne and McCaffery. The reduced chi-squared for this fit is 14% smaller, indicating that this is statistically a slightly better fit to the data than that reported by Osborne and McCaffery. The non-weighted fit also returns values of b_n^{max} and γ which are less than 4% different than the values reported by Osborne and McCaffery. However, because of the deviation at high ΔJ shown in Figure 82 and because a non-weighted fit does not produce a reduced chi-squared for assessing goodness-of-fit, the weighted fit is preferred and was used for all other work with the AM fitting law.

For additional validation, the AM fitting law was fit to I_2^*+He, $J_i = 41$ data from Dexheimer et al. [35] and Li_2^*+Ar, $J_i = 8$ data from Scott et al. [111] and compared to results reported by Osborne and McCaffery [86]. In both cases, fits were performed with all three parameters unconstrained and with b_n^{max} and γ constrained to replicate the results of Osborne and McCaffery. Some fits were also performed with just b_n^{max} or γ constrained to observe the effects on the results. In all cases, the fits were weighted by

215

the reported uncertainties in the state-to-state data. The results of these two additional

validations of the AM fitting law are listed in Tables 29 and 30.

Table 29. Values of Fitting Parameters and Reduced Chi-Squared for Fits to the I_2^*+He, J_i = 41 Data of Dexheimer *et al.* [35] Compared to the Fit Reported by Osborne and McCaffery (OM) [86]

	C ($\times 10^{-13}$ cm^3/s)	b_n^{max} (Å)	γ	χ^2/ν
Reported values from OM	3011	1.46	1.92	0.76
Weighted fit with b_n^{max} and γ fixed to MO values	9033	1.46 (fixed)	1.92 (fixed)	0.72
Difference from OM	+200%	–	–	–5.3%
Weighted fit with no γ fixed to MO value	9189	1.44	1.92 (fixed)	0.66
Difference from OM	+205%	–1.4%	–	–13%
Weighted fit with no b_n^{max} fixed to MO value	11060	1.46 (fixed)	1.91	0.70
Difference from OM	+267%	–	–0.5%	–7.9%
Weighted fit with no constraints	23720	1.41	1.87	0.55
Difference from OM	+690%	–3.4%	–2.6%	–28%

The Mathematica version of the AM fitting law produced fits to the I_2^*+He,

J_i = 41 data with b_n^{max} and γ values which agree with those reported by Osborne and

McCaffery to within 4%. The fits to the Li_2^*+Ar, J_i = 8 data produced values of b_n^{max} and

γ which agree with those reported by Osborne and McCaffery to within 9%. There are no

apparent systematic trends to the discrepancies. For I_2^*+Xe, the value of C was low,

while b_n^{max} and γ were a bit high. On the other hand, for I_2^*+He and Li_2^*+Ar, the C

216

values were high while b_n^{max} and γ were low. In general, there appears to be a trade-off

between small changes in b_n^{max} or γ and large compensating changes in C.

Table 30. Values of Fitting Parameters and Reduced Chi-Squared for Fits to the Li_2^*+Ar, $J_i = 8$ Data of Scott *et al.* [111] Compared to the Fit Reported by Osborne and McCaffery (OM) [86]

	C ($\times 10^{-13}$ cm^3/s)	b_n^{max} (Å)	γ	χ^2/ν
Reported values from OM	4540	0.71	2.05	0.66
Weighted fit with b_n^{max} and γ fixed to MO values	2613	0.71 (fixed)	2.05 (fixed)	1.72
Difference from OM	−42%	−	−	+161%
Weighted fit with γ fixed to MO value	2675	0.69	2.05 (fixed)	1.61
Difference from OM	−41%	−2.8%	−	+144%
Weighted fit with no constraints	28046	0.65	1.93	1.29
Difference from OM	+518%	−8.5%	−5.9%	+95%

After the Mathematica implementation of the AM fitting law was validated, the

code was used to explore the J_i-dependence of the law. This has not been done

previously; Osborne and McCaffery showed the success of the AM fitting law for a wide

range of absorbers and perturbers but fit each collision pair for only one value of J_i [86].

The exploration in the current study was performed using state-to-state data from the

literature for which values from more than one J_i were reported. One such data set is the

I_2^*+Xe data of Dexheimer *et al.* [35], which was reported for $J_i = 41, 81, 91,$ and 113.

The fits were performed twice, once with γ fixed to the value reported by Osborne and

McCaffery for $J_i = 41$ and again with all three parameters unconstrained. The fitting parameters and reduced chi-squared values from these two runs are listed in Tables 31 and 32.

Table 31. Values of Fitting Parameters and Reduced Chi-Squared for Fits to the I_2^*+Xe Data of Dexheimer *et al.* [35] with the Fitting Parameter γ Held Constant

	C ($\times 10^{-13}$ cm^3/s)	b_n^{max} (Å)	γ	χ^2/ν	# data points
$J_i = 41$	3888	1.63	1.94	0.37	20
$J_i = 81$	2782	1.03	1.94	0.72	15
$J_i = 91$	2703	0.85	1.94	0.85	11
$J_i = 113$	2391	0.92	1.94	2.83	7
Apparent trend with J_i	decreasing	decreasing	(fixed)		

Table 32. Values of Fitting Parameters and Reduced Chi-Squared for Fits to the I_2^*+Xe Data of Dexheimer *et al.* [35] with No Fitting Parameters Constrained

	C ($\times 10^{-13}$ cm^3/s)	b_n^{max} (Å)	γ	χ^2/ν	# data points
$J_i = 41$	6173	1.60	1.92	0.32	20
$J_i = 81$	12231	0.78	1.87	0.41	15
$J_i = 91$	15659	0.85	1.85	0.42	11
$J_i = 113$	180846	0.40	1.73	0.42	7
Apparent trend with J_i	increasing	decreasing	decreasing		

In the fits with γ constrained, both C and b_n^{max} show a gently decreasing trend with increasing J_i. In the unconstrained fits, the values of γ for $J_i = 81$ and 91 differ by less than 4% from the value for $J_i = 41$, while the value for $J_i = 113$ differs by less than 8% from the average of the first three values. The huge increase in C with J_i occurs because small changes in γ cause large compensating changes in the scaling parameter C.

The small value of b_n^{max} also contributes to the large value of C for that fit. Based on these results, it can be argued that γ is constant with J_i, while C and b_n^{max} are J_i-dependent. Unfortunately, the number of data points available for the fit decreases with increasing J_i, so it becomes more difficult to fit the data with a high degree of certainty as J_i increases.

The next data set examined was the I_2^*+He data of Dexheimer *et al.* [35], which was reported for $J_i = 41$ and 91. The fits were again performed twice, once with γ fixed to the value reported by Osborne and McCaffery for $J_i = 41$ and again with all three parameters unconstrained. The fitting parameters and reduced chi-squared values from these two runs are listed in Tables 33 and 34.

Table 33. Values of Fitting Parameters and Reduced Chi-Squared for Fits to the I_2^*+He Data of Dexheimer *et al.* [35] with the Fitting Parameter γ Held Constant

	C ($\times 10^{-13}$ cm^3/s)	b_n^{max} (Å)	γ	χ^2/ν	# data points
$J_i = 41$	9189	1.44	1.92	0.66	20
$J_i = 91$	8878	1.45	1.92	0.33	11
Difference	−3.4%	+0.7%	−		
Apparent trend with J_i	~ constant	~ constant	(fixed)		

Table 34. Values of Fitting Parameters and Reduced Chi-Squared for Fits to the I_2^*+He Data of Dexheimer *et al.* [35] with No Fitting Parameters Constrained

	C ($\times 10^{-13}$ cm^3/s)	b_n^{max} (Å)	γ	χ^2/ν	# data points
$J_i = 41$	23720	1.41	1.87	0.55	20
$J_i = 91$	9977	1.44	1.91	0.33	11
Difference	−58%	+2.1%	+2.1%		
Apparent trend with J_i	decreasing	~ constant	~ constant		

For I_2^*+He with γ fixed, both C and b_n^{max} are effectively constant, differing by less than 4% between J_i = 41 and 91. When γ is unconstrained, it still stays effectively constant, differing by only about 2% between J_i = 41 and 91. The value of b_n^{max} also remains constant to within about 2% for the unconstrained fit. Only C shows a clear decrease in this case and this large decrease in C may be more indicative of the sensitivity of the C parameter to small changes in b_n^{max} and γ rather than an actual physical decrease in the total removal rate. Based on the O_2+He and NO+He broadening cross sections measured in the current study, the I_2+He total removal rate would not be expected to decrease by almost 60% between J_i = 41 and 91. The lack of apparent J_i dependence in b_n^{max} is likely due to the sudden nature of the I_2+He collision. Again it can be argued that γ is J_i independent, just as for I_2+Xe.

The third and final data set examined was the Li_2^*+Ar data of Scott et al. [111], which was reported for J_i = 8 and 22. Once again, the fits were performed twice, once with γ fixed to the value reported by Osborne and McCaffery for J_i = 8 and again with all three parameters unconstrained. The fitting parameters and reduced chi-squared values from these two runs are listed in Tables 35 and 36.

Table 35. Values of Fitting Parameters and Reduced Chi-Squared for Fits to the Li_2^*+Ar Data of Scott et al. [111] with the Fitting Parameter γ Held Constant

	C ($\times 10^{-13}$ cm^3/s)	b_n^{max} (Å)	γ	χ^2/ν	# data points
J_i = 8	2675	0.69	2.05	1.61	16
J_i = 22	1462	0.52	2.05	1.20	8
Difference	−45%	−25%	−		
Apparent trend with J_i	decreasing	Decreasing	(fixed)		

Table 36. Values of Fitting Parameters and Reduced Chi-Squared for Fits to the Li_2^*+Ar Data of Scott *et al.* [111] with No Fitting Parameters Constrained

	C ($\times 10^{-13}$ cm³/s)	b_n^{max} (Å)	γ	χ^2/ν	# data points
$J_i = 8$	28046	0.65	1.93	1.29	16
$J_i = 22$	1082	0.53	2.06	1.19	8
Difference	−96%	−18%	+6.7%		
Apparent trend with J_i	decreasing	decreasing	increasing		

For Li_2^*+Ar with γ fixed, both C and b_n^{max} are clearly decreasing, by 45% and 25%, respectively. When γ is unconstrained, it still stays effectively constant, differing by less than 7% between $J_i = 8$ and 22. In the unconstrained case, C decreases quite a bit more than in the constrained fit, while b_n^{max} decreases a bit less. The large decrease in C for the unconstrained fit again is more likely a result of a compensation in C due to small changes in b_n^{max} and γ rather than an actual physical decrease in the total removal rate. The 45% drop of the γ-constrained fit is much more believable for a decrease in total removal rate than the 96% drop of the unconstrained case. The decrease in b_n^{max} with increasing J_i is large enough in both cases to be significant.

Looking at the fits to the three different collision pairs, it appears a reasonable assumption that γ is independent of the initial rotational state of the molecule; an assumption which concurs with the physical picture of γ as a description of the steepness of the intermolecular potential. The b_n^{max} parameter, which relates to the anisotropy of the potential, appears to remain constant for a short-duration collision and to increase with J_i for interactions of longer duration. This is consistent with the idea that rapid rotation of the molecule during a collision of finite duration tends to average out the

221

anisotropy of the potential. Finally, the C parameter has been observed to vary with J_i, sometimes dramatically. For the fits in which γ is constrained, C appears to decrease with J_i at approximately the same rate the broadening cross sections would decrease with J_i. This lends support to the claim that C is related to the total removal rate. The behavior of C when γ is unconstrained varies much more wildly, which is more likely due to the sensitivity of C to small changes in γ and b_n^{max} rather than to changes in the total removal rate. It appears safe to conclude that γ is independent of J_i, while C and b_n^{max} have a J_i dependence, and that the best values of C and b_n^{max} are obtained when γ is fixed in the fit.

Since the parameters of the AM fitting law are apparently not all independent of initial rotational state, the AM fitting law cannot be combined with a sum rule to fit pressure broadening data as was done in the previous section with the semi-empirical fitting laws. To apply the AM fitting law directly to pressure broadening data, one would need to have analytical expressions to describe how C and b_n^{max} vary as functions of J_i. The current research project has not developed such analytical expressions, but the observations made about the J_i dependence may lead to the development of such expressions in the future.

The AM fitting law has been shown, however, to work well on state-to-state data for a single initial rotational level. In the last analysis of this research project, the semi-empirical fitting laws of the previous section were used to generate synthetic state-to-state data from the total removal rates for oxygen with the noble gases. This synthetic data was then modeled using the AM fitting law to see to what extent the retrieved fitting parameters made physical sense.

For the oxygen data set, there are 22 initial rotational energy levels, ten perturbing species, and ten different semi-empirical fitting laws, for a possible total of 2200 different synthetic state-to-state data sets which could be generated. To reduce this to a manageable number, the set was first restricted to just the five noble gases and just the six most successful fitting laws: EGL-0, SPG-0, SPG-Δ, EPGL-0, EPGL-Δ, and ECS-P. To see how the state-to state rates differ for each fitting law, the synthetic state-to-state rates for O_2+Ar, J_i = 15, were plotted for the six fitting laws. This is shown in Figure 83. For all synthetic state-to-state data sets, all even values of ΔJ up to 30 were calculated. Since the AM fitting law only works for upward rates, the downward rates are not displayed.
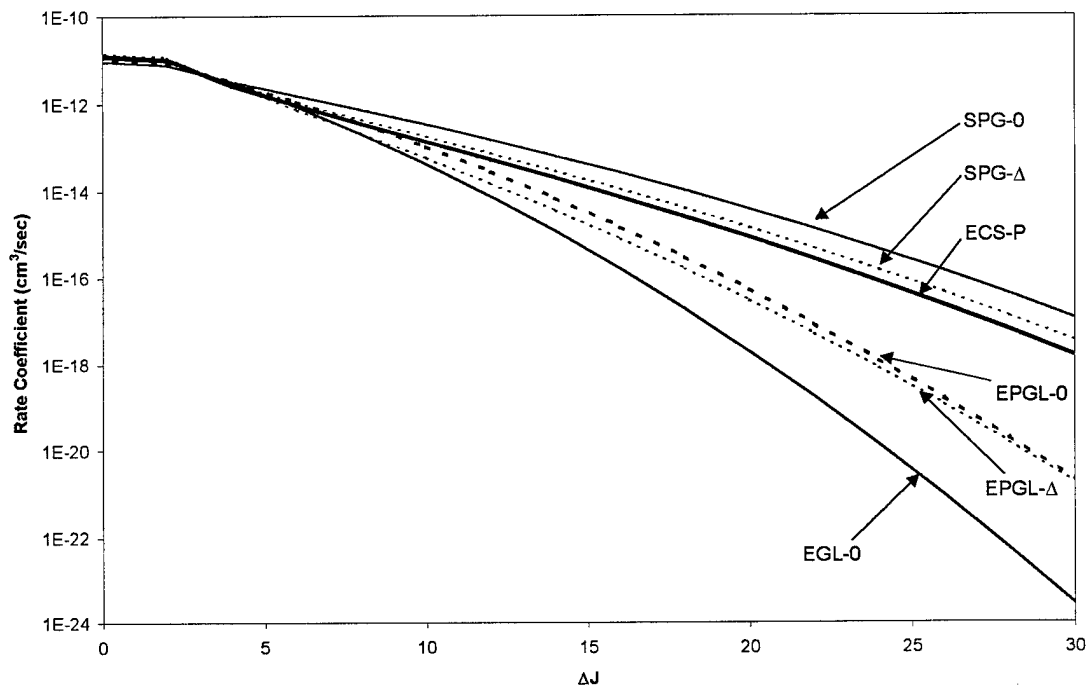
Figure 83. Synthetic State-to-State Rates for O_2+Ar, J_i = 15, Generated from Total Removal Rates Using Six Different Semi-Empirical Fitting Laws

Figure 83 shows that the synthetic state-to-state rates fall into three groups. The SPG-0, SPG-D, and ECS-P rates are at the top of the plot. The rates from these three models fall off the slowest with increasing ΔJ. The synthetic rates from each of the three models also appear to have the same slope for most of the plot, differing only by a scaling factor. This is consistent with the observations of Brunner and Pritchard [25] that the ECS-P and SPG laws are all power-law fits and share several mathematical similarities, even though they are derived based on very different mechanisms (energy transfer vs. momentum transfer). The EGL-0 law is at the bottom of the Figure 83, indicating that rates from the exponential-law fits drop the most rapidly with increasing ΔJ. Between the power-law fits and the exponential fit are the two EPGL law fits. This is a reasonable location for these rates, since the EPGL laws are hybrid of the exponential and power-law models.

Figure 83 clearly shows large differences in the predicted state-to-state rates by using different laws to fit the observed total removal rates. The rates from the power-law fits fall about five orders of magnitude from $\Delta J = 0$ to 30, while the rates from the exponential-law fits fall about twelve orders of magnitude. To help to choose which of these laws to use, the quality of the fit to the broadening cross sections by each law was considered. The EGL-0 model was the worst of the models used, so the synthetic EGL-0 rates were not used. The EPGL-0 and EPGL-Δ models both fit the observed data very well, with the EPGL-0 model fitting just slightly better. The ECS-P law also produced very good fits to the pressure broadening data, much better than the SPG laws. Therefore, the EPGL-0 and ECS-P laws were used to generate synthetic state-to-state data for oxygen broadened with the noble gases.

To further reduce the data set, data for only three of the five noble gases, He, Ar, and Xe, were used. Results for Ne would be expected to fall between He and Ar, while results for Kr would fall between Ar and Xe. Finally, rates were calculated for only a few initial rotational levels. For O_2+He, rates were generated for J_i = 1, 10, and 20. For O_2+Ar, synthetic rates were generated for J_i = 1, 5, 10, 15, and 20. Finally, for O_2+Xe, rates were generated for J_i = 1 and 19.

Since it was found during the validation of the AM fitting law code that weighted fits produced better results than simple fits, a method was developed to place an approximate weight on each synthetic data point. Looking at the I_2^*+Xe data used in the validation, it was found that the uncertainty on each measurement was between 6.7% and 17.6%, with average uncertainty of 10.6%. It was thus decided that a good approximation was to give each synthetic data point an equal percent error; a 10% error was chosen. Because the magnitude of the error is rather arbitrary, the reduced chi-squared values returned from the fits to these synthetic data sets have no absolute meaning. However, they serve as a good relative indicator of the quality of the fit.

The general fitting procedure was to start by fixing b_n^{max} to the half-bond length of O_2, which is 0.604 Å [130], and to find the best combination of C and γ for this value of b_n^{max}. Next, b_n^{max} was allowed to vary; it was usually observed to jump rapidly to a value more consistent with the current values of C and γ. Then b_n^{max} was fixed to this new value and C and γ allowed to find a new best combination. This method of alternately constraining and unconstraining b_n^{max} was followed until the reduced chi-squared reached a stable value; an interactive procedure which took several hours for each data set. Even though it was found during the exploration of the J_i-dependence of

225

the parameters that the fits produced the best results when γ was fixed, there was no

convenient theoretical value to use to constrain it. The γ parameter was thus allowed to

vary for these fits with the understanding that C would likely show large variations as a

result.

The results of these fits are shown in the next several tables. Tables 37 lists the

results from AM fits to synthetic O_2+He data generated by the ECS-P law, while Table

38 reports the results to AM fits from EPGL-0-generated data.

Table 37. Values of Fitting Parameters and Reduced Chi-Squared for Fits to Synthetic
State-to-State Rates for O_2+He Generated by the ECS-P Fitting Law

	C ($\times 10^{-13}$ cm^3/s)	b_n^{max} (Å)	γ	χ^2/ν
$J_i = 1$	4.16	1.22	2.24	0.35
$J_i = 10$	1.82	1.07	2.24	1.03
$J_i = 20$	2.22	0.94	2.20	2.91
Apparent trend with J_i	~ decreasing	decreasing	~ constant	

Table 38. Values of Fitting Parameters and Reduced Chi-Squared for Fits to Synthetic
State-to-State Rates for O_2+He Generated by the EPGL-0 Fitting Law

	C ($\times 10^{-13}$ cm^3/s)	b_n^{max} (Å)	γ	χ^2/ν
$J_i = 1$	54900	0.93	1.77	0.68
$J_i = 10$	11.6	0.78	2.16	1.61
$J_i = 20$	0.53	0.64	2.28	7.01
Apparent trend with J_i	decreasing	decreasing	increasing	

Based on the relative magnitudes of the reduced chi-squared values and the behavior of

the parameter values, the AM fitting law appears to produce better fits to synthetic data

generated by the ECS-P law. Further, the γ parameter in the ECS-P law data is approximately constant with J_i, while γ in the EPGL-0 data appears to be increasing. The constant value of γ in the ECS-P data is more consistent with the expected results. An impulsive classical calculation predicts $\gamma = 2.4$ for an r^{-6} potential, with slightly smaller values of γ for higher-order potentials. Thus, for the quadrupole-induced dipole potential expected for the O_2+noble gas interaction, one expects the value of γ to be just slightly less than 2.4. The values in Tables 37 and 38 are in the range from 1.77 to 2.24, which is consistent with the impulsive classical prediction. In both Table 37 and Table 38, b_n^{max} decreases with increasing J_i. This is the same behavior which was observed in the fits to the actual state-to-state data discussed previously. Interestingly, all values of b_n^{max} are larger than the half-bond length of O_2, which is contrary to the predictions of Osborne and McCaffery. Finally, the C parameter appears to be decreasing in the fits to both data sets, though the decrease is much smaller in the ECS-P data. Since the actual decrease in the O_2+He total removal rates with J_i is small compared to the other perturbers studied, the ECS-P data again appears to be more consistent with the expected trends.

Tables 39 and 40 present the results of the AM fitting law to data generated from the ECS-P and EPGL-0 laws, respectively. However, only the $J_i = 1$ data from the ECS-P law was fit using the constrained/unconstrained b_n^{max} procedure described previously. The remaining results were obtained using an unconstrained procedure which produced unreliable results for C. This procedure may have also moderately affected (10-20%) the values of b_n^{max} and γ.

227

Table 39. Values of Fitting Parameters and Reduced Chi-Squared for Fits to Synthetic State-to-State Rates for O_2+Ar Generated by the ECS-P Fitting Law

	C ($\times 10^{-13}$ cm^3/s)	b_n^{max} (Å)	γ	χ^2/ν
$J_i = 1$	0.099	0.52	2.42	0.43
$J_i = 5$ *	–	0.46	1.87	5.72
$J_i = 10$ *	–	0.43	1.85	8.28
$J_i = 15$ *	–	0.41	1.83	10.3
$J_i = 20$ *	–	0.39	1.81	11.8
Apparent trend with J_i	–	decreasing	decreasing ?	

* poor fitting procedure; C parameter is incorrect, which may also affect b_n^{max} and γ

Table 40. Values of Fitting Parameters and Reduced Chi-Squared for Fits to Synthetic State-to-State Rates for O_2+Ar Generated by the EPGL-0 Fitting Law

	C ($\times 10^{-13}$ cm^3/s)	b_n^{max} (Å)	γ	χ^2/ν
$J_i = 1$ *	–	0.36	1.93	1.50
$J_i = 5$ *	–	0.33	1.90	0.60
$J_i = 10$ *	–	0.29	1.87	4.50
$J_i = 15$ *	–	0.26	1.85	14.6
$J_i = 20$ *	–	0.24	1.83	28.5
Apparent trend with J_i	–	decreasing	decreasing ?	

* poor fitting procedure; C parameter is incorrect, which may also affect b_n^{max} and γ

The reduced chi-squared values clearly show that the fits become increasingly poor with increasing J_i, making it difficult to assign J_i-dependent trends with certainty. The value of b_n^{max} appears to be decreasing in both the ECS-P and EPGL-0 data, in agreement with previous observations. The values of b_n^{max} are all less than the half-bond length of O_2. This is consistent with the theory, since the torque arm must be less than the half-bond length to conserve energy when the colliding atom is more massive than the diatomic. The values of γ could be argued to be constant for both models, though they appear to be

slightly decreasing (3-5% from $J_i = 1$ to 20). The magnitude of γ is between 1.81 and

2.42, which is again reasonably consistent with the impulsive classical prediction.

Because of the problems with the fitting procedure, it is difficult to conclude whether the

ECS-P or EPGL-0 data appears to be more consistent with the AM model of rotational

transfer.

The results of the AM fitting law fits to the O_2+Xe synthetic data generated by the

ECS-P and EPGL-0 laws are listed in Tables 41 and 42. The constrained/unconstrained

b_n^{max} procedure was used for all of these fits. However, significant problems were

encountered with the $J_i = 19$ fits. In an attempt to improve the results for $J_i = 19$, both

weighted and non-weighted fits were performed. The weighted fits emphasize data at

large ΔJ, while the non-weighted fits emphasize data at small ΔJ. It was hoped that one

or the other of these methods would yield clues to the behavior of the O_2+Xe system at

high J_i.

Table 41. Values of Fitting Parameters and Reduced Chi-Squared for Fits to Synthetic
State-to-State Rates for O_2+Xe Generated by the ECS-P Fitting Law

	C ($\times 10^{-13}$ cm^3/s)	b_n^{max} (Å)	γ	χ^2/ν
$J_i = 1$	1.47	0.44	2.29	0.48
$J_i = 19$ (weighted)	1.45	0.096	2.28	120
$J_i = 19$ (non-weighted)	0.035	0.23	2.42	57
Apparent trend with J_i	decreasing	decreasing	~ constant	

The high-J_i runs did not fit well under any circumstances, so it is difficult to say

much about any J_i dependence from these results. However a few observations can still

229

Table 42. Values of Fitting Parameters and Reduced Chi-Squared for Fits to Synthetic State-to-State Rates for O_2+Xe Generated by the EPGL-0 Fitting Law

	C ($\times 10^{-13}$ cm^3/s)	b_n^{max} (Å)	γ	χ^2/ν
$J_i = 1$	45.8	0.36	2.14	5.04
$J_i = 19$ (weighted)	0.041	0.36	2.19	91
$J_i = 19$ (non-weighted)	239	0.21	2.00	43
Apparent trend with J_i	?	decreasing ?	~ constant	

be made. The γ parameter is approximately constant and is in the range from 2.00 to 2.42, consistent with the impulsive classical prediction. The b_n^{max} parameter appears to decrease with increasing J_i and is at all times less than the half-bond length of O_2, as required for conservation of energy when the perturber is more massive than the diatom. This decrease of the impact parameter with increasing J is also consistent with the difference potentials calculated using the elastic theory. Trends in the values of the C parameter are not possible to infer because of the difficulties in fitting the high-J_i data. It is also not possible to say whether the ECS-P or EPGL-0 data is more consistent with the AM fitting law model.

Finally, the perturber-dependence of the fitting parameters from the AM fitting law was examined. Table 43 collects the values for $J_i = 1$ from the ECS-P data for O_2+He, Ar, and Xe. The value of γ appears to be approximately constant with perturber and less than or equal to 2.4. Thus γ appears to be both perturber-independent and reasonably consistent with the impulsive classical value of $\gamma < 2.4$ predicted for an r^{-7} intermolecular potential. The value of b_n^{max} decreases with increasing perturber mass, which is consistent with conservation of energy requirements. There are no apparent trends in the

value of C, which is probably due to the extreme sensitivity of C to small changes in b_n^{max} and γ.

Table 43. Values of Fitting Parameters and Reduced Chi-Squared for Fits to Synthetic State-to-State Rates for O_2+Noble Gases, $J_i = 1$, Generated by the ECS-P Fitting Law

	C ($\times 10^{-13}$ cm^3/s)	b_n^{max} (Å)	γ	χ^2/v
He	4.16	1.22	2.24	0.35
Ar	0.099	0.52	2.42	0.43
Xe	1.47	0.44	2.29	0.48
Apparent trend with perturber	?	decreasing	~ constant	

In summary, the AM fitting law of Osborne and McCaffery cannot be directly applied to pressure broadening data in the same manner as the semi-empirical fitting laws because of the dependence of the fitting parameters on the initial rotational state of the molecule. However, the application of the AM fitting law to synthetic state-to-state data generated by the ECS-P and EPGL-0 fits to the O_2+noble gas pressure broadening coefficients indicates that the AM fitting law parameters are consistent with the expected physics, even for this roundabout method. The fact that the parameters retrieved from the AM fitting law are even close to the expected values indicates that the ECS-P and EPGL-0 laws fit the pressure broadening cross sections well. This provides an additional measure of confidence in the reported ECS-P and EPGL-0 fits reported in the previous section. However, the orders-of-magnitude differences in the synthetic RT rate coefficients generated from the various empirical fits to the pressure broadening cross sections shows that total removal rates cannot be used to infer state-to-state rates.

The important step which must be taken if the AM fitting law is to be used directly on pressure broadening data is the development of expressions for the J_i-dependence of the fitting parameters C and b_n^{max}. Hopefully, the observations of the current study are the first steps down the road to discovering these relations.

VI. Summary, Conclusions, and Recommendations

This study used a Fourier transform spectrometer to measure a large number of rotational spectra of the oxygen A band and the nitric oxide fundamental band, each broadened with several perturbers at a range of bath gas pressures. The primary advantage of FTS for this research was the ability to collect data over a wide spectral range at high resolution. This allowed the simultaneous acquisition of an entire ro-vibrational band with enough resolution to measure line broadening as a function of J and as a function of bath gas pressure. The FTS technique offers much better resolution than is achievable with a grating spectrometer, while the simultaneous acquisition of an entire ro-vibrational band makes this technique more appropriate than laser spectroscopy for J-dependent broadening studies.

This study reports broadening coefficients for the oxygen A band in collisions with five noble gases and with the molecules N_2, CO, O_2, CO_2, and SF_6. Additionally, pressure-induced line shifting coefficients are reported for O_2+Xe. This study presents the first reported measurement of pressure broadening in the oxygen A band using Fourier transform spectroscopy. Previously, only O_2 self- and air-broadening have been studied in any systematic manner by any measurement technique. The O_2+O_2 broadening coefficients reported in the current study are well within the range of values determined by previous researchers using other measurement techniques. This provides a strong measure of confidence for both the FTS measurements and the subsequent analysis techniques used in the current study. Thus the high-precision measurements of the

broadening coefficients for O_2 in collisions with the five noble gases and with the molecules N_2, CO, CO_2, and SF_6 are a new contribution to the field. Line shifting coefficients in the oxygen A band have not previously been measured using FTS, so the O_2+Xe shifting coefficients are also a significant contribution to the pressure broadening literature.

In the nitric oxide fundamental band, this study reports broadening coefficients in the P and R branches for collisions with five noble gases. Previously, only NO+Ar had previously been studied in any systematic manner. The results of the three previous systematic studies are 9 - 18% lower than the results of the current study. However, two of these previous studies used techniques of lower precision than the FTS technique of the current study, and the third actually measured the first overtone rather than the fundamental band, so the discrepancies are reasonable. Thus, this study presents the first systematic study of the NO fundamental band broadened with the five noble gases. This study also presents the first results of NO+Ar broadening in the Q branch and the first report of line coupling the Q branch of NO measured by infrared spectroscopy.

The shapes and widths of spectral lines are important for several reasons. The Air Force relies on absorption or emission spectra collected from satellites and other sensor platforms to measure such atmospheric parameters as temperature, pressure, humidity, and abundance of various molecular species. These measurements are then used in such diverse applications as meteorology, remote monitoring of pollutants or effluent signatures, and determination of transmission windows for laser propagation in the atmosphere. Since the O_2 and NO broadening coefficients from this study are new and of high precision, they are directly useful; they will be submitted to the Air Force Research

Laboratory for possible inclusion in the HITRAN [56] atmospheric transmission database. Lineshape parameters in the HITRAN database are used by the Air Force and by other atmospheric researchers to model the atmosphere and to interpret remote-sensing measurements.

In general, the Air Force has a strong interest in chemical kinetics, since an understanding of reaction rates and energy transfer processes is necessary to model everything from lasers to chemical explosives to plasmas. The collisional transfer of energy among rotational-vibrational states is described by state-to-state rate coefficients. While precise values of these state-to-state rate coefficients are vital to modeling processes such as rocket fuel combustion and chemical laser operation, the necessary coefficients are very difficult and time-consuming to measure. On the other hand, it is relatively easy to simultaneously measure pressure broadening rate coefficients for an entire rotational-vibrational band. If a set of pressure broadening coefficients could be used to generate state-to-state rate coefficients, this would be a great help to the modeling of many important kinetic processes.

This research project shows some ways that pressure-broadening coefficients may be related to the state-to-state rate coefficients. Specifically, this study applied inelastic RT fitting laws which contain state-to-state information to pressure broadening rates in the oxygen A band. This is also the first known application of semi-empirical inelastic RT fitting laws to pressure broadening with a large number of perturbers, which allowed the fitting parameters to be explored for physical significance.

The inelastic model of pressure broadening was explored using the rotational-transfer fitting laws. Of the ten semi-empirical fitting laws applied to the O_2 data, the

EPGL-0 and ECS-P laws fit the best. However, the fitting parameters of the EPGL-0 law were found to have no correlation with the physical parameters of the perturber, leaving this model apparently inadequate to describe the physical broadening mechanism. The ECS-P law, on the other hand, was found to correlate with perturber reduced mass and to predict the order of the intermolecular potential. Further, the results suggest a dependence on reduced mass consistent with an angular-momentum-transfer picture of pressure broadening. The inelastic models accurately followed the observed decrease in broadening coefficient with increasing J. A consistent inelastic-collision explanation for this dependence is that the increasing spacing between rotational levels with increasing J reduces the probability of an inelastic RT transfer, reducing the effective broadening probability.

An elastic-broadening theory, developed to describe pressure broadening in atoms, was also applied to the O_2 and NO broadening coefficients. Application of the elastic broadening theory found that the magnitude of the broadening cross section was strongly correlated with perturber parameters like polarizability and reduced mass, even for the molecular perturbers. The elastic theory applied to O_2 predicted an r^{-7} intermolecular potential, which was consistent with the expected quadrupole-induced dipole potential. The elastic theory, however, failed to predict a constant intermolecular potential for NO, which may be due to the asymmetry of the molecule. The elastic theory used in this study had no explicit J-dependence since the theory was developed to describe atomic broadening rather than molecular broadening. However, the angular part of the intermolecular potential was assumed to be constant in this analysis. In reality, the angular part of the intermolecular potential may depend on rotational quantum number, J.

236

Proper consideration of the angular part of the intermolecular potential may show that the elastic-broadening theory does indeed have a J-dependence.

The elastic model was also used to compute difference potentials for collisions between O_2 and Xe. It was found that the repulsive wall of the potential occurs at decreasing O_2-Xe separation distances with increasing J. According to the angular-momentum-based, inelastic-collision theory of Osborne and McCaffery [86], the atom-molecule collision occurs at the hard repulsive wall of the potential. If the collision occurs at the repulsive wall, then the elastic model indicates that the impact parameter decreases with increasing J. This decrease in impact parameter with increasing J may be a manifestation of elastic collisions, which may explain, in part, the observed decrease in broadening coefficient with increasing J.

The pressure-broadening coefficients from this study were also used to explore the AM fitting law of Osborne and McCaffery. This was the first study of the dependence of the AM fitting law parameters on the initial rotational level of the molecule. In the AM fitting law, two of the three fitting parameters were found to depend on the initial rotational quantum number, so this law cannot be directly applied to pressure broadening data. Of particular interest, the parameter b_n^{max} decreased with increasing J. Since the parameter b_n^{max} is the effective impact parameter, the decrease in impact parameter with increasing J in the AM model is consistent with the analysis of the difference potentials calculated from the elastic model. A possible mechanism for this is the averaging of the anisotropy at increasing J because the collision samples several degrees of rotation during the interaction (not a "sudden" collision, as postulated by the theory). The value of the fitting parameter γ appeared to be constant with J, which is

237

consistent with the explanation that γ represents the order of the intermolecular potential, a quantity which should be independent of J.

Although the AM fitting law could not be applied directly to the pressure broadening data, it was applied to synthetic state-to-state data generated by fitting the ECS-P and EPGL-0 laws to the O_2+noble-gas pressure-broadening cross sections. In fits to the synthetic data, the value of b_n^{max} decreased with increasing perturber mass, which is consistent with energy conservation requirements. The value of b_n^{max} also decreased with increasing J, which is consistent with the behavior of the AM model applied to state-to-state data from the literature and to the behavior of the difference potentials calculated from the elastic model. The value of the fit parameter γ remained relatively constant for a wide range of angular-momentum quantum numbers and perturber masses. Furthermore, the value was consistent with the value an r^{-7} intermolecular potential, which is the expected order of the O_2+noble-gas intermolecular potentials .

The results of this study cannot definitively say whether pressure broadening is primarily caused be elastic or inelastic collisions. The inelastic, angular-momentum-transfer theory provides an appealing picture of the collisional process and provides a way to explain the J-dependence of the broadening cross sections. On the other hand, the elastic theory also demonstrated some successes in predicting the order of the intermolecular potential and describing the difference potentials. Furthermore, the elastic theory shows that the rotational behavior of the molecule, which influences the angular part of the intermolecular potential and alters the shape of the difference potential, may also be a mechanism to explain the J-dependence in the broadening cross sections. The current, almost universally-accepted view of molecular pressure broadening held by other

238

researchers in this field is that inelastic collisions are the dominant mechanism. It is the belief of this researcher, based on an analysis of the sensitivity of RT fitting laws to the presence of a constant elastic component, that inelastic collisions determine the J-dependence of the broadening cross sections. However, elastic collisions may also contribute in some non-negligible way to the broadening cross sections. The elastic component may well be J-dependent; molecules in lower rotational states have energy levels which are more closely spaced, increasing the chances of a collision being inelastic. Molecules in higher rotational states, however, have energy levels which are spaced further apart, decreasing the chances of a collision being inelastic.

There are several possible areas for further study. First, it would be useful to more-closely examine the applicability of the elastic-collision model to pressure broadening in molecules. It would be interesting to discover why the elastic broadening theory predicts a J-independent intermolecular potential of the correct order for the oxygen A band but not for the nitric oxide fundamental band. A further exploration of the constant scaling term in the elastic broadening equation may discover a way to include J-dependent mechanism in the physical constants collected together in this single scaling parameter.

Another important further study in the theoretical understanding of the physics of collisional broadening would come from further study of the AM fitting law. The application of the AM fitting law to a large set of state-to-state data for many different collision pairs would help to further explore the J-dependence and collision partner dependence of the fitting parameters of this law. The data for this study could come from the literature or from new measurements. A complete understanding of the dependence

239

of the fitting parameters on the initial rotational level of the molecule could lead to a form of the AM fitting law which could be applied to pressure broadening data.

The most important follow-on experiment of all would be to find a molecule which can be studied by both state-to-state and pressure broadening experiments. Performing both experiments on the same molecule would allow a direct look at the connection between state-to-state rates and pressure broadening rates. The relative contributions of elastic and inelastic collisions could be assessed and the semi-empirical fitting laws could be rigorously tested. However, selection of a molecule which is amenable to both types of experiments is nontrivial. If this experiment could be performed, it would be the next logical step in devising a way to calculate state-to-state rate coefficients from experimental measurements of pressure-broadening coefficients.

Appendix A. Significant O_2 and NO Values from the Literature

Table 44 lists the line positions for the oxygen A band, as reported by Burch and Gryvnak [27]. These values were used in the analysis of the data in the current study.

Table 44. Oxygen A Band Line Positions from Burch and Gryvnak [27]

P Branch					R Branch				
Label	J''	J	K''	Position (cm^{-1})	Label	J''	J	K''	Position (cm^{-1})
$^PP(21)$	21	20	21	13041.111	$^RR(1)$	1	2	1	13126.384
$^PQ(21)$	20	20	21	13042.934	$^RQ(1)$	2	2	1	13128.261
$^PP(19)$	19	18	19	13050.467	$^RR(3)$	3	4	3	13131.485
$^PQ(19)$	18	18	19	13052.309	$^RQ(3)$	4	4	3	13133.434
$^PP(17)$	17	16	17	13059.453	$^RR(5)$	5	6	5	13136.204
$^PQ(17)$	16	16	17	13061.313	$^RQ(5)$	6	6	5	13138.191
$^PP(15)$	15	14	15	13068.069	$^RR(7)$	7	8	7	13140.559
$^PQ(15)$	14	14	15	13069.949	$^RQ(7)$	8	8	7	13142.574
$^PP(13)$	13	12	13	13076.316	$^RR(9)$	9	10	9	13144.532
$^PQ(13)$	12	12	13	13078.216	$^RQ(9)$	10	10	9	13146.570
$^PP(11)$	11	10	11	13084.192	$^RR(11)$	11	12	11	13148.127
$^PQ(11)$	10	10	11	13086.113	$^RQ(11)$	12	12	11	13150.187
$^PP(9)$	9	8	9	13091.699	$^RR(13)$	13	14	13	13151.340
$^PQ(9)$	8	8	9	13093.643	$^RQ(13)$	14	14	13	13153.420
$^PP(7)$	7	6	7	13098.837	$^RR(15)$	15	16	15	13154.169
$^PQ(7)$	6	6	7	13100.810	$^RQ(15)$	16	16	15	13156.268
$^PP(5)$	5	4	5	13105.605	$^RR(17)$	17	18	17	13156.613
$^PQ(5)$	4	4	5	13107.616	$^RQ(17)$	19	20	19	13158.669
$^PP(3)$	3	2	3	13112.007	$^RR(19)$	18	18	17	13158.731
$^PQ(3)$	2	2	3	13114.090	$^RQ(19)$	21	22	21	13160.336
$^PP(1)$	1	0	1	13118.036	$^RR(21)$	20	20	19	13160.805

Table 45 lists the NO self-broadening coefficients reported by Ballard *et al.* [8] for the P and R branches. Since the Λ doublets were not resolved, only one coefficient is reported for each magnetic substate. Also, no value was reported for $m = 2.5$ in the R

branch because the lines were too overlapped. The values in Table 45 were used to subtract the self-broadening component from the P- and R-branch data collected in the current study.

Table 45. Self-broadening coefficients for the NO P and R branches from Ballard *et al.* [8]. (all γ values are x 10^{-5} cm^{-1}/torr; errors are 1-σ)

$|m|$	P branch		R branch	
	$\gamma_{1/2}$	$\gamma_{3/2}$	$\gamma_{1/2}$	$\gamma_{3/2}$
1.5	9.93(4)	–	10.01(4)	–
2.5	9.72(4)	10.17(8)		
3.5	9.45(2)	9.92(4)	9.75(3)	9.28(6)
4.5	9.21(2)	9.71(5)	9.50(2)	9.28(5)
5.5	9.11(2)	9.39(4)	9.24(2)	9.43(3)
6.5	9.05(3)	9.49(5)	9.000(18)	9.26(3)
7.5	9.03(4)	9.41(4)	8.908(18)	9.26(3)
8.5	9.04(5)	9.12(4)	8.803(13)	9.22(3)
9.5	8.93(7)	9.12(6)	8.67(2)	9.08(2)
10.5	8.72(8)	9.09(8)	8.64(2)	9.11(2)
11.5	8.72(7)	9.29(10)	8.579(18)	9.09(3)
12.5	8.76(7)	8.87(14)	8.434(18)	9.03(2)
13.5	8.49(7)		8.408(18)	9.01(4)
14.5			8.368(18)	8.91(3)
15.5			8.36(2)	8.86(4)
16.5			8.276(18)	8.76(4)
17.5			8.25(4)	8.82(5)
18.5			8.25(4)	8.72(5)
19.5			8.05(3)	8.70(5)
20.5			8.20(4)	8.57(8)

Table 46 lists the self-broadening coefficients for the Q branch of the NO fundamental. This is believed to be all published data for self-broadening of the Q branch of the NO fundamental. The data comes from Lempert *et al.* [68], Pine [95], and Garside *et al.* [40]. The values reported by Lempert *et al.* were used to subtract the self-broadening component from the Q-branch data collected in the current study.

Table 46. Self-Broadening Coefficients from the Literature for the NO Q Branch
(γ values are x 10^{-5} cm^{-1}/torr; errors are 1-σ) (ref [95] is first overtone band)

| J | $\gamma\ \Omega=1/2$ | | $\gamma\ \Omega=3/2$ | | |
	ref [68]	ref [95]	ref [40]	ref [68]	ref [95]
0.5	10.5 ± .9	10.0 ± .3		-	-
1.5	8.4 ± .4	9.5 ± .3		9.9 ± 2	9.3 ± .3
2.5	8.2 ± .4			9.5 ± .5	9.1 ± .3
3.5	8.0 ± .5			9.1 ± .5	9.1 ± .3
4.5	8.0 ± .3			8.4 ± .4	
5.5	7.8 ± .3			7.6 ± .4	
6.5	7.6 ± .3			7.9 ± .8	
7.5	7.4 ± .4			8.0 ± .4	
8.5	7.4 ± .3			8.2 ± .5	
9.5	7.5 ± .4		6.6, 8.2	8.7 ± .7	
10.5	7.8 ± .3			7.9 ± .4	
11.5	7.4 ± .3			8.0 ± .4	
12.5	7.4 ± .3			8.8 ± .8	
13.5	7.1 ± .3			8.3 ± .8	
14.5				7.5 ± .4	
15.5	7.1 ± .3			7.9 ± .4	
16.5	7.0 ± .3				
17.5			7.1, 8.7		

Appendix B. Experimental Parameters for FTS Measurements

Tables 47 through 49 list the gas pressures and numbers of co-added FTS scans performed for each oxygen spectrum analyzed for this research project.

Table 47. Oxygen Self-Broadened Data Runs. All measurements were performed at 0.032 cm^{-1} resolution; all pressures are in torr.

Oxygen Pressure	Number of Scans
150	100
200	100
250	100
300	100
350	100
400	400

Table 48. Data Runs for Oxygen Broadened with the Noble Gases. All measurements were performed at 0.032 cm^{-1} resolution; all pressures are in torr. Oxygen pressure was 200 torr for each run.

Noble Gas Pressure	Number of Scans				
	Helium	Neon	Argon	Krypton	Xenon
100	100	100	100	100	100
150	100	100	100	100	100
200	100	100	100	100	100
250	100	100	100	100	100
300	100	152	100	400	400
350	100	400	400	400	400
400	400	400	100	400	400

Table 49. Data Runs for Oxygen Broadened with Molecules. All measurements were performed at 0.032 cm^{-1} resolution; all pressures are in torr.

N$_2$			CO			CO$_2$			SF$_6$		
P$_{O2}$	P$_{N2}$	scans	P$_{O2}$	P$_{CO}$	scans	P$_{O2}$	P$_{CO2}$	scans	P$_{O2}$	P$_{SF6}$	scans
200	100	100	200	100	100	200	100	100	200	100	100
200	150	100	200	150	100	200	150	100	200	150	100
200	200	100	200	200	100	200	200	100	200	200	100
200	250	100	200	250	100	200	250	100	200	250	100
200	300	400	200	300	100	200	300	100	200	300	100
200	350	400	200	350	100	200	350	100	200	350	100
200	400	400	200	400	100	200	400	100	200	400	100
			600	800	400	200	400	400	600	800	400
						500	800	400			

Tables 50 through 56 list the gas pressures, FTS resolution, and numbers of co-added FTS scans performed for each nitric oxide spectrum analyzed for this research project. Tables 50 through 54 list the spectra acquired for each noble gas perturber. Table 55 lists the spectra acquired with the notch filter selected to enhance signal in the P branch. Table 56 lists the spectra acquired for analysis of the Q branch of NO+Ar.

Table 50. Spectra Acquired for Nitric Oxide Broadened with Helium

He Pressure (torr)	NO Pressure (torr)	# Scans	Resolution (cm^{-1})
40	0.5	100	0.004
55	0.5	100	0.004
100	5	100	0.005
200	10	100	0.005

Table 51. Spectra Acquired for Nitric Oxide Broadened with Neon

Ne Pressure (torr)	NO Pressure (torr)	# Scans	Resolution (cm^{-1})
25	1	100	0.005
50	2	100	0.005
100	4.5	100	0.005
200	11	100	0.005

Table 52. Spectra Acquired for Nitric Oxide Broadened with Argon

Ar Pressure (torr)	NO Pressure (torr)	# Scans	Resolution (cm^{-1})
10	0.5	32	0.004
17.5	0.5	100	0.004
35	0.5	32	0.004
40	0.5	100	0.004
80	1.5	100	0.005
100	0.5	100	0.004
150	0.5	100	0.004

Table 53. Spectra Acquired for Nitric Oxide Broadened with Krypton

Kr Pressure (torr)	NO Pressure (torr)	# Scans	Resolution (cm^{-1})
17.5	0.5	100	0.004
40	0.5	100	0.004
100	3	100	0.005
200	8	100	0.005

Table 54. Spectra Acquired for Nitric Oxide Broadened with Xenon

Xe Pressure (torr)	NO Pressure (torr)	# Scans	Resolution (cm^{-1})
40	0.5	100	0.004
55	0.5	100	0.004
100	5	100	0.005
200	10	100	0.005

Table 55. Spectra Acquired for Nitric Oxide Broadened with Argon
Using New Band-Pass Filter

Kr Pressure (torr)	NO Pressure (torr)	# Scans	Resolution (cm^{-1})
25	1	100	0.005
50	1.5	100	0.005
75	2.5	100	0.005
100	3	100	0.005

Table 56. Spectra Analyzed for Argon Broadening of the Nitric Oxide Q Branch

Ar Pressure (torr)	NO Pressure (torr)	# Scans	Resolution (cm^{-1})	Band-Pass Filter Center (cm^{-1})
10	0.5	32	0.004	1886
25	1.0	100	0.005	1840
35	0.5	32	0.004	1886
40	0.5	100	0.004	1886
50	1.5	100	0.005	1840
75	2.5	100	0.005	1840
100	3.0	100	0.005	1840

Appendix C. Line Positions, Separations, and Doppler Widths

for the NO Fundamental Band

Tables 57 and 58 list the line positions, separations, and Doppler widths used in
the analysis of the NO data in this study. The line positions are from Spencer *et al.* [118].
The Doppler width were calculated at T = 295 K using Equation (3) and were converted
to Gaussian standard deviation σ using Equation (72). The Gaussian standard deviation
is tabulated rather than the Doppler half-widths because the peak-fitting software
required the Doppler parameter to be given in the form of the Gaussian standard
deviation. The values in Tables 57 and 58 were used in the analysis of the nitric oxide
data collected in the current study.

Table 57. Line Positions, Separations, and Doppler Parameters for Voigt Fits for the P Branch of the Nitric Oxide Fundamental Band (all values are in wavenumbers)

Label	3/2 substate			1/2 substate		
	Position	Difference	Doppler σ	Position	Difference	Doppler σ
P 13.5 f	1826.494191			1828.056352		
P 13.5 e	1826.496791	0.002600	0.001741	1828.065809	0.009457	0.001742
P 12.5 f	1830.364461			1831.827070		
P 12.5 e	1830.366721	0.002260	0.001744	1831.836870	0.009800	0.001746
P 11.5 f	1834.201618			1835.563851		
P 11.5 e	1834.203548	0.001930	0.001748	1835.573924	0.010073	0.001749
P 10.5 f	1838.005544			1839.266617		
P 10.5 e	1838.007164	0.001620	0.001752	1839.276972	0.010355	0.001753
P 9.5 f	1841.775990			1842.935196		
P 9.5 e	1841.777320	0.001330	0.001755	1842.945898	0.010702	0.001756
P 8.5 f	1845.512704			1846.569733		
P 8.5 e	1845.513784	0.001080	0.001759	1846.580626	0.010893	0.001760
P 7.5 f	1849.215588			1850.170083		
P 7.5 e	1849.216438	0.000850	0.001762	1850.181159	0.011076	0.001763
P 6.5 f	1852.884235			1853.736253		
P 6.5 e	1852.884875	0.000640	0.001766	1853.747569	0.011316	0.001767
P 5.5 f	1856.518525			1857.268248		
P 5.5 e	1856.518975	0.000450	0.001769	1857.279694	0.011446	0.001770
P 4.5 f	1860.118057			1860.766055		
P 4.5 e	1860.118357	0.000300	0.001773	1860.777688	0.011633	0.001773
P 3.5 f	1863.682747			1864.229643		
P 3.5 e	1863.682927	0.000180	0.001776	1864.241390	0.011747	0.001777
P 2.5 f	1867.212201			1867.659150		
P 2.5 e	1867.212291	0.000090	0.001780	1867.670927	0.011777	0.001780
P 1.5 f				1871.054271		
P 1.5 e				1871.066056	0.011785	0.001783

Table 58. Line Positions, Separations, and Doppler Parameters for Voigt Fits for the R Branch of the NO Fundamental (all values are in wavenumbers)

Label	1/2 substate			3/2 substate		
	Position	Difference	Doppler σ	Position	Difference	Doppler σ
R 0.5 e	1881.034990					
R 0.5 f	1881.046809	0.011809	0.001793			
R 1.5 e	1884.293251			1884.323153		
R 1.5 f	1884.304927	0.011676	0.001796	1884.323243	0.000090	0.001796
R 2.5 e	1887.517380			1887.636262		
R 2.5 f	1887.529015	0.011635	0.001799	1887.636442	0.000180	0.001799
R 3.5 e	1890.707216			1890.912440		
R 3.5 f	1890.718705	0.011489	0.001802	1890.912730	0.000290	0.001802
R 4.5 e	1893.862744			1894.151450		
R 4.5 f	1893.874054	0.011310	0.001805	1894.151870	0.000420	0.001805
R 5.5 e	1896.983892			1897.353112		
R 5.5 f	1896.995033	0.011141	0.001808	1897.353692	0.000580	0.001808
R 6.5 e	1900.070604			1900.517178		
R 6.5 f	1900.051627	0.011023	0.001811	1900.517958	0.000780	0.001811
R 7.5 e	1903.122853			1903.643468		
R 7.5 f	1903.133603	0.010750	0.001814	1903.644428	0.000960	0.001814
R 8.5 e	1906.140518			1906.731812		
R 8.5 f	1906.151026	0.010508	0.001817	1906.732982	0.001170	0.001817
R 9.5 e	1909.123402			1909.782002		
R 9.5 f	1909.133673	0.010271	0.001819	1909.783402	0.001400	0.001820
R 10.5 e	1912.071579			1912.793903		
R 10.5 f	1912.081517	0.009938	0.001822	1912.795533	0.001630	0.001823
R 11.5 e	1914.984851			1915.767413		
R 11.5 f	1914.994560	0.009709	0.001825	1915.769293	0.001880	0.001826
R 12.5 e	1917.863074			1918.702135		
R 12.5 f	1917.872539	0.009465	0.001828	1918.704285	0.002150	0.001829
R 13.5 e	1920.706102			1921.598228		
R 13.5 f	1920.715347	0.009245	0.001831	1921.600638	0.002410	0.001831
R 14.5 e	1923.513932			1924.455429		
R 14.5 f	1923.522862	0.008930	0.001833	1924.458099	0.002670	0.001834
R 15.5 e	1926.286245			1927.273572		
R 15.5 f	1926.294859	0.008614	0.001836	1927.276502	0.002930	0.001837
R 16.5 e	1929.022907			1930.052644		
R 16.5 f	1929.031286	0.008379	0.001838	1930.055844	0.003200	0.001839
R 17.5 e	1931.723811			1932.792540		
R 17.5 f	1931.731911	0.008100	0.001841	1932.796010	0.003470	0.001842
R 18.5 e	1934.388825			1935.493025		
R 18.5 f	1934.396645	0.007820	0.001844	1935.496765	0.003740	0.001845
R 19.5 e	1937.017572					
R 19.5 f	1937.025101	0.0007529	0.001846			

250

Appendix D. O_2 and NO Broadening Cross Sections

Tables 59 through 62 present the broadening cross sections calculated from the measured broadening coefficients of this study.

Table 59. O_2+Noble Gas Broadening Cross Sections ($\times$ 10^{-15} cm^2)

$|m|$	He	Ne	Ar	Kr	Xe
1	0.37(6)	0.62(8)	1.10(9)	1.38(5)	1.71(13)
2	0.45(3)	0.75(2)	0.96(7)	1.18(8)	1.52(9)
3	0.429(11)	0.56(4)	1.04(3)	1.25(6)	1.54(3)
4	0.38(2)	0.59(4)	1.04(5)	1.16(3)	1.42(5)
5	0.350(6)	0.525(13)	0.994(19)	1.18(2)	1.41(3)
6	0.35(2)	0.56(3)	0.91(3)	1.090(12)	1.35(6)
7	0.370(12)	0.585(17)	0.977(18)	1.074(17)	1.42(4)
8	0.363(18)	0.56(3)	0.94(4)	1.03(2)	1.19(3)
9	0.353(7)	0.498(7)	0.91(2)	1.036(19)	1.365(18)
10	0.392(18)	0.52(2)	0.90(3)	1.12(3)	1.35(5)
11	0.353(10)	0.513(12)	0.85(3)	0.92(2)	1.33(2)
12	0.304(13)	0.44(3)	0.78(3)	0.83(3)	1.13(3)
13	0.346(7)	0.497(14)	0.83(2)	0.95(2)	1.27(3)
14	0.37(3)	0.473(16)	0.81(4)	0.92(4)	1.24(8)
15	0.343(15)	0.484(16)	0.817(18)	0.89(2)	1.22(3)
16	0.341(19)	0.49(4)	0.71(5)	0.80(4)	1.11(5)
17	0.336(17)	0.455(17)	0.76(2)	0.82(2)	1.19(17)
18	0.26(2)	0.48(4)	0.68(8)	0.79(6)	1.15(15)
19	0.329(10)	0.42(2)	0.66(5)	0.71(3)	1.14(4)
20	0.26(3)	0.44(6)	0.61(8)	0.83(8)	
21	0.288(17)	0.40(5)	0.65(5)	0.65(6)	1.07(7)
22			0.57(12)	0.57(12)	

Table 60. O_2+Molecule Broadening Cross Sections ($\times 10^{-15}$ cm^2)

$|m|$	O_2	N_2	CO	CO_2	SF_6
1	1.29(13)	1.15(4)	0.98(9)	1.23(3)	1.52(11)
2	1.17(4)	1.04(5)	1.17(6)	1.35(8)	2.08(2)
3	1.161(16)	1.11(3)	1.08(3)	1.37(4)	1.81(5)
4	1.111(15)	0.99(6)	1.06(3)	1.24(3)	1.67(5)
5	1.143(18)	0.99(2)	1.016(16)	1.23(2)	1.63(4)
6	1.085(14)	1.01(4)	1.03(2)	1.26(3)	1.53(6)
7	1.069(14)	0.974(16)	1.069(16)	1.17(2)	1.58(5)
8	1.08(2)	0.88(2)	0.99(2)	1.24(4)	1.53(5)
9	1.039(10)	0.944(13)	0.989(16)	1.18(2)	1.55(3)
10	1.014(18)	0.92(3)	0.96(3)	1.07(3)	1.51(7)
11	1.042(8)	0.908(18)	0.974(16)	1.170(16)	1.51(2)
12	1.005(11)	0.79(5)	0.97(2)	1.08(2)	1.44(3)
13	1.016(12)	0.888(13)	0.965(18)	1.08(2)	1.49(3)
14	0.970(19)	0.81(7)	0.94(4)	1.11(5)	1.43(5)
15	0.964(13)	0.841(19)	0.887(17)	1.04(3)	1.38(2)
16	0.90(2)	0.85(5)	0.85(4)	1.14(3)	1.14(7)
17	0.942(17)	0.82(2)	0.884(19)	1.02(3)	1.45(3)
18	0.85(3)	0.58(10)	0.96(3)	0.96(5)	1.45(10)
19	0.917(10)	0.80(2)	0.86(2)	0.97(3)	1.29(3)
20	0.82(2)		0.86(5)	0.92(5)	1.28(5)
21	0.88(3)	0.79(5)	0.88(4)	0.98(6)	1.18(12)
22	0.79(3)		0.87(9)	0.89(8)	1.30(6)

Table 61. NO+Noble Gas Broadening Cross Sections ($\times$ 10^{-15} cm^2) , $\Omega = 1/2$

$|m|$	He	Ne	Ar	Kr	Xe
1.5	0.478(9)	0.89(5)	1.38(5)	1.75(10)	1.73(5)
2.5	0.440(8)	0.79(5)	1.22(3)	1.50(7)	1.62(4)
3.5	0.453(6)	0.76(2)	1.143(19)	1.42(3)	1.516(17)
4.5	0.458(6)	0.72(2)	1.16(2)	1.39(2)	1.438(7)
5.5	0.473(8)	0.711(19)	1.101(17)	1.33(4)	1.413(15)
6.5	0.467(3)	0.70(4)	1.07(3)	1.31(5)	1.341(15)
7.5	0.464(10)	0.71(4)	1.070(19)	1.22(3)	1.27(3)
8.5	0.457(6)	0.70(3)	1.051(19)	1.24(5)	1.26(2)
9.5	0.443(12)	0.65(2)	1.05(2)	1.23(4)	1.23(4)
10.5	0.452(6)	0.68(4)	0.99(2)	1.17(5)	1.227(16)
11.5	0.462(6)	0.67(2)	0.977(10)	1.14(5)	1.21(2)
12.5	0.441(4)	0.634(14)	0.972(17)	1.09(5)	1.149(15)
13.5	0.456(5)	0.64(2)	0.930(17)	1.12(5)	1.14(2)
14.5	0.429(5)	0.63(3)	0.92(3)	1.07(5)	1.13(3)
15.5	0.405(6)	0.64(3)	0.88(6)	0.98(3)	1.08(2)
16.5	0.404(7)	0.61(3)	0.92(2)	1.02(5)	1.055(15)
17.5	0.394(7)	0.63(3)	0.84(3)	0.98(2)	1.06(3)
18.5	0.400(3)	0.61(3)	0.82(5)	1.00(9)	0.984(15)
19.5	0.397(3)	0.61(3)	0.71(8)	1.05(3)	0.949(11)
20.5	0.383(2)	0.58(3)	0.96(5)	0.91(7)	0.95(3)

Table 62. NO+Noble Gas Broadening Cross Sections ($\times 10^{-15}$ cm^2) , $\Omega = 3/2$

$|m|$	He	Ne	Ar	Kr	Xe
2.5	0.487(6)	0.79(6)	1.25(5)	1.66(10)	1.62(4)
3.5	0.498(4)	0.78(3)	1.22(3)	1.49(4)	1.621(17)
4.5	0.493(2)	0.78(4)	1.21(3)	1.395(12)	1.552(16)
5.5	0.497(5)	0.77(4)	1.15(2)	1.31(9)	1.46(2)
6.5	0.5017(9)	0.74(5)	1.16(3)	1.34(3)	1.41(3)
7.5	0.503(12)	0.73(5)	1.13(2)	1.35(5)	1.36(3)
8.5	0.531(14)	0.74(5)	1.11(3)	1.28(3)	1.336(18)
9.5	0.513(7)	0.73(5)	1.08(2)	1.19(12)	1.33(2)
10.5	0.495(12)	0.71(5)	1.035(16)	1.195(12)	1.24(3)
11.5	0.488(8)	0.68(5)	1.022(18)	1.23(3)	1.238(18)
12.5	0.473(6)	0.69(4)	0.986(16)	1.21(5)	1.22(4)
13.5	0.460(5)	0.65(4)	0.93(2)	1.24(3)	1.176(16)
14.5	0.4382(14)	0.66(4)	0.96(3)	1.12(5)	1.11(2)
15.5	0.4266(5)	0.63(4)	0.82(3)	1.088(10)	1.05(2)
16.5	0.4203(12)	0.63(2)	0.88(2)	1.16(7)	1.033(15)
17.5	0.412(2)	0.60(4)	0.82(5)	0.93(5)	1.07(5)
18.5	0.404(5)	0.59(3)	0.93(3)	1.16(9)	1.02(3)
19.5	0.393(2)	0.56(3)	0.73(5)	0.91(5)	0.94(3)

(*Fitting Law: EPGL-0

fit law calculates all rates directly
corrected to include R ∆E
m−conserving degeneracy)

`<< Graphics`Graphics` `

`<< Statistics`NonlinearFit` `

`<< Graphics`MultipleListPlot` `

(*Physical constants*)
h = 6.626 * 10^{-27}; (* Planck's constant, erg sec *)
c = 2.99792458 * 10^{10}; (* velocity of light, cm/sec *)
k = 1.38066 * 10^{-16}; * Boltzmann constant, erg K *
masscon = 1.66057 * 10^{-24}; * unit conversion for mass, g amu *

(*Parameters for this fit*)
B = 1.44566; (* lower state rotational constant, cm^{-1} *)
T = 296; (* temperature, Kelvin *)
μamu = 16.00 ; (* reduced mass of collision pair, amu *)
μ = μamu * masscon; (* convert to cgs units *)
Jlo = 1; (* lowest value of J−initial *)
Jhi = 22; (* highest value of J−initial *)
Jrange = 30; (* maximum ∆J *)

$$vavg = \frac{\overline{8\,k\,T}}{\pi\,\mu} \; ;$$ * relative velocity of collision pair, cm sec *

(*Experimental data: broadening cross sections and errors, cm^2*)
(* this data set is O_2+O_2 *)
σexp = {{1, 1.29*10^{-15}}, {2, 1.17*10^{-15}},
  {3, 1.161*10^{-15}}, {4, 1.111*10^{-15}}, {5, 1.143*10^{-15}}, {6, 1.085*10^{-15}},
  {7, 1.069*10^{-15}}, {8, 1.08*10^{-15}}, {9, 1.039*10^{-15}}, {10, 1.014*10^{-15}},
  {11, 1.042*10^{-15}}, {12, 1.005*10^{-15}}, {13, 1.016*10^{-15}}, {14, .970*10^{-15}},
  {15, .964*10^{-15}}, {16, .90*10^{-15}}, {17, .942*10^{-15}}, {18, .85*10^{-15}},
  {19, .917*10^{-15}}, {20, .82*10^{-15}}, {21, .88*10^{-15}}, {22, .79*10^{-15}}};

σerr = {{1, 0.03*10^{-15}}, {2, 0.04*10^{-15}}, {3, 0.016*10^{-15}}, {4, 0.015*10^{-15}},
  {5, 0.018*10^{-15}}, {6, 0.014*10^{-15}}, {7, 0.014*10^{-15}}, {8, 0.02*10^{-15}},
  {9, 0.010*10^{-15}}, {10, 0.018*10^{-15}}, {11, 0.008*10^{-15}}, {12, 0.011*10^{-15}},
  {13, 0.012*10^{-15}}, {14, 0.019*10^{-15}}, {15, 0.013*10^{-15}}, {16, 0.02*10^{-15}},
  17, 0.017*10^{-15} , 18, 0.03*10^{-15} , 19, 0.010*10^{-15} , 20, 0.02*10^{-15} ,
  21, 0.03*10^{-15} , 22, .03*10^{-15} ;

```
(*list manipulation; calculate weights*)
σerrflat = σerr // Flatten;
σwunnorm = Table[(1 / σerrflat[[x+1]])^2, {x, Jlo, Jhi * 2, 2}];
σwsum = Sum[σwunnorm[[x]], {x, Jlo, Jhi, 1}];
σweights = Table[σwunnorm[[x]] / σwsum, {x, Jlo, Jhi, 1}];


(*list manipulation;
adjust magnitude of data for numerical stability*)
σexpflat = σexp   Flatten;
σexp12 = Table   x+1   2., σexpflat   x+1   * 10^12 , x, Jlo, Jhi*2, 2  ;

(*Energy Gap*)
Egap[jf_, ji_] = h c B (jf * (jf + 1) - ji * (ji + 1));


(*the "reduced" rotational energy transfer*)
Δ[j1_, j2_] = (h c B (j1 (j1 + 1) - j2 (j2 + 1))) / (2 k T);


(*dimensionless phase space factor from information theory*)
R[Ji_, Jf_] = Re[Exp[Δ[Ji, Jf]] Δ[Ji, Jf] BesselK[1, Δ[Ji, Jf]]];


(*Degeneracy choices*)
degen[ji_, jf_] = (2 * If[ji < jf, ji, jf] + 1) / (2 * ji + 1); (* m-conserving *)

(*degen[ji_,jf_]=2*jf+1;*)(* m-randomizing *)


(*n123[ji_,jf_,λ_] = Sort[{ji,jf,λ},Greater];
αtest[ji_,jf_,λ_] =
  n123[ji,jf,λ][[2]]+n123[ji,jf,λ][[3]]-n123[ji,jf,λ][[1]];
α[ji_,jf_,λ_] = If[αtest[ji,jf,λ]>0,αtest[ji,jf,λ],0];
degen[ji_,jf_,λ_] = 1/(2*j1 + 1) ((2 n123[ji,jf,λ][[2]]+1)
      (2 n123[ji,jf,λ][[3]]+1)-α[ji,jf,λ] (α[ji,jf,λ]+1));*)
(*|Δm| ≤ λ*)


(*Hybrid Exponential Power Gap Law*)
kEPGL[ji_, jf_, A_, β_, γ_] =
  A degen[ji, jf] R[ji, jf] (Abs[Egap[jf, ji]] / (h c B))^-γ Exp[-β * Abs[Egap[jf, ji]] / (k T)];


(*Perform the fitting law calulation*)
klist = {};
kdlist = {};
Do[
  Do[
    klist = Append[klist, {{ji, jf, kEPGL[ji, jf, A, β, γ]}}] // Flatten;
  , {jf, ji + 2, ji + Jrange, 2}]
, {ji, 0, Jhi, 1}]
Do[
  Do[
    kdlist = Append[kdlist, {{ji, jf, kEPGL[ji, jf, A, β, γ]}}] // Flatten;
  , jf, If EvenQ ji , 0, 1 , ji - 2, 2
, ji, 2, Jhi, 1
```

(*Detailed balance to calculate downward rates*)

(*kup[j1_,j2_] :=klist[[3*($\frac{Jrange}{2}$*j1+($\frac{j2-j1}{2}$))]]

kdown[j2_,j1_] := kup[j1,j2] $\left(\frac{2\ j1+1}{2\ j2+1}\right)$ Exp[h c B (j2*(j2+1)-j1*(j1+1))/(k T)]*)

(* up and down rates calculated directly from fitting law*)

kup[j1_, j2_] := klist[[3*$\left(\frac{Jrange}{2}*j1+\left(\frac{j2-j1}{2}\right)\right)$]]

ΔΔ[x_] := If[x == 1, 1, If[EvenQ[x], $\frac{x}{2}$, $\frac{x-1}{2}$]]

kdown[j1_, j2_] :=
 kdlist[3* Sum[ΔΔ[x] , {x, 1, j1-1}] + $\frac{\text{If}[\text{EvenQ}[j2], j2, j2-1]}{2}$]

(*Sum rule to calculate the total removal rates (20 July mod)*)

sumrule[ji_] := (Sum[kup[ji-1, jup], {jup, ji+1, ji-1+Jrange, 2}] +
    Sum[kup[ji, jup], {jup, ji+2, ji+Jrange, 2}] +
    Sum[kdown[ji-1, jdown], {jdown, If[EvenQ[ji-1], 0, 1], ji-3, 2}] +
    Sum[kdown[ji, jdown], {jdown, If[EvenQ[ji], 0, 1], ji-2, 2}]) /2.0

(* Calculate Broadening Cross Sections,
   set up interpolating function *)

σtable = Table[{x, sumrule[x] /vavg}, {x, Jlo, Jhi, 1}];
σx = σtable // Flatten;
σinterp = Interpolation[σtable] ;
σinterp2[Ji_, A_, β_, γ_] = σinterp[Ji] ;

(*Perform the Fit*)

NonlinearRegress[
 σexp12, σinterp2[Ji, A, β, γ] , Ji, {A, 52.747} , {β, .648961} , {γ, .238198} ,
 Method -> LevenbergMarquardt, Weights -> σweights, ShowProgress -> True

Iteration:1 ChiSquared:5.33174×10⁻¹⁰ Parameters: 52.747, 0.648961, 0.238198

Iteration:2 ChiSquared:5.33174×10⁻¹⁰ Parameters: 52.747, 0.648961, 0.238198

Iteration:3 ChiSquared:5.33174×10⁻¹⁰ Parameters: 52.747, 0.648961, 0.238198

SingularValues::svdf :
 SingularValues has received a matrix with infinite precision.

NonlinearRegress::nosvd :
 NonlinearRegress was unable to obtain the singular value decomposition
    for the design matrix corresponding to the linearized problem.

{BestFitParameters →
   {A→ 52.747, β → 0.648961, γ → 0.238198}, ParameterCITable → $Failed,
  EstimatedVariance → 2.806179296283×10⁻¹¹, ANOVATable →

(*Detailed balance to calculate downward rates*)

(*kup[j1_,j2_] :=klist[[3*($\frac{Jrange}{2}$*j1+($\frac{j2-j1}{2}$))]]

kdown[j2_,j1_] := kup[j1,j2] $\left(\frac{2\ j1+1}{2\ j2+1}\right)$ Exp[h c B (j2*(j2+1)-j1*(j1+1))/(k T)]*)

(* up and down rates calculated directly from fitting law*)

kup[j1_, j2_] := klist[[3*$\left(\frac{Jrange}{2}*j1+\left(\frac{j2-j1}{2}\right)\right)$]]

ΔΔ[x_] := If[x == 1, 1, If[EvenQ[x], $\frac{x}{2}$, $\frac{x-1}{2}$]]

kdown[j1_, j2_] :=
 kdlist[3* Sum[ΔΔ[x] , {x, 1, j1-1}] + $\frac{\text{If}[\text{EvenQ}[j2], j2, j2-1]}{2}$]

(*Sum rule to calculate the total removal rates (20 July mod)*)

sumrule[ji_] := (Sum[kup[ji-1, jup], {jup, ji+1, ji-1+Jrange, 2}] +
    Sum[kup[ji, jup], {jup, ji+2, ji+Jrange, 2}] +
    Sum[kdown[ji-1, jdown], {jdown, If[EvenQ[ji-1], 0, 1], ji-3, 2}] +
    Sum[kdown[ji, jdown], {jdown, If[EvenQ[ji], 0, 1], ji-2, 2}]) /2.0

(* Calculate Broadening Cross Sections,
   set up interpolating function *)

σtable = Table[{x, sumrule[x] /vavg}, {x, Jlo, Jhi, 1}];
σx = σtable // Flatten;
σinterp = Interpolation[σtable] ;
σinterp2[Ji_, A_, β_, γ_] = σinterp[Ji] ;

(*Perform the Fit*)

NonlinearRegress[
 σexp12, σinterp2[Ji, A, β, γ] , Ji, {A, 52.747} , {β, .648961} , {γ, .238198} ,
 Method -> LevenbergMarquardt, Weights -> σweights, ShowProgress -> True

Iteration:1 ChiSquared:5.33174×10^{-10} Parameters: 52.747, 0.648961, 0.238198

Iteration:2 ChiSquared:5.33174×10^{-10} Parameters: 52.747, 0.648961, 0.238198

Iteration:3 ChiSquared:5.33174×10^{-10} Parameters: 52.747, 0.648961, 0.238198

SingularValues::svdf :
 SingularValues has received a matrix with infinite precision.

NonlinearRegress::nosvd :
 NonlinearRegress was unable to obtain the singular value decomposition
    for the design matrix corresponding to the linearized problem.

{BestFitParameters →
   {A→ 52.747, β → 0.648961, γ → 0.238198}, ParameterCITable → $Failed,
  EstimatedVariance → $2.806179296283\times10^{-11}$, ANOVATable →

	DF	SumOfSq	MeanSq
Model	3	1.03994×10^{-6}	3.46648×10^{-7}
Error	19	$5.331740662937\times10^{-10}$	$2.806179296283\times10^{-11}$,
Uncorrected Total	22	1.04048×10^{-6}	
Corrected Total	21	7.104×10^{-9}	

AsymptoticCorrelationMatrix → $Failed, FitCurvatureTable → $Failed

(*List and plot the results of the fit*)

```
σcalc[Ji_, A_, β_, γ_] = σx[[Ji*2]];
σfit = Table[{Ji, σcalc[Ji, 52.747*10^-12, .648961, .238198]}, {Ji, Jlo, Jhi, 1}]
MultipleListPlot[
  σexp, σfit, PlotJoined-> {False, True}, SymbolShape -> {PlotSymbol[Box], None},
  PlotStyle -> {{Thickness[0.005], GrayLevel[0]}},
  AxesLabel -> "Ji", "Broadening Cross Section  cm^2 " ,
  PlotRange-> 0, 1.4*10^-15
```

Part::pspec :

Part specification 2 Ji is neither an integer nor a list of integers.

$\{\{1, 1.36447 \times 10^{-15}\}, \{2, 1.20872 \times 10^{-15}\}, \{3, 1.15374 \times 10^{-15}\}, \{4, 1.1188 \times 10^{-15}\},$
$\{5, 1.09482 \times 10^{-15}\}, \{6, 1.07789 \times 10^{-15}\}, \{7, 1.06547 \times 10^{-15}\}, \{8, 1.0557 \times 10^{-15}\},$
$\{9, 1.04712 \times 10^{-15}\}, \{10, 1.03862 \times 10^{-15}\}, \{11, 1.02937 \times 10^{-15}\},$
$\{12, 1.01875 \times 10^{-15}\}, \{13, 1.00634 \times 10^{-15}\}, \{14, 9.91887 \times 10^{-16}\},$
$\{15, 9.75289 \times 10^{-16}\}, \{16, 9.56558 \times 10^{-16}\}, \{17, 9.35806 \times 10^{-16}\},$
$18, 9.13219 \times 10^{-16} , 19, 8.89036 \times 10^{-16} , 20, 8.63535 \times 10^{-16} ,$
$21, 8.37009 \times 10^{-16} , 22, 8.09756 \times 10^{-16}$

- Graphics -

258
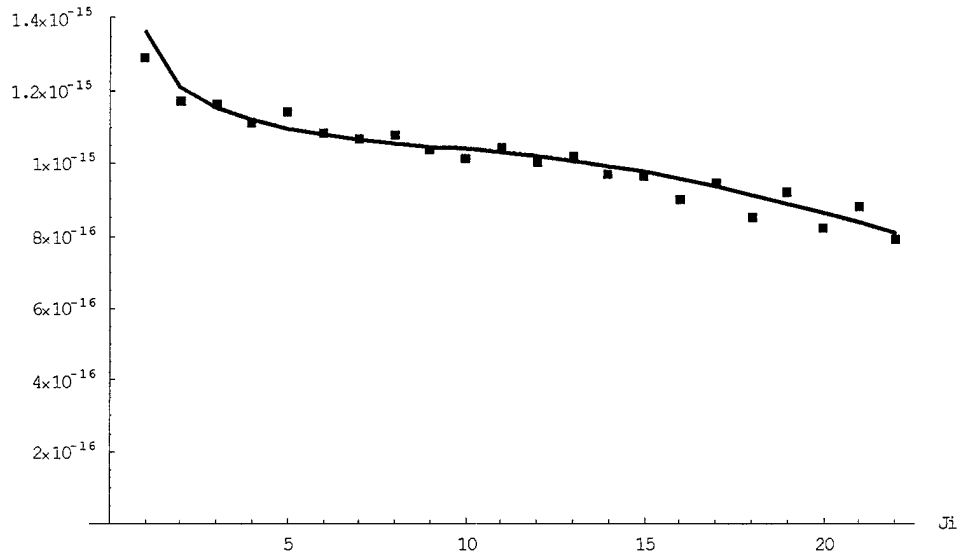
(*Calculate Reduced Chi −Squared*)

σfitflat = σfit // Flatten;

freeparm = 3;

ndata = Jhi - Jlo + 1;

ν = ndata - freeparm;

$$rcs = \frac{1}{\nu} \, \text{Sum}\left[\left(\frac{\sigma\text{expflat}[[x+1]] - \sigma\text{fitflat}[[x+1]]}{\sigma\text{errflat}[[x+1]]}\right)^2, \ x, \ Jlo, \ Jhi*2, \ 2\right]$$

2.81399

(*Calculate weighted RMS fractional deviation (quality of fit)*)

$$Drms = \sqrt{\left(\text{Sum}\left[\left(\frac{\sigma\text{expflat}[[x+1]]}{\sigma\text{errflat}[[x+1]]}\right)^2 \left(\frac{\sigma\text{fitflat}[[x+1]] - \sigma\text{expflat}[[x+1]]}{\sigma\text{expflat}[[x+1]]}\right)^2, \{x, \ Jlo, \ Jhi*2, \ 2\}\right] \Big/ \text{Sum}\left[\left(\frac{\sigma\text{expflat}[[x+1]]}{\sigma\text{errflat}[[x+1]]}\right)^2, \ x, \ Jlo, \ Jhi*2, \ 2\right]\right)}$$

0.022637

(*Calculate weighted RMS average error (quality of data)*)

$$Erms = \sqrt{\left(\frac{\text{Sum}\left[\left(\frac{\sigma\text{expflat}[[x+1]]}{\sigma\text{errflat}[[x+1]]}\right)^2 \left(\frac{\sigma\text{errflat}[[x+1]]}{\sigma\text{expflat}[[x+1]]}\right)^2, \{x, \ Jlo, \ Jhi*2, \ 2\}\right]}{\text{Sum}\left[\left(\frac{\sigma\text{expflat}[[x+1]]}{\sigma\text{errflat}[[x+1]]}\right)^2, \ x, \ Jlo, \ Jhi*2, \ 2\right]}\right)}$$

0.0145208

(*The ratio below is equal to the reduced chi −squared*)

$$ratio = \frac{ndata}{\nu} \ \frac{Drms^2}{Erms}$$

2.81399

(*Calculate and list the synthetic state−to−state rates*)

A = 52.747 * 10^{-12};

β = .648961;

γ = .238198;

ktable = TableForm[
   Table[{klist[[n]], klist[[n+1]], klist[[n+2]]}, {n, 1, 3*(Jhi + 1) * $\frac{Jrange}{2}$, 3}]]

ubound =
   2*Sum[m, {m, 1, If[EvenQ[Jhi], If[EvenQ[$\frac{Jhi}{2}$], $\frac{Jhi}{2}$, $\frac{Jhi}{2}$ - 1], $\frac{Jhi-1}{2}$]}] +
   If[EvenQ[Jhi], If[EvenQ[$\frac{Jhi}{2}$], 0, $\frac{Jhi}{2}$], 0];

kdtable = TableForm
   Table[kdlist[[n]], kdlist[[n+1]], kdlist[[n+2]], n, 1, 3*ubound, 3]

* the output from this last set of statements has been deleted to save space;

the list of state−to−state rates runs for several pages*

259

Appendix F. Mathematica Implementation of an Approximation
to the ECS-P Fitting Law

In this study, all ECS-P fits were approximated using a method proposed by Smith and Pritchard [117]. This approximation eliminates the calculation of the 3-J coefficients and consequently cuts computer run time by about one third.

The true ECS law was presented in Equation (42) of Chapter II and is presented here again for convenience:

$$k_{i \to f}^{ECS} = (2J_f + 1) \exp\left(\frac{E_{J_i} - E_{J_>}}{kT}\right) \sum_L \begin{bmatrix} J_i & J_f & L \\ 0 & 0 & 0 \end{bmatrix}^2 (2L+1)\left(A_L^{J_>}\right)^2 k_{0 \to L} \tag{42}$$

The approximation to the ECS-P law proposed by Smith and Pritchard, under the assumption that $k_{0 \to L} = A[L(L+1)]^{-\gamma}$, is

$$k_{i \to f}^{ECS-P \; approx} = (2J_f + 1) \exp\left(\frac{E_{J_i} - E_{J_>}}{kT}\right) Q_A \tag{88}$$

where Q_A is an approximation to everything to everything to the right of the summation in Equation (42). This factor is given by

$$Q_A = A\left(1 + \beta^2 E_>\right)^{-2} \left(E_> - E_<\right)^{-(1+2\varepsilon)} \left\{ \Sigma^{2\varepsilon} F\left(\frac{\Delta}{\Sigma}, \varepsilon\right) + 2\Sigma\Delta^{1+2\varepsilon}\beta^2 \left[F\left(\frac{\Delta}{\Sigma}, -\varepsilon\right) + \frac{\beta^2}{2} F\left(\frac{\Delta}{\Sigma}, 1-\varepsilon\right) \right] \right\}$$

(89)

where $E_>$, $E_<$, Δ, Σ, β, $F(x,z)$, and ε are defined as follows:

$$E_> \equiv J_>\left(J_> + 1\right)$$

(90)

$$E_< \equiv J_<\left(J_< + 1\right)$$

(91)

$$\Delta \equiv \sqrt{E_>} - \sqrt{E_<}$$

(92)

$$\Sigma \equiv \sqrt{E_>} + \sqrt{E_<}$$

(93)

$$\beta \equiv \frac{\delta B l_c}{\sqrt{6}\langle v \rangle \hbar}$$

(94)

$$F(x,z) \equiv f(z) + \left[1 - f(z)\right] x^{[1+g(z)]}$$

(95)

$$f(z) \equiv \frac{1}{\sqrt{\pi}} \frac{\Gamma\left(z + \frac{1}{2}\right)}{\Gamma(z+1)}$$

(96)

$$g(z) \equiv \begin{cases} z & z \geq 0 \\ 2z - 0.05 & z < 0 \end{cases}$$

(97)

$$\varepsilon = \gamma - 1$$

(98)

In the above definitions, A, γ and l_c are the three parameters of the ECS-P fit. The only other undefined parameter is δ, which is 1 for a heteronuclear molecule and 2 for a homonuclear molecule. The Mathematica implementation of this approximation follows:

(*Fitting Law: ECS–P Approx

approximation derived by Smith and Pritchard
ECS–P directly calculates up and down rates
written 29 July 1998 *)

(*Energy Gap (modified for ECS)*)

Egap[jf_, ji_] = h c B (ji * (ji + 1) - If[ji > jf, ji, jf] * (If[ji > jf, ji, jf] + 1));

(*Approximation to Energy–Corrected Sudden Law*)

jg[ji_, jf_] = If[ji > jf, ji, jf];

jl[ji_, jf_] = If[ji > jf, jf, ji];

Er[j_] = j * (j + 1);

Σ[ji_, jf_] = $\sqrt{Er[jg[ji, jf]]}$ + $\sqrt{Er[jl[ji, jf]]}$;

Δ[ji_, jf_] = $\sqrt{Er[jg[ji, jf]]}$ - $\sqrt{Er[jl[ji, jf]]}$;

β[lc_] = $\dfrac{2 \pi \delta \, B \, c \, lc \, 10^{-8}}{\sqrt{6} \; vavg}$; (*10^{-8} converts lc from cm to Å*)

f[z_] = $\dfrac{1}{\sqrt{\pi}} \dfrac{Gamma[z + \frac{1}{2}]}{Gamma[z + 1]}$;

g[z_] = If[z $\geq$ 0, z, 2 z - 0.05];

FG[x_, z_] = f[z] + (1 - f[z]) x$^{(1+g[z])}$;

QA[ji_, jf_, lc_, γ] =
$\left(1 + \beta[lc]^2 \, Er[jg[ji, jf]]\right)^{-2}$ (Er[jg[ji, jf]] - Er[jl[ji, jf]])$^{-(1+2\,(\gamma-1))}$

$\left(\Sigma[ji, jf]^{2\,(\gamma-1)} \, FG\left[\dfrac{\Delta[ji, jf]}{\Sigma[ji, jf]}, \gamma - 1\right] + 2 \Sigma[ji, jf] \, \Delta[ji, jf]^{(1+2\,(\gamma-1))} \right.$

$\left. \beta[lc]^2 \left\{ FG\left[\dfrac{\Delta[ji, jf]}{\Sigma[ji, jf]}, -(\gamma - 1)\right] + \dfrac{\beta[lc]^2}{2} \, FG\left[\dfrac{\Delta[ji, jf]}{\Sigma[ji, jf]}, 1 - (\gamma - 1)\right] \right\} \right);$

kECS[ji_, jf_, A_, lc_, γ_] = A (2 jf + 1) Exp[Egap[jf, ji] / (k T)] QA[ji, jf, lc, γ];

(* Perform the fitting law calculation *)

klist = {};

kdlist = {};

Do[
  Do[
    klist = Append[klist, {{ji, jf, kECS[ji, jf, A, lc, γ]}}] // Flatten;
  , {jf, ji + 2, ji + Jrange, 2}]
, {ji, 0, Jhi, 1}]

Do[
  Do[
    kdlist = Append[kdlist, {{ji, jf, kECS[ji, jf, A, lc, γ]}}] // Flatten;
  , jf, If EvenQ ji , 0, 1 , ji - 2, 2
, ji, 2, Jhi, 1

Appendix G. Details of the EGL-0, SPG-0, SPG-Δ, and EPGL-Δ Fits to the Oxygen Pressure Broadening Cross Sections and Comparison of these Results with the Results of the EPGL-0 and ECS-P Fits

Chapter IV presented the details of the EPGL-0 and ECS-P fits to the broadening coefficients of the oxygen A band with all ten collision partners studied. This appendix lists the results of the fits of the EGL-0, SPG-0, SPG-Δ, and EPGL-Δ laws to the same data. These results were not presented in Chapter II because it was determined that these fits were poor compared to EPGL-0 and ECS-P. The results of the EGL-0 fits are in Table 63.

Table 63. Fitting Parameters and Fit Statistics for EGL-0 Fits to Oxygen with Ten Collision Partners

Collision Partner	A ($\times 10^{-12}$ cm^2)	β	χ^2/ν	Fit Quality, D (%)	Data Quality, E (%)
He	17.8	1.03	4.21	6.76	3.46
Ne	15.4	1.24	7.07	8.69	3.44
Ar	24.6	1.41	2.41	4.92	3.32
Kr	25.7	1.54	5.83	5.66	2.49
Xe	27.1	1.22	6.96	6.46	2.59
N_2	24.5	1.18	4.56	5.00	2.48
CO	24.8	1.07	4.70	4.83	2.34
O_2	25.4	1.09	8.89	4.13	1.45
CO_2	26.5	1.26	15.69	9.19	2.43
SF_6	35.2	1.37	20.57	9.81	2.27

Looking at Table 63, there appears to be an increasing trend of A with reduced mass. There is no apparent trend with β. Fits are especially poor for the heavy molecules CO_2 and SF_6.

Table 64 presents the results of the SPG-0 fits to the oxygen data. No clear trends are observable in either of the fit parameters.

Table 64. Fitting Parameters and Fit Statistics for SPG-0 Fits to Oxygen with Ten Collision Partners

Collision Partner	A ($\times 10^{-12}$ cm^2)	γ	χ^2/ν	Fit Quality, D (%)	Data Quality, E (%)
He	84.1	0.53	4.79	7.21	3.46
Ne	91.9	0.60	3.82	6.38	3.44
Ar	140	0.62	4.37	6.62	3.32
Kr	165	0.66	7.64	6.48	2.49
Xe	130	0.55	6.10	6.05	2.59
N_2	119	0.55	5.98	5.73	2.48
CO	126	0.55	6.57	5.73	2.34
O_2	135	0.56	22.17	6.52	1.45
CO_2	105	0.50	15.80	9.22	2.43
SF_6	188	0.61	7.93	6.09	2.27

Table 65 presents the results of the SPG-Δ fits to the oxygen data. The γ values may correspond to r^{-n}, since all γ values are between 1.17 and 1.50. However the values don't correlate with the order of the intermolecular potential as well as one would hope. There is some evidence of an increasing trend of A with reduced mass.

Table 65. Fitting Parameters and Fit Statistics for SPG-Δ Fits to Oxygen with Ten Collision Partners

Collision Partner	A ($\times 10^{-12}$ cm^2)	γ	χ^2/ν	Fit Quality, D (%)	Data Quality, E (%)
He	81.8	1.28	3.82	6.44	3.46
Ne	92.4	1.37	4.09	6.61	3.44
Ar	134	1.37	2.62	5.13	3.32
Kr	155	1.41	5.32	5.41	2.49
Xe	132	1.32	4.42	5.14	2.59
N_2	118	1.31	3.21	4.19	2.48
CO	117	1.29	3.46	4.16	2.34
O_2	127	1.31	9.63	4.30	1.45
CO_2	105	1.25	9.67	7.21	2.43
SF_6	202	1.38	8.10	6.16	2.27

Table 66 presents the results of the EPGL-Δ fits to the oxygen data. The EPGL-Δ fits were nearly indistinguishable from the EPGL-0 fits, which were reported in Chapter IV.

Table 66. Results of EPGL-Δ Fits to O_2 A Band Broadening Cross Sections with Ten Different Perturbers

Collision Partner	A ($\times 10^{-12}$ cm^2)	β	γ	χ^2/ν	Fit Quality, D (%)	Data Quality, E (%)
He	61.0	0.27	1.17	3.69	6.16	3.46
Ne	76.6	0.12	1.31	4.80	6.97	3.44
Ar	70.2	0.69	1.27	1.22	3.41	3.32
Kr	83.8	0.66	1.18	3.24	4.11	2.49
Xe	104	0.26	1.22	4.29	4.92	2.59
N_2	81.1	0.39	1.17	2.21	3.38	2.48
CO	73.5	0.41	1.12	2.24	3.26	2.34
O_2	75.3	0.48	1.11	2.60	2.17	1.45
CO_2	53.3	0.77	0.99	4.85	4.98	2.43
SF_6	200	0.014	1.38	8.53	6.16	2.27

There are no clear trends shown in Table 66. The one notable item in the table is the approximately constant value of γ in the range from 0.99 to 1.38. The SPG-Δ, EPGL-Δ, and ECS-P (Δ) all have γ values which may be consistent with the impulsive classical interpretation $\gamma = n/(n-1)$, while the SPG-0 and EPGL-0 models are nowhere close. This might indicate that the Δ form of the degeneracy expression holds more physical significance than the 0 or λ forms.

Finally, it was stated in Chapter IV that the ECS-P and EPGL-0 were selected as the best fitting laws for the oxygen data set based on the fit statistics. The fit statistics for the six fits applied to the data set are listed in Table 67.

Table 67. Reduced Chi-Squared Values for Six Different RT Fitting Laws Fit to the Oxygen Pressure Broadening Cross Sections; Best Fits for Each Collision Partner are Indicated with Bold Type

Collision Partner	Fitting Law					
	EGL-0	SPG-0	SPG-Δ	EPGL-0	EPGL-Δ	ECS-P
He	4.21	4.79	3.82	**3.10**	3.69	4.10
Ne	7.07	3.82	4.09	**3.59**	4.80	7.62
Ar	2.41	4.37	2.62	1.42	**1.22**	1.29
Kr	5.83	7.64	5.32	3.38	**3.24**	3.74
Xe	6.96	6.10	4.42	**4.21**	4.29	5.43
N_2	4.56	5.98	3.21	2.32	**2.21**	2.82
CO	4.70	6.57	3.46	2.69	**2.24**	2.85
O_2	8.89	22.17	9.63	2.81	**2.60**	3.26
CO_2	15.69	15.80	9.67	6.01	4.85	**4.79**
SF_6	20.57	7.93	8.10	**6.60**	8.53	32.18
Average	8.09	8.52	5.43	3.61	3.77	3.99[*]

([*]ECS-P average is without SF_6; average with SF_6 is 6.81)

Based on reduced chi-squared, listed in Table 67, EPGL-0 and EPGL-Δ are the best overall fits to the O_2 data set. They are nearly indistinguishable, but EPGL-0 appears to be just slightly better. Aside from the poor fit to SF_6, ECS-P is the next overall best fit. SPG-Δ is almost as good as ECS-P. EGL-0 and SPG-0 are much poorer fits than the other four models.

of Osborne and McCaffery

(*Angular Momentum Based Fitting Law

from Osborne and McCaffery, J. Chem. Phys., 101, 5604 1994
state-to-state version, 5 Aug 98.*

```
<< Graphics`Graphics`

<< Statistics`NonlinearFit`

<< Graphics`MultipleListPlot`
```

(*Physical constants*)
```
h = 6.626 * 10^-27;  (* Planck's constant, erg sec *)
ℏ = 1.054592 * 10^-27;  (* Planck's constant/2π, erg sec *)
cL = 2.99792458 * 10^10;  (* velocity of light, cm/sec *)
kB = 1.38066 * 10^-16;  (* Boltzmann constant, erg/K *)
masscon = 1.66057 * 10^-24;   * unit conversion for mass, g amu *
lencon = 10^-8;  * unit conversion for length, cm Å *
```

(*Parameters for this fit*)
```
Be = 1.44566;  (* lower state rotational constant, cm^-1 *)
T = 296;  (* temperature, Kelvin *)
μamu = 3.5558 ;   * reduced mass of collision pair, amu *
μ = μamu * masscon;  * convert to cgs units *
```

(*Synthetic data: state-to-state rates, cm^3/sec*)
(*this data set is O_2 + He from ECS-P*)
```
Ji = 10; (* initial rotational levell *)
Jrange = 30; (* maximum ΔJ *)
kexp = {{2, 127. * 10^-13}, {4, 43.4 * 10^-13}, {6, 19.0 * 10^-13},
   {8, 8.83 * 10^-13}, {10, 4.14 * 10^-13}, {12, 1.90 * 10^-13}, {14, 8.47 * 10^-14},
   {16, 3.63 * 10^-14}, {18, 1.49 * 10^-14}, {20, 5.82 * 10^-15}, {22, 2.17 * 10^-15},
    24, 7.67 * 10^-16 , 26, 2.58 * 10^-16 , 28, 8.22 * 10^-17 , 30, 2.48 * 10^-17   ;
```

(*list manipulation;
adjust magnitude of data for numerical stability)
```
kexpflat = kexp // Flatten;
kexp12 = Table[{ΔJ, kexpflat[[ΔJ]] * 10^12}, {ΔJ, 2, Jrange, 2}];


kerr =
 Table[{x, kexpflat[[x]] * 0.1}, {x, 2, Jrange, 2}];  (*synthetic 10% error on each point*)


kerrflat = kerr // Flatten;
kwunnorm = Table[(1 / kerrflat[[x]])^2, {x, 2, Jrange, 2}];
kwsum = Sum kwunnorm x  , x, 1, Jrange 2, 1  ;
kweights = Table kwunnorm x   kwsum, x, 1, Jrange 2, 1  ;
```

(*Define ΔE and ΔJ, relate angular momentum transferred to ΔJ*)
ΔE[Jf_, Ji_] := h cL Be (Jf* (Jf + 1) - Ji* (Ji + 1)) ;
ΔJ := Jf - Ji;
ℓ[ΔJ_] := ℏ ΔJ;

(*Define relative velocity and threshold velocity required for energy and
  angular momentum conservation. Also define upper limit of integration.*)

$$v = \text{Table}\left[\text{vth}[ΔJ] = \sqrt{\frac{2\,ΔE[Jf, Ji]}{\mu}}\;, \{Jf, Ji + 1, Ji + Jrange\}\right];$$

$$b = \text{Table}\left[\text{bth}[ΔJ] = \frac{ℓ[ΔJ]}{\mu\,\text{vth}[ΔJ]}\;, \{Jf, Ji + 1, Ji + Jrange\}\right];$$

$$\text{vr}[ΔJ\_] = \frac{ℓ[ΔJ]^2 + (\mu\,\text{vth}[ΔJ]\,bn)^2}{2\,ℓ[ΔJ]\,\mu\,bn}\;;$$

(*Conditional probability density function (ℓ conditional on bn)*)

$$\text{dd}^\wedge\text{vr}[ΔJ\_] = \text{Abs}\left[\frac{1}{\mu\,bn} - \frac{ℓ[ΔJ]^2 + (\mu\,bn\,\text{vth}[ΔJ])^2}{2\,\mu\,bn\,ℓ[ΔJ]^2}\right];$$

$$\text{P}^\wedge\text{bn}[ΔJ\_] = 4\,\pi\,ℏ\,\left(\frac{\mu}{2\,\pi\,kB\,T}\right)^{3/2} \text{vr}[ΔJ]^2 \text{Exp}\left[-\frac{\mu\,\text{vr}[ΔJ]^2}{2\,kB\,T}\right] \text{dd}^\wedge\text{vr}[ΔJ];$$

(*Probability density function for bn*)
Pbn[γ_] = bn^{-γ};

(*McCaffery Fitting Law*)
ClearAll[kif] ;

$$\text{kif}[ΔJ\_, \text{bint}\_, c\_, γ\_] := c\,N\left[\int_0^{\text{bint}} \text{P}^\wedge\text{bn}[ΔJ]\,\text{Pbn}[γ]\,bn\,dbn\right];$$

(*Conditional statement to define the upper limit of integration*)
bint[ΔJ_, bnmax_] = If[b[[ΔJ]] > bnmax, bnmax, b[[ΔJ]]] ;

(*Calculate kif[ΔJ]*)
klist = {} ;
Do[
   temp[ΔJ, c, bnmax, γ] = kif[ΔJ, bint[ΔJ, bnmax] , c, γ] ;
   klist = Append[klist, {{ΔJ, temp[ΔJ, c, bnmax, γ]}}] ;
   , {Jf, Ji + 2, Ji + Jrange, 2}] ;
kflat1 = Flatten[klist, 1] ;
kflat = klist   Flatten;
TimeUsed

5814.77

269

```
(* Set up interpolating function *)
kinterp = Interpolation kflat1 ;
kinterp2 deltaJ_, c_, bnmax_, γ_ = kinterp deltaJ ;

HBL = 0.604 * lencon;
bfix = 1.01 * lencon;
(*Perform the Fit*)
NonlinearRegress[kexp12, kinterp2[deltaJ, c, bnmax, γ],
  deltaJ, c, .188324 , bnmax, 1.07192 * lencon , γ, 2.23976 ,
  Method -> LevenbergMarquardt, Weights -> kweights, ShowProgress -> True
```

Iteration:1 ChiSquared:6.96399×10^{-11} Parameters:
    0.188324, 1.07192×10^{-8}, 2.23976

Iteration:2 ChiSquared:6.96295×10^{-11} Parameters:
    0.188266, 1.07206×10^{-8}, 2.23979

Iteration:3 ChiSquared:6.88217×10^{-11} Parameters:
    0.182194, 1.07236×10^{-8}, 2.24148

$\{$BestFitParameters $\rightarrow \{$c $\rightarrow$ 0.182194, bnmax $\rightarrow 1.07236 \times 10^{-8}$, γ $\rightarrow$ 2.24148$\}$,

ParameterCITable $\rightarrow$ \$Failed, EstimatedVariance $\rightarrow 0. \times 10^{-12}$,

	DF	SumOfSq	MeanSq
Model	3	8.30695×10^{-9}	2.76898×10^{-9}
ANOVATable $\rightarrow$ Error	12	$0. \times 10^{-11}$	$0. \times 10^{-12}$
Uncorrected Total	15	8.37578×10^{-9}	
Corrected Total	14	7.31178×10^{-9}	

AsymptoticCorrelationMatrix $\rightarrow$ \$Failed, FitCurvatureTable $\rightarrow$ \$Failed

```
(*List and plot the results of the fit*)
kcalc[deltaJ_, c_, bnmax_, γ_] = kflat[[deltaJ]];
kfit = Table[{deltaJ, kcalc[deltaJ, .182194 * 10^-12, 1.07236 * lencon, 2.24148]},
  {deltaJ, 2, Jrange, 2}]
LogListPlot[kexp]
LogListPlot[kfit]
MultipleListPlot[kexp, kfit,
  PlotJoined -> {False, True}, SymbolShape -> {PlotSymbol[Box], None},
  PlotStyle ->   Thickness 0.005 , GrayLevel 0   ,
  AxesLabel -> "ΔJ", "Rate Coefficient  cm^3 sec " , PlotRange -> 0, 6.0 * 10^-11
```

$\{\{2, 1.10359 \times 10^{-11}\}, \{4, 3.75891 \times 10^{-12}\}, \{6, 1.69196 \times 10^{-12}\},$
$\{8, 8.20486 \times 10^{-13}\}, \{10, 4.02665 \times 10^{-13}\}, \{12, 1.94496 \times 10^{-13}\},$
$\{14, 9.02803 \times 10^{-14}\}, \{16, 3.97763 \times 10^{-14}\}, \{18, 1.65342 \times 10^{-14}\},$
$20, 6.45863 \times 10^{-15} , 22, 2.36439 \times 10^{-15} , 24, 8.09634 \times 10^{-16} ,$
$26, 2.5897 \times 10^{-16} , 28, 7.72964 \times 10^{-17} , 30, 2.15122 \times 10^{-17}$

- Graphics -

- Graphics -

271

Rate Coefficient (cm^3/sec)
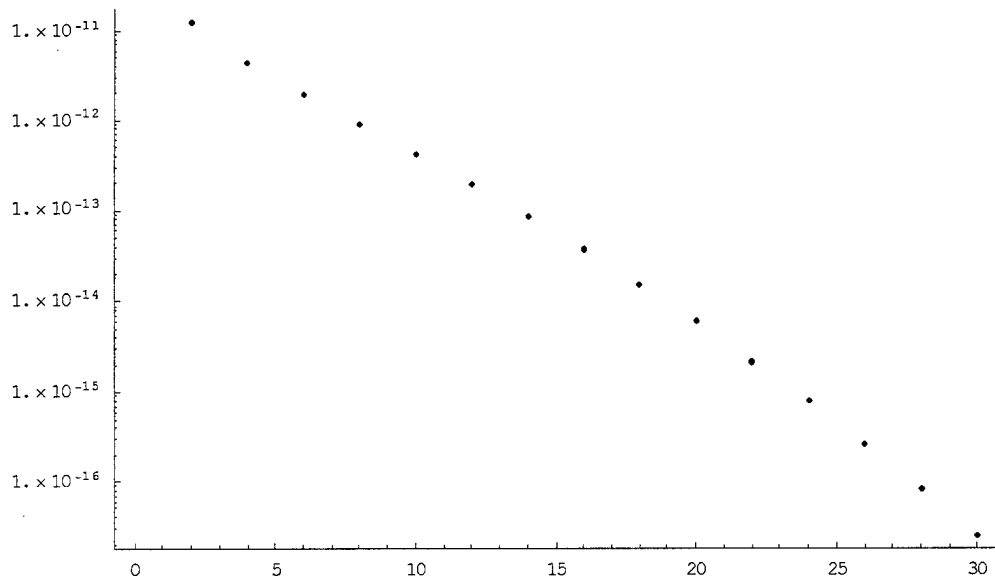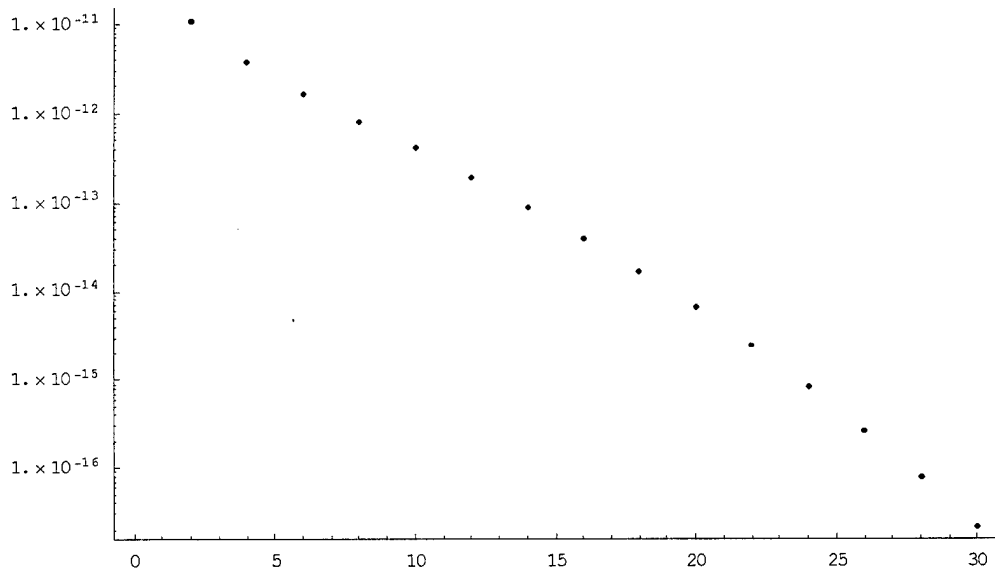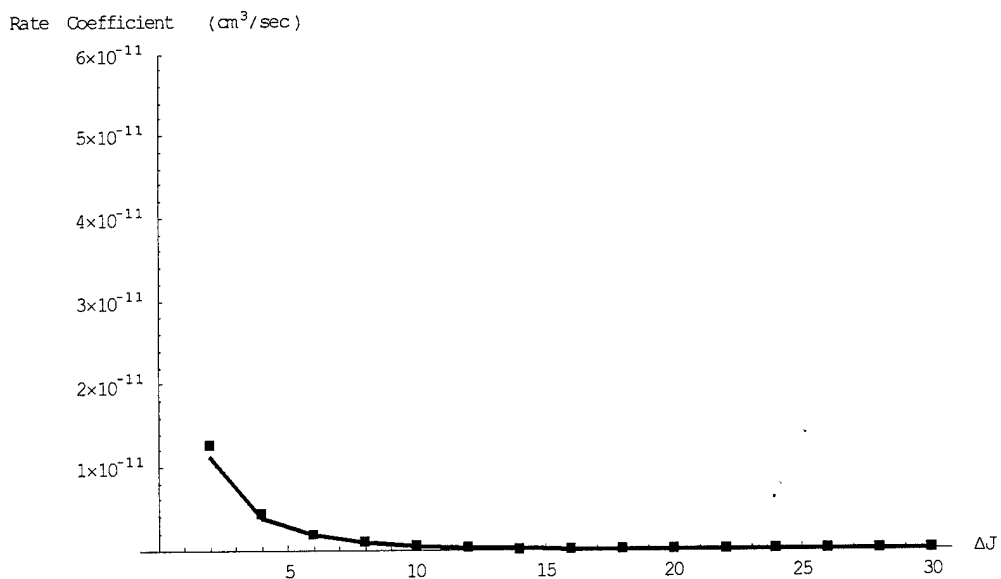
- Graphics -

(*Calculate Reduced Chi –Squared*)

kfitflat = kfit // Flatten;

freeparm = 3;

ndata = Jrange / 2;

ν = ndata - freeparm;

$$rcs = \frac{1}{\nu} \, Sum\left[\left(\frac{kexpflat_x - kfitflat_x}{kerrflat_x}\right)^2, \, x, \, 2, \, Jrange, \, 2\right]$$

1.02709

272

Bibliography

1. Ables, L. L., and DeBall, L. M. "Deviation from Lorentzian shape in the wings of collision-broadened infrared absorption lines of NO," *Journal of Quantitative Spectroscopy and Radiative Transfer*, 13: 663-667 (1973).

2. Abels, L. L., and Shaw, J. H. "Widths and strengths of vibration-rotation lines in the fundamental band of nitric oxide, " *Journal of Molecular Spectroscopy*, 20: 11-28 (1966).

3. Adiks, T. G. and Dianov-Klokov, V. I. "Shock shift of lines in the 0.762-μm band of oxygen and its effect on the transmission function in an inhomogeneous atmosphere," *Optics and Spectroscopy*, 30: 110-111 (1971).

4. Amiot, C., Bacis, R., and Guelachvili, G. "Infrared study of the $X^2\Pi$ v = 0, 1, 2 levels of $^{14}N^{16}O$. Preliminary results on the v = 0, 1 levels of $^{14}N^{17}O$, $^{14}N^{18}O$, and $^{15}N^{16}O$," *Canadian Journal of Physics*, 56: 251-265 (1978).

5. Anderson, P. W. "Pressure Broadening in the Microwave and Infra-Red Regions," *Physical Review*, 76: 647-661 (1949).

6. Andresen, P., Joswig, H., Pauly, H., and Schinke, R. "Resolution of interference effects in the rotation al excitation of NO (N = 0) by Ar," *Journal of Chemical Physics*, 77: 2204-2205 (1982).

7. Babcock, Harold D. and Herzberg, Luise. "Fine structure of the red system of atmospheric oxygen bands," *Astrophysical Journal*, 108: 167-190 (1948).

8. Ballard, J., Johnston, W. B., Kerridge, B. J., and Remedios, J. J. "Experimental spectral line parameters in the 1-0 band of nitric oxide," *Journal of Molecular Spectroscopy*, 127: 70-82 (1988).

9. Banwell, C. N. *Fundamentals of Molecular Spectroscopy*, Second Edition. London: McGraw-Hill, 1972.

10. Bell, Robert John. *Introductory Fourier Transform Spectroscopy*. New York: Academic Press, 1972.

11. Besley, Nicholas A., McCaffery, Anthony J., Osborne, Mark A., and Rawi, Zaid. "Quantized momentum mechanics of inelastic and reactive collisions; the role of energy and angular momentum constraints," submitted for publication, 1998.

12. Bevington, Philip R., and Robinson, D. Keith. *Data Reduction and Error Analysis for the Physical Sciences.* New York: McGraw-Hill Inc., 1992.

13. Bhattacharyya, Subir, Hazra, Anindya, and Ghosh, Pradip N. "Near-infrared diode laser spectroscopic study of Dicke narrowing and pressure broadening in the oxygen A-band," *Journal of Molecular Structure*, 327: 139-144 (1994).

14. Billingsley, F. P. II. "Calculated vibration-rotation intensities for $NO(X^2\Pi)$," *Journal of Molecular Spectroscopy*, 61: 53-70 (1976).

15. Birnbaum, George. "Microwave Pressure Broadening and Its Application to Intermolecular Forces," *Advances In Chemical Physics, Volume 12: Intermolecular Forces*, edited by Joseph O. Hirschfelder. New York: John Wiley and Sons, 1967.

16. Biswas, Debasish, Ray, Biswajit, and Ghosh, Pradip N. "He-broadening of the O_2 A-band transitions studied by diode laser spectroscopy," *Chemical Physics Letters*, 275: 314-318 (1997).

17. Blum, F. A., Nill, K. W., Calawa, A. R., and Harman, T. C. "Observation of nuclear hyperfine splitting in the infrared vibration-rotation absorption spectrum of the NO molecule," *Chemical Physics Letters*, 15: 144-146 (1972).

18. Boissoles, J., Boulet, C., Bonamy, L., and Robert, D. "Calculation of absorption in the microwindows of the 4.3 µm CO_2 band from an ECS scaling analysis," *Journal of Quantitative Spectroscopy and Radiative Transfer*, 42: 509-520 (1989).

19. Boissoles, J., Thibault, F., Khalil, B., and Boulet, C. "Line broadening and band profile of CO_2 in helium at 193 K," *SPIE Reports*, Volume 3090: 264-266 (1997).

20. Bonamy, J., Khayar, A., and Robert, D. "Fine structure dependence of the molecular line-broadening mechanism: application to the $^2\Pi_{1/2}$ and $^2\Pi_{3/2}$ states of NO perturbed by Ar and N_2," *Chemical Physics Letters*, 83: 539-544 (1981).

21. Bonczyk, P. A. "Pressure broadening of magnetically-tuned infrared absorption spectrum on NO using a CO laser," *Chemical Physics Letters*, 18: 147-149 (1973).

22. Bosanac, S. "Two-dimensional model of rotationally inelastic collisions," *Physical Review A*, 22: 2617-2622 (1980).

23. Boulet, C. and Boissoles, J. "Line mixing effects in the impact limit: ECS analysis of various experiments made on some IR bands of CO_2 in helium," *AIP Conference Proceedings 328: Spectral Line Shapes*, Volume 8. New York: AIP Press, 1995.

274

24. Brunner, Timothy A., Smith, Neil, Karp, Allan W., and Pritchard, David E. "Rotational energy transfer in $Na_2^*(A\Sigma)$ colliding with Xe, Kr, Ne, He, H_2, CH_4, and N_2: Experiment and fitting laws," *Journal of Chemical Physics*, 74: 3324-3341 (1981).

25. Brunner, Timothy A. and Pritchard, David. "Fitting laws for rotationally inelastic collisions," *Advances in Chemical Physics, Volume 50: Dynamics of the Excited State*, edited by K. P. Lawley. John Wiley and Sons, Ltd., 1982.

26. Bulanin, M. O., Dokuchaev, A. B., Tonkov, M. V., and Filippov, N. N. "Influence of line interferences on the vibration-rotation band shapes," *Journal of Quantitative Spectroscopy and Radiative Transfer*, 31: 521-543 (1984).

27. Burch, Darrell E. and Gryvnak, David A. "Strengths, widths, and shapes of the oxygen lines near 13,100 cm^{-1} (7620 Å)," *Applied Optics*, 8: 1493-1499 (1969).

28. Corey, G. C., McCourt, F. R., and Liu, W.-K. "Pressure-broadening cross sections of multiplet-Σ molecules: O_2-noble gas mixtures," *Journal of Physical Chemistry*, 88: 2031-2036 (1984).

29. Corey, Gregory C. and McCourt, Frederick R. "Infinite-order sudden calculations of pressure broadening cross sections for noble gas-oxygen binary mixtures," *Journal of Chemical Physics*, 81: 3892-3907 (1984).

30. Cornicelli, John Joseph. *Collisional Broadening of Spectral Lines in the X→b System of O_2 and the First Vibrational Band of NO by the Noble Gases*. MS thesis. Wright-Patterson AFB, Ohio: Graduate School of Engineering, Air Force Institute of Technology, December 1997. (AFIT/GAP/ENP/97D-01)

31. DeAngelis, M., L. Gianfrani, F. Pavone, A. Sasso, and G. M. Tino. "Temperature dependence of self-broadening in molecular oxygen spectrum," *Il Nuovo Cimento*, 18: 557-564 (1996).

32. Demtroder, Wolfgang. *Laser Spectroscopy*, Second Edition. Berlin: Springer, 1996.

33. DePristo, Andrew E. and Rabitz, Herschel. "Direct inversion of pressure-broadened half-widths to yield rotationally inelastic rate constants," *Journal of Molecular Spectroscopy*, 70: 476-480 (1978).

34. DePristo, Andrew E. "Collisional influences on vibration-rotation spectral line shapes: a scaling theoretical analysis and simplification," *Journal of Chemical Physics*, 73: 2145-2155 (1980).

35. Dexheimer, S. L., Durand, M., Brunner, T. A., and Pritchard, David E. "Dynamical constraints on the transfer of angular momentum in rotationally inelastic collisions of $I_2(B^3\Pi)$ with He and Xe," *Journal of Chemical Physics*, 76: 4996-5004 (1982).

36. Falcone, P. K., Hanson, R. K., and Kruger, C. H. "Tunable diode laser measurements of the band strength and collision halfwidths of nitric oxide," *Journal of Quantitative Spectroscopy and Radiative Transfer*, 29: 205-221 (1983).

37. Fanjoux, G., Millot, G., Saint-Loup, R., Chaux, R., and Rosenmann, L. "Coherent anti-Stokes Raman spectroscopy study of collisional broadening in the O_2-H_2O Q branch," *Journal of Chemical Physics*, 101: 1061-1071 (1994).

38. Galkin, V. D. "Broadening of oxygen absorption lines in the air in the 762- and 688-nm regions," *Optics and Spectroscopy*, 57: 616-620 (1984).

39. Galkin, V. D. "Line shifts in the A oxygen band as a function of the pressure," *Optics and Spectroscopy*, 35: 630-633 (1973).

40. Garside, B. K., Ballik, E. A., Elsherbiny, M., and Shewchun, J. "Resonance absorption measurements of NO with a line-tunable CO laser: spectroscopic data for pollution monitoring," *Applied Optics*, 16: 398-402 (1977).

41. Gersten, Joel I. and Henry M. Foley. "Theory of Pressure Broadening of Microwave Spectral Lines," *Physical Review*, 182: 24-38 (1969).

42. Gillette, R. H. and Eyster, Eugene H. "The fundamental rotation-vibration band of nitric oxide," *Physical Review*, 56: 1113-1119 (1939).

43. Giver, Lawrence P., Boese, Robert W., and Miller, Jacob B. "Intensity measurements, self-broadening coefficients, and rotational intensity distribution for lines of the oxygen B band at 6880 Å," *Journal of Quantitative Spectroscopy and Radiative Transfer*, 14: 793-802 (1974).

44. Goldman, A., and Schmidt, S. C. "Infrared spectral line parameters and absorptance calculations of NO at atmospheric and elevated temperatures for the $\Delta v = 1$ bands region," *Journal of Quantitative Spectroscopy and Radiative Transfer*, 15: 127-138 (1975).

45. Gordon, R. G. "On the pressure broadening of molecular multiplet spectra," *Journal of Chemical Physics*, 46: 448-455 (1967).

46. Graham, C., Imrie, D. A., and Raab, R. E. "Measurement of the electric quadrupole moments of CO_2, CO, N_2, Cl_2 and BF_3," *Molecular Physics*, 93: 49-56 (1998).

47. Green, Sheldon, Monchick, Louis, Goldflam, Rudolf, and Kouri, Donald J. "Computational tests of angular momentum decoupling approximations for pressure broadening cross sections," *Journal of Chemical Physics*, 66: 1409-1412 (1977).

48. Hanson, R. K., Monat, J. P., and Kruger, C. H. "Absorption of CO laser radiation by NO," *Journal of Quantitative Spectroscopy and Radiative Transfer*, 16: 705-713 (1976).

49. Hastings, N. A. J., and Peacock, J. B. *Statistical Distributions*. London: Butterworth and Co. Ltd., 1975.

50. Hawkins, Robert. DUDV Computer Program. Air Force Research Laboratory, Space Vehicles Directorate, Hanscom AFB, MA (Private Communication), 1998.

51. Henry, A. Severin, F., and Henry, L. "Magnetic moment effect on pressure broadening: lines from the $^2\Pi_{1/2}$ and $^2\Pi_{3/2}$ states of the (1-0) band of NO colliding with N_2 and Ar," *Journal of Molecular Spectroscopy*, 75: 495-497 (1979).

52. Herzberg, Gerhard. *Molecular Spectra and Molecular Structure, Volume I: Spectra of Diatomic Molecules*, Second Edition. New York: Van Nostrand Reinhold (Litton Educational Publishing), 1950.

53. Hindimarsh, W. R. and Farr, Judith, M. "Collision Broadening of Spectral lines by Neutral Atoms," *Progress in Quantum Electronics*, Volume 2, Oxford: Pergammon Press, 1972.

54. Hirschfelder, Joseph O., Curtiss, Charles F., and Bird, R. Byron. *Molecular Theory of Gases and Liquids*. New York: John Wiley and Sons Inc, 1954.

55. Hirono, Mikihiko, and Ichikawa, Kenji. "Line shapes in the R-branch of the 5.3 μm NO band," *Optical Review*, 4: 362-365 (1997).

56. HITRAN 1996 Atmospheric Transmission Database, edited by Dr. Laurence S. Rothman, Air Force Research Laboratory, Hanscom AFB, MA.

57. HITRAN Website. *Reference Tables* (list of data sources for HITRAN 96), n. pag. WWWeb, http://www.hitran.com/Download/TABLE_97.TXT. 23 June 1998.

58. Houdeau, J. P., Boulet, C., Bonamy, J., Khayar, A., and Guelachvili, G. "Air broadened NO linewidths in a temperature range of atmospheric interest," *Journal of Chemical Physics*, 79: 1634-1640 (1983).

59. Hourri, A., St-Arnaud, J. M., and Bose, T. K. "Dielectric and pressure virial coefficients of imperfect gases: CO_2-SF_6 mixtures," *Journal of Chemical Physics*, 106: 1780-1785 (1997).

60. Hoy, A. R., Johns, J. W. C., and McKellar, A. R. W. "Stark spectroscopy with the CO laser: dipole moments, hyperfine structure, and level crossing effects in the fundamental band of NO," *Canadian Journal of Physics*, 53: 2029-2039 (1975).

61. James, T. C. "Intensity of the forbidden $X^2\Pi_{3/2}$ - $X^2\Pi_{1/2}$ satellite bands in the infrared spectrum of nitric oxide," *Journal of Chemical Physics*, 40: 762-771 (1964).

62. Jansson, Peter A. *Deconvolution with Applications in Spectroscopy*. Orlando, FL: Academic Press Inc., 1984.

63. Kauranen, P. and Avetisov, V. G. "Determination of absorption line parameters using two-tone frequency modulation spectroscopy with diode lasers," *Optics Communications*, 106: 213-217 (1994).

64. Kearns, David R. "Physical and chemical properties of singlet molecular oxygen," *Chemical Reviews*, 71: 395-411 (1971).

65. Kronfeldt, H.-D., Basar, G., and Sumpf, B. "Application of a CW tunable infrared spectrometer based on difference-frequency generation in $AgGaS_2$ for self-broadening investigations of NO at 5 μm," *Journal of the Optical Society of America B*, 13: 1859-1863 (1996)

66. Kunimori, K., Horiguchi, H., and Tsuchiya, S. "Intensity and line-width measurements of the NO fundamental by infrared molecular absorption spectrometry," *Journal of Quantitative Spectroscopy and Radiative Transfer*, 19: 127-133 (1978).

67. Lavorel, B., Millot, B., Bonamy, J., and Robert, D. "Study of rotational relaxation fitting laws from calculation of SRS N_2 Q branch," *Chemical Physics*, 115: 69-78 (1987).

68. Lempert, W., Rosasco, G. J., and Hurst, W. S. "Rotational collisional narrowing in the NO fundamental Q branch, studied with cw stimulated Raman spectroscopy," *Journal of Chemical Physics*, 81: 4241-4245 (1984).

69. Levy, Armand, Lacome, Nelly, and Chackerian, Charles Jr. "Collisional Line Mixing," *Spectroscopy of the Earth's Atmosphere and Interstellar Medium*, edited by K. Narahari Rao and Alfons Weber. Boston: Academic Press, 1992.

70. Lundqvist, S., Margolis, J., and Reid, J. "Measurements of pressure-broadening coefficients of NO and O_3 using a computerized tunable diode laser spectrometer," *Applied Optics*, 21: 3109-3113 (1982).

71. Mandin, J.-Y., Amiot, C., and Guelachvili, G. "Intensity and self broadening coefficient measurements from Fourier transform spectra: application to the nitric oxide fundamental band," *Annales de Physique*, 5: 91-112 (1980).

72. *Mathematica*, Version 3.0, Champaign, IL: Wolfram Research Inc., 1996.

73. McCaffery, A. J. and Alwahabi, Z. T. "Mechanism of rotational transfer," *Physical Review A*, 43: 611-614 (1991).

74. McCaffery, Anthony J., Alwahabi, Zeyad T., Osborne, Mark A., and Williams, Colin J. "Rotational transfer, an angular momentum model," *Journal of Chemical Physics*, 98: 4586-4602 (1993).

75. McCaffery, Anthony J. and Wilson, Ruth J. "Atom-molecule scattering: classical simplicity beneath quantum complexity," *Physical Review Letters*, 77: 48-50 (1996).

76. McCaffery, Anthony J. and Wilson, Ruth J. "Evidence for hybrid classical-quantal behavior in state- and angle-resolved atom-diatom scattering," *Journal of Physics B*, 30: 5773-5789 (1997).

77. McCurdy, Clyde W., and Miller, William H. "Interference effects in rotational state distributions: propensity and inverse propensity," *Journal of Chemical Physics*, 67: 462-468 (1977).

78. Miller, J. H., Boese, R. W., and Giver, L. P. "Intensity measurements and rotational intensity distribution for the oxygen A-band," *Journal of Quantitative Spectroscopy and Radiative Transfer*, 9: 1507-1517 (1969).

79. Millot, G. "Rotationally inelastic rates over a wide temperature range based on an energy corrected sudden-exponential-power theoretical analysis of Raman line broadening coefficients and Q branch collapse." Journal of Chemical Physics, 93: 8001-8010 (1990).

80. Millot, G., Saint-Loup, R., Santos, J., Chaux, R., Berger, H., and Bonamy, J. "Collisional effects in the stimulated Raman Q branch of O_2 and O_2-N_2," *Journal of Chemical Physics*, 96: 961-971 (1992).

81. Neiss, T. G. and Lovejoy, R. W. "Pressure broadening coefficients of $^{14}N^{16}O$-N_2 gas mixtures," *Journal of Molecular Spectroscopy*, 124: 229-235 (1987).

82. Nill, K. W., Blum, F. A., Calawa, A. R., and Harman, T. C. "Observation of L-doubling and Zeeman splitting in the fundamental infrared absorption band of nitric oxide," *Chemical Physics Letters*, 14: 234-238 (1972).

83. Orlikowksi, Tadeusz, and Alexander, Millard H. "Quantum studies of inelastic collisions of $NO(X^2\Pi)$ with Ar," *Journal of Chemical Physics*, 79: 6006-6016 (1983).

84. Osborne, Mark A. Private communication (1998).

85. Osborne, Mark A., Marks, Alison J., and McCaffery, Anthony J. "A simple model indicating the origin of the angular momentum gap law in rotational transfer," *Journal of Physical Chemistry*, 100: 3888-3891 (1996).

86. Osborne, Mark A. and McCaffery, Anthony J. "A fitting law for rotational transfer rates: an angular momentum model with predictive power," Journal of Chemical Physics, 101: 5604-5614 (1994).

87. Osborne, M. A. and McCaffery, A. J. "Recovery of the intermolecular potential from inelastic transfer cross sections," *Journal of Physical Chemistry*, 100: 13346-13347 (1996).

88. *PCDA Software User's Guide*, Revision 1.1. Quebec: Bomem, Inc, 1993.

89. *Peak Fit User's Manual*. AISN Software, Inc., 1995.

90. *Periodic Chart of the Atoms*, Revised Edition 1979, Catalog No. S-18808-10, Sargent-Welch Scientific Company, Skokie, IL, 1979.

91. Perram, G. P., Determan, D. A., Dorian, J. A., Lowe, B. F., and Thompson, T. L. "Radial diffusion between coaxial cylinders and surface deactivation of $O_2(b^1\Sigma_g^+)$," *SPIE Proceedings*, volume 1871: 181-192 (1993).

92. Phillips, William Joe. *Pressure Broadening Effects on the Lambda Doublets of Nitric Oxide*. PhD Dissertation. The University of Tennessee, Knoxville, March 1986.

93. Phillips, W. J. and Walker, H. C. "Nitrogen-broadened linewidths and strengths of nitric oxide utilizing tunable diode laser spectroscopy," *Journal of Chemical Physics*, 85: 3211-3216 (1986).

94. Pine, A. S., Johns, J. W. C., and Robiette, A. G. "Λ-doubling in the $v = 2 \leftarrow 0$ overtone band in the infrared spectrum of NO," *Journal of Molecular Spectroscopy*, 74: 52-69 (1979).

95. Pine, A. S., Maki, A. G., and Chou, N. Y. "Pressure broadening, lineshapes, and intensity measurements in the $2 \leftarrow 0$ band of NO," *Journal of Molecular Spectroscopy*, 114: 132-147 (1985).

96. Pine, A. S. "Photoacoustic measurement of differential broadening of the Λ doublets in NO($X^2\Pi_{1/2}$, v=2-0) by Ar," *Journal of Chemical Physics*, 91: 2002-2009 (1989)

97. Pine, A. S. "Self-, N_2- and Ar-broadening and line mixing in HCN and C_2H_2," *Journal of Quantitative Spectroscopy and Radiative Transfer*, 50: 149-166 (1993).

98. Pope, R. S., Wolf, P. J., Perram, G. P., and Cornicelli, J. J. "Collision broadening of spectral lines in the $X^3\Sigma_g^- \rightarrow b^1\Sigma_g^+$ system of O_2," CP430, *Fourier Transform Spectroscopy*: 11th International Conference, edited by J. A. de Haseth. American Institute of Physics, 1998. (1-56396-746-4/98)

99. Procaccia, I. and Levine, R. D. "Rotational excitation of HD by collisions with He," *Physica A*, 82: 623-630 (1976).

100. Rabitz, Hershel. "Rotation and Rotation-Vibration Pressure-Broadened Spectral Lineshapes," *Annual Review of Physical Chemistry*, Volume 25, Palo Alto, CA: Annual Reviews Inc., 1974.

101. Rahn, L. A., and Palmer, R. E. "Studies of nitrogen self-broadening at high temperature with inverse Raman spectroscopy," *Journal of the Optical Society of America*, 3: 1164-1169 (1986).

102. Ralston, Mary L., and Jennrich, Robert I. "Dud, a derivative-free algorithm for nonlinear least squares," Technometrics, 20: 7-14 (1978).

103. Ray, Biswajit and Ghosh, Pradip N. "Collisional narrowing and pressure broadening of the oxygen A-band transitions," *Spectrochimica Acta Part A*, 53: 537-543 (1997).

104. Ray, Biswajit, Biswas, Debasish, and Ghosh, Pradip N. "Diode laser spectroscopic study of the O_2 A-band line shape perturbed by N_2," *Journal of Molecular Structure*, 407: 39-46 (1997).

105. Richton, R. E. "NO line parameters measured by CO laser transmittance," *Applied Optics*, 15: 1686-1687 (1976).

106. Ritter, Kenneth James. *A High Resolution Spectroscopic Study of Absorption Line Profiles in the A-Band of Molecular Oxygen*. PhD Dissertation. The University of Maryland, 1986.

107. Ritter, K. J. and Wilkerson, T. D. "High-resolution spectroscopy of the oxygen A band," *Journal of Molecular Spectroscopy*, 121: 1-19 (1987).

108. Robert, D. and J. Bonamy. "Short range force effects in semiclassical molecular line broadening calculations," *Journal de Physique*, 40: 923-942 (1979).

109. Rohrbeck, W., Winter, R., Herrmann, W., Wildt, J., and Urban, W. "Pressure broadening coefficients for nitric oxide, measured with a spin-flip Raman-laser spectrometer," *Molecular Physics*, 39: 673-681 (1980).

110. Rothman, L. S. *et al.* "The HITRAN molecular database: editions of 1991 and 1992," *Journal of Quantitative Spectroscopy and Radiative Transfer*, 48: 469-507 (1992).

111. Scott, Thomas P., Smith, Neil, and Pritchard, David E. "Application of fitting laws to rotationally inelastic rate constants: $Li_2^*(A^1\Sigma)$+Ne, Ar, Xe," *Journal of Chemical Physics*, 80: 4841-4850 (1984).

112. Sell, J. A. "Infrared diode laser spectroscopy of nitric oxide," *Journal of Quantitative Spectroscopy and Radiative Transfer*, 25: 19-24 (1981).

113. Serri, J. A., Bilotta, R. M., and Pritchard, D. E. "Classical two-dimensional model for rotational-vibrational atom-diatom inelastic scattering," *Journal of Chemical Physics*, 77: 2940-2946 (1982).

114. Smith, Earl W., M. Giraud, and J. Cooper. "A Semiclassical theory for spectral line broadening in molecules," *Journal of Chemical Physics*, 65: 1256-1267 (1976).

115. Smith, Arlee V., and Johnson, A. Wayne. "Rotational transfer rates and propensity rule in nitric oxide-rare gas collisions," *Chemical Physics Letters*, 93: 608-612 (1982).

116. Smith, Earl W. "Absorption and dispersion in the O_2 microwave spectrum at atmospheric pressures," *Journal of Chemical Physics*, 74: 6658-6673 (1981).

117. Smith, Neil and Pritchard, David E. "Simple analytical approximation for rotationally inelastic rate constants based on the energy corrected sudden scaling law," *Journal of Chemical Physics*, 74: 3939-3946 (1981).

118. Spencer, M. N., Chackerian, C. Jr., Giver, L. P., and Brown, L. R. "The nitric oxide fundamental band: frequency and shape parameters for rovibrational lines," *Journal of Molecular Spectroscopy*, 165: 506-524 (1994).

119. Spencer, M. N., Chackerian, C. Jr., Giver, L. P., and Brown, L. R. "Temperature dependence of nitrogen broadening of the NO fundamental vibrational band," *Journal of Molecular Spectroscopy*, 181: 307-315 (1997).

120. Steel, W. H. "Interferometers without collimation for Fourier spectroscopy," *Journal of the Optical Society of America*, 54: 151-156 (1964).

121. Steinfeld, Jeffery I. *Molecules and Radiation: An Introduction to Modern Molecular Spectroscopy*, second edition, Cambridge, MA: The MIT Press, 1993.

122. Steinfeld, Jeffery I., Franscisco, Joseph S., and Hase, William L. *Chemical Kinetics and Dynamics*, Englewood Cliffs, NJ: Prentice-Hall, 1989.

123. Steinfeld, J. I., Ruttenberg, P., Millot, G., Fanjoux, G., and Lavorel, B. "Scaling laws for inelastic collision processes in diatomic molecules," *Journal of Physical Chemistry*, 95: 9638-9647 (1991).

124. Sudbo, A. S., and Loy, M. M. T. "Measurement of absolute state-to-state rate constants for collision-induced transitions between spin-orbit and rotational states of NO ($X^2\Pi$, v=2)," *Journal of Chemical Physics*, 76: 3646-3654 (1982).

125. Sudbo, A. S., and Loy, M. M. T. "State-to-state rotational and electronic collisional relaxation study of nitric oxide," *Chemical Physics Letters*, 82: 135-137 (1981).

126. Taylor, John R. *An Introduction to Error Analysis*. Mill Valley, CA: University Science Books, 1982.

127. Tejwani, G. D. T., Golden, Bruce M., and Yeung, Edward S. "Pressure-broadened linewidths of nitric oxide," *Journal of Chemical Physics*, 65: 5110-5114 (1976).

128. Tsao, C. J. and B. Curnutte. "Line-widths of pressure-broadened spectral lines," *Journal of Quantitative Spectroscopy and Radiative Transfer*, 2: 41-91 (1962).

129. Varghese, Philip L. and Hanson, Ronald K. "Collisional narrowing effects on spectral line shapes measured at high resolution," *Applied Optics*, 23: 2376-2385 (1984).

130. Weast, Robert C., editor. *CRC Handbook of Chemistry and Physics*, 70th Edition, Boca Raton, FL: CRC Press Inc, 1990.

131. Weber, D., and Penner, S. S. "Rotational line-width measurements on NO, HCl, and HBr," *Journal of Chemical Physics*, 21: 1503-1506 (1953).

132. Weber, Mark, Sirota, J. Marcos, and Reuter, Dennis C. "*l*-resonance intensity effects and pressure broadening of N_2O at 17 μm," *Journal of Molecular Spectroscopy*, 177: 211-220 (1996).

133. Whiteley, T. W. J. and McCaffery A. J. "Angular momentum analysis of rotational transfer of superthermal relative velocity distributions," *Journal of Physics B*, 29: 6133-6141 (1996).

<u>Vita</u>

Captain Robert S. Pope was born on 2 March 1969 in Crawfordsville, Indiana. He graduated from Clare High School in Clare, Michigan in 1987 and attended Michigan State University, graduating with honors with a Bachelor of Science in Physics in June 1991. While at Michigan State University, he participated in the Air Force ROTC program, graduating from the program as a Distinguished Graduate and receiving his commission.

His first assignment was to the Air Force Institute of Technology, Wright-Patterson AFB, Ohio, where he graduated with a Master of Science in Nuclear Effects Physics in March 1993. Captain Pope's next assignment was to the Technical Operations Division, McClellan AFB, California, where he served as the Chief of the Nuclear Development Branch, in charge of developing new radiation detection technologies in support of nuclear weapons treaty monitoring. His third assignment brought him back to the Air Force Institute of Technology, where he entered the Doctor of Philosophy program in physics, starting in July 1995. In September 1998, Captain Pope transferred to the National Air Intelligence Center, Wright-Patterson AFB, Ohio, where he serves as a High-Energy Laser Weapons Analyst.

Permanent Address: 1305 Park Street
Clare, MI 48617

Robert_Pope@msn.com

REPORT DOCUMENTATION PAGE

Form Approved
OMB No. 0704-0188

Public reporting burden for this collection of information is estimated to average 1 hour per response, including the time for reviewing instructions, searching existing data sources, gathering and maintaining the data needed, and completing and reviewing the collection of information. Send comments regarding this burden estimate or any other aspect of this collection of information, including suggestions for reducing this burden, to Washington Headquarters Services, Directorate for Information Operations and Reports, 1215 Jefferson Davis Highway, Suite 1204, Arlington, VA 22202-4302, and to the Office of Management and Budget, Paperwork Reduction Project (0704-0188), Washington, DC 20503.

1. AGENCY USE ONLY *(Leave blank)*	2. REPORT DATE	3. REPORT TYPE AND DATES COVERED
	March 1999	Doctoral Dissertation

4. TITLE AND SUBTITLE
COLLISIONAL EFFECTS IN THE ABSORPTION SPECTRA OF THE OXYGEN A BAND AND NITRIC OXIDE FUNDAMENTAL BAND

5. FUNDING NUMBERS

6. AUTHOR(S)
Robert S. Pope, Captain, USAF

7. PERFORMING ORGANIZATION NAME(S) AND ADDRESS(ES)
Air Force Institute of Technology
2950 P Street, Bldg 640
Wright-Patterson AFB, OH 45433-7765

8. PERFORMING ORGANIZATION REPORT NUMBER

AFIT/DS/ENP/98-03

9. SPONSORING/MONITORING AGENCY NAME(S) AND ADDRESS(ES)
Air Force Research Laboratory/VSBM
29 Randolph Road
Hanscom AFB, MA 01731
Attn: Dr. Michael Hoke

10. SPONSORING/MONITORING AGENCY REPORT NUMBER

11. SUPPLEMENTARY NOTES

12a. DISTRIBUTION AVAILABILITY STATEMENT
Approved for public release; distribution unlimited

12b. DISTRIBUTION CODE

13. ABSTRACT *(Maximum 200 words)*
Fourier transform spectroscopy was used to measure pressure broadening coefficients in the absorption spectra of both the oxygen A band and the nitric oxide fundamental band. Oxygen spectra were recorded with O2, N2, CO, CO2, SF6 and noble gas collision partners, while nitric oxide spectra were recorded using noble gas collision partners. Pressure broadening coefficients were determined in the P and R branches for every resolved line for each of the fifteen collision pairs studied. In addition, broadening coefficints and qualitative evidence of line coupling were found for the Q branch of NO+Ar and pressure-induced line shifting coefficients were measured for O2+Xe. Elastic and inelastic theories of pressure broadening were used to interpret the observed broadening coefficients. The elastic model showed a strong correlation between the magnitude of the coefficientss and the polarizability and mass of the perturber. The inelastic contribution to pressure broadening was modeled using both angular-momentum-based and energy-based fitting laws. The ECS-P and EPGL-0 laws provided the best fits to the data. The results indicate that the inelastic component is an important contribution to collisional broadening in diatomic molecules and that angular-momentum transfer is a plausible governing mechanism for the inelastic collisions.

14. SUBJECT TERMS
Pressure broadening, oxygen A band, nitric oxide fundamental band, collisions, fitting laws

15. NUMBER OF PAGES
306

16. PRICE CODE

17. SECURITY CLASSIFICATION OF REPORT	18. SECURITY CLASSIFICATION OF THIS PAGE	19. SECURITY CLASSIFICATION OF ABSTRACT	20. LIMITATION OF ABSTRACT
Unclassified	Unclassified	Unclassified	UL